

CRANFIELD UNIVERSITY

Edouard Berrocal

**MULTIPLE SCATTERING OF LIGHT IN OPTICAL
DIAGNOSTICS OF DENSE SPRAYS AND OTHER
COMPLEX TURBID MEDIA**

School of Engineering

Ph.D. Thesis

2006

CRANFIELD UNIVERSITY

School of Engineering

Ph.D. Thesis 2006

Edouard Berrocal

**MULTIPLE SCATTERING OF LIGHT IN OPTICAL
DIAGNOSTICS OF DENSE SPRAYS AND OTHER
COMPLEX TURBID MEDIA**



Supervisor: Dr. Igor V. Meglinski

**This thesis is submitted in partial fulfillment of the requirements for the degree of
Doctor of Philosophy**

**© Cranfield University 2009 . All Rights Reserved. No part of this publication may be
reproduced without the written permission of the copyright holder.**

“The reasonable man adapts himself to the world; the unreasonable one persists in trying to adapt the world to himself. Therefore, all progress depends on the unreasonable.”

George Bernard Shaw (1856-1950).

Abstract

SPRAYS and other industrially relevant turbid media can be quantitatively and qualitatively characterized using modern optical diagnostics. However, current laser based techniques generate errors in the dense region of sprays due to the multiple scattering of laser radiation effected by the surrounding cloud of droplets. In most industrial sprays, the scattering of light occurs within the so-called intermediate scattering regime where the average number of scattering events is too great for single scattering to be assumed, but too few for the diffusion approximation to be applied. An understanding and adequate prediction of the radiative transfer in this scattering regime is a challenging and non-trivial task that can significantly improve the accuracy and efficiency of optical measurements. A novel technique has been developed for the modelling of optical radiation propagation in inhomogeneous polydisperse scattering media such as sprays. The computational model is aimed to provide both predictive and reliable information, and to improve the interpretation of experimental results in spray diagnostics. Results from simulations are verified against the analytical approach and validated against the experiment by the means of homogeneous solutions of suspended polystyrene spheres. The ability of the technique to simulate various detection conditions, to differentiate scattering orders and to generate real images of light intensity distributions with high spatial resolution is demonstrated. The model is used for the real case of planar Mie imaging through a typical hollow cone water spray. Versatile usage of this model is exemplified with its applications to image transfer through turbid media, correction of experimental Beer-Lambert measurements, the study of light scattering by single particles in the far-field region, and to simulate the propagation of ultra-short laser pulses within complex scattering media. The last application is fundamental for the development and testing of future optical spray diagnostics; particularly for those based on time-gating detection such as ballistic imaging.

Acknowledgements

FIRST of all I would like to truly thank my supervisor Dr. Igor Meglinski for his encouragement and guidance throughout the years. This thesis would not have been possible without his supervision. I am also sincerely grateful to Dr. Mark Jermy who initially gave me the opportunity to work on such an interesting project. I wish to thank the financial support of the Engineering and Physical Sciences Research Council (contract GR/R92653) who funded this project.

I would like to acknowledge Dr. Dmitry Churmakov for his valuable help in C programming and Dr. Girasole for his recommendations about MC modelling. I would like to thank Prof. Mark Linne who was at the origin of three month collaboration project with Lund University (Sweden). This collaboration work was supported by the European Union Large Scale Facility program (Laserlab Europe - project LLC001131). I am particularly grateful to Dr. Megan Paciaroni who kindly gave some of her time to read and correct this thesis.

I owe a debt of gratitude to all my friends over my four past years at Cranfield who cheered me up. As citing them all might take too long, I just would like to mention those who shared the PhD student office with me: Alessio Bonaldo, Adam Ruggles, Fatiha Moukaideche, Andrew Morrison, Eudoxios Theodorodos, Nicholas Kershaw, Christelle Magand, Eduardo Correia, Maz Hussain, Claudio Santos, Taib Mohamad and Yehya Al-Hadban. I would also like to thank Dr. Thierry Réveillé and David Sedarsky for useful and stimulating discussions. As promised I do not forget to mention my close friends, Ben, Sergio, Will, Jess, Claire, Marco, Caroline and many other, for their active “*msn*” support. I also wish to acknowledge Mrs. Binnie Hunt, Mrs. Barbara McGowan and Mrs. Catriona Rolf for solving many daily problems and Mrs. Audrey Hinson for kindly serving me 2928 ± 3 coffees during my time at Cranfield.

Most importantly, I would like to thank all my family for their much appreciated help and constant encouragement during this period of my life.

Contents

Abstract	iii
Acknowledgements	v
Nomenclature	xiii
1 Introduction	1
2 Characteristics and Generation of Sprays	7
2.1 Spray properties	8
2.1.1 Applications of sprays	8
2.1.2 Spray structure	10
2.1.3 Properties influencing spray formation	14
2.2 Disintegration process and droplets formation	20
2.2.1 Disintegration regimes	20
2.2.2 Breakup of droplets	23
2.2.3 Size distribution, number density and velocity of droplets	26
3 Optical Diagnostics of Dilute and Dense Sprays	31
3.1 Commonly used laser techniques	32
3.1.1 Fraunhofer diffraction	32
3.1.2 Point interferometry	34

3.1.3	Planar laser imaging	39
3.1.4	Limitation of current techniques	47
3.2	Emerging laser technics	50
3.2.1	Interferometric laser imaging	50
3.2.2	X-ray absorption	53
3.2.3	Double extinction	55
3.2.4	Ballistic imaging	58
3.2.5	Limitation of the new techniques	60
4	Propagation of Laser Radiation in Sprays	63
4.1	Terminology and definition	64
4.1.1	Extinction, scattering and absorption	64
4.1.2	Scattering orders, optical depth and scattering regime	68
4.1.3	Scattering phase function	72
4.2	Light-droplets interaction	75
4.2.1	Principles of scattering	75
4.2.2	Principles of absorption	81
4.2.3	Scattering of laser light by a single spray droplet	82
4.2.4	Scattering of laser light with a collection of droplets	85
5	Modelling of Photon Transport	87
5.1	Deterministic and stochastic models	88
5.1.1	Electromagnetic theory	88
5.1.2	Radiative transfer theory	89
5.1.3	The Monte Carlo (MC) technique	90
5.1.4	Modelling requirements	92

5.2	Development of the MC model	93
5.2.1	Assumptions	93
5.2.2	Implementation of the MC simulations	95
5.2.3	Classification of the MC codes	99
6	Verification and Validation of the Monte Carlo Model	103
6.1	Comparison against analytical results	104
6.1.1	Analytical description of low scattering orders	104
6.1.2	Description of the MC simulation	107
6.1.3	Comparison and discussion	109
6.2	Comparison against experimental results	112
6.2.1	Experimental setup and MC simulation description	112
6.2.2	Forward scattering detection	117
6.2.3	Side scattering detection	132
6.3	Verification of the phase function approximation	140
6.3.1	Calculation method	140
6.3.2	Description of the simulation	142
6.3.3	Results and comparison	143
7	Applications of Monte Carlo Simulations to Spray Diagnostics	151
7.1	Optical measurements and MC simulations of a hollow cone spray . . .	152
7.1.1	Experiments	152
7.1.2	Monte Carlo simulation	158
7.1.3	Comparison discussion	162
7.2	Crossed source-detector geometry analysis for spray diagnostics	164
7.2.1	Description of the MC simulations	164

7.2.2	Results and analysis for isotropic scattering	166
7.2.3	Results and analysis for anisotropic scattering	171
7.2.4	Comparisons and discussion	176
8	General Results of Monte Carlo Simulations	181
8.1	3D Investigation of light scattering by single spherical particles	182
8.1.1	Scattering by a single fuel droplet	183
8.1.2	Scattering from an averaged scattering phase-function from various distributions of fuel droplets	186
8.1.3	Scattering by a single polystyrene sphere	189
8.2	Image transfer through turbid media	192
8.2.1	Image analysis	192
8.2.2	Correction procedure	194
8.3	Propagation of ultra-short laser pulses through turbid media	195
8.3.1	MC simulation	195
8.3.2	Results and discussion	196
8.4	Extrapolation of the Beer-Lambert transmission to multiple scattering	200
9	Summary and Conclusion	203
A	Publications - Conferences - Recognitions	A-1
B	Polystyrene Spheres Solutions - Complementary Data and Results	B-1
C	Hollow cone spray experiment - Complementary Data and Results	C-1
D	Monte Carlo code	D-1

Nomenclature

Symbols

A	Albedo
c	Speed of light in a vacuum
d_0	Liquid jet (or sheet) thickness
d_a	Diameter of the laser beam profile at FWHM when $\theta_a = 1.5^\circ$
d_b	Diameter of the laser beam profile at FWHM when $\theta_a = 8.5^\circ$
d_f	Separation distance between interference fringes
D	Droplet diameter
\bar{D}	Mean droplet diameter
ΔD	Bin width for droplet diameters
D_k	Droplet diameter such that 63% of the total liquid volume is in smaller droplets
$f(\vec{s}', \vec{s})$	Scattering phase function
f	Focal length
F/#	F-number of camera aperture
g	Anisotropy factor
G	Geometrical shadow
I_b	Ballistic light intensity
I_d	Diffacted light intensity
I_i	Initial/incident light intensity
I_f	Final light intensity
\vec{k}	Wave vector
l_l	Length scale of the liquid flow
l_{fp}	Free path length
L_c	Length of the liquid core
L_P	Distance of spray penetration
M	Mass of fuel
M	Size parameter of the droplet distribution
n	Index of refraction

n	Scattering order
N	Number density of droplets
N	Number of interference fringes
Oh	Ohnesorge number
p_i	Pressure of injection
P	Order of refraction
$P(D)$	Droplet diameters distribution
\vec{q}	Scattering wave vector
$Q(D)$	Rosin-Rammler distribution of droplet sizes
Q_a	Absorption efficiency
Q_e	Extinction efficiency
Q_s	Scattering efficiency
r	Radial distance
Re	Reynolds number
\vec{s}', \vec{s}	Incident and scattered direction vectors of photons
T	Shape parameter of the droplet distribution
U_g	Gas velocity
U_l	Liquid velocity, nozzle flow rate
V	Scattering volume
We	Weber number
x	Particle size parameter
x	Axial distance

Greek Symbols

α_c	Collecting angle
α, β	Indices of polarization
β	Source-detector angle
λ	Light wavelength
Λ	Wavelength of disturbance
μ_a	Absorption coefficient
μ_e	Extinction coefficient
μ_l	Liquid viscosity
μ_m	Mass absorption coefficient
μ_s	Scattering coefficient
ω	Cycle frequency
ϕ_s	Azimuthal scattering angle in the UVW local coordinate system
Φ_f	Azimuthal scattering angle defining \vec{s} in the XYZ global coordinate system
Φ_i	Azimuthal scattering angle defining \vec{s}' in the XYZ global coordinate system
$\Delta\Phi$	Change in the phase of modulation recorded by a PDA instrument
ψ	Elevation angle
ρ_l	Liquid density
ρ_g	Gas density
σ	Standard deviation
σ_a	Absorption cross-section
σ_e	Extinction cross-section
σ_l	Liquid surface tension
σ_s	Scattering cross-section
θ	Spray angle
θ_a	Detection acceptance angle
θ_b	Angle related to the intersection of the 2 laser beams used in PDA
θ_s	Polar scattering angle in the UVW local coordinate system
Θ_f	Polar scattering angle defining \vec{s} in the XYZ global coordinate system
Θ_i	Polar scattering angle defining \vec{s}' in the XYZ global coordinate system
ξ	Random number

Abbreviations

CPDF	Cumulative Probability Density Function
FWHM	Full Width at Half Maximum
GDI	Gasoline Direct Injection
GO	Geometrical Optics
GPD	Global Phase Doppler
HPIV	Holographic Particle Image Velocimetry
ILIDS	Interferometric Laser Imaging for Drop Sizing
IPI	Interferometric Particle Imaging
LDA	Laser Doppler Anemometry
LDV	Laser Doppler Velocimetry
LHF	Locally Homogeneous Flow
LMT	Lorenz-Mie Theory
LSD	Laser Sheet Dropsizing
LSV	Laser Speckles Velocimetry
LVF	Liquid Volume Fraction
M ₁ , M ₂	Method 1 and Method 2
MC	Monte Carlo
MDR	Morphology Dependence Resonances
OD	Optical Depth
OKE	Optical Kerr Effect
PAD	Pixel Array Detector
PDA	Phase Doppler Anemometry
PDF	Probability Density Function
PDI	Phase Doppler Interferometry
PDS	Planar Drop Sizing
PIV	Particle Image Velocimetry
PLIF	Planar Laser Induced Fluorescence
PTV	Particle Tracking Velocimetry
RMS	Root Mean Square
RTE	Radiative Transfer Equation
SMD	Sauter Mean Diameter
SNR	Signal-to-Noise Ratio
SPIV	Stereoscopic Particle Image Velocimetry
SPTV	Stereoscopic Particle Tracking Velocimetry

Introduction

THE scientific and industrial interest in spray technology was almost nonexistent forty years ago, with no conferences, journals or university courses devoted to the science of atomization (Chigier 2006). Since that time, there have been many changes and the understanding of the generation of sprays has become a subject of considerable importance in a wide range of industrial applications. Nowadays, international conferences and congresses regarding atomization and sprays are currently held in Europe, America and Asia (e.g. ILASS - Institute of Liquid Atomization and Spray Systems). The facilities employed for optical characterization of sprays have increased exponentially during the last few years. For instance, the U.S. Argonne National laboratory has recently investigated the near nozzle region of a diesel spray using a one billion dollar X-ray facility (Wang 2006). This large increase in research and development activities related to spray technology is principally promoted by modern economical interests and new international environmental policies.

The most significant example of a spray application concerns the injection of liquid fuel into piston and gas turbine engines via spray systems. Fuel sprays are employed to generate the necessary mechanical power in cars, planes and other combustion based vehicles and devices. However, liquid fuel combustion is responsible for the emission of pollutants such as NO_x, hydrocarbons and soot. As a result of this atmospheric pollution, a global warming has been observed with scientists predicting future major climatic changes. To face this major problem, international legislatures have enforced regulations with significant reductions in emissions. Respecting such restrictive decisions requires on the one hand the development of new types of clean fuels while on the other hand the improvement of the energy efficiency of the combustion process. In parallel, the constant increase in oil prices is an important economic motivation for improving combustion energy efficiency. Liquid fuels are more attractive than gaseous fuel because they possess more energy per unit volume and they are easier to transport and manipulate. Due to

these crucial advantages and to the continuous increase in energy demands, worldwide use of liquid fuels is not likely to be reduced anytime soon. Liquid fuels must be vaporised within combustion chambers in a manner in which the stoichiometric gas/vapour mixture conditions are satisfied. This is performed by atomizing the injected liquid into the combustion zone and generating fine spray droplets which subsequently vaporise and burn. When employing the appropriate spray device, the desired size, velocity, concentration and trajectory of droplets can be produced in such that the energy efficiency is optimized with a consequent reduction in emissions. For each condition of operation and depending on the combustion chamber characteristics, liquid fuels must be injected in a specific way. In other words, for each individual application a specific spray system must be adequately designed and accurately tested before utilization. This requires reliable and complete characterization of fuel sprays.

Medical sprays, paint sprays, spray drying, agricultural sprays, and spray cooling are other examples in which the control and the optimization of atomization are extremely important. In medicine, inhaled droplets must satisfy a range of size comprised between 0.5 and 5 μm . Droplets above 5 μm hit and deposit on the surface of the throat; whereas, droplet less than 5 μm are exhaled just after inhalation. Cryogenic sprays are used to remove heat during laser surgery. For this application, optimal cryogen droplets of size between 3 and 20 μm with $\sim 35 \text{ ms}^{-1}$ velocity are required. In spray coating and painting the major challenge consists in the production of droplets which will deposit, spread and dry into uniform layers of desired thickness. In automobile painting, it has been also reported (Chigier 2006) that up to 40% of the paint misses the target. Reducing this off-spray amount would offer large savings to car companies while reducing the generation of toxic pollutants. Numerous other examples (e.g. agricultural sprays, spray drying and spray cooling) related to many industrial domains could also highlight the importance of understanding the physic of spray generation. However, a comprehensive list would be too extensive. It must be kept in mind that for each of these applications, a particular generation of droplets requires an adequate control allowing the increasing performances of spray systems.

Sprays are generated by the successive primary and secondary break up of the injected liquid body (Lefebvre 1989). In practice, break up of liquid fuels occurs under high pressure injection at high ambient temperature and pressure conditions. Occasionally, high velocity air flows are used to increase the quality of atomization. Other types of spray employ superheated liquid and/or generate bubbles into the liquid flow in order to produce fine droplets and increase the evaporation rate. In most cases, the liquid break up is then an unstable physical process which is difficult to control. The first

stage in monitoring such systems is to initially characterize the spray properties (size and concentration of droplets, the cone angle, the distance of penetration *etc*) under a variety of operating conditions.

Due to their remote sensing non-intrusive nature, optical techniques have rapidly become the methods of choice for spray diagnostics, as opposed to mechanical or electrical devices. During the past three decades, the development and improvement of new laser based techniques has been particularly extensive. As a result, a wide variety of instruments are now available for spray measurement. However, each of these instruments provides only specific and/or local information. Some laser techniques measure quantities such as the size, concentration, velocity, trajectory and temperature of the droplets. Some provide more general information regarding the geometry and structure of the spray like the cone angle, the distance of penetration, the length of the liquid core and the geometrical dimensions of the probed spray system. Finally, other techniques are employed to investigate specifically the break up (primary and secondary break up) and atomization processes in order to validate modern Computational Fluid Dynamic models. The combination of several complementary techniques is often necessary for complete spray characterization. Furthermore, even if laser diagnostics systems have considerably improved, they still continue to suffer from severe limitations especially in the dense spray region.

The most important source of errors in all optical diagnostics of sprays is the multiple scattering of the incident laser radiation from the surrounding droplets. In imaging techniques, multiple scattering of light causes blur, loss of contrast and attenuation. In point interferometry measurements, multiple scattering attenuates the signal creating a weak, noisy and difficult to process detected signal. As a result, the sampling rate of validated data generated by Phase Doppler Anemometry instruments is reduced considerably making the measurement impossible to perform in the dense spray region. In Fraunhofer diffraction techniques, multiple scattering introduces severe errors in the droplet sizing measurement as soon the single scattering approximation is no longer valid. Multiple scattering of light radiation results from the interaction of photon packets with several scattering centres. In sprays, these scattering centres are principally spherical droplets but can also be irregular liquid elements. The distribution and amount of multiply scattered photons depends on several parameters including: the optical depth of the system, the scattering process of individual droplets, the characteristics of the light source and the geometrical and physical properties of the probed spray. The experimental investigation of multiple scattering is highly complex as it is difficult to determine how many times a detected photon has scattered. Multiple scattering has been investigated analytically

using the electromagnetic theory, by calculating the statistical average of the electromagnetic field quantities (Pomraning 1973). This approach preserves the wave properties of the optical fields but does not generally lead to solvable equations especially in the case of spray diagnostics. The radiative transport theory is the most commonly used approach when dealing with light propagation within scattering media. For very dense scattering media, where the average number of scattering event is superior or equal to 10 (multiple scattering regime), the Radiative Transport Equation (RTE) is simplified to the diffusion approximation. However, most of the spray operates under the intermediate single-to-multiple scattering regime where the average number of scattering event is between 2 and 9. In this case, the diffusion approximation cannot be applied and the exact form of the RTE cannot be calculated.

As an alternative to deterministic models, stochastic numerical models can be employed for light transport in scattering media such as sprays. Nowadays, the Monte Carlo (MC) technique is the most widely used and versatile probabilistic approach giving satisfactory solutions to the RTE where analytical approaches encounter difficulties. In the MC technique, the trajectories of individual photons are traced through the probed medium. Each interaction is governed by random processes of scattering or absorption. When the photons exit the simulated volume or when absorption occurs, their history is known and the amount of scattering events experienced is recorded. This precious information allows deduction of the importance of each scattering order for a given spray structure and source-detector configuration. By sending an infinite number of photons, the exact solution of the RTE is reached. The principal advantage of MC models comes from the flexibility in considering various complex 3D structures. In the last decade, the MC method has been principally employed for photon transport in tissues (Keijzer 1993, Meglinski and Matcher 2001, Churmakov 2005). However, MC modelling has also been performed in under-water environments (Piskozub 2004), geological structures (Abubakirov 1990), and for atmospheric (Lavigne 2001) and astronomical purposes (Hogerheijde 2000). Most of the existent MC models assume homogeneous or layered structures. In sprays, concentration and distribution of scattering centres (droplets) varies strongly with position. Such characteristics require the development of a MC model able to cope with highly inhomogeneous structures.

The aim of this thesis is to comprehensively investigate and ultimately quantify errors introduced by multiple scattering in spray diagnostics. Since the early application of laser techniques, back to 30 years ago, multiple scattering was already identified as a major problem. Nowadays, efforts in developing and testing new optical techniques, in order to make the measurement reliable within the dense spray region, are considerable.

However these developments remain limited by the fact that multiple scattering effects are extremely difficult to predict, especially for inhomogeneous polydisperse media.

The benefits of using a MC model of type developed here, is that it offers accurate description of the physical processes when considering practical case of study. In terms of light scattering within turbid media, complex phenomena that could not be described in 3D in the past, can now be understood and analyzed using modern computational models. Predictions resultant from simulations offer a fundamental help in developing, improving and testing new optical techniques and reduce in the same time the cost of experimental investigations.

The specific objective in the framework of this thesis is the development of a computational model designed for the propagation of light radiation through spray systems. It is required that the model must be verified against the theory; be experimentally validated; be flexible enough to consider both different source-detector geometry and spray structures. Finally the model must be a numerical tool to easily investigate, understand and predict the effects of multiple scattering for various type of optical diagnostics. The main requirements for the computational model has been identified as follow:

- The model should be able to take into account a range of scattering phase functions representing the scattering of typical spray droplets from 1 up to 200 μm in diameter.
- The exact experimental laser source should be able to be simulated via the MC model.
- The detection of individual scattering orders should be performed separately in order to observe the importance of their individual contribution on the detected signal or image.
- The detection acceptances angle must be easily adjustable to those employed by the experimental collection optics considered.
- 2D mapping of light intensity distributions must be able to be generated by the model with spatial resolution equal to that obtained in the experiment.

This dissertation is divided into 8 chapters. The characteristics and the generation process of sprays are initially described in **Chapter 2**. Applications, properties, and formation of droplets are highlighted with the classification of the different breakup regimes.

In **Chapter 3**, the traditional and emerging optical diagnostic systems are presented. The chapter ends with a discussion of the limitations of each optical instrument demonstrating that multiple scattering is the major and recurrent factor introducing errors in laser measurements within the dense spray region.

A detailed explanation concerning the propagation of laser radiation within spray is provided in **Chapter 4**. After describing the adequate terminology, the physic of interaction between light and droplets is given (first for individual droplets and then for a collection of droplets).

Chapter 5 is focussed on the description of photon transport modelling within turbid media. The major part of this chapter is dedicated to the description of the MC model developed.

Chapter 6 is devoted to the verification and validation procedure. A complete set of comparison between experimental and analytical results is provided. It is demonstrated in this chapter that the MC code presented is reliable and generates realistic simulations.

In **Chapter 7**, the MC model is employed for the real case of spray diagnostics and the simulated results are compared with the experimental results. A new cross-detector configuration is also presented for optimizing the detection of the singly scattered light within a collection of fuel droplets.

Finally, **Chapter 8** provides various examples of applications that have been performed using the MC model. These examples concern the scattering of light by single droplets in the far field region, the transfer of images within turbid media, the analysis and correction of blurred images, and the propagation of femtosecond laser pulses in scattering environments. The chapter highlights the capability and flexibility of the model to tackle a wide number of important issues related to radiative transfer, with applications in many research domains including combustion engineering, meteorology and biomedicine.

Characteristics and Generation of Sprays

DEPENDING on their characteristics, sprays are used for a wide variety of applications. Performances of spray systems can be optimized and improved by achieving desirable spray properties. For example, in Combustion Engineering liquid fuels have to be sprayed in the combustion zone in a manner that the stoichiometric air/fuel ratio is respected. This requires a correct atomization of the liquid fuel such that the desired droplet size, number density, velocity and repartition in the combustion chamber is obtained. Such achievement allows increasing the fuel and energy efficiency while reducing the emission of pollutants from combusting sprays. In industry, high spray performances improve product quality and reduce the consumption of sprayed liquids. Increasing the efficiency and the control of industrial, biomedical, agricultural and fuel spray systems requires a fundamental understanding of the physic of spray disintegration.

This chapter is devoted to the importance of sprays in many applications and is an introduction to spray technology. The first section enumerates the applications of sprays with two subsections which describe their general structure and properties. The second section of the chapter is focused on the process of spray disintegration and the formation of liquid droplets. At the end of the chapter, the droplet properties of importance are highlighted. These properties are the droplet number density, size distribution, and velocity. Note that the measurement of such parameters is crucial for the complete characterization of a spray.

2.1 Spray properties

In this section, a summary of the applications and importance of sprays in the daily life is provided. A description of a typical spray structure is also given with a detailed section regarding the properties and parameters of influence in spray formation.

2.1.1 Applications of sprays

Sprays are considered as systems of droplets immersed in a gaseous continuous phase (Lefebvre 1989). They are commonly generated by atomizers but can also be produced naturally. In modern society, sprays are ubiquitous; nearly almost every industry and household employs some form of spray. They are used for painting, cooling, misting, cleaning, washing, coating, lubricating, drying, applying chemicals, and dispersing liquids. They are of importance in several domains including agriculture, food processing, medicine, combustion engineering and many industrial processes (Nars *et al* 2002).

In agriculture, spraying of chemicals (insecticides, herbicides and fertilizer) are extensively performed using tractors or aircraft. The agrochemical solutions must be properly applied to crops such as the wind does not carry the drops away from the desired target. For this application, the drops generated must be of large dimension with a relatively high velocity.

In food processing, the production of dry package foods and powders is carried out using spray drying (Oakley 1995). This technique is also used to remove moisture from the food and is primarily based on the atomization of non-Newtonian liquids.

In medicine, inhalation of drugs is performed using oral or nasal sprays. One of the main objectives in the use of inhalation sprays is to reach the lung surface of the patient. If drops are too large, depositions of the injected liquid on the walls of the mouth, throat and bronchial tubes occur. On the contrary if droplets are too small, they may be inhaled and immediately exhaled. Therefore, appropriate characteristics of droplet size, number density and velocity must be strictly respected.

It exists a large variety of industrial spray applications. Spray coating and painting (Burby 2006) are extensively utilized in production factories. Spray guns are used to coat metal, wood, ceramic, fabric, paper, and food products with paint or other coating solutions. One of the principal uses of this technique is related to cars, trucks and others vehicles which are spray painted using robots. The main issue in spray painting and coating processes is the loss of paint (or coating solution) due to the dispersion of the solution outside

of the desired target. It is important to note that the pollution generated by the off-spray can exceed the pollution generated by engine emission during the entire life time of the vehicle (Chigier 1993). The improvement and optimization of surface treatment processes are then once again governed by the spray characteristics. In electronic packaging industry layers of material are spread onto moving boards via spray systems. Ceramic and liquid metal sprays are being used in material processing to manufacture a wide variety of objects with complex shapes (such as tools and gear wheels) and for powdered metals production. A large variety of other spray applications are also worth mentioning: cooling nuclear cores, extinguishing fires, producing artificial snow on ski slopes, removing oxides (oxides of sulphur and oxides of oxygen) from flue gas (of furnaces and industrial boilers) among others. In the home, sprays are mainly utilized for watering, cleaning and cosmetic purposes and are produced by garden hoses, shower heads, body sprays, hair sprays *etc.* Sprays are also created naturally: waterfall mists, fog, drizzle, ocean sprays and rains are typical examples of natural sprays.

Even if sprays are involved in many different applications as enumerated above, it can be stated that most research efforts have historically focused on fuel spray generation for combustion. Furthermore, for the last few decades the scientific interest in the fuel-injection process has expanded due an increased desire for efficiency improvement in combustion and of reduced pollutant emission. In gas turbines, diesel engines, rocket engines, spark ignition engines, compression ignition engines and other combustion systems, fuels are used in their liquid form. Liquid fuels contain more energy per unit volume than gas fuels and are easier to store and transport. However, as normal fuels are not sufficiently volatile to produce vapour in the amounts required for ignition and combustion, they are atomized into a large number of droplets. This atomization process allows the conversion of the liquid phase to the vapour phase. The rate of evaporation of the fuels is inversely related to the size of the droplets generated. Smaller droplets yield faster rate of evaporation. The droplet size, repartition, and concentration are thus of special importance since they directly affect the combustion efficiency, stability limits and the emission level of smoke, unburned hydrocarbons and carbon monoxide (Lefebvre 1983). Therefore, spray quality and structure play a major role in the fuel/air mixture preparation and in the combustion process itself.

The current increase of interest in the science of atomization is accompanied by large progresses in the area of breakup process modelling and laser diagnostics. Every year, many numerical models are created in order to simulate the atomization process in varying conditions. In parallel, a range of optical diagnostic techniques are developed in order to improve the reliability of spray characterization in both the dilute and dense spray region.

2.1.2 Spray structure

Sprays are complex fluid mechanical structures generated by the disintegration of a liquid sheet or jet into droplets in a surrounding gas. Depending on the liquid inertia, surface tension, and aerodynamic forces on the jet, several spray regimes are identified (Reitz 1978). The Rayleigh breakup regime (Rayleigh 1878), or drip flow regime, the first wind-induced regime, the second wind-induced regime and the fully developed atomization regime. A precise description of these regimes is given in section 2.2. As the atomization regime is both the most typically used, the following description will be based on atomizing sprays.

The structure of a spray is influenced by a large number of parameters including the properties of the injected liquid (the dispersed phase), the properties of the surrounding gas (the continuous phase), and the characteristics on the injector itself. Depending on the operating conditions and on the design of the injector, a wide variety of sprays can be produced. A spray is composed of a series of fluid mechanical zones:

- The liquid core corresponding to the extension of the liquid body injected.
- The multi-phase mixing layers characterized by irregular elements and large drops and created by the atomization process.
- The dispersed flow in which small round drops are well formed.
- The vaporization zone where the small droplets are evaporated.

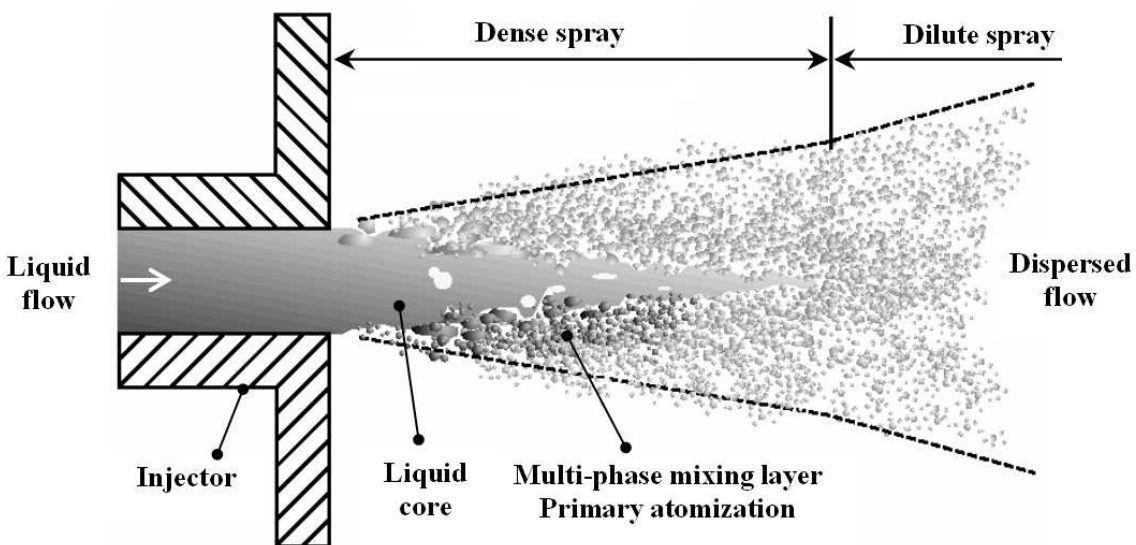


Figure 2.1: Illustration of the spray structure in the atomization regime (adapted from Faeth *et al* 1995).

Two main regions defined a spray. The “dense spray” and the “dilute spray” regions. The dense spray is situated directly downstream from the nozzle whereas the dilute spray is located in the far-field region where the flow is fully dispersed as illustrated in Fig.2.1.

Under favourable conditions, the incoming liquid flow emerging from the nozzle is subjected to perturbations and oscillations and fully disintegrates into a multiplicity of droplets. The complete process is divided into two successive steps corresponding respectively to primary and secondary atomization. Primary atomization is known as the disintegration of a liquid jet or sheet into ligaments and drops due to gas-liquid interfacial instabilities. These instabilities are created by the growth of disturbances during the penetration of the liquid body into the ambient gas (Lasheras and Hopfinger 2000). The primary atomization (or primary breakup) only occurs in the dense region where the periodic stripping of the liquid body breaks up into irregular large droplets. If these droplets exceed a critical size, they further disintegrate into spherical droplets of smaller size. This second breakup process corresponds to secondary atomization. A larger description of droplets formation and breakup is given in section 2.2.2.

In a spray, the Liquid Volume Fraction (LVF) varies strongly with position. In the near-injector region, the LVF starts at the maximum value of 1 (corresponding to the liquid core zone) and reduces rapidly with axial distance, x , and the radial distance, r , (see Fig.2.1). At high LVF, droplet-droplet interactions such as collisions and coalescence occurs generating large droplets which are subsequently secondary atomized. However, it has been remarked by Faeth (1995) that the high LVF of the dense region is principally due to the presence of the liquid core. The LVF in the dispersed flow adjacent to the liquid core is, on the contrary, surprisingly small (less than 0.1). According to the author, the flow in this region corresponds to a “dilute spray” but with added complications due to the presence of many irregular liquid elements, secondary breakups and with negligible effects of collision. Nevertheless, in some particular cases, collision effects cannot be neglected. This is the case for sprays generated by a series of injectors and for sprays subjected to turbulent air flows. As a result Faeth defined dense sprays dispersed flow “relatively dilute” with region with large liquid fraction caused by the presence of the liquid core. In the case of a single injector nozzle spray in still air, droplets collisions are then assumed improbable even in the dense spray region (Faeth 1996).

An example of measured and predicted time-average LVF along the axial distance, is presented Fig.2.2 for an atomized water jet in the dense region (Tseng *et al* 1992). The predictions are based on a Favre-averaged turbulence model under the Locally Homogeneous Flow (LHF) (Ruff *et al* 1989). In this model, the relative velocities between the phases are assumed to be small in comparison to the mean flow velocities. It can be seen

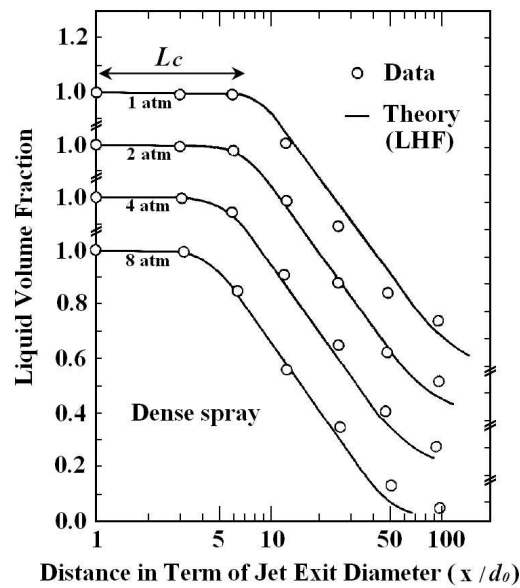


Figure 2.2: Time averaged liquid-volume fraction along the axis of round pressure-atomized water spray at various pressures for fully developed turbulent liquid flow at the nozzle exit (Tseng *et al* 1992).

from Fig.2.2 that the liquid core length L_c of the water jet is decreasing by increasing the ambient pressure from 1 to 8 atmospheres implying faster mixing rates at larger ambient gas densities. The length of the liquid core penetrating in the still gas gives good indications about the quality of the atomization. Small L_c is generally related to high atomization finesse. In some sprays, such as hollow cone sprays running at high injection pressure, the atomization process starts just beyond the injector tip and a distinct liquid core is not clearly noticeable. In other sprays such as diesel sprays, the amount of surrounding droplets is so high that the existence or non-existence of a liquid core has not yet been proven (Linne *et al* 2006). One solution for analysis of such turbid media is called ballistic imaging. This emerging technique produces high resolution shadowgraph images by time-gated detection (see section 3.2.4).

The structure of the dilute spray is easier to characterize than the structure in the dense spray region. The dilute spray is situated in the far-field region where the flow is defined by a dispersed-phase structure in which droplets are round and small. The dilute spray begins at the end of the liquid core. This corresponds to an axial distance $L_c \sim 200 - 500$ jet exit diameter, d_o , at normal temperature and pressure (Arai *et al* 1985). Hiroyasu (1991) showed that for diesel sprays injected at velocities ~ 200 m/s the average breakup length is comprised between 10 and 30 mm. Due to the decreasing of the liquid volume fraction in the dilute region (less than 0.1), distances from droplet to droplet are largely increased and the probability of collision and coalescence events is very low.

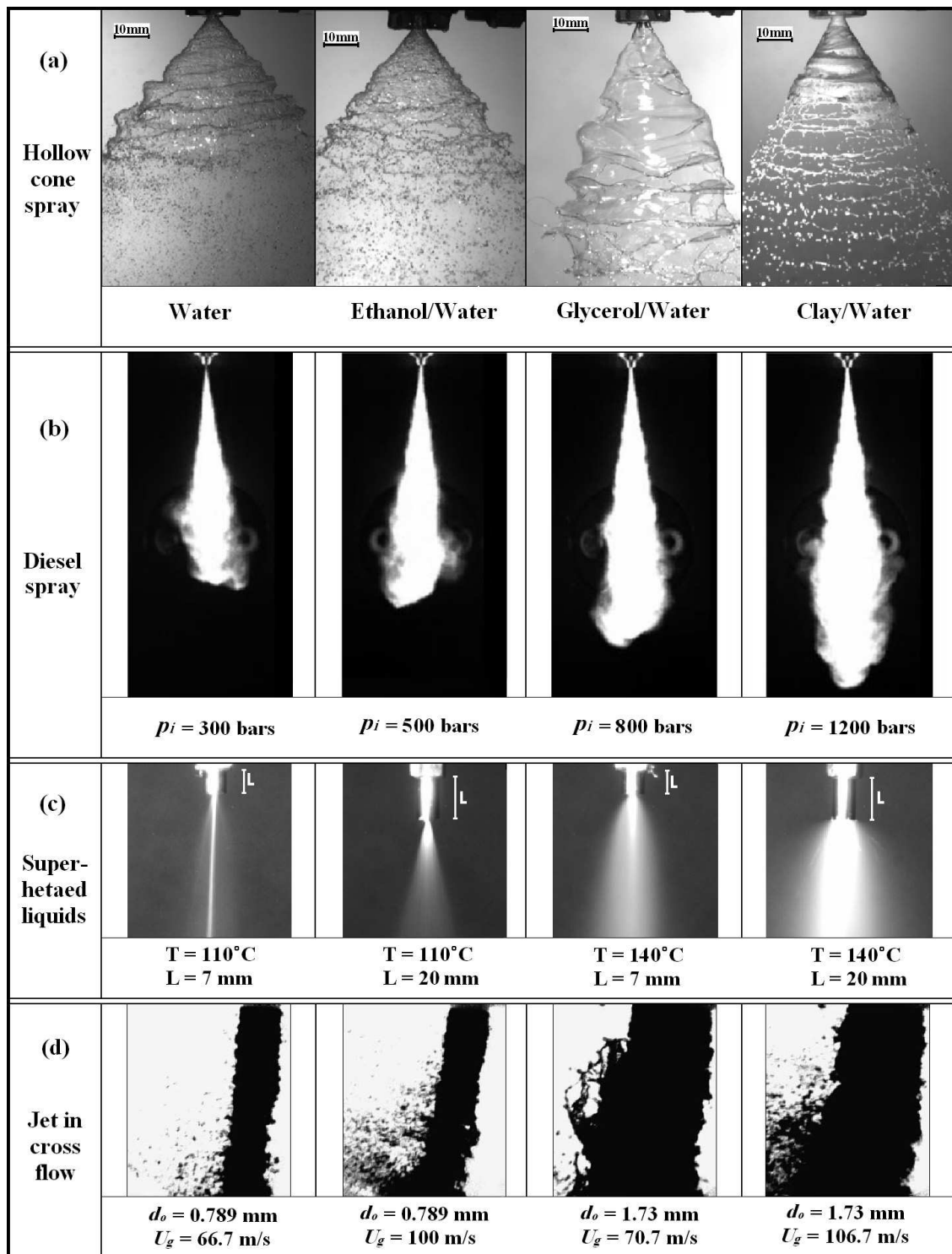


Figure 2.3: Example of sprays generated at different operating conditions. (a): Typical hollow-cone spray (Mulhem 2004) running with different injected liquids - (b): Single injection of a diesel spray (Suzzi 2004) at various injection pressure - (c): Spray patterns of superheated liquids (Rossmeißl 2004) at various liquid temperature and nozzle geometry - (d): Ballistic images of a jet in cross flow (Linne 2005) for several gas velocities U_g and orifice diameters d_o .

At the same time, droplets are well formed and have strong interaction with the turbulent airflow. At the end of the dilute spray, droplets advance with time and evaporate in the “the vaporization zone”. The rate of evaporation is related to the temperature of the surrounding gas and depends on the droplet size and velocity. The final structure of a spray is affected by a large number of parameters. These parameters are the properties of the injected liquid, the surrounding gas, and the injector itself (see section 2.1.3). As a result, a large number of sprays of various shapes and geometries are producible.

Figure 2.3 shows some examples of sprays operating at different conditions. In Fig.2.3(a) photographs of hollow-cone sprays are generated at 1.2 bar injection pressure for several liquids are presented. It can be seen that the shape of the cone is largely affected by the liquid properties and in particular by the liquid viscosity (Mulhem 2004). On Fig.2.3(b) shadowgraph images of a diesel spray running at different initial injection pressures are illustrated at 20 ms after injection (the ambient gas is set to 20 kg/m³ density and 20°C temperature) (Suzzi *et al* 2004). Contrary to most other sprays, automotive sprays present the particularities to run under the single injection regime so that their steady state is never reached.

Figure 2.3(c) shows the influence of the nozzle geometry on the spray pattern of superheated liquids (100-150°C). The use of superheated liquids allows the generation of droplets of few micrometers while maintaining moderate velocities (Rossmeissl and Wirth 2004). Finally, the sequence of ballistic images in Fig.2.3(d) shows the effect of the initial jet diameter and gas velocity on a jet in cross flow (Linne *et al* 2005).

2.1.3 Properties influencing spray formation

The characteristics of the injected liquid (and of the liquid flow), the characteristics of the ambient gas (and of the gas flow) and the geometry of the nozzle all contribute to the final structure of a spray. A clear summary of the properties of influence in spray formation is given in Table.2.1. The most relevant liquid properties to spray generation are the viscosity, surface tension and density, respectively.

The viscosity is a quantity that characterizes a fluid resistance to flow. It is the most important liquid parameter to atomization owing to its effect on droplet size, liquid flow rate and on the geometrical shape of the spray. As liquid viscosity increases, flow rate is generally reduced and the development of instabilities in the liquid core is hindered. As a result, the disintegration process is delayed and a spray with narrow spray angle and large droplets is produced. Liquid viscosity is highly dependant on the temperature and

Relevant properties for atomization		Geometrical aspects and characteristics of sprays	Illustration
Injected liquid:	<ul style="list-style-type: none"> - Surface tension - Viscosity - Density 	<ul style="list-style-type: none"> - Nozzle flow rate: U_I - Liquid jet or sheet thickness: d_0 - Radial and axial distances: r and x - Length of the liquid core: L_c - Distance of penetration: L_p - Mean drop size: \bar{D} - Drop size distribution: $P(d)$ - Drop number density: N - Radial patterning - Circumferential patterning - Spray angle: θ - Evaporation rate - Wavelength of disturbance: λ 	
Liquid flow:	<ul style="list-style-type: none"> - Injection pressure - Velocity - Turbulence in the liquid stream 		
Ambient gas:	<ul style="list-style-type: none"> - Gas density - Temperature 		
Gas flow:	<ul style="list-style-type: none"> - Absolute velocity - Relative gas-to-liquid velocity - Turbulence in the gas stream 		
Injector:	<ul style="list-style-type: none"> - Dimension of the orifice diameter - Internal structure and geometry of the nozzle 		

Table 2.1: Most relevant properties for atomization with the related characteristics and geometrical aspects of sprays.

generally decreases with increasing in temperature (Lefebvre 1989).

Due to its property to resist liquid expansion, the liquid surface tension is the second most important parameter in atomization. Liquids of high surface tension are more difficult to disintegrate by aerodynamic, centrifugal or pressure forces comparing to those of lower surface tension. In general, the surface tension decreases as temperature increases for most pure liquids in contact with air.

The effects of liquid density on atomization has been poorly investigated in the literature as its variation from one injected liquid to another remains generally small. However, Rizk (1976) reported that more resistance to disintegration are expected for liquid of high density with resulting effects on the formation of ligaments.

The fundamental parameters of the liquid flow are the injection pressure, liquid velocity and turbulence in the liquid stream. High pressure injection and high liquid velocity increase the formation of instabilities and disturbances at the nozzle exit and increase the atomization efficiency. Schweitzer (1937) described the three regimes of turbulent flow

and their effects on atomization as follows: The flow is called laminar when the liquids particles flow in streams parallel to each other and to the axis of the tube. When, however, the paths of the liquid particles cross each other in a more or less disorderly manner having varying transverse velocity components, the flow is turbulent. If the centre of the flow is turbulent, and if its periphery is laminar, the flow is defined as semi-turbulent. Figure 2.4 illustrates the laminar and fully-developed turbulent regimes with the exiting velocity distribution.

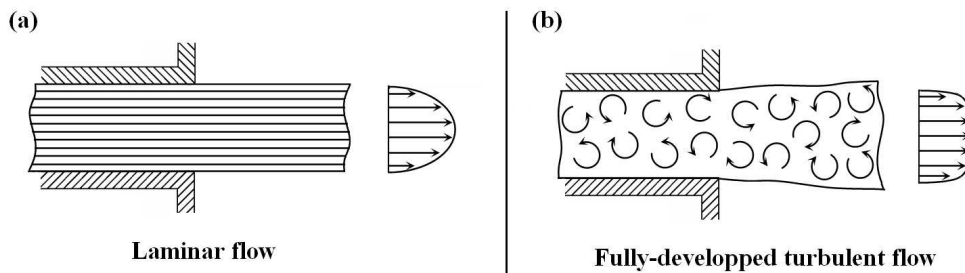


Figure 2.4: Example of flow state at the nozzle exit of an orifice plain nozzle.

The state of flow at the orifice exit has a direct effect on the quality of atomization. The Reynolds number gives a generally good indication regarding the state of a flow. Re is proportional to the inertial forces divided by viscous forces:

$$Re = \frac{l_l \rho_l U_l}{\mu_l} \quad (2.1.1)$$

where ρ_l is the liquid density, U_l is the velocity of the fluid, l_l is a characteristic length scale of the liquid flow and μ_l is the liquid viscosity. If Re is greater than a critical value, a flow originally turbulent will remain turbulent. If Re is smaller than the critical, the flow will turn laminar in a straight tube. In an absence of a disturbance, a flow originally laminar would remain laminar even for high Reynolds number. However, its susceptibility to turn turbulent increases with Re . According to Shiller the critical Reynolds number equals ~ 2320 (Shiller 1922).

The level of turbulence imparted onto the liquid flow influences the atomization process. Under the fully-developed turbulent regime, a jet disintegrates due to the effects of its own turbulence. The delineation of the different flow regions as a function of the initial flow velocity is illustrated in Fig.2.5.

The absolute velocity and the relative gas-liquid velocity are the two gas flow variables of importance. Even in a stagnant gas, the air velocity can reach high values due to the momentum transfer from the liquid to the surrounding gas (Rizk 1985) (specifically within the atomization region). However, the determination of gas turbulence characteristics on

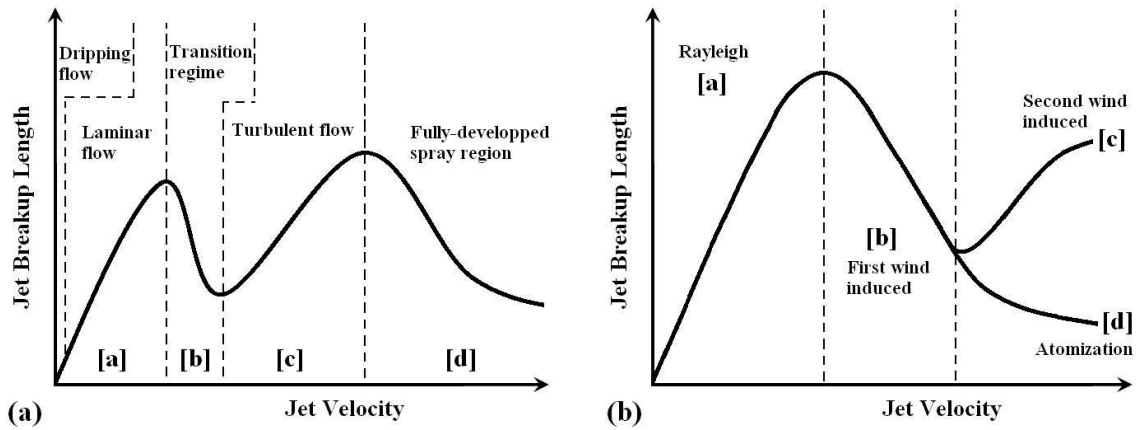


Figure 2.5: Change of the breakup length with the initial jet velocity. Depending on the nozzle flow and geometry different descriptions regarding the variation of the breakup length at high jet exit velocities are reported in the literature (Hiroyasu 1991 and Lin and Reitz 1998).

the atomization process has not been undertaken yet due to the difficulties associated with the determination of the gas velocity field in the dense spray region. A gas flow can also be created in order to accelerate the disintegration process. Most of the time the direction of the gas flow employed is either parallel or perpendicular to the liquid flow (see picture (d) of Fig.2.3).

The density of the surrounding gas (generally air) is the final gas property of importance regarding spray formation. For a given distance from the nozzle, the size of droplets is smaller at higher air densities than lower air densities and the liquid jet disintegration is more efficient. The jet loses velocity more quickly at higher air pressures than at lower air pressures with less propagation along the axial axis. As a result, the spray penetration distance, L_p , and the liquid core length, L_c , are reduced (see Fig.2.2). The spray cone angle becomes also wider with air density, changing the geometrical shape of the spray.

Both the temperature of the liquid and of the ambient gas have a direct influence on the droplet evaporation rate. Superheated liquids produce finer atomization due to the creation of the vapour phase prior to injection starts.

In general, breakup processes are governed by a balance of energy between the inertial forces and the surface tension. The non-dimensional Weber number is defined as the ratio of the inertial forces tending to break apart the liquid core to the surface tension forces tending to hold it intact. Its general form is given as:

$$We = \frac{l_l \rho_l U_l^2}{\sigma_l} \quad (2.1.2)$$

where σ_l is the surface tension of the liquid considered. The Weber number is a useful

parameter in classifying the disintegration regimes (Table 2.3) and the breakup regimes of single droplets (Table 2.4). It is also of use to determine if single droplets will or not breakup. The critical Weber number is defined as the threshold value above which breakup generally occurs and below which droplets remain stable.

The final dimensionless number of importance is the ratio of viscous friction and surface tension called the Ohnesorge number:

$$Oh = \frac{\sqrt{We}}{Re} = \frac{\mu_l}{\sqrt{l\rho_l\sigma_l}} \quad (2.1.3)$$

A high Oh number (related to high liquid viscosity), an increase in inertial forces is required for breakup to occur. For a given spray, the liquid breakup length, the cone angle, the averaged droplet size and number density can be semi-empirically correlated to the values of Oh and We . Note that the ratio ρ_l/ρ_g between the liquid density and the gas density is also of use for such correlations. The physical modelling of spray breakup is based on the use of Re , We and Oh . However, it is important to remark also that the theoretical development has been somewhat limited by the lack of direct experimental observation from within the dense region.

The shape, size, and flow state of the initial liquid body injected into a gaseous environment is mainly controlled by the nozzle geometry. Depending on nozzle characteristics, either a “liquid jet” or a “liquid sheet” is generated. The dimension of the liquid core is determined by the size of the nozzle orifice d_o . A finer atomization process is obtained with smaller nozzle orifice.

Spray injectors are designed specifically depending on desired application and a large variety of spray injectors can be enumerated. Injector involving atomization are categorized as: Pressure atomizers, rotary atomizers and two-fluid atomizers. Figure 2.2 depicts each atomizer types.

Pressure atomizers are based on the discharge of the liquid through a small aperture under high pressure. Depending on the geometry of the nozzle different type of pressure atomizers can be constructed. The simplest is the plain orifice atomizer where a simple circular orifice is used to produce a round liquid jet. The pressure-swirl is a more complex, though common, pressure atomizer characterized by a swirl chamber preceding the outlet orifice. The liquid emerges from the nozzle as an annular sheet which spreads to form a hollow-cone spray generally characterized by a spray angle ranging from 30° up to almost 180°. Other pressure atomizers such as the “duplex”, the “square spray”, the “spill return” and the “fan spray” are also available.

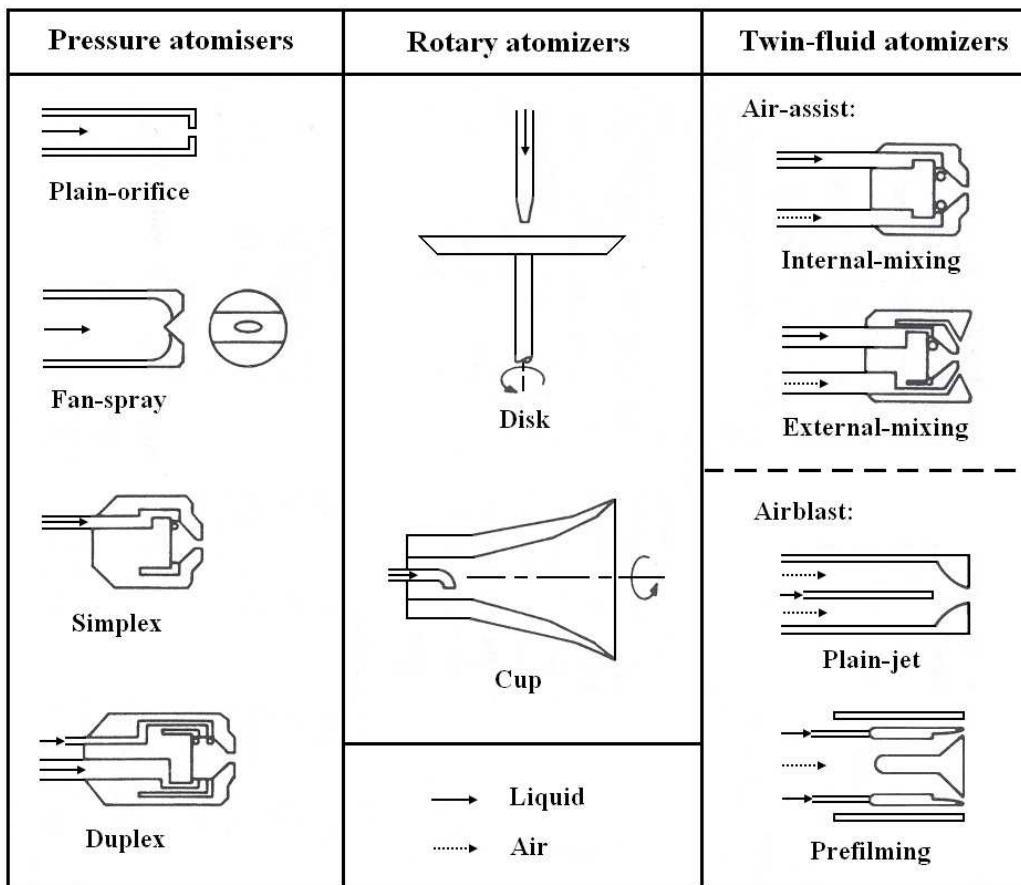


Table 2.2: Atomizers characteristics (Lefebvre 1989).

Rotary atomizers are based on the use of centrifugal energy. The mechanism employs a high-speed rotating disk in which the liquid is introduced at its center. The liquid is guided to the disk periphery and discharged at high velocity. Such a technique allows independent variation of flow rate and disk spin providing more flexibility in operation than pressure atomizers. However, the system is more complex and is restricted to certain applications such as liquid painting operations and spray drying. The droplets produced respect fairly monodisperse size distributions.

Two-fluid atomizers (also called twin-fluid atomizers) expose the spray liquid to a stream of air flowing at high velocity; the two types are named air-assist and air-blast atomizers. The main difference is that the air-assist nozzles employ a relatively small quantity of air flowing at high velocities; whereas, air blast nozzles use large amounts of air flowing at lower velocities. Note that the air blast atomizer is ideally suited for fuel atomization in gas turbines engines. Air-assist nozzles can be used as either an external or internal mixing atomizer. Internal mixing produces a more efficient atomization but encounters problems due to back pressure during the gas/liquid mixing process. The principal advantage of two-fluid atomizers is the large improvement of the atomization efficiency

especially for high-viscosity liquids.

Even if the three common type of atomizers described above are the most representative, other types have been developed for specific applications. Some examples are electrostatic, ultrasonic, sonic and vibrating capillary atomizers. For detailed information on atomizers, the reader should refer to the well established book *Atomization and Sprays* from A. Lefebvre (1989).

2.2 Disintegration process and droplets formation

The generation of droplets is a complex phenomenon governed by the opposition of consolidating forces (surface tension) with external disruptive forces (aerodynamic forces). Droplets are formed by the breakup of liquid ligaments (primary breakup) or by the disintegration of a large droplet into a multiplicity of small droplets (secondary breakup). This section initially enumerates the regimes under which a spray can operate. An explanation of the different modes of droplets disintegration is also detailed. Finally the size, velocity and number density of droplets within the various regions of the spray are described.

2.2.1 Disintegration regimes

Based on the differences in liquid inertia, surface tension, and aerodynamic forces, the breakup of a jet may be classified into four regimes (Ohnesorge 1936, Reitz 1978): The Rayleigh breakup regime (Rayleigh 1878) (or drip flow regime), in a very low jet speed, the first and second wind induced breakup regime where aerodynamic drag effects begin to dominate, and the fully developed atomization regime at high speed where flow field instability makes a strong contribution to the breakup. Figure 2.6 shows the categorization of these regimes in terms of Ohnesorge number versus Reynolds number on a logarithmic scale.

The Rayleigh regime occurs at very low jet speed when the aerodynamic forces are assumed insignificant. At the exit of the liquid jet, axisymmetric surface waves (so called dilational waves or "varicose") are formed by the interaction of primary disturbances in the liquid and surface tension forces. If the wavelength of the initial disturbance is less than a minimum value, Λ_{min} , (such that Λ_{min} equals the initial jet circumference) the surface forces tends to damp out these disturbances. If, on the contrary, the wavelength of the disturbance is greater than Λ_{min} the surface tension forces tends to increase these disturbances. The growth of disturbances eventually leads to the breakup of the jet.

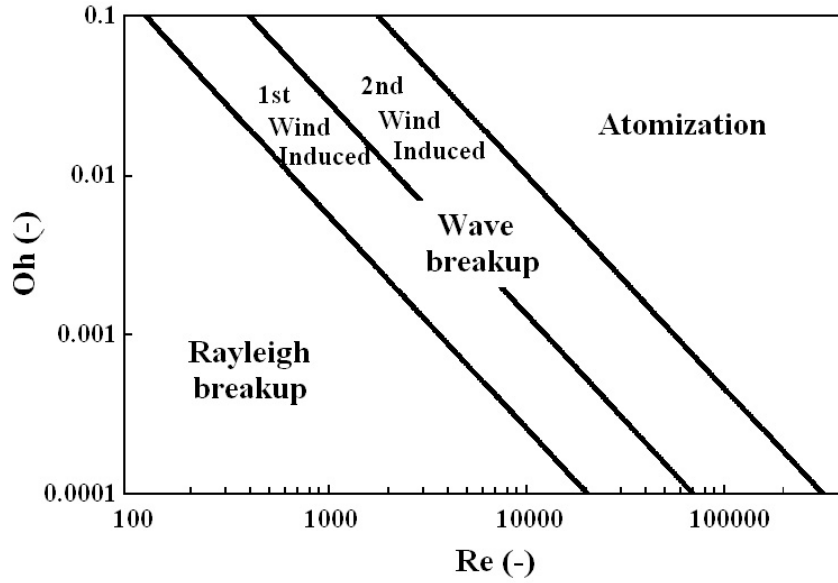


Figure 2.6: Classification of the disintegration regimes as a function of the Ohnesorge number versus Reynolds number (Reitz 1978).

The fastest growing disturbance is reached when Λ equals the optimal value Λ_{opt} . Rayleigh calculated this optimal value to be $\Lambda_{opt} = 4.51d_o$ for non-viscous liquids. The volume of the spherical droplets formed after jet breakup corresponds to the volume of a cylinder of diameter d_o and length Λ_{opt} . Therefore the diameter of resulting droplets is equal to $D = 1.89d_o$. These theoretical results have been confirmed experimentally by Tyler (1933) who found a relationship of $D = 1.92d_o$. Tyler deduced the wavelength of the fastest growing disturbance from the frequency of droplet formation. In the Rayleigh linear stability theory, liquid viscosity is neglected and the inviscid flow is assumed. In 1931, Weber extended the Rayleigh theory to viscous liquids. He deduced that the minimum wavelength of disturbance remains the same for both viscous and non-viscous liquids, but the optimum wavelength is greater for viscous liquids. His generalized equation relating Λ_{opt} to the droplet diameter D and liquid properties is:

$$\Lambda_{opt} = \sqrt{2}\pi\left(1 + \frac{3\mu_l}{\sqrt{\rho_l\sigma_l D}}\right)^{1/2} \quad (2.2.1)$$

Assuming a non-viscous liquid, equation 2.2.1 gives: $\Lambda_{opt} = 4.44d_o$ which remains approximately the relation found by Rayleigh. Weber also examined the effect of air resistance and deduced that an increase of relative air velocity reduces the optimum wavelength. He further deduced that the air motion induces the formation of waves on the liquid surface if the relative air velocity is above a certain value. This analysis is supported by the experimental results found by Haenlein in 1932.


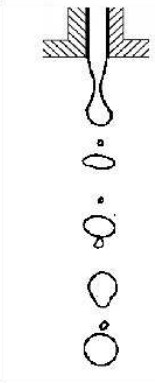
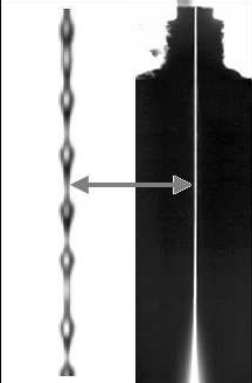
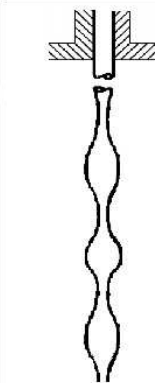
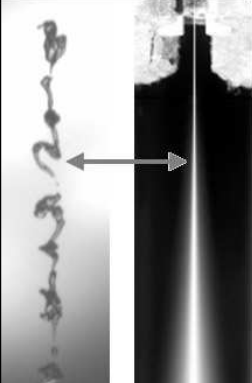
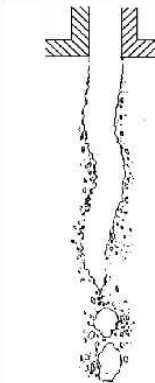
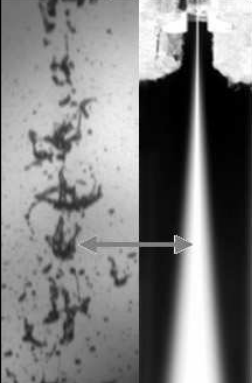

Spray regime	Picture	Illustration	Predominant drop formation mechanism	Transition to next regime
(1) Rayleigh breakup			Surface tension force	$We > 0.4$
(2) First wind-induced breakup			- Surface tension force - Dynamic pressure of ambient air	
(3) Second wind-induced breakup			- Surface tension force - Dynamic pressure of ambient air opposed by surface tension force initially	$We > 40.3$
(4) Atomization			- Aerodynamic and shear forces - Turbulence - Expansion - Surface tension force initially	$We \rightarrow \infty$

Table 2.3: Classification of the disintegration regimes (Source: Lin and Reitz 1998 - Pictures: Vahedi *et al* 2003).

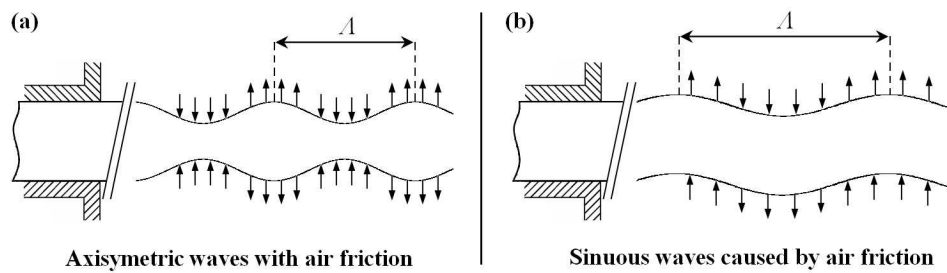


Figure 2.7: Influence of air friction and oscillations formation on the surface of a liquid jet.

When the aerodynamic forces increase the axisymmetric surface waves (formed under the Rayleigh regime), the disintegration regime becomes the first wind-induced breakup. In this case, the diameter of the drops is about the same as the jet diameter and the breakup process occurs several jet diameters downstream from the nozzle.

If, however, the aerodynamic forces are responsible for sinuous (or axisymmetric) waves by increasing the relative air velocity, the disintegration regime is called second-wind breakup regime. An illustration of the axisymmetric and sinuous oscillations on the surface of a liquid jet is given in Fig.2.7. In the second-wind induced breakup regime, the aerodynamic forces are responsible for the formation and growing of short wavelength disturbances (or harmonics) producing smaller droplets. As a result, the average droplet size is much smaller than the orifice diameter and a wide drop size distribution is generated. In this regime, breakup also occurs at several jet diameters downstream of the nozzle.

Finally in the fourth disintegration regime known as atomization, the liquid core is broken up directly at the nozzle exit. This process occurs at high relative liquid-gas velocities and produces a multitude of droplets much smaller than the original jet diameter. Note that most fuel and industrial sprays operates in the atomization regime. Each disintegration regime is described their own characteristics in Table 2.3.

2.2.2 Breakup of droplets

Under the action of aerodynamic forces, a single large droplet can breakup into several smaller droplets. In spray atomization this secondary breakup process controls the mixing rate of the dense spray in a similar manner as droplet vaporization controls the mixing rate of the dilute spray (Hsiang and Faeth 1992). Droplet breakup occurs in various ways depending on both the dynamic and physical conditions. The most important properties influencing breakup mechanisms are the droplet size and the relative velocity between the

droplet and the ambient gas. Other parameters, such as the liquid viscosity and surface tension, and the gas and liquid densities, are also of importance. Breakup of droplets follows two successive stages as discussed by Lee and Reitz (2001).


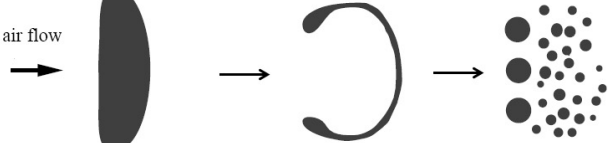

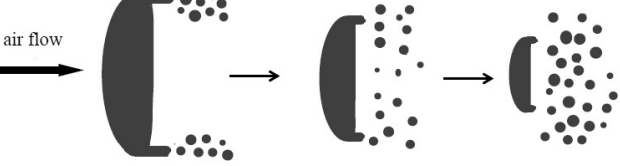
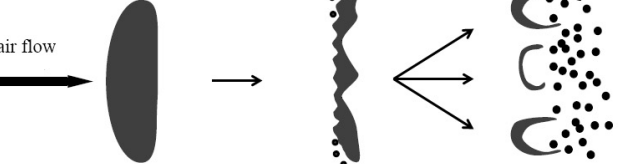
Deformation or breakup regime	Breakup process	Weber number
Deformation and flattening		$We < 12$
Bag Breakup		$12 < We < 80$
Boundary breakup or shear breakup		$We \sim 80$
Stripping Breakup		$80 < We < 350$
Catastrophic Breakup		$We \sim 350$

Table 2.4: Secondary breakup regimes (Adapted from Lee and Reitz 2001 and Tanner 2004).

During the first stage, the droplet experiences a shape change from its original spherical shape into a thin disk shape due to the action of the gas pressure around the droplet. Such phenomenon requires exposure of the droplet to a steady gas flow. After this deformation and flattening process, the secondary stage consists of the breakup of the initial droplet into many small droplets. Several regimes involving different breakup mechanisms have

been reported depending on the value of the relative velocity between the droplet and the ambient gas. Note that such mechanisms and regimes scale with Weber numbers and not with Reynolds numbers; they correspond respectively to the bag breakup regime, the shear breakup or boundary layer stripping breakup regime, the stretching/thinning breakup regime and the catastrophic breakup regime. This classification originally detailed by Pilch and Erdman (1987) is succinctly described below and illustrated in Table 2.4.

The bag breakup process deforms the initially flattened droplet created during the first stage into a thin bag which extends in the downstream direction and subsequently breaks up into droplets. An illustration of the process is illustrated in the photographs shown in Fig.2.8.

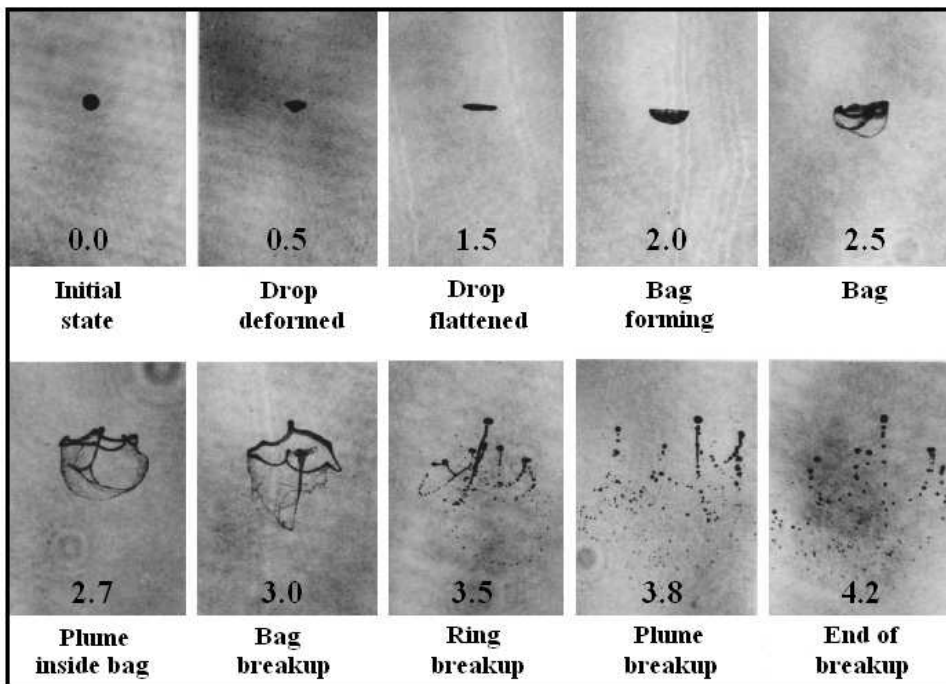


Figure 2.8: Pulse shadowgraphy of secondary breakup of a water drop in the bag regime with $We = 20$ and $Oh = 0.0045$ (Dai and Faeth 2001).

The shear regime is observed at higher relative velocities and involves deflection and stripping on the periphery of the droplet rather than on the center. This regime is also termed multimode breakup regime due to the different mechanisms that it contains such as the parachute breakup, chaotic breakup, transition breakup, *etc.*

The stretching/thinning breakup is similar to the shear breakup but occurs at higher relative velocities. The mechanism is based on the lateral extension and distortion of the initial droplet into thin sheets at the periphery which reduce the initial droplet mass while the thickness of the flattened droplet decreases from its center to its edge.

The catastrophic breakup mechanism occurs under the effect of high dynamic pressure on the surface of the flattened drop. It consists of a cascading process in which the initial droplet breaks up into fragments and fragments of fragments until all fragments and the resulting droplets possess a Weber number below a critical value.

2.2.3 Size distribution, number density and velocity of droplets

Due to the heterogeneous nature of the atomization process, practical sprays are characterized by a range of droplet diameters (polydispersity). In practice, atomizers produce droplets sizes from $\sim 1 \mu\text{m}$ up to $\sim 500 \mu\text{m}$. However, the measurement of droplets larger than $100 \mu\text{m}$ is infrequent in most of fuel sprays where the geometrical mean diameter is on the order of $\sim 20 \mu\text{m}$. Both the generation of monodisperse sprays and the control of droplet size are of interest for many applications and present a major challenge in spray technology. Modern monodisperse droplet generators are able to create thin stream of small droplets (for some droplet generators, particle size can be controlled from a few microns up to $20 \mu\text{m}$ - Xu and Nakajima, 2004) of fairly constant size. However, the generation of large conical monodisperse sprays containing high number densities of droplets of equal dimension has not yet been achieved. The droplet size distribution is generally represented via histogram plots. Each bin or ordinate represents the number of droplets whose dimension fall between the limits $D - \Delta D/2$ and $D + \Delta D/2$.

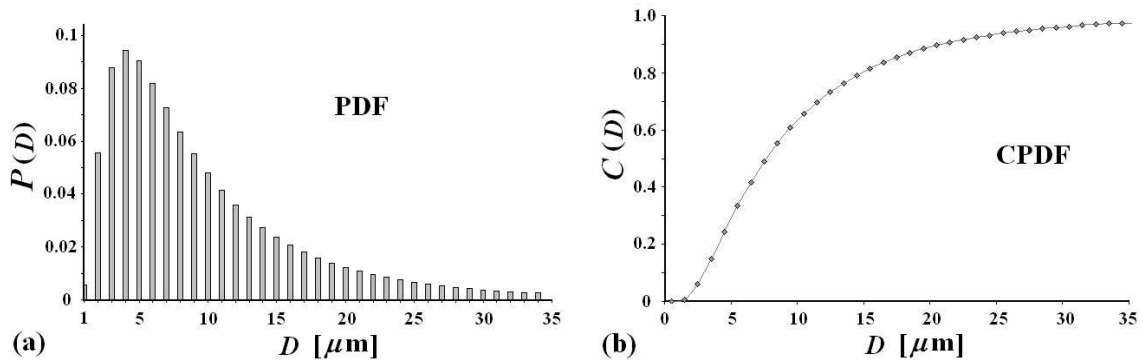


Figure 2.9: Example of droplet size distribution with $\bar{D} = 10 \mu\text{m}$. (a) is the Probability Density Function (PDF) and (b) is the Cumulative Probability Density Function (CPDF).

By reducing the width of the bins, ΔD , the histogram assumes a frequency curve which can be representative of the complete spray or of a given position within the spray. However, the total number of droplets recorded must be sufficient for valid statistics and accurate spray characterizations. These frequency distribution histograms are generally presented under their normalized form such as the Probability Density Function (PDF). Each bin represents in this case the fraction of the total number of droplet sampled for

a particular class of particle size. By summing the data from a given PDF, the Cumulative Probability Density Function (CPDF) is deduced. Occasionally, the volume of liquid produced by a particle size class is plotted instead of the number of droplets. This representation highlights the presence of large droplets in the spray.

Several empirical distribution functions have been developed to match experimentally measured droplet size distributions. These include the Normal, the Log-Normal and the Rosin-Rammler distribution. The Normal distribution is presented by the following equation:

$$P(D) = \frac{1}{\sigma \sqrt{2\pi}} e^{-(D-\bar{D})^2/(2\sigma^2)} \quad (2.2.2)$$

where σ is the standard deviation and \bar{D} is the mean arithmetic diameter.

The Log-Normal distribution is given by:

$$P(D) = \frac{1}{T \sqrt{2\pi} D} e^{-(\ln D - M)^2/(2T^2)} \quad (2.2.3)$$

where T is the shape parameter and M is the scale parameter. The mean diameter and the standard deviation are respectively given by:

$$\bar{D} = e^{(M+T^2/2)} \quad (2.2.4)$$

$$\sigma = \sqrt{e^{T^2+2M}(e^{T^2} - 1)} \quad (2.2.5)$$

The Rosin-Rammler formula gives the probability, Q , to have a particle diameter smaller than the diameter D and is given as:

$$Q(D) = 1 - e^{-\left[\frac{D}{D_k}\right]^q} \quad (2.2.6)$$

where D_k is the particle diameter such that 63% of particles are smaller than D , and q is a constant which provides a measure of the spread of drop diameters. Based on the analysis of several experimental results, Rizk and Lefebvre (1985) rewrote the Rosin-Rammler function and obtained much better fit to the droplet size data especially for the larger droplets. Similar to the conventional function, the modified Rosin-Rammler distribution is given by:

$$Q(D) = 1 - e^{-\left[\frac{\ln D}{\ln D_k}\right]^q} \quad (2.2.7)$$

The quality of atomization can be characterized by a number of representative droplet diameters. The use of mean diameters instead of the complete droplet distribution simplifies the calculations of mass transfer and flow processes. The notation of mean diameters

has been initially developed by Mugele and Evans (1951).

Symbol	Weighting	Expression	Physical meaning
D_{10} or \bar{D}	Number of length	$\frac{\sum_{i=0}^{\infty} N_i D_i}{\sum_{i=0}^{\infty} N_i}$	Average dimension
D_{20}	Surface area	$\left(\frac{\sum_{i=0}^{\infty} N_i D_i^2}{\sum_{i=0}^{\infty} N_i} \right)^{1/2}$	Average surface area
D_{30}	Volume	$\left(\frac{\sum_{i=0}^{\infty} N_i D_i^3}{\sum_{i=0}^{\infty} N_i} \right)^{1/3}$	Average volume (or mass)
D_{32}	Surface-volume SMD	$\frac{\sum_{i=0}^{\infty} N_i D_i^3}{\sum_{i=0}^{\infty} N_i D_i^2}$	Surface-volume which is related to mass transfer

Table 2.5: Table of the mean diameters with their physical meanings.

The “geometrical” or arithmetic mean diameter \bar{D} (or D_{10}), is, in terms of scattering process, the most representative mean diameter. Several additional mean diameters providing other useful information are respectively, the “surface area” mean diameter, D_{20} , the “volume mean diameter”, D_{30} and the “Sauter Mean Diameter” (SMD), D_{32} . The annotation and equation defining each of these mean diameters are given in Table 2.5. Other averaged diameters could be deduced by increasing the power to which D is raised in the numerator and/or in the denominator. However as they do not describe any physical quantity they are not used in practice.

The mass transfer of fuel from the liquid to the vaporized state is of major interest in combustion. Therefore, the surface area of a spray is important as the vaporization of droplets increases exponentially as droplet size decreases. D_{20} and D_{32} , which are both function of the droplet area are relevant values in spray combustion. Sowa (1992) demonstrated that, in a statistical sense, D_{32} was a better representation of the surface area mean diameter for evaporating sprays. This conclusion approved the convention of using the SMD

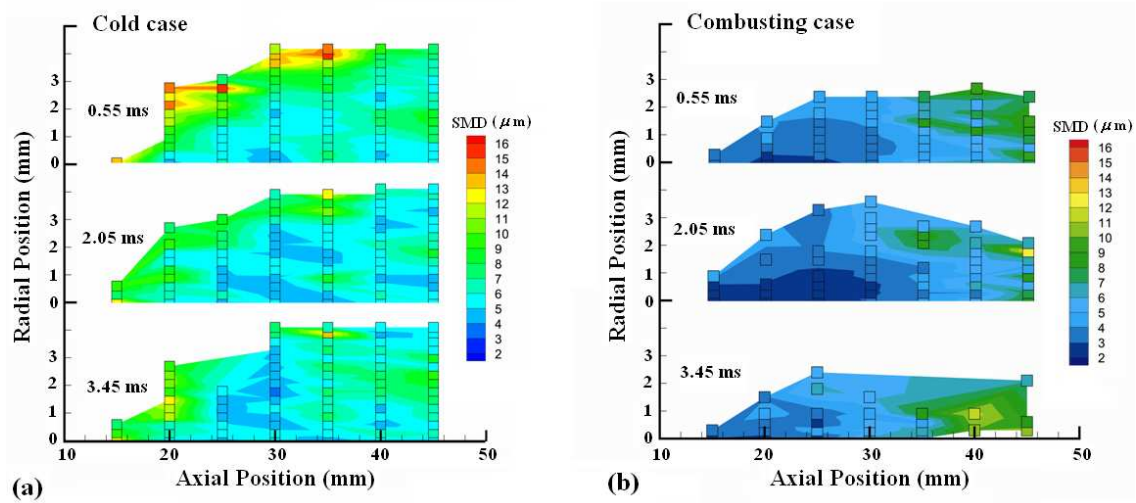


Figure 2.10: Example of a 2D Sauter Mean Diameter distribution in a diesel spray at different time after injection: Spray development (0.55 ms), steady state (2.05 ms) and spray dissipation (3.45 ms). (a) is the cold case and (b) the combusting case. (Source: Labs and Parker 2006).

in reporting results. Due to the variation of the SMD with position within the spray, D_{32} is generally measured at different points along an axis or across a grid of data as shown in Fig.2.10. A global average SMD can be deduced from these data sets.

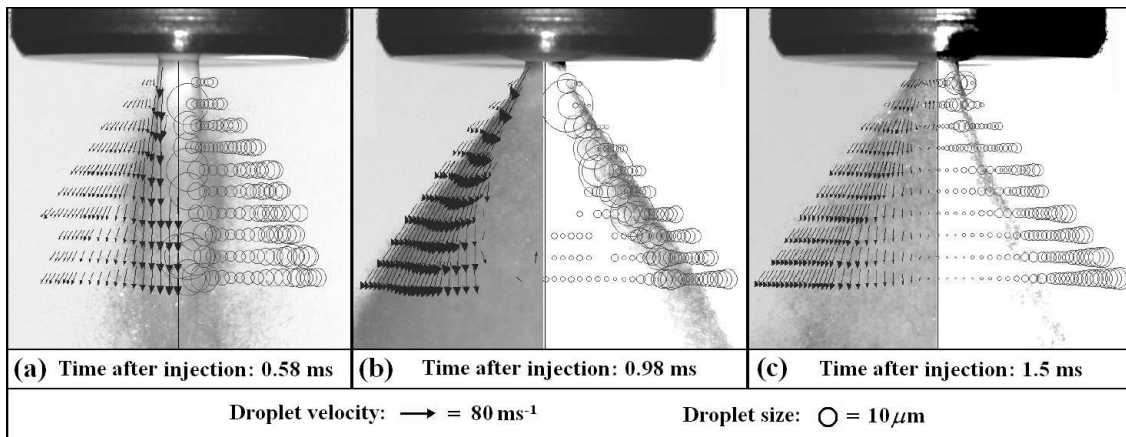


Figure 2.11: Velocity and droplet diameter within a GDI spray at different time after injection (Wigley 2002).

Similarly to the droplet size, the droplet velocity varies with position within the spray. Distributions of droplet velocity are related to nozzle geometry, injection pressure, liquid viscosity, and the ambient gas pressure. Large droplet in the near nozzle region have high velocities and subsequently breakup into small droplets of slower velocities. For each sprays and operating condition, the velocity distributions is different and their accurate measurement is often required in most practical application of sprays. Figure 2.11 is a good illustration showing strong variation of in both the velocity and droplets distribu-

tions of a Gasoline Direct Injection (GDI) spray for three different times after injection (Wigley 2002).

Optical Diagnostics of Dilute and Dense Sprays

THE optical characterization of sprays serves three main purposes: In terms of “research”, detailed information is necessary for understanding the physics of spray formation from an initial turbulent liquid flow. In terms of “development and testing”, it is necessary to obtain the complete spray properties in order to evaluate the effects of modifying the nozzle design and geometry. This is useful for the creation of new injector types and increasing the atomization efficiency. Finally, in terms of “quality control”, quick reliable characterization is required for checking and monitoring the desired spray structure (Bachalo 2000). As described in Chapter 2, spray formation is based on the disintegration of a liquid body into a multiplicity of small droplets. This complex fluid mechanical process called atomization is still not fully understood due to the difficulties of observation and the lack of information extracted in the near-injector region. Spray characterization has been performed during the past years via an extremely large number of techniques. Photographic, mechanical and electrical methods were firsts applied. However, due to their non-intrusive nature and high measurement accuracy laser diagnostics have become rapidly the method of choice. As a result of important innovations in laser technology over the last 30 years, optical sensors sensitivity, computer performances and softwares development various laser technics have been tested and applied.

The classification of laser techniques for spray analysis remains a problem. They can be categorized on the information provided (droplet size, droplet velocity, evaporation rates, phase transitions *etc*), on the “direct” or “indirect” nature of the method applied, or on the optical principles employed. The hybrid characteristic of certain techniques complicates classification. In this chapter, a description of the three well established techniques is initially reported. A second section concerns the promising techniques which have recently emerged. Finally, the limitations of each technique are highlighted with particular attention given to multiple scattering phenomena.

3.1 Commonly used laser techniques

A large number of laser techniques are and have been used for spray characterization. Some of them are in the development process whereas, some are no longer used owing to their limitations. This section is limited to the well established techniques which are enumerated as follow:

- Fraunhofer diffraction
- Point interferometry
- Planar laser imaging

The final section summarizes the major limitations for each of these techniques.

3.1.1 Fraunhofer diffraction

One of the first particle sizer instrument based on diffraction was developed by Cornillaut in 1972 for size measurements of powders. In 1976, Swithenbank *et al.* applied the technique for droplet sizing. Owing to the low cost and the simple system of the optical instrument, Fraunhofer diffraction technique, more correctly named Low-Angle Laser Light Scattering (LALLS), has been attractive and widely used. In order to avoid any confusions, it is important to note that “diffraction” such as “refraction” and “reflection” is only one component of the complete “scattering” process (see section 4.2.3). The well established commercial instrument based on diffracted light detection for particle sizing is the Malvern Particle Sizer and the recent version is named Spraytec.

The technique consist of illumination of the spray with a coherent collimated monochromatic light source (normally a HeNe laser beam) and analysis of the Fraunhofer diffraction pattern created by the scattering of the incident light from the droplets in the near forward direction. For spherical droplets, the resulting diffraction pattern represents a series of large concentric laser light rings around the central geometrical image. The spacing between the rings is related to the scattering angle, θ_s , which is inversely proportional to the particle diameter. The intensity of light diffracted, I_d , by a single spherical droplet of diameter, D , is analytically given by (Huzarewicz 1991):

$$I_d = I_i \left[\frac{2J_1(x\theta_s)}{x\theta_s} \right]^2 \quad (3.1.1)$$

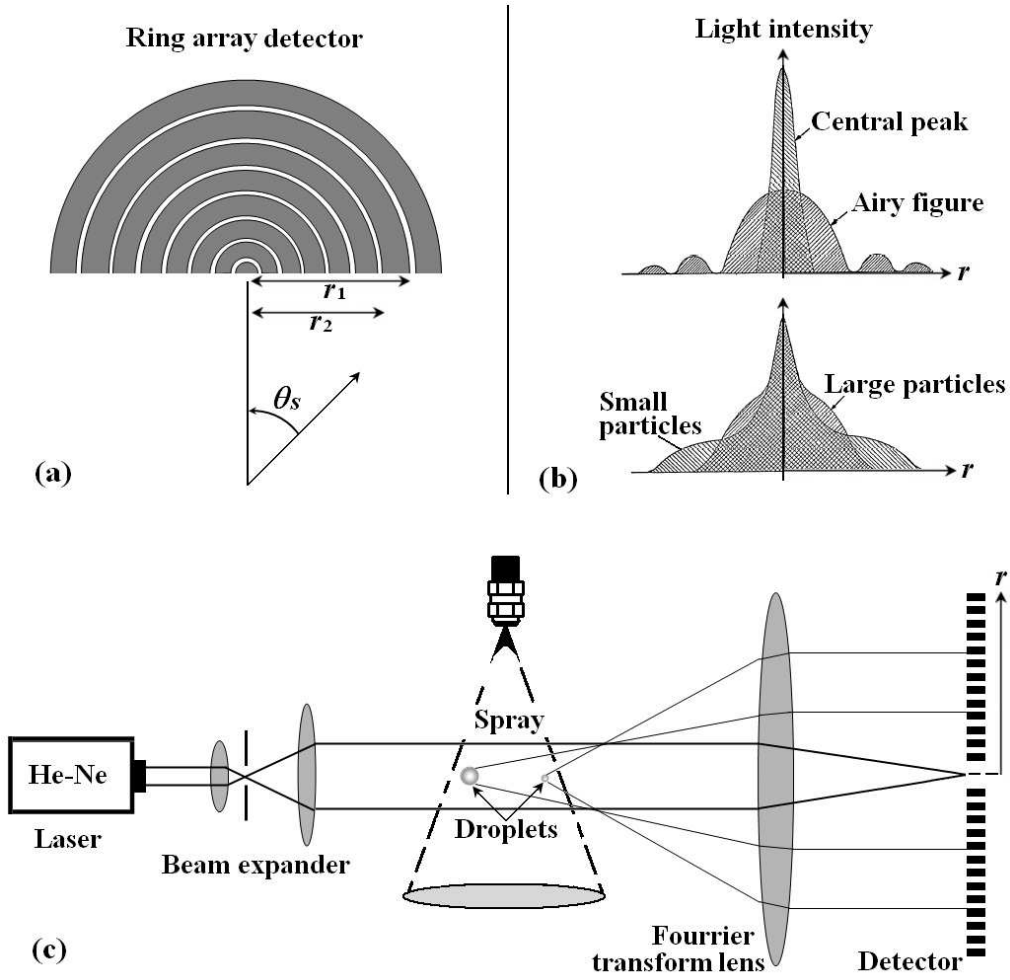


Figure 3.1: Principle of the small angle light scattering (Fraunhofer diffraction) detection. (a) represents the detector array with the scattering angle θ_s , (b) is an illustration of different intensity profiles detected and (c) is the optical arrangement of the system.

where I_i is the incident light intensity, J_1 is the Bessel function of the first kind and of the first order and x is the particle size parameter (see Eq.4.1.7). The fraction of the total energy $L(r_1)$ contained within a circle of radius r_1 in the image plane centered on the geometrical image is obtained by integrating the right hand side of equation 3.1.1 over the enclosed area to give:

$$L(r_1) = 1 - J_0^2(xr_1) - J_1^2(xr_1) \quad (3.1.2)$$

where J_0 is the Bessel function of the first kind and of order zero. The energy contained within concentric circles of respective radius r_1 and r_2 (such that $r_1 \leq r_2$) is:

$$E(r_1, r_2) = C_p \pi \frac{D^2}{4} [(J_0^2(xr_1) + J_1^2(xr_1)) - (J_0^2(xr_2) + J_1^2(xr_2))] \quad (3.1.3)$$

where C_p is a constant proportional to the laser power. In practice, it is not only one droplet but a collection of droplets of various sizes that are considered along the laser line-of-sight. In absence of multiple scattering, the resulting light energy corresponds directly to the sum of the light energy scattered by each individual droplets as:

$$E(r_1, r_2) = C_p \pi \sum_{i=0}^m N_i \frac{D_i^2}{4} [(J_0^2(xr_1) + J_1^2(xr_1)) - (J_0^2(xr_2) + J_1^2(xr_2))] \quad (3.1.4)$$

where N_i is the number of spheres of diameter D_i . The relationship between a radius of dimension r_d and its scattering angle, θ_s , is given by the relation $\theta_s \approx r_d/f$ where f is the focal length of the Fourier transform lens.

An illustration of the experimental setup is given in Fig. 3.1(c). The laser beam is initially magnified by a beam expander and traverses the spray from one side to the other. The light exiting the spray encounters a Fourier transform lens in the far field region which displays the diffraction pattern and focus the the non-scattered light (ballistic photons) at the Fourier transform plane. Finally, for each particle size distribution, a distribution of light energy $E(r_1, r_2)$ can be determined. This distribution is measured using a photodiode array (or a Charge Coupled Device (CCD) chip) in the form of rings positioned on the Fourier transform plane. Information regarding the droplet size distribution is extracted using signal reconstruction algorithms. These algorithms are based on the assumption that the drops size follow a Rosin-Rammler or a Log-normal distribution. Finally, the size distribution which gives the most closely fitting diffraction pattern is chosen and the mean diameter is extrapolated along with its standard deviation.

3.1.2 Point interferometry

The first interferometry point technique was developed by Yeh and Cummins (1964) for the measurement of flow velocity using seeding particles. Shortly after this first publication, a large variety of systems have been proposed in order to optimize the measurement (Durst and Whitelaw 1971). The method is based on dividing a coherent laser beam into two beams which intersect in the spray with a given angle θ_b (see Fig.3.2). The recombination of the two coherent beams creates an interference pattern in the probe volume due to superposition of the two electric fields.

When a droplet crosses the interference fringes, it scatters intensity-modulated light. This light signal is collected by a lens and focused onto a photo-detector which converts the light intensity fluctuations into voltage fluctuations. The rate of intensity variation, named the Doppler frequency, indicates the time for a droplet to travel the distance between two

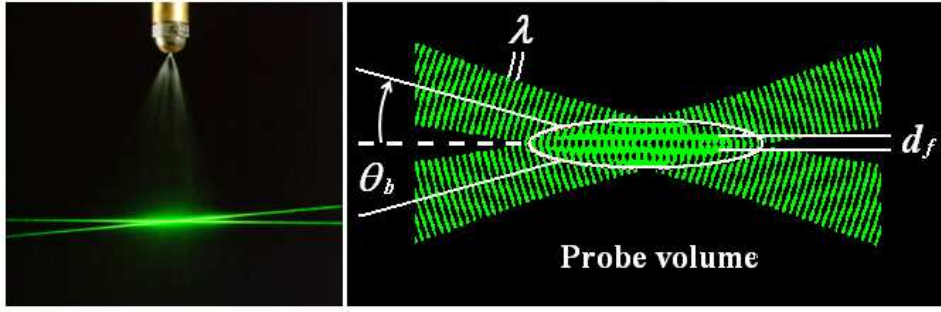


Figure 3.2: Interference fringes created by two crossing laser beam (source: Dantec).

fringes. By knowing the separation distance of the fringes, $d_f = \frac{\lambda}{2 \sin \theta_b}$, the velocity of the droplets can be deduced. The use of interference fringes to determine droplet velocity is known as Laser Doppler Velocimetry (LDV), or Laser Doppler Anemometry (LDA), and was largely developed in the early 70's (Durst 1971, Farmer 1972a and 1972b).

A major extension of the LDV consists of the use of a second photo-detector in order to measure not only the droplet velocity but also the droplet diameter. This new technique called the Phase-Doppler Anemometry (PDA), or Phase-Doppler Interferometry (PDI), was initially implemented by Durst and Zare (1975). The principle is as follows: When two detectors record the Doppler signal at slightly different scattering angles, changes in the phase of modulation occurs. This changes of phase, $\Delta\Phi$, (see Fig.3.3), is found to be linearly dependant to the diameter, D , of spherically homogeneous (constant index of refraction) particles when the signal detected is dominated by only one scattering mode. Generally, the mode of interest is the reflection for opaque particles and the first order refraction for droplets with significant transparency. A detailed description of the scattering modes for spherical droplets is given in section 4.2.3.

When only reflection is considered, the phase shift $\Delta\Phi$ is given as (Durst 2000):

$$\Delta\Phi = \frac{2\pi D}{\lambda} \frac{\sin \theta_b \sin \psi}{\sqrt{2(1 - \cos \theta_s \cos \psi \cos \theta_b)}} \quad (3.1.5)$$

where θ_s is the scattering angle, ψ is the elevation angle as shown on figure 3.3(a) and D is the particle diameter. If, however, the dominant scattering mode is the first order refraction, the difference of phase between the two detectors is calculated as (Durst 2000):

$$\Delta\Phi = \frac{-2\pi D}{\lambda} \frac{n_r \sin \theta_b \sin \psi}{\sqrt{2(1 + \cos \theta_s \cos \psi \cos \theta_b)(1 + n_r^2 - n_r \sqrt{2(1 + \cos \theta_s \cos \psi \cos \theta_b)}}} \quad (3.1.6)$$

where n_r is the real part of the droplet refractive index.

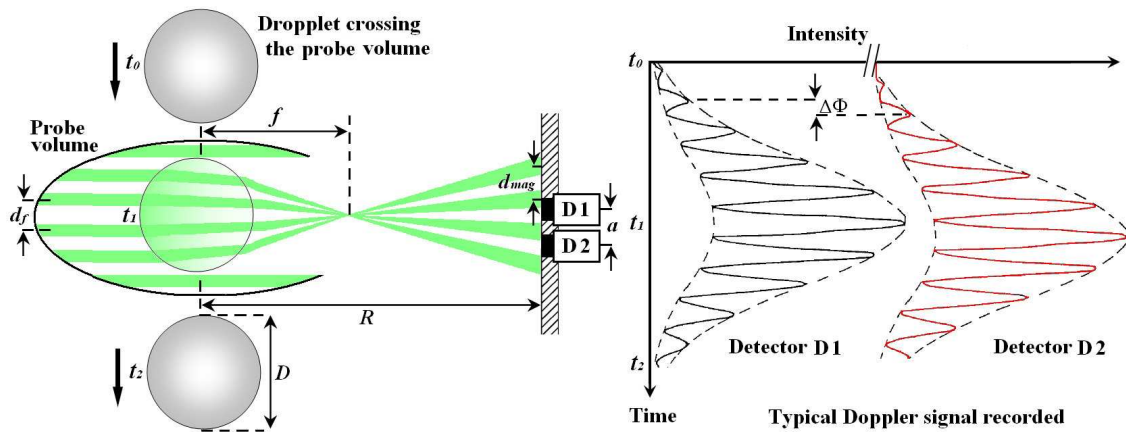


Figure 3.3: Illustration of the PDA principle. The phase shift $\Delta\Phi$ between the two recorded Doppler signals is directly related to the droplet diameter D . An approximation consists of considering the droplet as a thick lens. In this case, $d_{mag} = (R - f) \cdot \frac{d_f}{f}$ and as $R \gg f$, $d_{mag} \approx R \cdot \frac{d_f}{f}$.

As mentioned above, it is convenient in practice to detect the first order refracted light as a dominant scattering order when probing droplets of significant transparency. This is achieved by positioning the detectors at the Brewster's angle $\theta_s = 2 \tan^{-1}(1/n_r)$. This angle is generally between 30° and 80° . For water droplet of refractive index $n = 1.33$ in air and for parallel polarized light this angle equals 70° (Saffman 1986, Wigley 1994).

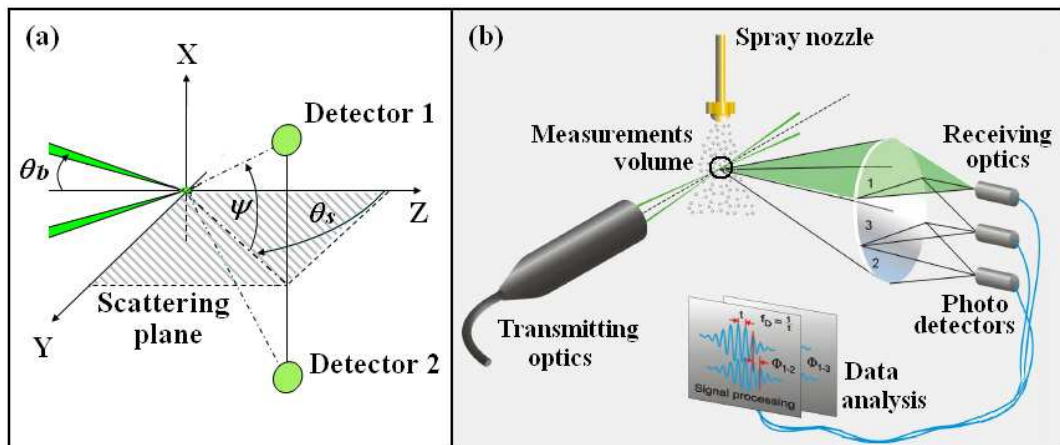


Figure 3.4: Standard configuration of the Phase Doppler Anemometry system. Angles annotations are given in (a) and the optical arrangement is illustrated in (b) (source: Dantec).

Since its first appearance, the PDA technique has been corrected from several sources of errors. The first one, known as ‘‘Gaussian beam defect’’, is explained as follows: Depending on the droplets trajectory through the probe volume, reflected and refracted light may have roughly equal intensities. This problem occurs also for laser beams with approximately uniform intensity profile or for top hat intensity profiles but the problem is much more difficult to control for Gaussian beams (Bachalo 2000). When the first order

refracted light does not dominate, a deviation of the linearity between the measured phase shifts and the drop size occurs causing serious errors in the droplets size measurement. This problem is described in detail by Aizu *et al.* (1993). Numerical studies have been also published and some suppression strategies have been suggested by Grehan *et al.* (1991, 1992).

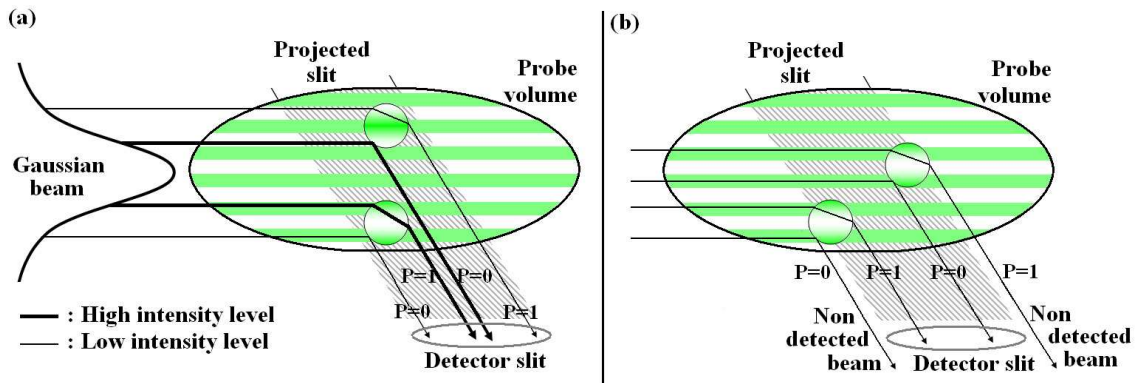


Figure 3.5: (a) Gaussian beam defect: depending on the position of the droplet, reflected ($P=0$) and first order refracted ($P=1$) light can have similar intensities. (b) Slit effect: for particle trajectories at one edge of the slit projection, unwanted scattering mode dominates.

The second source of errors, also related to the detection of unwanted scattering modes, is “the slit effect”. It occurs when the droplets traverse an edge of the detection volume. The defined detection volume is delineated in the probe volume by the projection of the receiving slit aperture (see Fig.3.5). In some cases, the desired scattering mode is totally suppressed. The slit effect is discussed by Xu and Tropea (1994), and Durst *et al.* (1994).

The third source of errors concerns the detection of phase shifts greater than 360° . This occurs when measuring polydisperse sprays with extreme variations in droplets size. To avoid such problems, a third detector is always used in practice (see figure 3.4(b)) providing a second determination of the phase shift and serves to place the measurement in its appropriate cycle. The first instrument commercially available using three detectors, is the Phase/Doppler Particle Analyzer (P/DPA) (Bachalo and Houser 1985).

Another limitation in PDA measurements is known as “droplet shape effects”. As mentioned previously, conventional PDA systems assume the droplets to be perfectly spherical. However, depending on the internal and external pressure forces under which droplets are subjected, irregular-shaped particles, such as prolate and oblate ellipsoids, are produced. When probing such non-spherical particles, errors related to the degree of distortion are introduced in the measurement. These errors can result in overestimation of droplet diameters up to 45%. Sizing non-spherical particles via conventional PDA systems appears to be unachievable despite the research effort expended (Damaschke

1998; Doicu 1998). In modern PDA instruments, the sphericity validation is performed by comparing the phase differences measured from two pairs of detectors and rejecting the detected sample whose deviation exceeds a certain amount. In the dense spray region, the rejection rate can be extremely high making the measurement unreliable.

The fifth source of errors is referred to “multiple occupancy” and appears when several droplets occupy the probe volume. This issue occurs at high number density of droplets (in the near field region) and leads to unprocessable overlapping signals reducing the validation rate of the optical instrument. One solution consists in reducing the probe volume. However, reducing the measurement volume leads to a reduction of the interference fringes. As a result, the burst signal generated by the probed droplets will be weaker, thereby increasing the difficulty in the Doppler frequency determination. Multiple occupancy is also responsible for count errors (e.g. at each detection time photo-detectors validate only 1 droplet within the probe volume instead of 2 or 3) which affect the determination of droplet flux and concentration. A statistical correction of such a problem has been proposed by Roisman and Tropea (2000).

Finally, the last source of errors introduced in PDA measurements is caused by multiple scattering and attenuation processes. These phenomena are mentioned in subsection 3.1.4 and described accurately in section 4.2.4. To overcome attenuation issues (often named “obscuration” in spray diagnostics) within the dense sprays region, one solution consists in using high power PDA systems. This has been proposed by Wigley *et al.* (1999) and applied to the case of a Gasoline Direct Injection (GDI) spray operating at pressure injection of 50 bars (2002). Due to the complexity of the problem, a corrective method for multiple scattering has not been offered yet. As mentioned by Berrocal *et al.* (2005b), multiple scattering depends both on the source-detector configuration and on the spray structure (high number density and size of droplets). Nowadays, multiple scattering presents the most important source of errors limiting the PDA technique to the dilute region. One solution for understanding and quantifying such errors consists in the simulation of the propagation of the laser light within the spray (Berrocal *et al.* 2005a). Detailed information about multiple scattering is provided in the two next chapters.

The historical development and improvement of PDA (Durst-1997) can be reviewed as follows: After the first the introduction of the technique in 1975, further development and its application to spray diagnostics did not occur until 1980 (Bachalo 1980, Bachalo and Houser 1984). Figure 3.4 (a) and (b) is an illustration of the optical arrangement which is referred in the literature as the “standard configuration”. The influence of the incident polarization state on the accuracy of particle sizing has been investigated by Saffman (1986). For the measurements of fine particles ($D \ll 10\mu\text{m}$), another optical arrangement

called the “Planar configuration” has been developed by Naqwi (1991, 1992). The planar PDA positions the two laser beams, their electric vector and the two detectors all on the same plane (XY plane on figure 3.6 (a)).

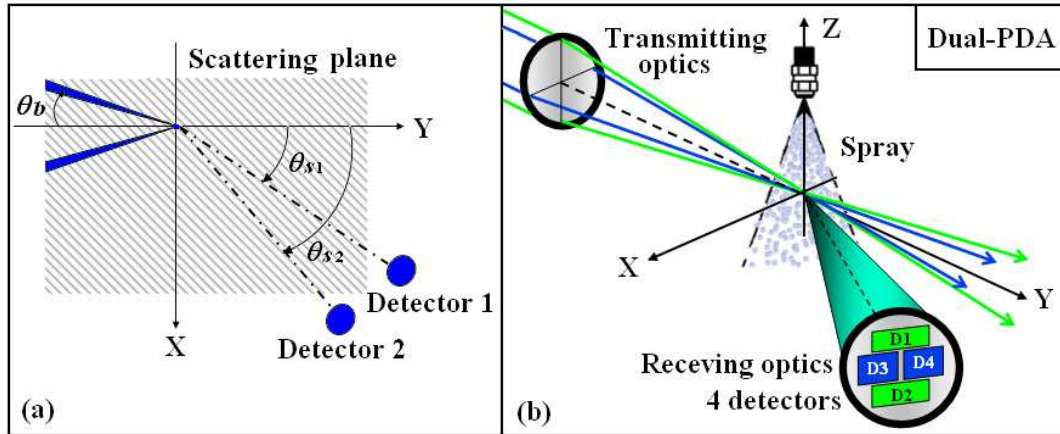


Figure 3.6: (a) Planar PDA configuration. (b) Dual PDA (source: Dantec).

Finally, the most advanced instrument, initially developed by Tropea *et al.* (1995), is the so called Dual-PDA from DANTEC/invent. The technique consists in the combination of the standard PDA (Fig.3.4 (a)) with the planar configurations (Fig.3.6 (a)). In order to differentiate in the same setup each configuration, two laser wavelengths ($\lambda = 514.5$ nm (green) and $\lambda = 488$ nm (blue)) are generated from an argon-ion laser and the emitted signal detected by two pairs of photo-detectors (one pair for each wavelength). By means of this new arrangement, the system is able to reduce the Gaussian beam defect and the slit effect allowing considerable improvements in the measurement accuracy of mass flux and droplet concentration. A comparison with other PDA instruments given by Dullenkopf *et al.* (1998) demonstrates the high performances and accuracy of the technique. The Dual-PDA is actually the most reliable instrument for spray characterization and offers simultaneous measurements of droplet size, velocity, flux, number density and time-of-arrival statistics. The refractive index can also be deduced from such modern interferometric point measurement as demonstrated by Onofri *et al.* (1994). However, in phase-Doppler measurements, only local information are extracted and the complete characterizations of sprays is time consuming.

3.1.3 Planar laser imaging

There also exists an ensemble of techniques based on planar laser imaging. The basic concept consists in the creation of a thin laser sheet which traverses the spray and this illuminated plane imaged via a camera (Fig.3.7). The laser sheet is formed from the

incident cylindrical beam by the association of positive and negative cylindrical lenses or in the case of diverging sheet by only one positive cylindrical lens. Photons scattered from the droplets are generally collected at $\theta_s=90^\circ$ by a CCD camera. This geometry results in a spatially resolved measurement across a plane in the spray. From the recorded images, a description of the spray structure on a macroscopic scale such as the cone angle, the length of penetration and the length of the liquid core can be obtained. Further information, like droplets characteristics (geometrical size, SMD, number density) and the spray dynamic (droplet and gas velocity vectors, evaporation rate, vortices), can also be extracted depending on the scattering process and on the detection technique involved. The most relevant methods based on spray planar imaging are enumerated within each paragraph below.

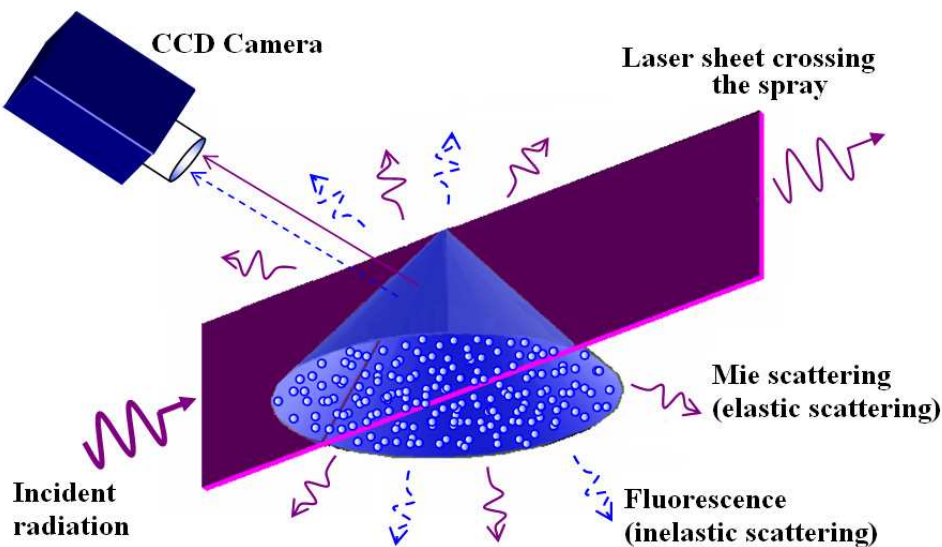


Figure 3.7: Illustration of planar laser imaging for Mie scattering and Laser Induce Fluorescence emission.

- *Planar Mie imaging:*

Planar Mie imaging corresponds to the detection of the elastic light scattered by the droplets and the irregular liquid elements of size comparable to the incident wavelength. By definition, “elastic scattering” is the term given when the light scattered from the illuminated particles (or molecules) has a wavelength identical to the incident radiation. When, on the contrary, the scattered light is characterized by a different wavelength than the incident radiation (longer or smaller) the process is called “inelastic scattering”. In laser diagnostics of non-combusting sprays Mie scattering is the “natural” and dominant scattering process from the interaction of the incident laser light with the various liquids elements resulting from atomization. For spherical and homogeneous droplets of size

much bigger than the wavelength, the total amount of light elastically scattered in all direction (quantified by the scattering cross-section) is found to be linearly dependant to the square of the droplet diameter D^2 (see Fig.4.2 in section4.2.3). However, considering a given collection angle (e.g. for θ_s equal 90° or 60° degrees) and/or for small particles (D less than $10 \mu\text{m}$), this dependence is not valid any longer and correction procedures are required (Domann 2002, Domann and Hardalupas 2003 and Charalampous 2004). Planar Mie images are generally used to provide information related to geometrical aspects of the spray structure.

- *Planar Laser Induced Fluorescence:*

Planar Laser Induced Fluorescence (PLIF) is based on the initial absorption of the incident laser radiation followed by the emission of a new electromagnetic radiation at a longer wavelength. This inelastic scattering process is caused by the addition of a dye or tracer within the injected liquid or by the natural fluorescence of the probed species. Some liquids of interest such as water, alcohol and pure aliphatic hydrocarbons do not fluoresce and require a doping agent. On the contrary, commercial fuels contain a variety of fluorescing compounds that can be excited in the ultra-violet spectral region. However, in this last case, the signal emitted is often difficult to quantify and for practical applications tracers are mostly added in a manner that the fluorescing signal can be selectively detected. PLIF techniques are used for the visualization of the liquid phase in non-evaporating sprays and for the identification of both the liquid and vapor phase in evaporating sprays. The measurement of species concentration and temperature is also performed via PLIF especially in combusting sprays. The principle of the technique is as follows:

When the appropriate doped droplets or species cross the laser sheet, the incident optical excitation induced produces the emission of an incoherent fluorescence signal which is optically filtered and detected. The signal intensity generated is a function of the absorber concentration, the temperature and the ambient pressure. In the past, a variety of fluorescent tracers have been used including acetone (Thurber 2001), p-Terphenyl (PTP) (Le Gal 1999), and strongly fluorescing large organic molecules like chinine, sodium salicylate (Jermy 2000), azulene as well as laser dyes. Mixtures of tracer (e.g. 1% Pentanone - 1% Hexagone in 98% of Iso-octane solution) have been also tested in the case of an evaporating GDI spray at temperature and pressure conditions by Réveillé (2005). For small droplets containing the appropriate doping agent at correct concentrations, the emission of the fluorescence signal is isotropic and proportional to the incident light intensity. In such conditions, and for constant incident radiation, the fluorescence signal is volume de-

pendant and linear to D^3 for spherical droplets. Increasing the size of the droplets and/or the concentration of the tracer leads to an increase in light attenuation within the droplets. In this case, the light emitted becomes anisotropic with a dominant back scattering.

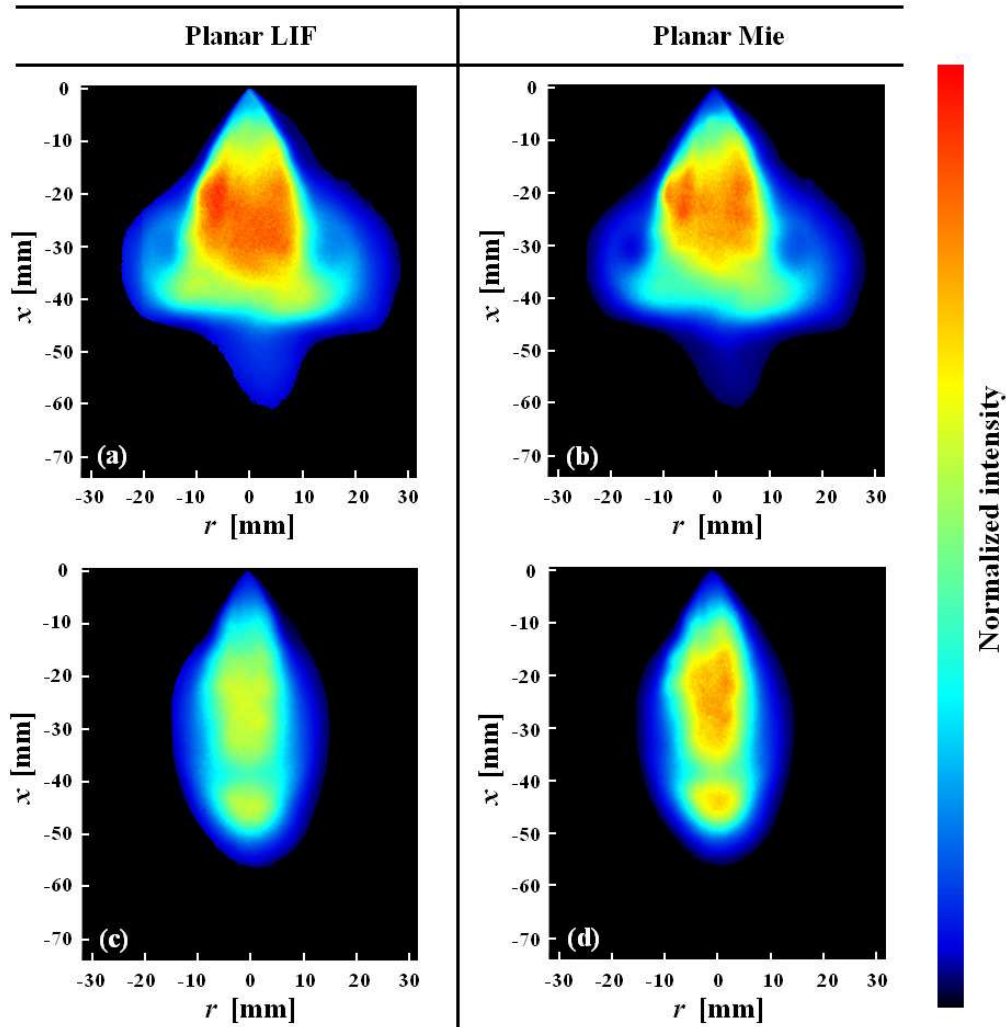


Figure 3.8: Averages of 200 LIF and Mie images for an evaporating diesel sprays at different time after injection. The ambient gas is set to 1 bar and 25°C in (a) and (b) and to 3 bars and 135°C in (c) and (d). All images correspond to 1.7 ms after injection (Réveillé 2005).

At high dye concentrations, the linearity between the emitted signal and the incident intensity is no longer respected due to saturation. Such phenomena have been investigated by Domann 2002 and Charalampous 2004. To guarantee the proportionality of the Laser Induce Fluorescence (LIF) signal with the droplet volume, concentrations of tracer and laser light intensities must be then carefully chosen. A main strategy of LIF is to differentiate one phase from the other. This is performed by choosing the adequate doping agent which reduces the fluorescence signal in one phase while emitting a strong signal in the other. The ionic dye Rhodamine 6G is commonly used for the detection of the

liquid phase in sprays. At low concentration Rhodamine 6G has poor quantum efficiency in the vapor phase; whereas, its liquid phase is characterized by high quantum efficiency. This liquid fluorescence predominance presents the main advantage to highlight the formation of liquid ligaments and droplet during the breakup processes. For combusting and evaporating sprays subjected to high temperature and pressure conditions, one key point is to find a tracer which evaporates in the same manner than the injected fuel and that is characterized by an identical boiling point. If the tracer evaporates faster than the fuel (indicating that the boiling point of the tracer is below that of the fuel), the tracer concentration inside the droplet will decrease and the LIF signal will under predict the droplet volume. If, on the contrary, the fuel evaporate faster than the tracer (indicating that the boiling point of the tracer is below that of the fuel), the tracer accumulates in the droplets and the detected LIF signal will over predict the actual droplet volume. The temperature dependent fluorescence cross-section must also be carefully considered when investigating evaporation rates at high temperature conditions. The main advantage of the LIF signals over other inelastic processes, such as Raman scattering, is due to the good resultant Signal to Noise Ratio (SNR) obtained in the planar configuration.

- *Laser Sheet Dropsizing:*

Laser Sheet Dropsizing (LSD) called also Planar Drop Sizing (PDS) is based on the combination of planar Mie imaging and PLIF. The method was originally developed and described by Yeh *et al.* 1993. Le Gal presented some experimental results in 1999 whereas Domann 2002 and Charlalampous and Hardalupas 2004 calculated theoretically the errors in the measurement of single droplets and for different Rosin-Rammler droplet distributions. The technique is based on the simple concept that, for a doped droplet which is excited, the fluorescence signal will give a measure of the droplet volume; whereas, the Mie elastically scattered light will represent the surface area. By dividing the LIF signal S_{LIF} by the Mie signal S_{Mie} , the Sauter Mean Diameter can be deduced, as:

$$SMD = \frac{S_{LIF}}{S_{Mie}} = \frac{C_{LIF}}{C_{Mie}} \cdot \frac{\sum_{i=0}^m D_i^3}{\sum_{i=0}^m D_i^2} = K \cdot \frac{\sum_{i=0}^m D_i^3}{\sum_{i=0}^m D_i^2} \quad (3.1.7)$$

Here C_{LIF} and C_{Mie} include experimental factors such as scattering efficiency, detector response, signal collection solid angle, laser power, *etc.* The ratio C_{LIF}/C_{Mie} is assumed constant in LSD and is deduced after system calibration (e.g. using PDA measurements). However, Domann (2002) showed the variations of this ratio as a function of the droplet diameter and proposed a correction procedure to determine the appropriate value of K for different droplet distributions. In practice, both signals are recorded simultaneously

by two separated CCD cameras or by one camera using two separated optical channels. If a sufficiently large amount, N_s , of sample are recorded, a statistically good average is obtained. Although LSD presents clear advantages for fast 2D SMD measurements, the technique suffers from serious limitations especially in the measurement of small droplets, where the dependance of the Mie signal in D^2 is no longer respected. Réveillé (2005) showed experimentally that the technique gives results with $\sim 25\%$ errors when compared with PDA whereas Domann and Hardalupas (2003) calculated theoretically an error on SMD measurements ranging from 4% for a distribution of droplets with $\bar{D} \sim 150 \mu\text{m}$ to 31% with $\bar{D} \sim 10 \mu\text{m}$ assuming the perfect case of single scattering. These results are presented Fig.3.9.

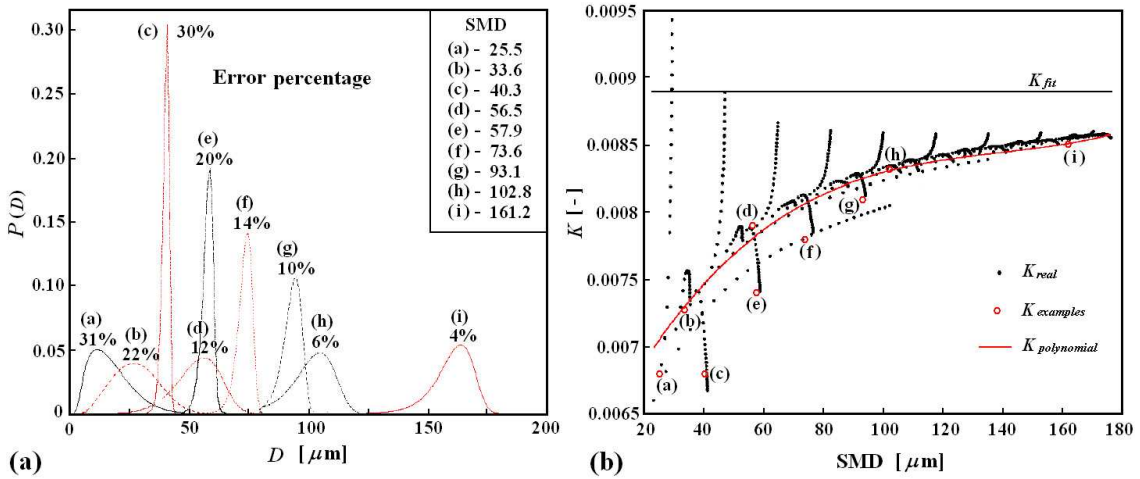


Figure 3.9: Estimation of the error on the SMD estimation via LSD measurement. Different droplet distributions are presented in (a) with the error on the measurement of the SMD when assuming a constant value of K . (b) shows the variation of the calibration constants K as a function of the SMD: K_{fit} is obtained from experimental results with $\sim 200 \mu\text{m}$ monodisperse droplets, K_{real} is the real K deduced from calculation, and $K_{polynomial}$ is the best polynomial fit of the calculated data (Domann and Hardalupas 2003).

Other limitations are described in section 3.1.4 demonstrating that the technique still requires some improvements before being reliable and must be manipulated with care.

- *Lasing imaging:*

Lasing imaging is a less common planar laser technique originally developed and applied to spray diagnostics by Serpenguzel (1992 - 2002). The principle is to consider spherical droplets as perfect microcavities which act as optical resonators for light rays of specific wavelengths when the Morphology Dependent Resonances (MDR's) is satisfied. These rays are internally reflected within the droplet and return to their starting position in phase after one round trip. If the roundtrip gain is bigger than the roundtrip loss, lasing

occurs. The gain is increased by adding an appropriate dye which produces a more effective optical feedback for the fluorescence radiation. In the case of droplets doped with Rhodamine 6G and illuminated at 532 nm, the lasing emission is red shifted from the yellow fluorescence emission (the red side of the fluorescence maximum).

As described by Serpenguzel (1992), lasing requires the gain to be larger than the absorption and leakage losses of the fluorescence radiation, and is more effective for the large droplets. The big droplets are then seen as red on the recorded images; whereas, ligaments and small droplets that do not achieve the lasing threshold are seen as yellow from the fluorescence only (as illustrated in Fig.3.10 (c) and (d)). This technique allows an original visualization of the spray structure. An example of lasing image is given picture 3.10. The determination of the droplet size can also be performed by determining the separation distance between the two high intensity glare points.

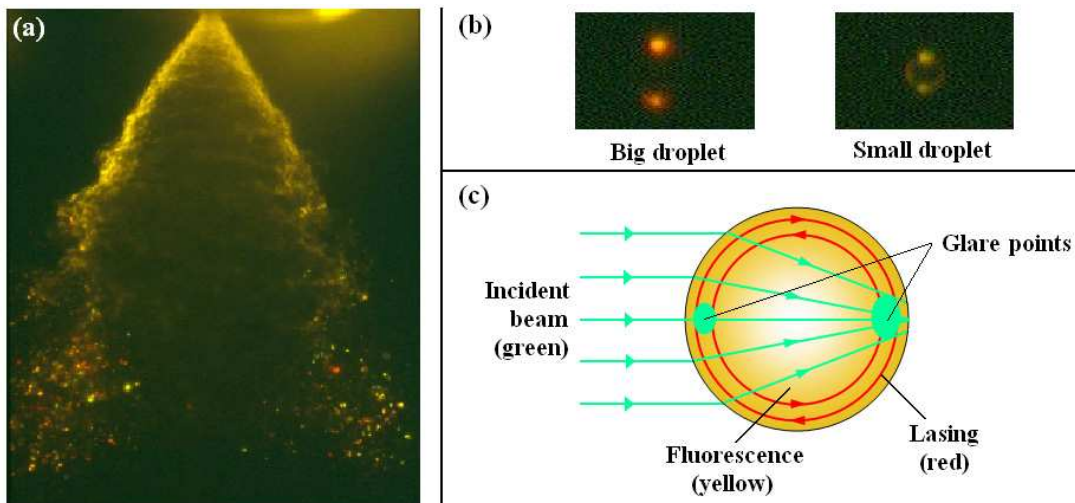


Figure 3.10: Image of the lasing and fluorescing Rhodamine-6G doped water spray. Droplets are identified and measured by their pair of two reciprocal lasing spots (Serpenguzel 2002).

- *Particle Image Velocimetry:*

Particle Image Velocimetry (PIV) is a planar laser based technique for the determination of instantaneous flow motion within fluids. In the early stage of the PIV elaboration, several researchers used double exposure photographs to measure the parabolic shape of laminar flows (Grousson and Mallick 1977). The technique, named Laser Speckles Velocimetry (LSV), was based on the measurement of laser speckles displacement and was largely improved by Meynard until 1983 (Meynard 1980, 1983). In 1984, the term “Particle Image Velocimetry” appeared in the literature with the respective articles of Pickering and Halliwell (1984) and Adrian (1984). The new approach images directly

the individual particles instead of the speckles. After 1984, the use of PIV increased considerably due to the potential of the technique to understand and visualize complex fluid dynamics processes within semi-turbulent and turbulent flow regimes. The evolution of PIV during the 20 years succeeding its introduction has been reviewed by Adrian (2005). Other review papers have been published by Westerweel (1997) and Prasad (2000).

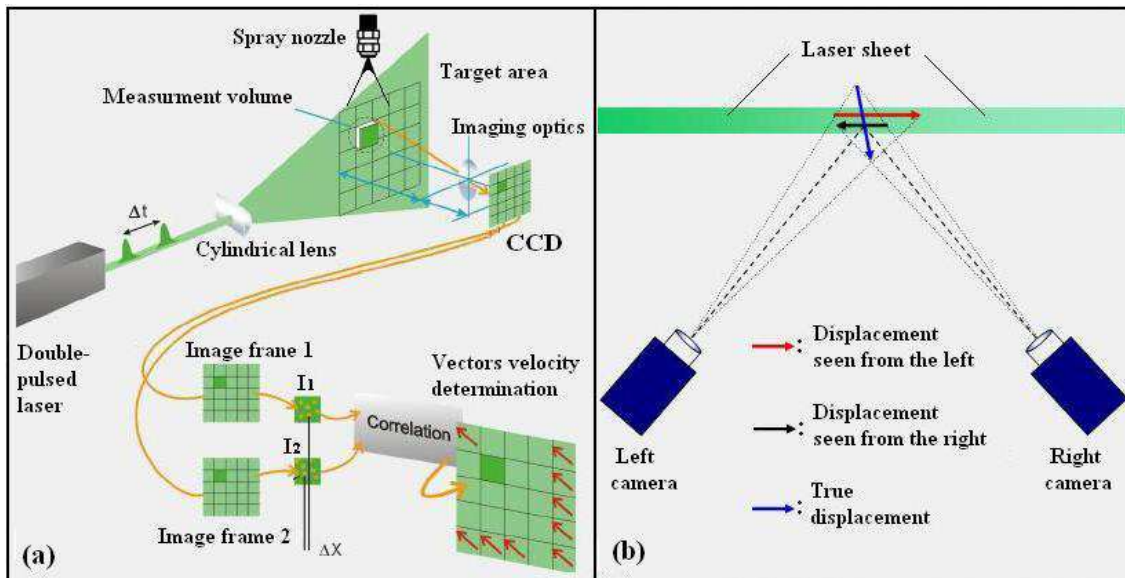


Figure 3.11: Principle of PIV measurement in (a) with the stereoscopic arrangement in (b) (Source: Dantec).

The PIV technique makes visible the fluid motion by adding adequate particles, called tracers, which scatter light when illuminated by the incident laser sheet. The laser sheet is generally imaged at 90° via a CCD camera and two successive images are captured using a pulsed laser as illustrated in Fig.3.11. The displacement of the particles between the two images and their respective velocity vectors are deduced from the time delay between the two images and auto-correlation procedures. In PIV, these procedures are based on the averaged motion of small groups of particles within small interrogation spots, and each vector deduced is the statistical average for many particles offering a high SNR. When the motion of individual particles is tracked instead of a group of particles, the technique is called Particle Tracking Velocimetry (PTV). The first advantages of PTV over the standard cross-correlation PIV, is that the velocity vectors deduced are not averaged (as they are related to individual particle displacement) and the method is capable of higher resolution. The second advantage is the possibility of full three dimensional measurements by the use of volumetric lighting and stereoscopic analysis. PTV is, however, restricted to a low density of distributed particles due to the difficulty of detection and tracking of individual particles at high concentrations of seeding particles and offers a lower SNR than PIV. New algorithms have been developed in order to increase the capabilities of PTV

(Ohmi 2000), and a recent variational approach is presented by Ruhnau *et al* (2005).

In standard PIV and PTV, only two velocity components are measured due to the 2D geometry of the imaging system. By using 2 cameras with separate viewing angles, the third velocity component can be derived allowing instantaneous 3D velocity vectors for the whole area. This optical arrangement is called stereoscopic (Stereoscopic Particle Image Velocimetry - SPIV - or Stereoscopic Particle Image Velocimetry - SPTV) and is illustrated in Fig.3.11(b). Similarly, Holographic Particle Image Velocimetry (HPIV) can be used in a stereoscopic arrangement (Royer 1997). However, HPIV increases drastically the cost and the complexity of the system and is not commonly used.

PIV and PTV have been applied to spray diagnostics for independent or simultaneous analysis of liquid and gas motion. The 2D simultaneous measurements of both phases (fuel and air) have been produced within a dense fuel spray by Driscoll *et al* (2003). 2D-PIV velocity maps of a GDI spray is presented by Lee *et al* (2003) for different times after injection. Since few years, the use of SPIV and SPTV has considerably increased. Some examples concerns the 3D structure of evaporating and combusting fuel sprays (Palero and Ikeda 2002b and 2002a). Two main conditions must be respected when choosing the appropriate tracer particles: First they must not cause distortion within the flow, and second they must scatter efficiently the incident laser radiation. A discussion of the adequate tracers is given by Melling (1997). Fluorescence tracers are generally used in non-combusting and evaporating sprays analysis.

3.1.4 Limitation of current techniques

Fraunhofer diffraction, interferometry point and laser sheet imaging are the three well established laser techniques for spray diagnostic. They offer accurate measurements in the dilute spray region where the number density of droplets remains relatively low. However, a number of complications arise in the near-injector region where the spray is optically dense making the measurement difficult to perform. The limitations of each technique are reviewed in Table 3.2 and enumerated in the following paragraphs.

Fraunhofer diffraction is a scattering-ensemble (or scattering-average) technique which assumes that each droplet scatters the light only once before reaching the detector. This single scattering approximation is satisfied in the single scattering regime where the optical depth is low such as $OD \ll 1$ (a low optical depths is characterized by both a low droplet number density and a small scattering volume - see section 4.1.2). When probing within the dense region, photons experience a succession of scattering events due

to high concentration of droplets. As a result, an amount of multiply scattered light which dominates the single scattering signal is detected and introduces errors in the measurement. The number of publications related to multiple scattering errors in diffraction measurements is very large (Hirlemann *et al* 1988 and Kokhanovsky and Weichert 2001). Correction procedures have been developed and tested in order to improve modern optical instruments (e.g. the Malvern Spraytec). However, these corrections are not efficient enough and multiple scattering is still the major problem for dropsizing with LALLS.

Method Applied	Date	Techniques	Information provided	Advantages	Disadvantages
Fraunhofer Diffraction	1976	LALLS Malvern Particle Sizing Spraytec	-Droplet size -Number density	-Simple -Easy calibration -Low cost	- Line-of-sight - Low spatial resolution -Complex in dense spray -Requires multiple scattering corrections -Spherical droplets required -Based on empirical distributions
Point Interferometry	1964	LDV - LDA	-Droplet velocity	-High spatial resolution -Easy calibration -Real time data -Many parameters measured simultaneously	-Point data only -Restricted to medium density sprays -Off axis forward scatter optical access -Spray mapping time consuming -Spherical droplets required -Expensive
	1975	PDA - PDI Planar-PDA Dual-PDA	-Droplet size -Droplet velocity -Liquid flux -Number density		
Laser Sheet Imaging	~1990	LIF Mie LSD - PDS PIV - PTV SPIV - SPTV	-Phase transitions -Species concentration -Droplet and flow-field velocity	-Simple -Whole field: 2D mapping -Cheap -Easy to record different scattering processes	-Requires careful calibration -Requires additives (LIF) -Requires attenuation corrections -Sensitive to multiple scattering

Table 3.1: Comparison of the techniques commonly used in spray characterization technology.

The second major limitation in Fraunhofer diffraction, is the use of a pre-defined distribution function (generally Log-Normal or Rosin-Rammler). Coefficients related to the mean-diameter and to the standard deviation are calculated as a function of the detected scattered light pattern assuming a pre-defined distribution function. The droplet size distribution is thus reconstructed from an empirical equation able to produce only monomodal distributions. The last limitation concerns the fact that the optical device is optimized for spherical and opaque particles. The scattering of light by irregular elements, and ligaments is not considered by the system.

Since the first optical instrument based on interferometric point measurements, many restrictive problems have been corrected thereby successively improving the quality and the performance of modern instruments (e.g. the Dual-PDA - see end of section 3.1.2). However, the technique is still limited by a number of factors: Firstly the method concerns the measurement of spherical droplets only. Secondly, at high optical depth the Doppler signal is altered by multiple scattering processes between the probed volume and the detector making the signal difficult to analyze and process. Thirdly, at high droplet concentration, the probed volume may contain more than one droplet. In this case of multiple-occupancy, the signal emitted from the probe volume is the result of light scattering by several droplets and cannot be processed. Finally, the last major limitation is related to the single point measurement nature of the technique providing only local information at a given time.

In laser sheet imaging, the amount of multiple light scattering detected is particularly significant due to the wide detection acceptance angles and the large intensity profiles of the light source employed. Important efforts in laser sheet imaging have been recently performed for deducing the droplet SMD distribution by dividing an averaged LIF signal by an averaged Mie signal. The main point of the method is to eventually suppress the multiple scattering errors from this ratio. However, it must be pointed out that multiple scattering generated from a Mie scattering process is fundamentally different from the multiple scattering generated from a LIF process. Spray dropletsizing via such a method does not provide yet sufficiently reliable measurements and further work is required to develop adequate corrective procedures. At present, laser sheet imaging remains, then, mainly restricted to the measurement of velocity components (PIV-PTV) and for qualitative purposes.

3.2 Emerging laser technics

Even if current optical measurements are reliable in the dilute spray, the characterization of the dense region where atomization occurs remains an unsolved problem due to the optical thickness within this region and to the occurrence of multiple scattering (see section 3.1.4). In order to overcome such issues, several new laser-based diagnostics have been recently developed and proposed. The four most promising ones are described in this section and are:

- Interferometric laser imaging
- X-ray absorption
- Double extinction
- Ballistic imaging

In the last subsection, the limitations of these novel techniques are discussed and improvement strategies are suggested.

3.2.1 Interferometric laser imaging

The Interferometric Laser Imaging for Droplet Sizing (ILIDS) - or Interferometric Particle Imaging IPI - was originally proposed by Raguccy *et al.* (1990) and applied to the study of sprays by Glover *et al.* in 1995. The increasing numbers of papers published on ILIDS, along with the consequent improvements during the last 5 years, demonstrates the growth of interest for this technique. Before entering in the description of the method itself, some considerations must be discussed. As explained in the description of the PDA technique (section 3.1.2), the reflected and first-order refracted light are both dominant in the wide angle forward scatter region $\sim 30^\circ$ - 80° . The light scattered in this region consist on regular fringes of light intensity. These fringes arise from the interference between the reflected ($P=0$) and first order refracted ($P=1$) rays as explained by Glantschnig and Chen (1981). One fundamental point extracted from this observation is that the angular frequency of the fringes is directly proportional to droplet diameter. By observing experimentally a set of these fringes, an accurate measure of the droplet diameter can be made for an individual droplet. Such studies have been performed by König *et al.* (1986) and Hesselbacher *et al.* (1991). When detected within this observation angle (θ_s between 30° up to 80°), the in-focus image of a spherical droplet illuminated by a laser source

consists of two spots of light named glare points (Van de Hulst 1991). One of these glare points is produced by reflection $P=0$; whereas, the other one is due to refraction $P=1$. The distance of separation between the two glare points is related to the detection scattering angle, the relative refractive index, and the particle size. By knowing the first two quantities, the particle size can be deduced. However, such measurements requires a high spatial resolution with the necessity of magnification by the receiving optics.

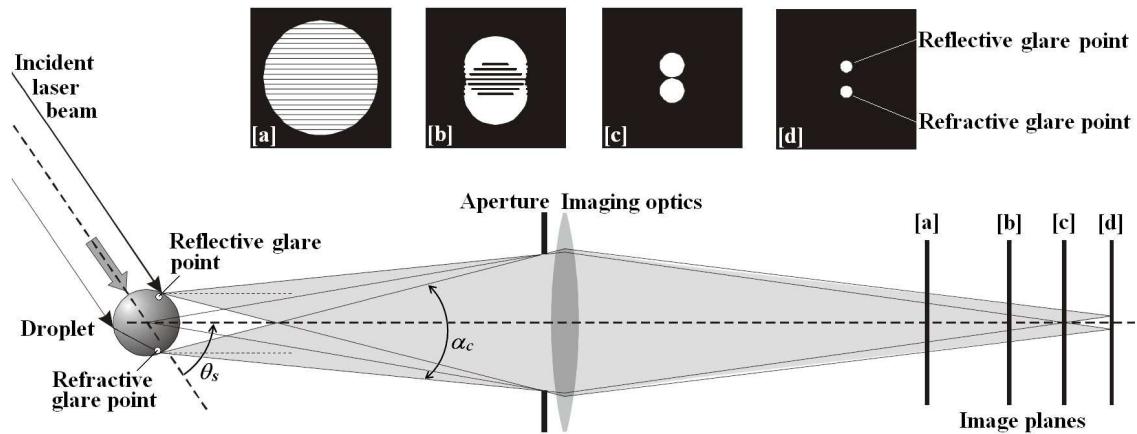


Figure 3.12: Standard configuration for ILIDS (Damaschke 2005).

When the droplet is imaged, out-of-focus interference fringes appears on the image due to the interference between the two rays. By choosing the adequate defocusing length (Girasole *et al.* 2000), the droplet shape is reconstructed via interference patterns and the diameter of the droplet is deduced from the calculation of the number of fringes. As illustrated in Fig.3.12, the size of the defocused image of each glare point depends on the degree of defocusing. ILIDS is the name given to the technique of imaging such interference patterns and determining the size of a number of droplets traversing the area of the spray illuminated by the laser sheet. A description of the optical arrangement is given in Fig.3.12. The relationship between the particle diameter, D , and the number of fringes, N , is given by (Hesselbacher *et al.* 1991, Maeda 2000):

$$D = \frac{2\lambda N}{\alpha_c} \left[\cos(\theta_s/2) + \frac{n \sin(\theta_s/2)}{\sqrt{n^2 - 2n \cos(\theta_s/2) + 1}} \right]^{-1} \quad (3.2.1)$$

where α_c is the collecting angle as defined in Fig.3.12 and n is the droplet refractive index. A major improvement to the technique has been performed by Maeda *et al.* in 2000 and consists of compressing optically the image via a pair of cylindrical lenses between the imaging plane and the collective lens (see Fig.3.13(b)). The degree of horizontal defocusing is adjusted by moving the cylindrical lenses along the optical axis of the receiving optics. By means of this compression process, overlapping of the droplet interferograms observed on the recorded images (using the conventional ILIDS system) is largely re-

duced allowing the measurement within the dense region of sprays. A comparison of the captured images between the improved technique and the conventional ILIDS technique is presented in Fig.3.13.

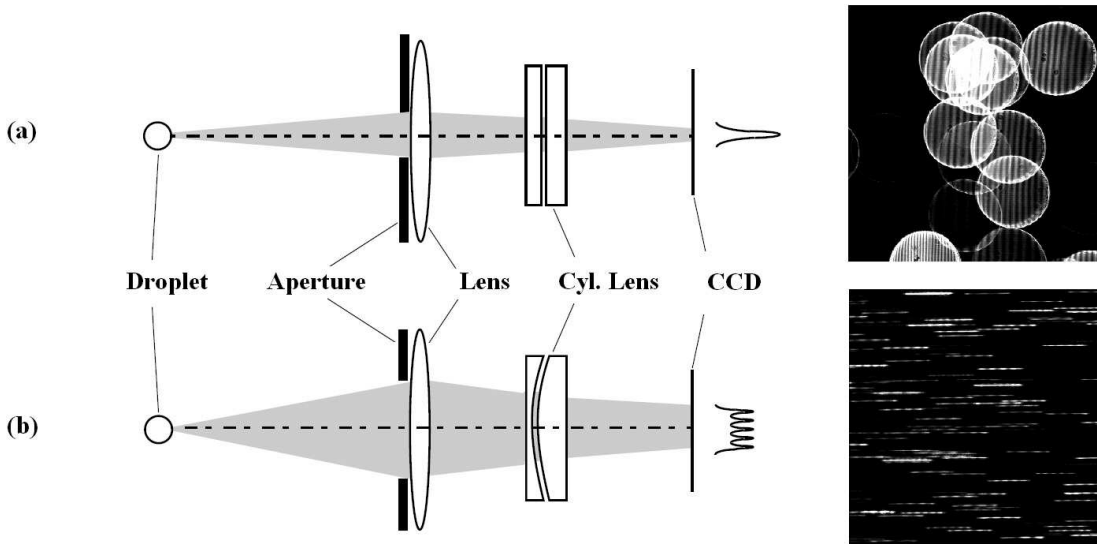


Figure 3.13: Comparison between the conventional ILIDS (a) and the ILIDS system using the optical compression technique. For an interferometric image of $4 \times 4 \text{ mm}^2$, 15 droplets becomes difficult to identify using the conventional system, whereas more than 100 droplets can be measured on an equal image area by the improved technique (Maeda 2000 and Kawagushi 2002).

The advanced ILIDS system improves the optical Signal to Noise Ratio, simplifies the image processing procedure and increase the accuracy of the measurement of fringe spacing (Kawagushi 2002). In the original article in 2000, Maedea also calculates the 2D component vectors by combining the advanced ILIDS system with PIV or PTV.

Other improvements and investigations of ILIDS have also been performed recently. For instance Kurosawa *et al.* 2002 used ILIDS in combination with LIF in order to extract simultaneously the droplet size, the 2D velocity vectors and the vapor concentration. In 2005, Zama extended the combined technique ILIDS-PTV using a stereoscopic arrangement of two cameras and deduced the three components of the velocities vectors from one focused and one defocused image. Stereoscopic ILIDS has also been tested by recently by Matsuura *et al.* (2006) for an airblast fuel spray. Finally, the last paper of importance published by Damaschke *et al.* in 2005 describes the standard ILIDS combined with a new technique called Global Phase Doppler (GPD). Similarly to PDA, GPD is based on the formation of interference fringes but employs two intersecting laser light sheet instead of two laser beams creating a larger probe volume. The first motivation to the GPD configuration is to obtain similar detection of the glare points (necessary for the ILIDS method) on both cameras when performing 3D-PTV. Other advantages of the technique,

with a comparison between ILIDS and GPD are reported by Damaschke 2005. Due to the increasing of interest in the recent years, ILIDS is a technique that might become a method of choice for future spray diagnostics.

3.2.2 X-ray absorption

X-ray absorption is a technique recently applied to high pressure fuel sprays in order to locate the phase transitions of 2D images. The first x-ray radiography of fuel spray has been investigated by Char *et al* and dates from 1990. The technique was based on polychromatic x-ray beams, and was principally applied to observe breakup mechanisms. The use of monochromatic x-ray for quantitative measurement of fuel mass has been introduced in spray diagnostics in 2000 by Powell *et al*.

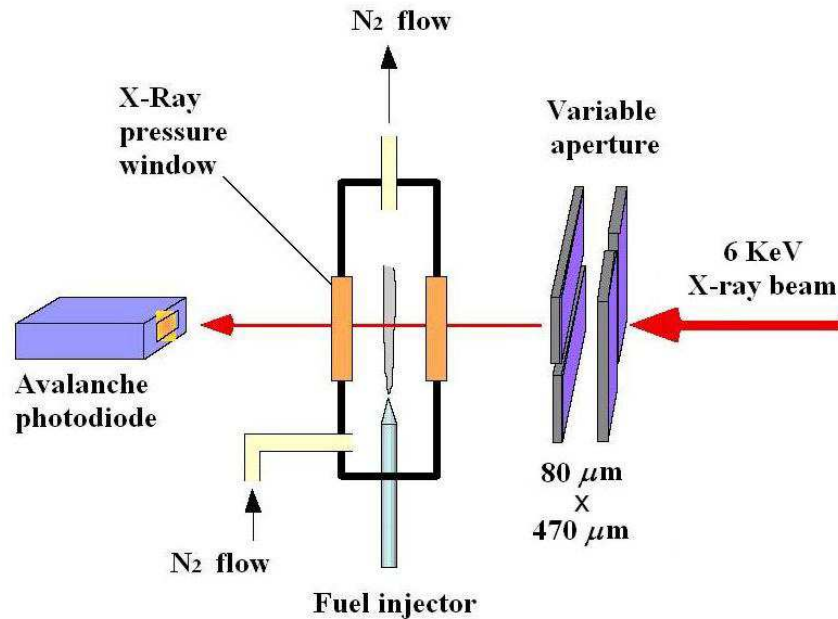


Figure 3.14: Illustration of an x-ray experimental set up (Powell 2004).

The technique can be described as follows: The fuel spray is illuminated with an x-ray beam generated from a monochromatic synchrotron in a line-of-sight configuration. Fuel mass locations are determined by the level of x-ray beam attenuation measured by a fast framing Pixel Array Detector (PAD). An illustration of a X-ray set up is presented Fig.3.14. In the same manner as visible radiation, monochromatic x-rays are attenuated when transmitted through an attenuating material such as a fuel spray in respect to the Beer-Lambert law (see also equation 4.1.3):

$$\frac{I_f}{I_i} = e^{-\mu_M M} \quad (3.2.2)$$

where I_f and I_i are respectively the transmitted and incident x-ray intensities, μ_M is the mass absorption coefficient of the fuel and M is the mass of fuel in the beam. μ_M is initially calibrated at the single wavelength via a sample solution of the fuel probed. The time evolution of fuel mass along a line-of-sight is then easily deduced from the transmission measurement (I_f/I_i) at each point in the radiograph. X-ray measurement has revealed that the fuel of a high pressure diesel spray can travel at supersonic speeds under certain experimental conditions. The shock-waves generated have been quantitatively measured by MacPhee *et al* (2002). The main advantage of x-rays over visible wavelengths is that the extinction of the incident laser beam is due to absorption only and without the contribution of scattering. X-rays are then not affected by multiple scattering phenomena and are highly penetrative in material with low atomic numbers. It has been recently demonstrated that the technique allows determining the presence of the liquid core and deducing accurately the breakup length (see fig.3.14(b)). Such information is crucial for the development of modern breakup modelling. However, several important limitations can also be noticed. These limitations described in section 3.2.5 concern mainly the cost of the technique, the low SNR obtained, the use of additive to increase absorption, and the necessity of averaging the data over several injection cycles.

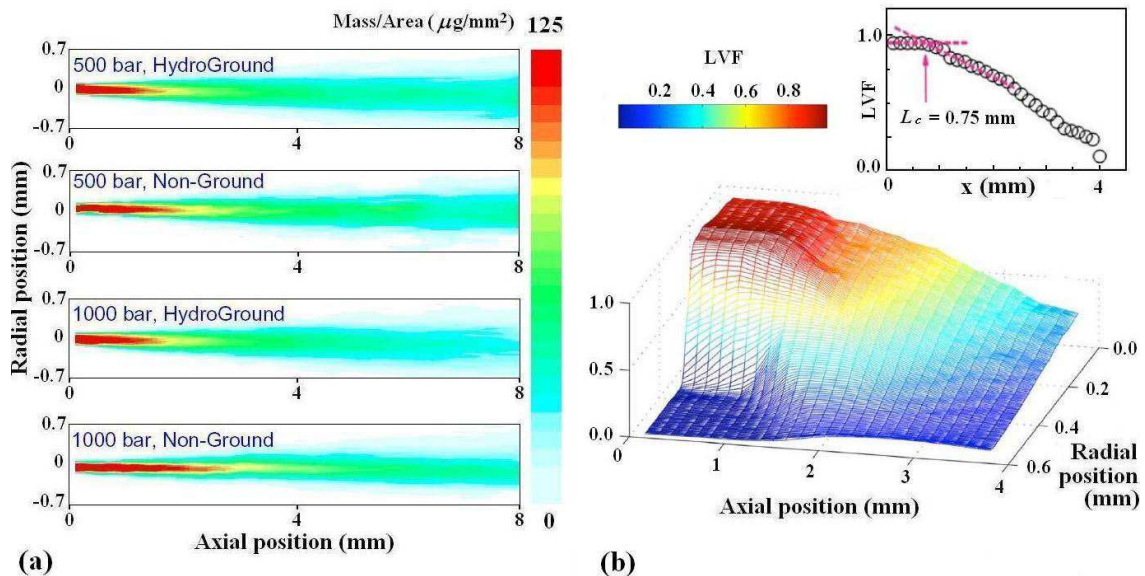


Figure 3.15: (a) X-ray images from two different nozzles at $118 \mu\text{s}$ after the start of injection (Powell 2004). (b) Deduction of the LVF in 3D for a water spray using X-ray measurement. The inset shows the deduction of the breakup length (Wang 2006).

3.2.3 Double extinction

The double extinction (called 2λ or two-color technique) was originally developed by Ariessohn *et al* (1980) for the measurement of the SMD of ash droplets in high-temperature high-velocity coal-fired combustion flows using visible ($\lambda_1 = 325 \text{ nm}$) and near-infrared ($\lambda_2 = 3.39 \mu\text{m}$) wavelengths. In 1987, Gougeon *et al* applied the technique (with $\lambda_1 = 633 \text{ nm}$ visible from a He-Ne laser and $\lambda_2 = 337 \mu\text{m}$ far infrared light from a HCN laser) for the measurement of size and concentration of coal particles in densely laden media. In this study, the measurement of the particle diameters showed good agreement with the results from the Malvern instrument. In 1998, Parker *et al* applied this method to a combusting diesel spray and gave a detailed explanation of the technique using infrared light.

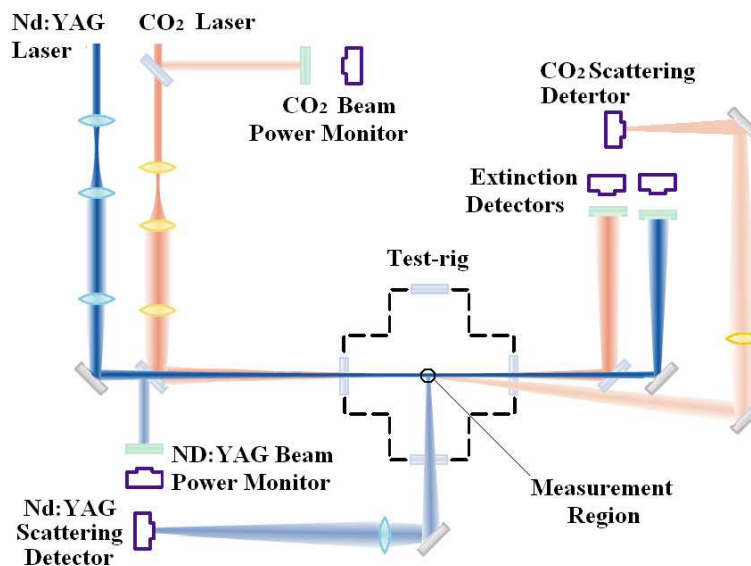


Figure 3.16: 2λ technique (Labs and Parker 2005).

The use of infrared instead of visible wavelengths presents the principal advantage of reducing the scattering efficiency of the probed droplets. The optical thickness is thus reduced making the measurement more effective and less affected by multiple scattering phenomena in the infrared domain. In 2005, Labs and Parker employed two infrared wavelengths $\lambda_1 = 1.06 \mu\text{m}$ and $\lambda_2 = 9.27 \mu\text{m}$ for measuring the SMD and the LVF within combusting and evaporating diesel sprays. In the same investigation, the authors calculated also the amount of error introduced in the measurement due to multiple scattering by measuring the state of polarization of the scattered light. As mentioned in the paper, the light that is multiply scattered from spherical particles becomes randomly polarized; whereas, the singly scattered light contains no cross-polarization scattering component. By quantifying the cross polarized light intensity, a measurement of the multiply scat-

tered light is then obtained. Finally, the intensity ratio of the parallel to perpendicular polarized scattered light allows estimating the amount of multiple scattering in the spray. Note that this measurement requires the use of a single wavelength associated with a polarized beam splitter. In 2006, the same authors (Labs and Parker) gave a detailed two dimensional distribution of SMD (see Fig.2.10 section 2.2.3) and LVF (see Fig.3.18) from the near injector region of a high-pressure diesel sprays in combusting and “cold” conditions. The double extinction technique offers a measurement of the droplet size distribution along a line-of-sight based on the Beer-Lambert law (see section 6.2.3). As illustrated in Fig.4.16, two laser beams of different wavelength traverse the spray along an identical axis and with the same direction (collinear beams). The two wavelengths are chosen to span a large wavelength range and to coincide with readily available lasers. The laser extinctions of the two beams are independently deduced from the measurement of the light intensity with and without the spray. The ratio of the two extinctions is described as:

$$\frac{(\ln I_i / \ln I_f)_{\lambda_2}}{(\ln I_i / \ln I_f)_{\lambda_1}} = \frac{\int_{D=0}^{\infty} n(D)\sigma_{e\lambda_2}(D)dD}{\int_{D=0}^{\infty} n(D)\sigma_{e\lambda_1}(D)dD} \quad (3.2.3)$$

where $n(D)$ and $\sigma_e(D)$ are respectively the number and the extinction cross-section of each droplet of diameter D . The subscripts λ_1 and λ_2 indicate the probe wavelength. Assuming monodisperse droplets, or an analytical distribution of droplets distribution (Log-normal or Rosin Rammler - see section 2.2.3) with a pre-defined standard deviation, the extinction ratio presented in Eq.3.2.3 gives a unique solution of the droplet diameter in the range 0-15 μm as presented Fig.3.17. Similarly, the extinction ratio gives a unique solution to the SMD value of predefined distributions (Parker 1998).

By positioning the beams at various positions within the spray, two-dimensional information can be obtained. The 2D distribution of the SMD for a diesel spray at different time after injection has been previously presented in Fig.2.10. Once the droplet size distribution is known with the associate attenuation along the line-of-sight, the number density and the LVF can be deduced. Figure 3.18 shows the 2D LVF distribution of the same diesel spray presented Fig.2.10. As the technique is based on an attenuation ratio, the effects introduced by multiple scattering in both measurements are partially canceled. However corrections procedure are still required. Furthermore, in the same manner than for the diffraction method, the droplet size distribution is deduced from empirical distribution functions that do not allow bimodal distributions. The technique suffers also from other limitations which are detailed section 3.2.5.

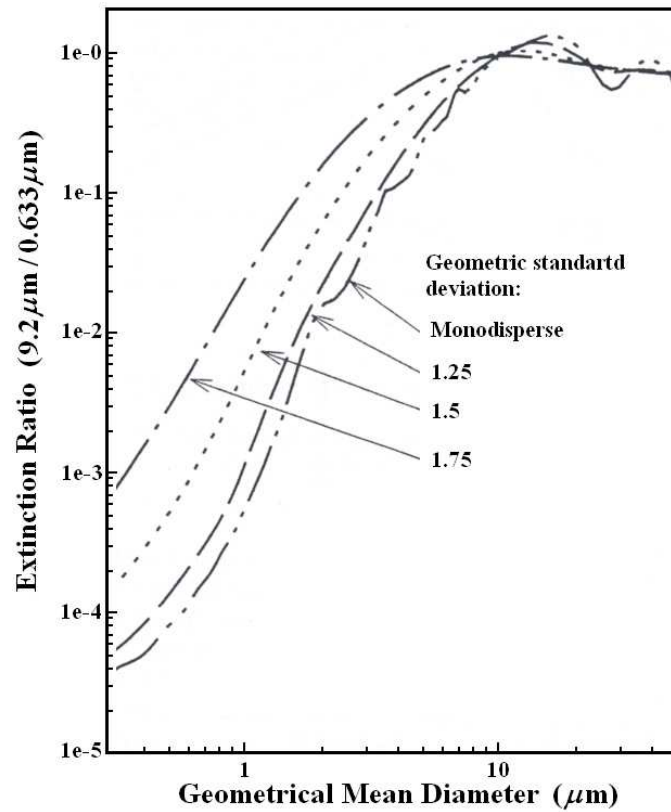


Figure 3.17: Extinction ratio for different log-normal droplet distributions as a function of the geometrical mean diameter (Parker 1998).

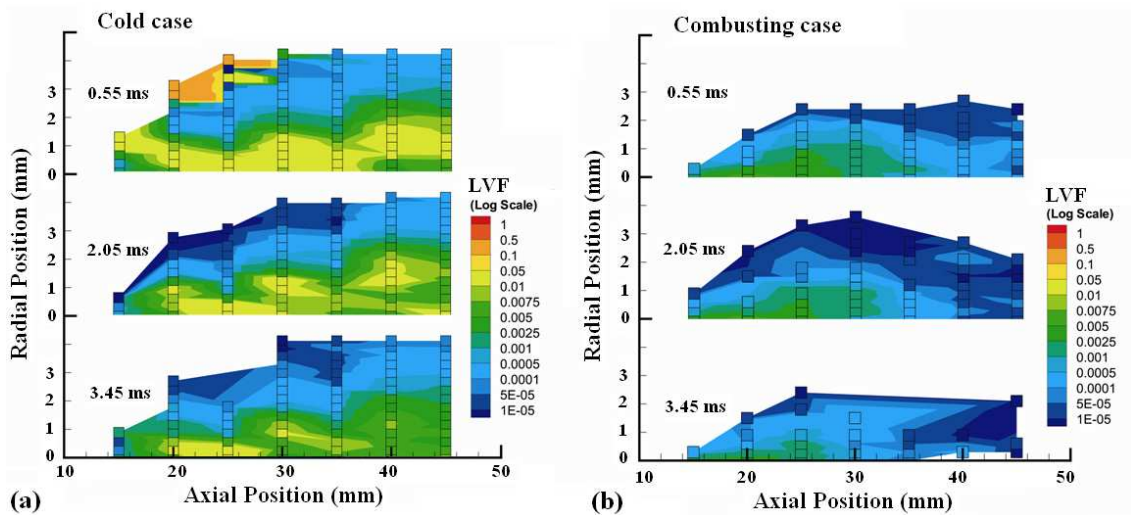


Figure 3.18: 2D LVF as of a diesel spray at different time after injection: Spray development (0.55 ms), steady state (2.05 ms) and spray dissipation (3.45 ms). (a) is the cold case and (b) the combusting case. (Labs and Parker 2006).

3.2.4 Ballistic imaging

Even if the application of ballistic imaging to spray research is new, the technique was originally applied for imaging through tissues and was developed in bio-medical applications for over a decade (Hebden *et al* 1991). The first ballistic image of spray was obtained in 1995 by Galland *et al* with a spatial resolution of 0.5 mm. In 2004, Paciaroni and Linne adapted an optical configuration originally developed for medical imaging (illustrated in Fig.3.19) and obtained a single shot ballistic image of a water jet spray with high spatial resolution (20-30 μm for a dilute spray and 40-50 μm for a dense spray). A complete review of the technique will be presented by Linne *et al* (2006) where transient ballistic imaging diagnostics have been used in a Lox injector, a turbulent water jet, a water jet in cross-flow, and a transient diesel fuel spray. Detailed information of the technique is also provided by Paciaroni (2004).

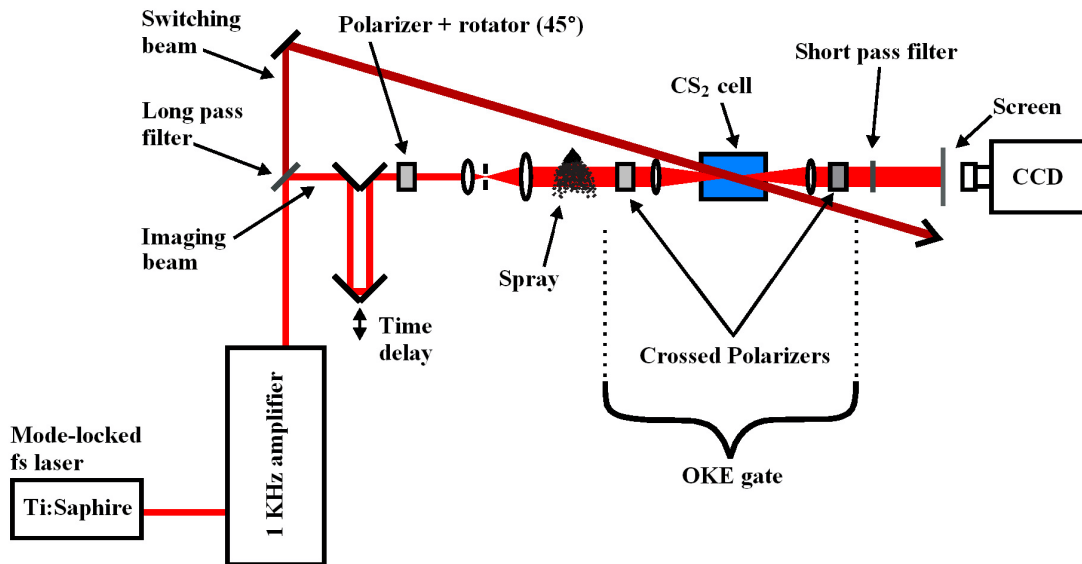


Figure 3.19: Optical configuration for ballistic imaging (Paciaroni 2004).

Ballistic imaging is a two-dimensional time-gated shadowgraphy technique. The method relies upon the fact that when light traverses a highly turbid medium, some of the photons pass straight through without scattering, exiting the medium with the same solid angle that they entered. These photons are termed “ballistic” because they travel the shortest path and exit first. A second group of photons is the “snake” photons group. Snake photons are photons scattered several times (from once up to 9 times) within the forward direction. Because they travel a bit further, they exit just after the ballistic photons with a larger solid angle. Ballistic and early snake photons (scattered from 1 up to 3 times within the forward direction) construct a quasi-undistorted image of the spray structure. Photons scattered more than 3 times seriously lose memory of the structure within the

material. Finally, photons scattered 10 times and beyond retain no memory of the spray structure and are called “diffuse” photons. An illustration of ballistic, snake and diffuse photons is depicted next section (Fig.4.6) with the related terminology.

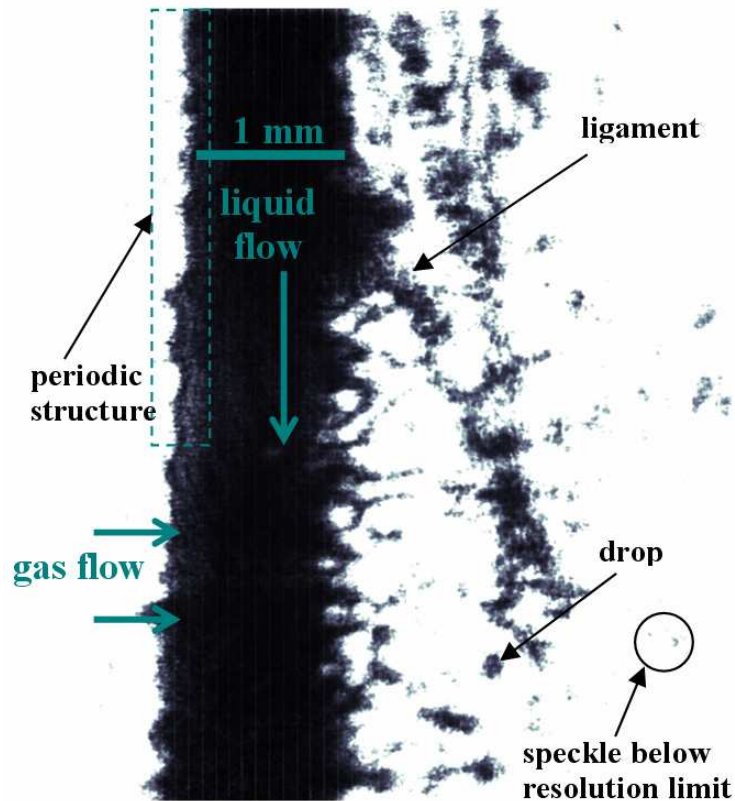


Figure 3.20: Example of a ballistic image for a jet in cross-flow (Sedarsky *et al* -2007).

The key point of ballistic imaging consists in extracting the coherent component (ballistic and early snake photons) of the laser light exiting the spray which provide faithful information of the medium structure and removing the diffuse component that introduce complication on the detected signal using an ultra fast detection system and femtosecond incident laser pulses (~ 100 fs). When exiting the spray, ballistic and early snake photons possess the following properties:

- Directionality: same axis as the input light, narrow solid angle.
- Preservation of the input polarization.
- Coherence with the input beam.
- Early exit time.

The Optical Kerr Effect (OKE) gate is an optical device which acts as a high speed shutter, gating the early light and rejecting the later light. The system uses the polarization

properties of light and the gate time is governed by the molecular relaxation time of the Kerr medium. For the case of a CS_2 as a Kerr active liquid, a gate time of 2 ps is achieved. Detailed information about the operation of the OKE gate can be found in Paciaroni (2004). By positioning a CCD camera at the exit of the OKE gate, a time-gated shadowgraph image of the spray is produced. These images possess a much higher spatial resolution than common shadowgrams owing to the suppression of the diffuse light.

The major advantage of ballistic imaging over other optical diagnostics techniques is its capability to produce instantaneous images of the liquid core in atomizing sprays; this region has been heretofore inaccessible. Using ballistic images, primary and secondary breakup can be visualized within the dense spray region where traditional techniques are limited. Furthermore, the determination of vector velocities can also be deduced from two successive ballistic images as presented by Sedarsky *et al* (2005). Finally droplet size and extinction measurement can also be performed (Sedarsky 2006). An example of ballistic image is presented in Fig.3.20. The drawbacks of the technique are explained in the next section.

3.2.5 Limitation of the new techniques

The common point between the new techniques described above is that they all are designed for probing within the dense spray region where the well established techniques (see section 3.1) are limited. Even if each of them possesses particular characteristics, and offers specific information they all suffer from a number of limiting factors:

Interferometric laser imaging has largely improved since its initial appearance in 1995 especially with the application of the optical compression by Maeda in 2000. Using such a system, the overlapping droplets on the image are suppressed allowing probing within media containing higher droplet number density. However, the optical compression compression is responsible to a loss of contrast between black and white fringes making the determination of the droplet size more difficult to perform. Three other limitations can also be noticed: Firstly spherical particles are required in order to create interference pattern from the two glare points imaged. Secondly, due to the out-of-focus nature, only relatively small areas are imaged (for instance: $4 \times 4 \text{ mm}^2$) eliminating one major advantage of the laser sheet configuration. Finally, the detector must be positioned at specific angles where interference pattern can be produced.

Technique Applied	Date and Characteristics		Information provided	Advantages	Disadvantages
Inter-ferometric Laser Imaging	1995	Standard ILIDS IPI	-Droplet size -Droplet concentration -Velocity vectors	-Simple -Whole field: 2D mapping -Cheap -Easy calibration -Low cost -Adaptation of the technique for 3D velocity measurement -Can be used in the dense region	-Small probed surfaces -Spherical droplets required -Detection angle restricted to the range: 30°- 80°
	2000	Improved ILIDS: Optical compression			
X-ray	1990	Polychromatic X-ray	-Visualisation of shock-waves for high pressure diesel sprays -Phase transition -Fuel mass	-Does not suffer from multiple scattering phenomena -Provides unique type of information	-Poor resolution -Require averaged data -Complex system -Not readily available -Expensive
	2000	Monochromatic X-Ray: Quantitative measurement			
Double Extinction	1998	Infrared wavelengths	Averaged -Geometrical mean diameter -SMD -LVF -Optical depth along a line-of-sight	-Simple -Cheap -Easy calibration -Low cost -Operable in dense sprays	- Line-of-sight - Low spatial resolution -Requires multiple scattering corrections -Spherical droplets required -Based on empirical distributions
Ballistic Imaging	1995	Image resolution: ~0.5 mm	-Phase transitions -Droplet size -Number density -Velocity vectors	-Single shot image -High resolution -Operable in dense sprays	-Resolution may be insufficient to resolve smaller droplet -Shadowgraph image
	2004	Image resolution: ~30 μm			

Table 3.2: Comparison of the emerging laser techniques used for spray characterization.

Even if X-ray absorption is the only technique that does not suffer from multiple scattering, the method is not without limitations: First, a costly synchrotron source is required limiting the number of researchers who have access to the diagnostic. Second, due to the insufficient absorption of fuel, some additives are required. Third, the low SNR requires averaging over several injection cycles. The image of one spray produced is thus developed over a fairly large number of injection events. Fourth the liquid-vapour phase separation is difficult to observed. Furthermore, the PAD detector is sensitive and easily damaged by the high-energy source.

Due to its line-of-sight geometry, the double extinction possesses the same limitations than any ensemble-averaging techniques. In other words, the data extracted are not local but correspond to an estimation averaged along the cylindrical volume of the incident laser beam crossing the spray. As the method is based on the ratio of two light extinction measurements, the errors introduced by multiple scattering are minimized (they are, for instance, less important than for the Fraunhofer diffraction technique). Nevertheless, corrections from multiple scattering are still required. Other limitations concern the assumption of spherical droplets and the 2D spray mapping requires moving the nozzle at different positions (which is time consuming). Furthermore, it is seen in Fig.3.17 that when $D > 20 \mu\text{m}$ an identical value of the extinction ratio can be related to several droplet diameter. Such issue limits then the sizing procedure to small droplets only ($D < 20 \mu\text{m}$). Finally, the technique is based on empirical functions that do not allow bimodal distributions and requires a standard deviation to be originally determined.

The major advantage of ballistic imaging is the high spatial resolution obtained and the clear visualization of the boundary between the two-phases on the edge of the spray. Regions with low droplet density and presence of voids are also clearly identified as seen in Fig.3.20. The main drawback concerns the lack of contrast within the spray itself due to the shadowgraph nature of the resultant images. Another issue of the technique is the correct adjustment of the time gate. Such problem requires the calculation of photons time of flight within the spray. This can be accomplished via Monte Carlo modelling as presented in section 8.3. Finally, the optical system employed is more complex than the majority of the other techniques and requires accurate alignment. It is important to note that ballistic imaging has recently demonstrated the capabilities of modern optical instruments to employ ultra-fast time gating detection in order to remove the diffuse light from the detected signal and to produce high resolution images. Such an approach seems to be very promising especially if it can be applied to other methods such as those employing laser sheet imaging.

Propagation of Laser Radiation in Sprays

MODERN techniques for advance characterization and study of sprays are mostly based on the direct measurement of scattered radiations from an incident laser beam. When the mean free path of photons is much larger than the scale of the experiment (in the single scattering regime), the relationship between the scattered light and the properties of the system is straightforward providing unambiguous information. When however, the mean free path of photons is smaller than the scale of the experiment (in the intermediate scattering regime) the incident light is multiply scattered generating ambiguous information. Most practical sprays, operate in such conditions where the total amount of multiply scattered photons is much more important than the amount of singly scattered photons. This issue has been mentioned in the last chapter as the major recurrent factor limiting both traditional and new optical diagnostics.

The current chapter provides a detailed description of laser radiation propagation and scattering within sprays. The first section is devoted to the appropriate terminology employed to describe such processes. In the second section, the physical basis of scattering and absorption phenomena are successively described with a particular attention given to light scattering by a single droplets and by a collection of droplets. Finally, the chapter details multiple scattering and attenuation of light within a spray.

4.1 Terminology and definition

The appropriate terms and definitions related to the scattering of light within turbid media are given in this section.

4.1.1 Extinction, scattering and absorption

When a beam of light enters a medium containing a collection of scattering particles such as droplets, the incident light intensity is attenuated. This attenuation is due to the loss of energy caused by the interactions between light and particles. Scattering and absorption represent the two types of interactions. The sum of scattering and absorption processes is called extinction:

$$\text{Extinction} = \text{Scattering} + \text{Absorption}$$

By definition, the change of intensity $dI(\vec{r}, \vec{s})$ of a laser beam of initial intensity $I_i(\vec{r}, \vec{s})$ (also called radiance or specific intensity and of units $\text{W}/\text{sr}/\text{cm}^2$) crossing an elementary volume of length dx depends on the extinction coefficient μ_e as:

$$dI(\vec{r}, \vec{s}) = -I_i(\vec{r}, \vec{s}) \cdot \mu_e(\vec{r}) \cdot dx \quad (4.1.1)$$

and

$$\frac{dI(\vec{r}, \vec{s})}{I_i(\vec{r}, \vec{s})} = -\mu_e(\vec{r}) \cdot dx \quad (4.1.2)$$

where dx is the elementary length, \vec{r} is the vector position and \vec{s} is the direction of propagation.

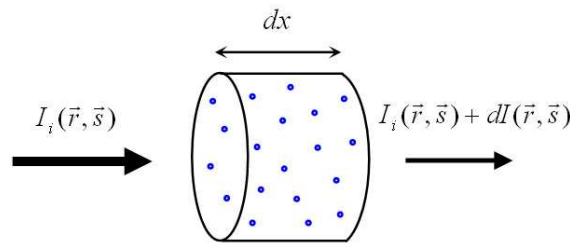


Figure 4.1: Change of radiation energy through an elementary volume.

The Beer-Lambert law is given by integrating Eq.4.1.2 over a distance l . Assuming a homogeneous medium with constant extinction coefficient, it is deduced that the initial

light intensity is exponentially reduced along a line-of-sight of length l such as:

$$I_f = I_i \cdot e^{-\mu_e l} \quad (4.1.3)$$

where I_i and I_f are, respectively, the initial and final light intensity along the same direction of propagation \vec{s} . As shown in Eq.4.1.2, the attenuation equals the ratio of the light intensity extinction with the initial light intensity. The attenuation can also be written (from Eq.4.1.3) under the form $1 - (I_f/I_i)$ where the term (I_f/I_i) is the transmission. In optical characterization of sprays, “extinction” is often referred to as “obscuration”. However, for ease and clarity, the term “obscuration” will not be used in this report. The extinction coefficient is equal to the sum of the scattering coefficient and the absorption coefficient:

$$\mu_e = \mu_s + \mu_a \quad (4.1.4)$$

Each of these coefficients (in cm^{-1}) is proportional to the number density, N , (number of droplets per cm^3) and to the respective extinction, scattering and absorption cross-section σ_e , σ_s and σ_a (in cm^2) as:

$$\mu_e = N \cdot \sigma_e \quad \mu_s = N \cdot \sigma_s \quad \mu_a = N \cdot \sigma_a \quad (4.1.5)$$

The scattering cross-section, σ_s , corresponds to a surface-area where the energy of the incident wave falling on this area equals the total energy scattered in all direction. In a similar manner, the energy absorbed may be set equal to the energy of the incident wave falling on the area σ_a . Finally, as the total energy removed from the original beam is the sum of the scattering energy and the absorbed energy, the extinction cross-section, σ_e , is deduced from the sum of σ_s and σ_a . Detailed derivation of each cross-section is given in Van de Hulst (1981) and Bohren and Huffman (1983). In the case of spherical particles, it is found that the the scattering cross-section is linearly dependent on D^2 as seen in Fig.4.2.

By dividing the extinction cross-section by the geometrical cross-sectional area projected onto a plane perpendicular to the incident beam, the extinction efficiency Q_e is deduced. In the same way, the respective scattering and absorption efficiency Q_a , Q_s are deduced:

$$Q_e = \frac{\sigma_e}{G} \quad Q_a = \frac{\sigma_a}{G} \quad Q_s = \frac{\sigma_s}{G} \quad (4.1.6)$$

For spherical particles, $G = \pi \cdot (D/2)^2$, where D is the diameter. Note that the extinction efficiency factor, Q_e , can be smaller or bigger than 1.

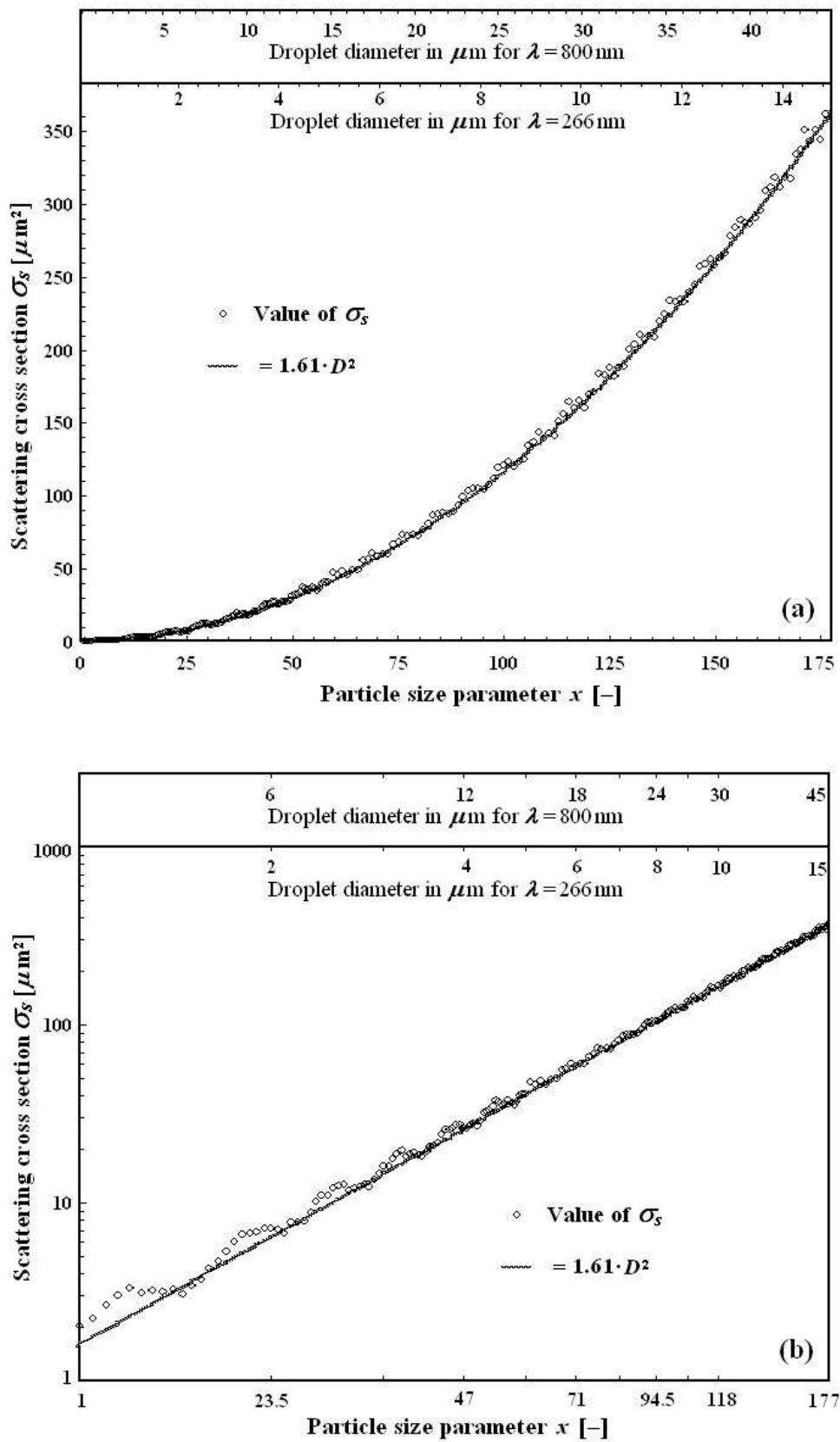


Figure 4.2: Scattering cross-section of spherical fuel droplet ($n = 1.4 + 0.0i$) as a function of the particle size parameter. The droplet size scale is also added for $\lambda = 266$ nm and $\lambda = 800$ nm on the top of each graph. (a) is the standard scale and (b) is the logarithmic scale.

In other words, if we consider only one particle illuminated by a light beam, the particle casts a shadow of area which can be bigger or smaller than the geometrical shadow G (Van de Hulst - 1981). Many particles, of a rather common sort, scatter and absorb more light than is geometrically incident upon them ($G < \sigma_e$). This is partially due to the fact that the scattered wave removes some of the energy of the initial wave by interference.

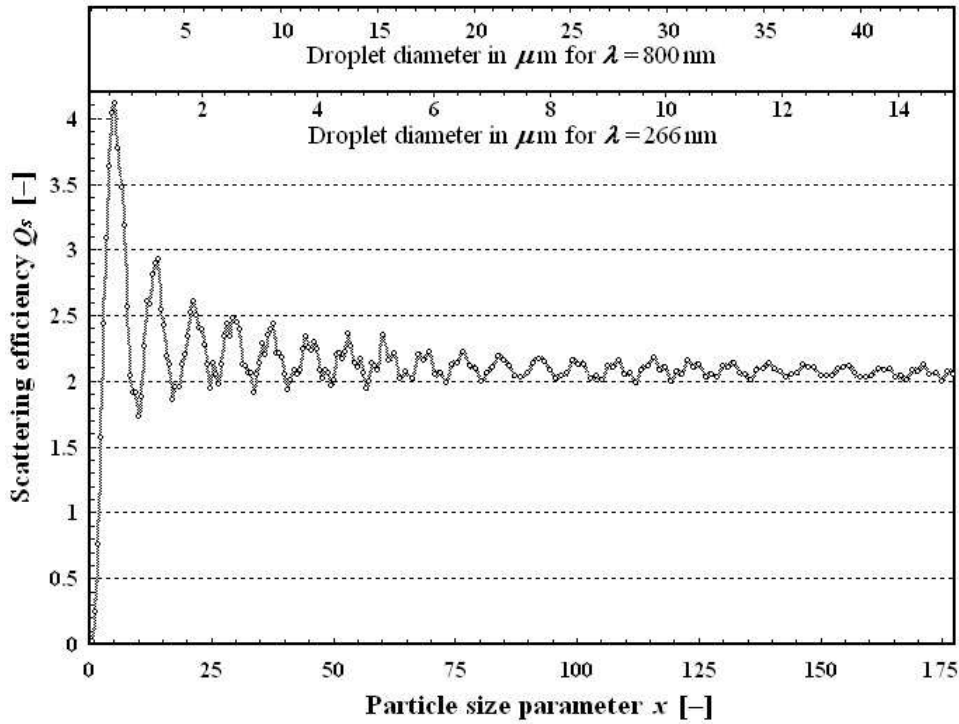


Figure 4.3: Scattering efficiency of spherical fuel droplet ($n = 1.4 + 0.0i$) as a function of the particle size parameter. The droplet size scale is also added for $\lambda = 266$ nm and $\lambda = 800$ nm.

The curve in Fig.4.3 shows the evolution of the extinction efficiency for non-absorbing spherical fuel droplet ($n = 1.4 + 0.0i$) as a function of the particle size parameter x . By definition, x is given as:

$$x = \frac{\pi D}{\lambda} \quad (4.1.7)$$

In the theory of light scattering by particles, the particle size parameter is an important dimensionless number; for an identical value of x the same scattering process will occur. Note that in Fig.4.3 the scale of the droplet diameter has been added for two different wavelengths $\lambda = 266$ nm and $\lambda = 800$ nm showing identical extinction efficiency for different drop diameters.

It is important to mention that all parameters related to extinction, scattering and absorption can either correspond to a single particle or to a collection of particles. Figure 4.4 illustrates the extinction of light by a collection of particles (a) and by a single particle (b) only. Experimentally, it is difficult to isolate a single particle and the extinction mea-

measurements are generally deduced from samples of many particles. The deduction of σ_e , σ_s , and σ_a for individual droplets can, however, be performed using a droplet generator.

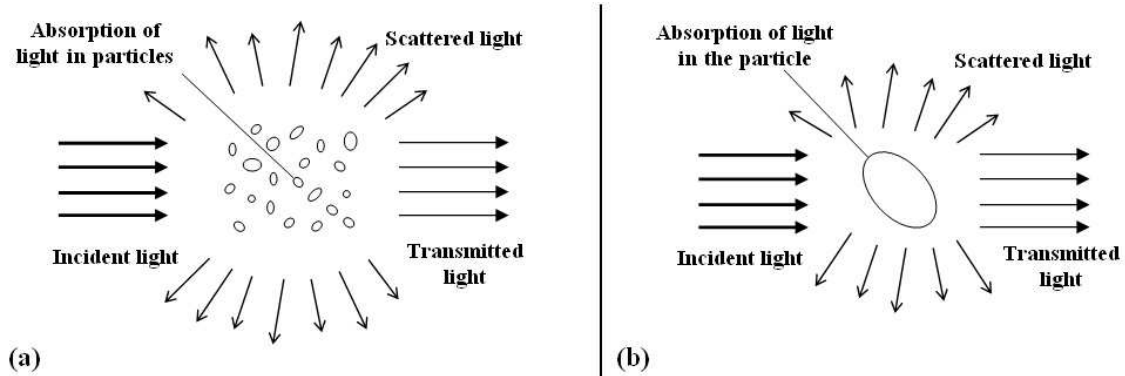


Figure 4.4: Extinction of light by a collection of particles (a) and by a single particle (b).

Depending on the characteristics of the medium, the light and the particles, one interaction process (absorption or scattering) dominates the other. For example, visible light traversing a cloud or fog is almost entirely attenuated by scattering. However, in media such as black smoke, scattering is nearly absent and the extinction of the light is mainly due to absorption (Bohren and Huffman 1983). The importance of scattering over the extinction is quantified by the albedo, A :

$$A = \frac{\mu_s}{\mu_s + \mu_a} = \frac{\sigma_s}{\sigma_e} \quad (4.1.8)$$

For a non-absorbing medium, the albedo equals 1 and the extinction of the light is governed by scattering only (the absorption level of a particle is related to the value of the imaginary part of its refractive index). In fuel sprays, natural absorption occurs generally at very low levels and the light-droplets interaction is dominated by the elastic scattering of the incident laser radiation. When fluorescence occurs (by adding a given tracer in the injected liquid - see the PLIF technique section 3.1.3), the incident wavelength is absorbed and reemitted into a wavelength of lower energy. During this inelastic-scattering process, the albedo is largely reduced and absorption must be considered.

4.1.2 Scattering orders, optical depth and scattering regime

Scattering orders, optical depth and scattering regimes are parameters related to media containing a collection of scattering particles. The scattering order corresponds to the number of times that an individual photon interacts with the droplets (or other scattering particles) prior to spray (or other turbid medium) exit. The total intensity of optical radi-

ation propagating in a turbid medium can be represented as an infinite series of scattering orders usually represented by ladder diagrams (Fig.4.5).

$$I_{(\text{tot})} = \begin{array}{c} \leftarrow \\ \rightarrow \\ I_{(0)} \end{array} + \begin{array}{c} \leftarrow \\ \updownarrow \\ \rightarrow \\ I_{(1)} \end{array} + \begin{array}{c} \leftarrow \\ \updownarrow \\ \updownarrow \\ \rightarrow \\ I_{(2)} \end{array} + \begin{array}{c} \leftarrow \\ \updownarrow \\ \updownarrow \\ \updownarrow \\ \rightarrow \\ I_{(3)} \end{array} + \dots$$

Figure 4.5: Schematic presentation of the scattering intensity as a series of ladder diagrams representing each scattering orders.

At scattering order 0, no interaction occurs, and photons cross the spray keeping their initial direction. This group of photons is called ballistic (see subsection 3.2.4). The scattering order 1 (or single scattering) is, in optical measurement of spray, the order of interest as the information extracted from it is straightforward and directly related to the droplet characteristics (e.g. droplets size, concentration). The average photon path length through a spray is increased when assuming larger scattering orders. As mentioned in section 3.2.4, the range of scattering order from 2 up to 9 is associated to the “snake” photons group (when assuming a forward scattering detection). These photons travel a longer path through the spray than the ballistic photons and exit the spray along approximately the same axis as the input light with a somewhat larger solid angle. Photons scattered more than 10 times are the diffuse photons and exit the medium with a large solid angle after traveling long path in the spray. In terms of time gating detection, the ballistic, snake and diffuse photons group, are defined as a function of the photon time of flight and time of arrival to the detector. An illustration of the three categories is given in Fig.4.6.

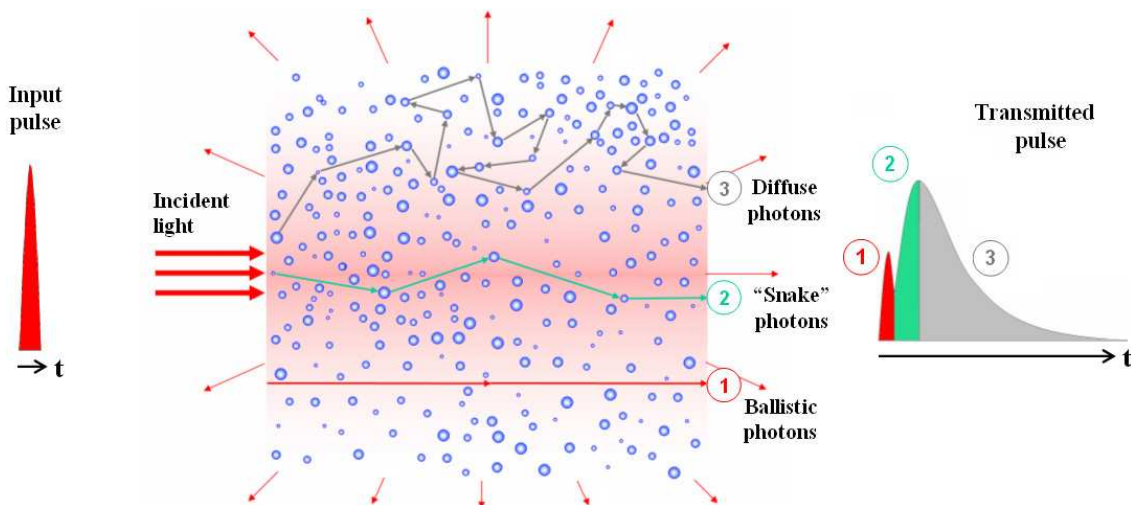


Figure 4.6: Trajectories of ballistic, snake and diffuse photons through a scattering medium containing spherical particles.

The distance of propagation between two scattering or absorbing events is called the free path length l_{fp} . The mean free path length is deduce from the value of the extinction coefficient such as:

$$\bar{l}_{fp} = \frac{1}{\mu_e} \quad (4.1.9)$$

This relationship shows that the average distance traveled by a photon between two droplets is inversely proportional to the extinction coefficient. By dividing the length, l , traversed by a light beam, by the mean free path length, \bar{l}_{fp} , the number of average path lengths along l is deduced. The resultant term is the optical depth, OD :

$$OD = l/\bar{l}_{fp} = l \cdot \mu_e \quad (4.1.10)$$

The optical depth is an approximation of the mean number of scattering events occurring through a scattering medium of length l . It provides a crucial indication of the optical thickness of a probed spray. Depending on the value of the optical depth and/or of the average scattering order, the scattering of light within a spray can be classified into 3 regimes.

Single scattering regime	Intermedietate scattering regime	Multiple scattering regime
$OD \leq 1$	$2 \leq OD \leq 9$	$OD \geq 10$

Table 4.1: Classification of the scattering regimes as a function of the optical depth. Most of industrial and fuel sprays fall in the intermediate single-to-multiple scattering regime.

The single scattering regime is defined when the average scattering order is inferior than 2. In this regime, ballistic photons are clearly dominant. For a “side” (out-of-plane) detection, the series of scattering order (see Fig.4.5) is reduced to the term describing the single scattering and all other terms of the series are neglected or considered as a perturbation to the single scattering. This is the single scattering approximation.

The intermediate single-to-multiple scattering regime operates when the average of scattering events is comprised from 2 up to 9. In this case and assuming anisotropic forward scattering phase functions, the mean scattering order dominates all other orders. As both single and high order terms of the series must be considered, no approximation can be performed in this regime.

The last regime is the multiple scattering regime where the average number of scattering events is greater or equal to 10. In this regime, the relative amount of each scattering order tends to be equal and no dominant scattering order is clear. In other words, it can

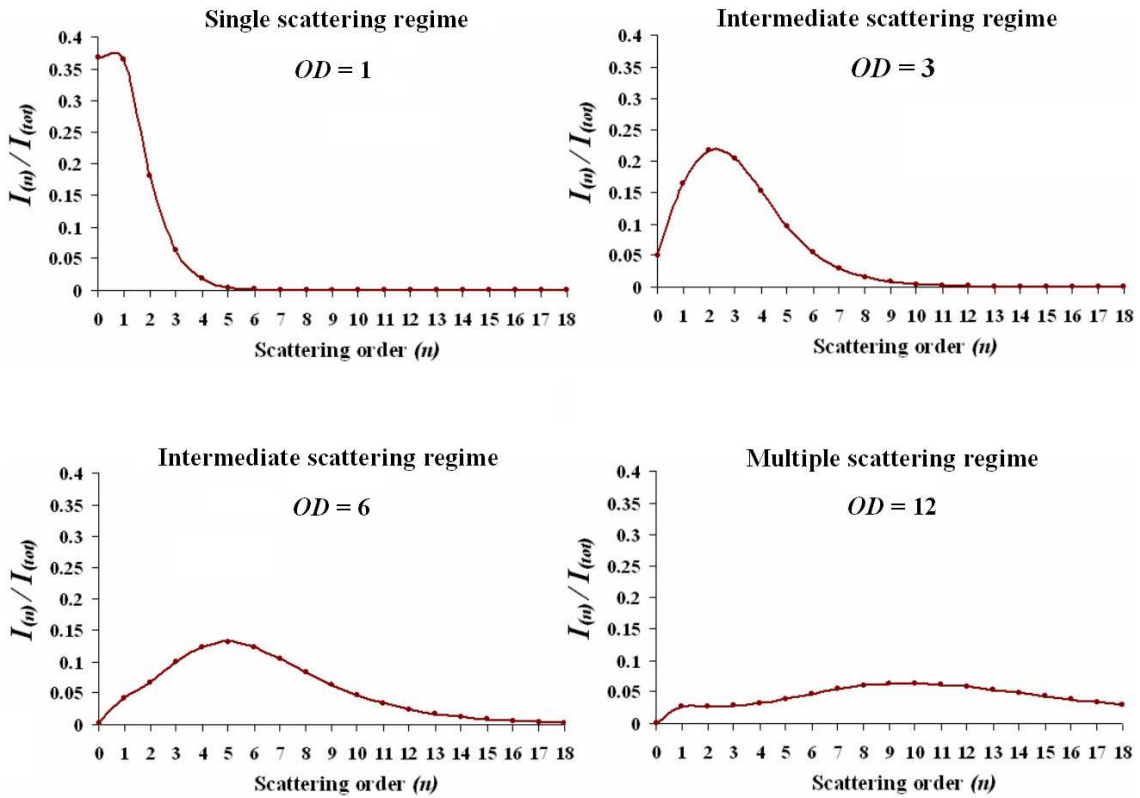


Figure 4.7: Distribution of scattering orders for a collection of spherical fuel droplets at various optical depth. Results are obtained from Monte Carlo simulations for a Log-Normal distribution characterized by $\bar{D}=5 \mu\text{m}$ and $\sigma=0.5 \mu\text{m}$ (see subsection 6.3.1).

be assumed that all terms of the series have the same order of magnitude and the diffusion approximation is applied. It is important to differentiate the “*multiple scattering regime*” from the “*process of multiple scattering*” which also occurs in the intermediate regime.

The shape of the scattering orders PDF is characteristics of the optical depth value and of the scattering regime. Figure 4.7 illustrates the relative amount of each scattering orders for $OD = 1$, $OD = 3$, $OD = 6$ and $OD = 12$. These results show the transition from the single scattering to the multiple scattering regime in the case of anisotropic scattering phase function with A close to 1. Note that for isotropic scattering ($A=0$), the single scattering remains the dominant scattering order even in the intermediate scattering regime. This characteristic is described in the subsection 7.2.4.

Current laser diagnostics of sprays fall into the intermediate scattering regime where the average number of light scattering events is too great for the single scattering assumption, but too few for the diffusion approximation. Measurements in this regime are affected by errors due to both multiple scattering and attenuation (see section 4.2) and present the most difficult case of study.

4.1.3 Scattering phase function

When a packet of photon encounters a single scattering particle, photons are scattered in all directions with preferential scattering angles. The change in direction caused by scattering shows a distinct distribution which can be expressed in terms of the differential scattering cross-section (Ishimaru 1978):

$$\frac{d\sigma(\vec{s}, \vec{s}')}{d\Omega} = r^2 \frac{I_s(\vec{s})}{I_i(\vec{s}')} \quad (4.1.11)$$

where $d\Omega$ is a solid angle spanning around the scattered direction \vec{s} as illustrated Fig.4.8(b) and r is the distance from the point of observation to the scattering centre.

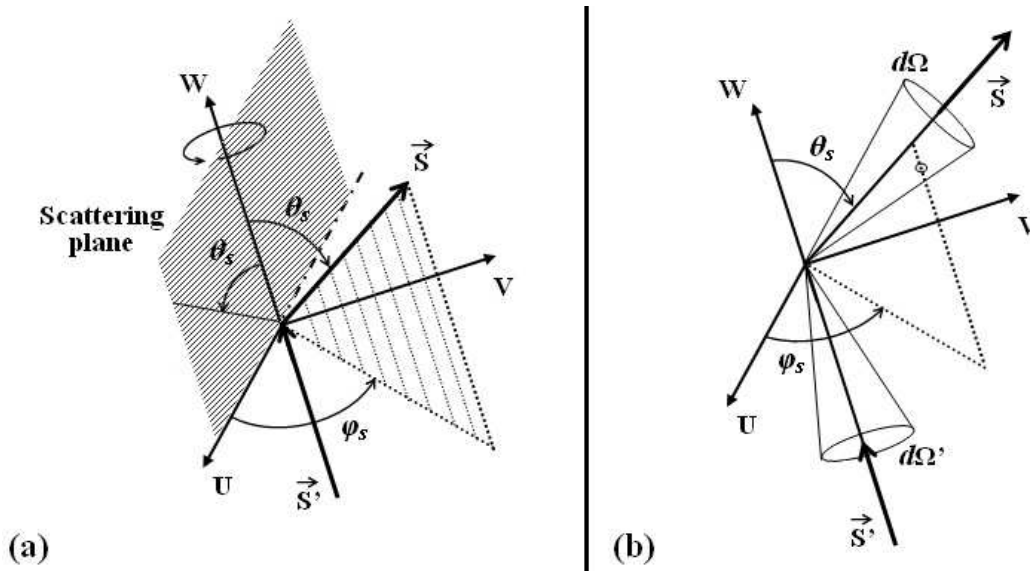


Figure 4.8: Directions and angles of incident and scattered photons.(a) shows the scattering angles θ_s and ϕ_s and (b) defines the respective solid angles $d\Omega$ and $d\Omega'$.

By integrating the differential scattering cross-section over 4π , the total scattering cross-section, σ_s , is found:

$$\sigma_s = \iint_{4\pi} \frac{d\sigma(\vec{s}, \vec{s}')}{d\Omega} .ds \quad (4.1.12)$$

In the last equation, the differential cross-section $\frac{d\sigma(\vec{s}, \vec{s}')}{d\Omega}$ can be replaced by $\sigma_s . f(\vec{s}, \vec{s}')$ where $f(\vec{s}, \vec{s}')$ is the normalized single scattering phase function. By definition, the scattering phase function gives the probability of a photon to be scattered from the direction \vec{s}' into the direction \vec{s} . Note that this is a misleading term as $f(\vec{s}, \vec{s}')$ has nothing to do with the phase of a light wave. The parameters governing the scattering phase function are the incident light characteristics (wavelength, polarization state, intensity profile), the optical properties of the surrounding medium (external refractive index) and the droplet

characteristics (size, shape, refractive index, orientation). The scattering phase function is dimensionless and is given under its normalized form such as: $\int_{4\pi} f(\vec{s}, \vec{s}') d\Omega = 1$.

From $f(\vec{s}, \vec{s}')$, the intensity of light $I_s(\vec{r}, \vec{s})$ scattered into \vec{s} from the direction \vec{s}' is described as:

$$I_s(\vec{r}, \vec{s}) = \mu_e(\vec{r}) \cdot dx \int \int_{4\pi} f(\vec{s}, \vec{s}') \cdot I_i(\vec{r}, \vec{s}') \cdot d\Omega \quad (4.1.13)$$

where \vec{r} is the vector position. For non-spherical particles, the shape of the scattering phase function can be extremely complex and is characterized by asymmetric structures. An example of the scattering phase functions of oblate particles on the scattering plane is shown next section in Fig.4.14.

When the scattering phase function is only given on the scattering plane, $f(\vec{s}, \vec{s}') = f(\theta_s)$, where θ_s is the polar scattering angle described Fig.4.8(a). For spherical symmetry, the phase function becomes homogeneous relative to the mutual orientation of \vec{s} and \vec{s}' and $f(\vec{s}, \vec{s}') = f(\cos \theta_s)$. Therefore, there is no dependence on the azimuthal scattering angle, φ_s . In other words the scattering probability of spherical particles is homogenous over the angle φ_s (defined between 0 and 2π), and the scattering phase function depends only on its scattering angle, θ_s (defined between 0 and π).

When a homogeneous distribution of spherical particles is considered, the average scattering phase function $\bar{f}(\theta_s)$ is calculated as:

$$\bar{f}(\theta_s) = \frac{\int_{D=0}^{\infty} n(D) \cdot \sigma_e(D) f(D, \theta_s) \cdot dD}{\int_{D=0}^{\infty} n(D) \cdot \sigma_e(D) \cdot dD} \quad (4.1.14)$$

where $n(D)$ is the number of particle of diameter D . The determination of $\bar{f}(\theta_s)$ is employed when investigating homogeneous polydisperse scattering media (see section 5.2.3 and 6.3).

The ratio between the dimension of a scattering particle and the incident wavelength is of importance in the resultant scattering phase function. The particle size parameter, x , (described in Eq. 4.1.7), is representative of this ratio. For a constant value of x , an identical scattering phase function is obtained when considering spherical particles. Moreover, depending on the particle size parameter, the scattering phase function of spherical droplets can be either highly anisotropic with a dominant forward scattering and with a high number of fine lobes for $x > 10$ or more isotropic with a ‘‘homogeneous’’ distribution of the scattered radiation characterized by few large lobes when $x < 1$.

A convenient mathematical expression to describe the forward nature of the droplet phase

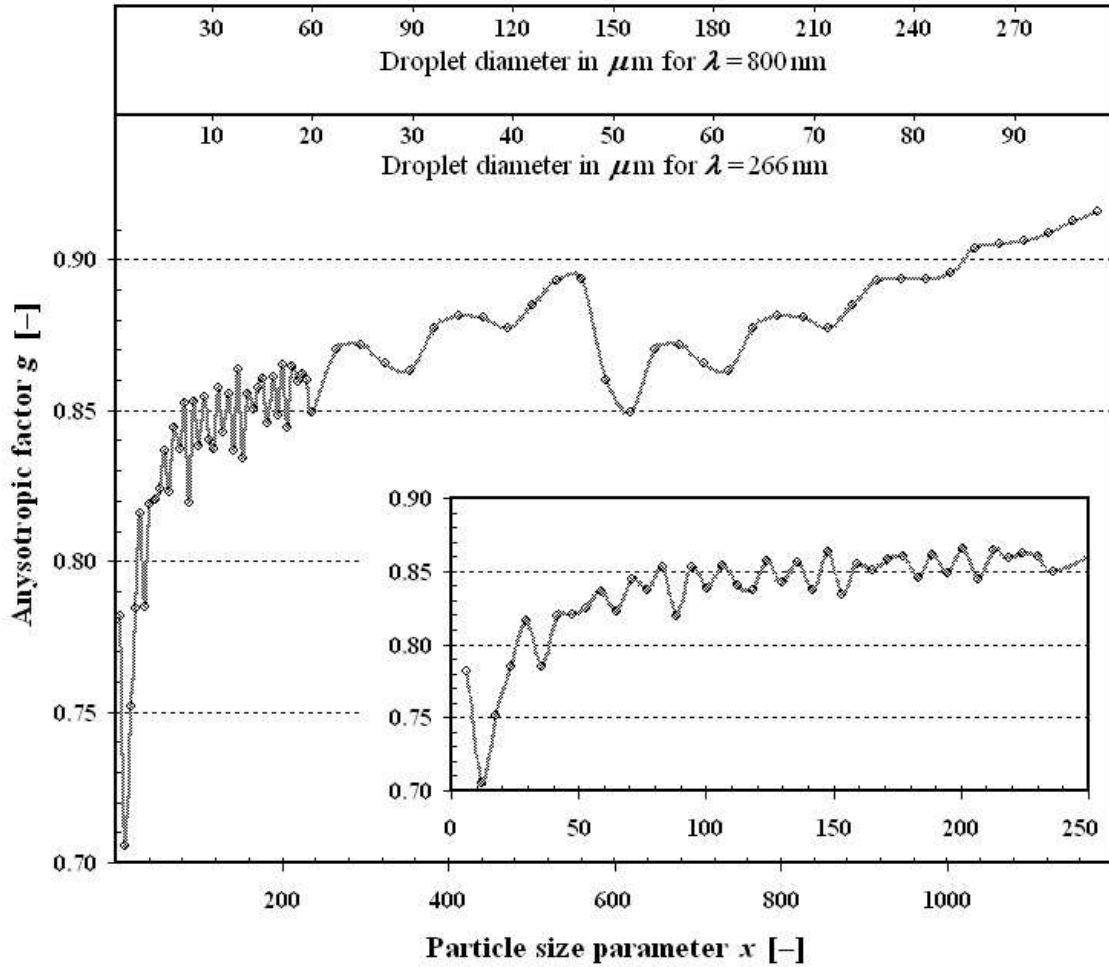


Figure 4.9: Anisotropy factor of homogeneous spherical fuel droplets ($n = 1.4 + 0.0i$) as a function of the particle size parameter. The droplet size scale is also added for $\lambda = 266$ nm and $\lambda = 800$ nm on the top of the graph.

function is the anisotropy factor g .

$$g = \iint_{4\pi} \cos(\theta_s) \cdot f(\theta_s) \cdot d\Omega \quad (4.1.15)$$

For isotropic scattering, g equals 0 and for highly forward scattering phase functions g tends to 1 (for strong back scattering, g tends to -1). In sprays, the factor of anisotropy ranges from 0.70 to 0.95. For a $20 \mu\text{m}$ water droplet in air illuminated at 532 nm incident light, $g = 0.86$. Figure 4.9 shows the anisotropy factor as a function of the particle size parameter for non-absorbing fuel droplet of refractive $n = 1.4 + 0.0i$.

4.2 Light-droplets interaction

Scattering is the light-particle interaction which acts to transform an incident electromagnetic radiation into a new electromagnetic radiation of identical or different properties. During this light-particle interaction, the incident electromagnetic energy can also be transformed into another sort of energy. This second interaction process is called absorption. In this chapter, both of the terms “*scattering*” and “*absorption*” are detailed and the description of light-droplet interaction is given.

4.2.1 Principles of scattering

The first consideration with regard to the scattering of light is to affirm that scattering is caused by the heterogeneity of a system. Assuming for example that a beam of light traverses a perfectly homogeneous medium, no scattering events would occur. As only a vacuum can be defined as a perfect homogeneous medium, all other media scatter light when illuminated by electromagnetic radiation. Depending on the arrangement of atoms (or molecules) in a medium, scattering will be more or less effective. For example, a crystal which has a perfect molecule arrangement will scatter less light than a layer of the human skin which is less ordered at the molecular level. The term scattering is very general and many different kind of scattering processes can be considered at different scale. In this section, scattering caused by the fluctuation of molecules (density fluctuation) or by the fluctuation of particle orientation (orientation fluctuation) are not considered. Only scattering by particles is described on a macroscopic scale with a particular attention given to spray droplets in the section 4.2.3.

When a particle (such as an atom, a molecule, a liquid or a solid particle) is illuminated by an electromagnetic wave, the discrete electric charges (the electrons and protons) are set into an oscillatory motion by the electric field of the incident wave. This oscillation causes the acceleration of the electric charges, which produces radiation of electromagnetic energy in all directions. This new radiation is called scattered radiation (Bohren and Huffman 1983). If a particle is divided into small regions such as each region is characterized by a dipole moment, then the oscillating field will cause the oscillation of the dipoles and a secondary radiation of scattered wavelets will be emitted by each region of the particle in all directions. Scattering is thus the result of the sum of all these wavelets as illustrated in Fig. 4.10. During the emission of the new electromagnetic waves, the scattered wavelets interfere one to each other, resulting in several preferential final scattering directions. Typically, back scattering and forward scattering are the

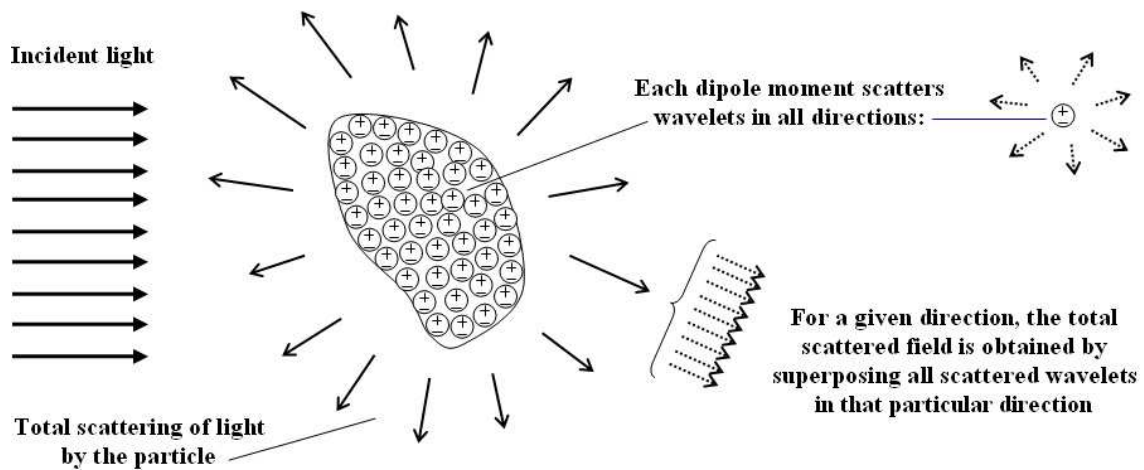


Figure 4.10: Scattering of light by a single particle: The total scattered field is the field resultant from all wavelets scattered by the regions into which the particle is subdivided (Bohren and Huffman 1983).

dominant scattering directions.

Both the size and the shape of a particle are responsible for the interference processes occurring. Depending also on the polarization state of the light an incident beam is scattered within preferential directions. In Fig.4.11, the polar Mie scattering phase function is illustrated for parallel and perpendicular polarization respectively.

The value of the particle size parameter determines the scattering processes. The Rayleigh scattering approximation is assumed when $x \ll 1$, corresponding to particles much smaller than the wavelength such as small aerosols and molecules. In Rayleigh scattering, it is assumed that any point of the particle is subjected to an identical electromagnetic field. The resultant scattering phase function is isotropic for the perpendicular polarization and anisotropic for the parallel polarization (in this case $f(\theta_s) = 0$ at 90°). Such results are illustrated in Fig.4.11, for $x = 0.0314$ and $x = 0.314$. The Rayleigh scattering intensity is proportional to $[2\pi/\lambda]^4$. Small particles scatter then much more shorter wavelengths than the longer wavelengths (note that this dependance into $1/\lambda^4$ is responsible to the blue color of the sky). The Rayleigh scattered intensity is also proportional to the square of the volume and then to D^6 when assuming spherical particles. Therefore, the scattering efficiency increase considerably with the particle size in the Rayleigh regime.

When $x \geq 1$ and when the particles shape is related to a sphere, the Lorenz-Mie Theory (LMT) and the Debye series apply. The LMT is mainly used for light scattering by spherical liquid droplets (the theory has been extended since for cylindrical and inhomogeneous particles). The resultant scattering phase function is characterized by many lobes due to diffraction with forward scattering dominating. The number of lobes and the

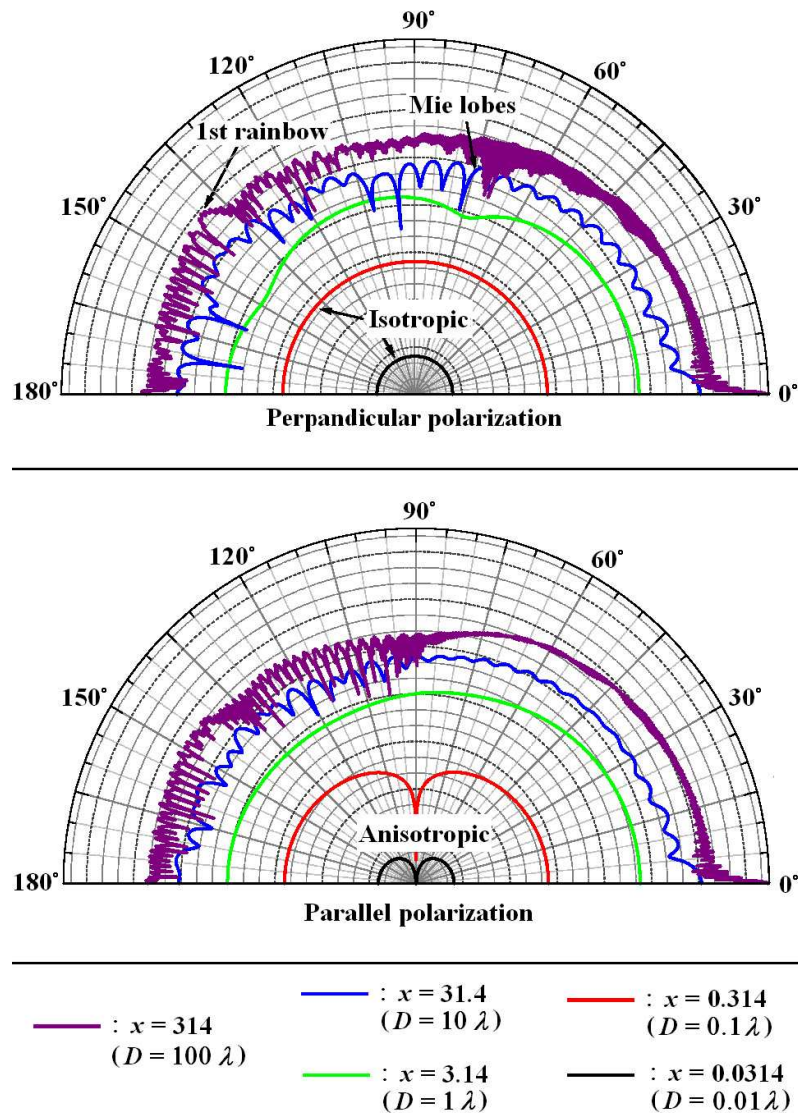


Figure 4.11: Polar scattering phase function (logarithmic scale) for a water droplet ($n=1.33+0.0i$) for different particle size parameter. The transition from Rayleigh ($x \ll 1$) to Mie scattering ($x \geq 1$) is illustrated (Onofri 2005).

distribution of light intensity within the forward and the backward direction increase with D . The light intensity scattered is, in the LMT, dependent on D^2 for $x \gg 1$ (see Fig.4.2) when the scattering efficiency becomes fairly constant (Fig.4.3). Advanced explanation of the LMT are provided section 4.2.3.

Finally for $x \gg 1$ and n real, the Geometrical Optics (GO) theory can be used. In GO, the reflected and refracted rays are separated at each refractive index changes. The intensity and directions of the new refracted and reflected rays are then calculated from the Snell-Descartes law and an order of refraction P is attributed for each new refracted ray. The method is termed “ray tracing”. Note that GO applies for particles much bigger than the incident wavelength and that diffraction phenomena are not considered in the method.

Figure 4.12 illustrates the GO approach with the first three orders of refraction. A typical example of the GO application is given in subsection 4.2.3 (Fig.4.18) for the case of a non-absorbing spherical droplet lighted with a gaussian beam.

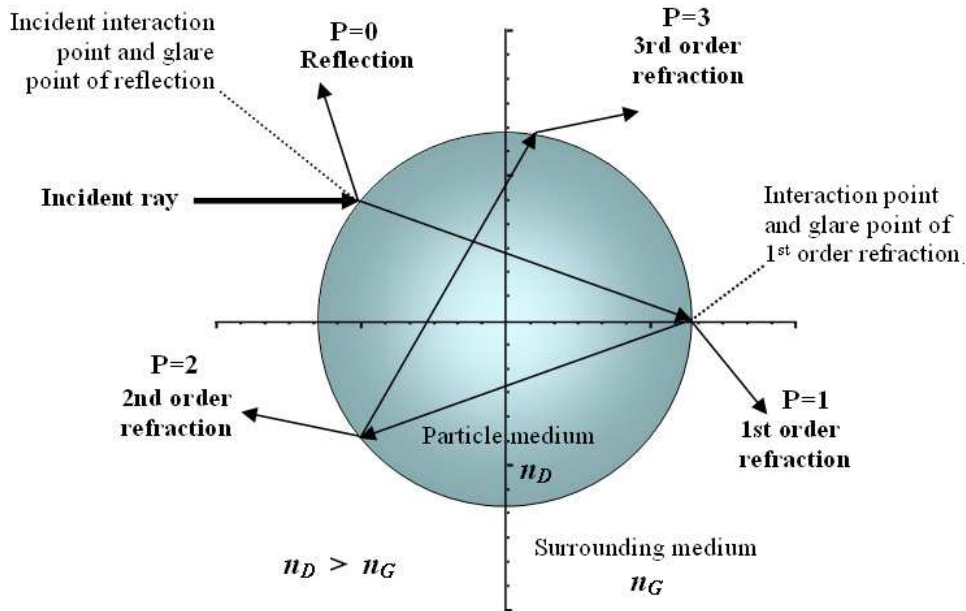


Figure 4.12: Schematic of Geometrical Optics approach for elastic light scattering within a spherical particle. The refractive indices of the surrounding medium and of the droplet are respectively given by n_G and n_D .

There exists a variety of scattering particles. Some are homogeneous, other are inhomogeneous; some are non-symmetrical, other are rotationally symmetrical. A classification of scattering particles is proposed in Fig.4.13 by Damaschke *et al* (1998). Scattering by non-spherical particles can be extremely complex to deduce especially when the GO approximation is not applicable. Table 2.5 gives examples of light scattering by different types of scattering particles whereas Fig.4.14 shows the scattering by oblate particles.

In the last explanations, the scattering of light has been described for single particles only and the effects of the neighbouring particles have been neglected. Indeed, in highly dense medium the total scattered field is not just the sum of the fields scattered by individual particles. Interference processes occur between scattering waves emitted from different neighbouring particles and must be considered in the determination of the total scattered field. In other words, if the scattering particles are very close to each other, there is a cooperative effect which is responsible for the total light scattering in the medium. This process is called “*dependent scattering*”. If spherical particles are considered in the given medium, and if a minimum distance of three times the radius is respected between each particle then “*independent scattering*” can be assumed (Van de Hulst 1981).

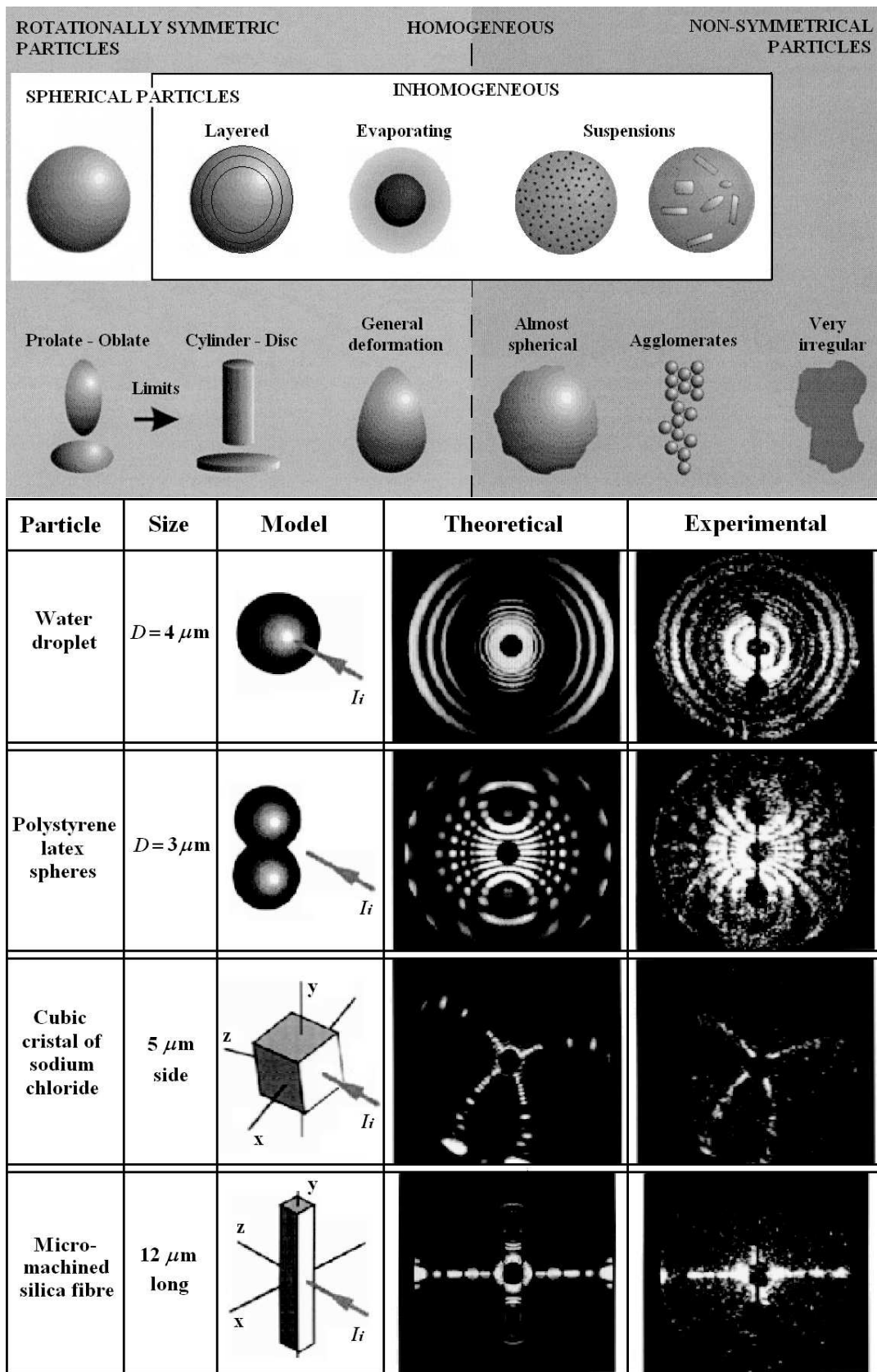


Figure 4.13: Top picture: Classification of scattering particles commonly probed (Damaschke *et al* 1998). Bottom picture: Table showing the scattering of light by particles of various shape (Kaye 1998).

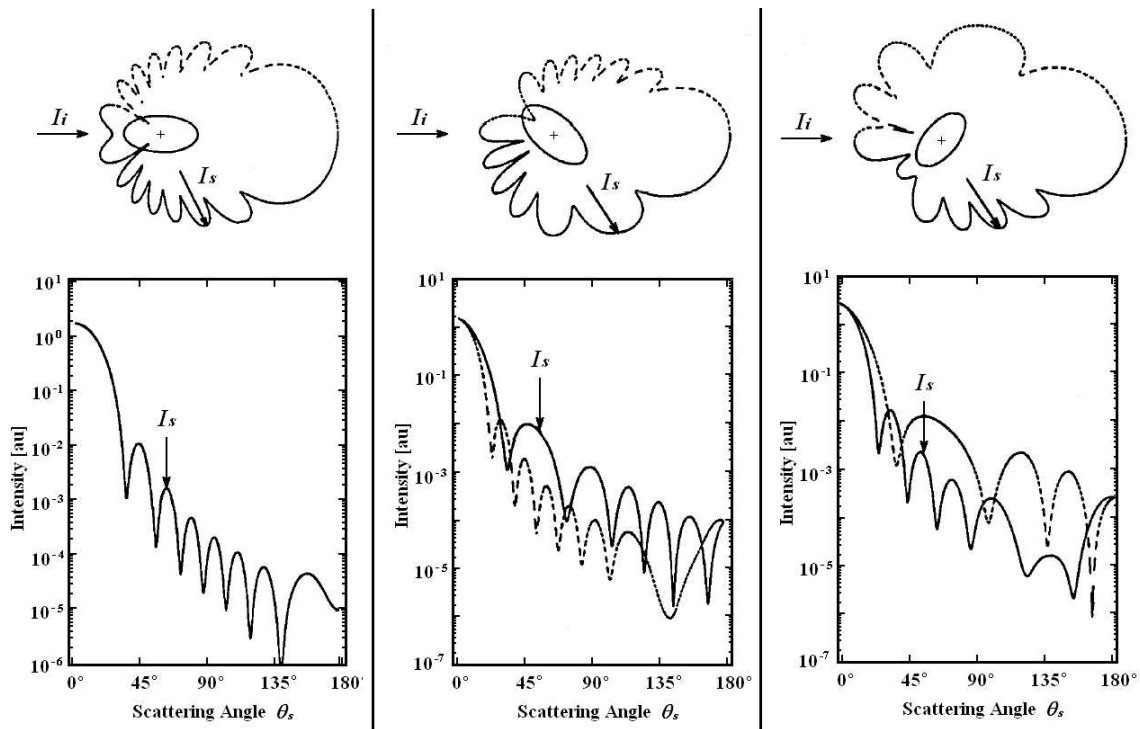


Figure 4.14: Scattering by oblate particles (Latimer 1978).

In natural environments containing a collection of particles and in most of industrial two phase flow media, the condition of independent scattering is respected. In many dense turbid media even in independent scattering, each particle also scatters the scattered field of other particles and not only the incident field. In this case, an effect of “*multiple scattering*” occurs and “*single scattering*” can no longer be assumed.

Single scattering is considered when the total energy removed removed by a collection of particles is proportional to the energy removed by a single particle. One solution for deducing the presence of multiple scattering in a medium is to double the concentration of particles and to measure the scattered intensity. If scattered intensity doubles, then single scattering was dominant in the initial medium. If not, then the multiple scattering must be considered. This situation may be illustrated in a large number of natural (clouds, fog, smoke) and industrial (sprays, two phase flows) scattering media. A detailed explanations about multiple scattering is given in the subsection 4.20.

A final consideration is whether a given scattering process is “*elastic*” or “*inelastic*”. When the frequency of the scattered field is the same as that of the incident light, then elastic scattering is respected. When, however, the frequency of the scattered field is larger or smaller than the incident light, inelastic scattering is considered. Inelastic scattering is often associated with a process of absorption and reemission. Finally, it is important to note that most optical phenomena such as the reflection and the refraction at

optically smooth interfaces, or the diffraction of light by gratings, edges and slits are, in fact, the results of scattering processes (Bohren and Huffman 1983).

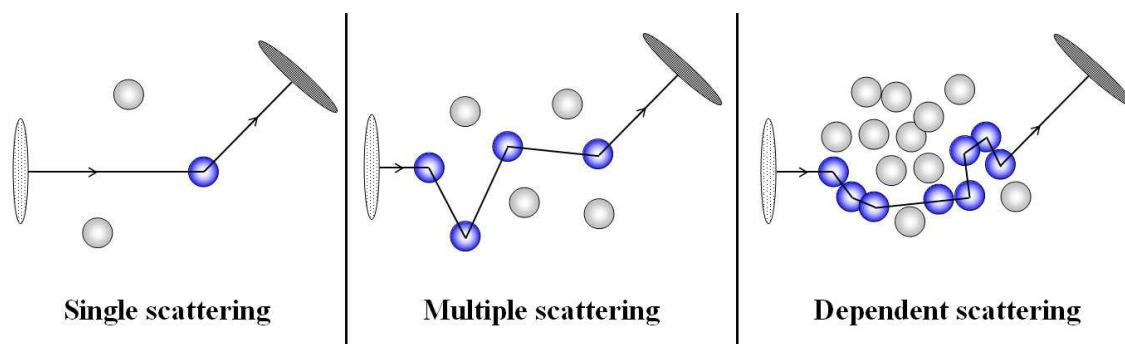


Figure 4.15: Effect of neighbouring particles and classification of scattering processes.

4.2.2 Principles of absorption

A proper understanding of absorption requires a description of light-matter interaction on a molecular scale. Without any excitation, the energy of a given molecule (or atom) is fixed to an initial quantum state. When the molecule is subjected to electromagnetic radiation, the incident radiation is absorbed and the increased energy level of the molecule leads to an excited state. By emitting a new electromagnetic radiation (the scattered radiation), the molecule can return to its initial state. Depending on the mechanisms through which this relaxation process occurs, different types of scattering are defined (see previous section).

The term “absorption” refers to the transformation of the incident electromagnetic energy into energy of another form. For instance, absorbed radiation can be transformed into thermal energy. This energy is produced by inter-molecular (molecular vibration and rotation) and extra-molecular (molecular collision and translation) de-excitation processes. The dissipation of the energy by heat is not the only sort of energy conversion which exists.

Scattering and absorption are two different results of the same cause and thus are dependent on each other. However, they diverge based on the fact that absorption is a more selective process. In other words, scattering has a smoothly varying efficiency with wavelength contrary to absorption. In practice, paints and liquids doped by fluorescing tracers have high absorption. However, most other sprayed liquids have generally low levels of absorption.

4.2.3 Scattering of laser light by a single spray droplet

Depending on their location within the spray, droplets produced by atomization have various geometrical forms and size distributions. In the near injector region, the spray is characterized by ligaments along the liquid core (which are subject to primary atomization), large droplets of high velocity (which are subsequently deformed and subject to secondary atomization), and other irregular liquid elements.

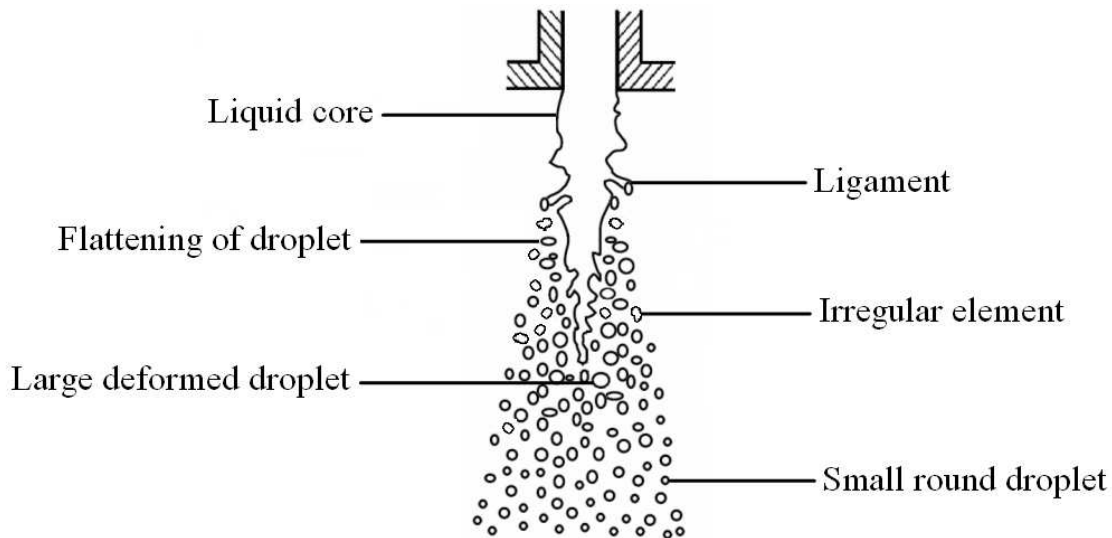


Figure 4.16: Geometrical characteristics and shapes of droplets within a typical atomizing spray.

The scattering of light from such arbitrarily shaped drops is extremely complex and dependent on the particle's orientation to the incident light. After secondary atomization, the velocity of the droplets is considerably reduced. In this case, the aerodynamic pressure applied to the droplet is small in comparison to the internal pressure due to surface tension forces. The droplets formed on the periphery of the dense spray and in the dilute spray region have finally a quasi-perfect sphericity. Figure 4.16 depicts the different geometrical forms of droplets and liquid elements within an atomizing spray.

As previously mentioned (see subsection 4.2.1) the physical phenomenon of light scattering by spherical particles is described in the classical LMT often called the Mie theory (Mie 1908). The LMT is restricted to homogeneous, isotropic and non-magnetic particles in a non-absorbing medium. The size of the particles, D , must also be of dimension bigger or comparable to the wavelength λ and the incident light is assumed to be plane waves. Such considerations apply for most laser diagnostics of spray, where practical droplets is from 1 up to $\sim 500 \mu\text{m}$ in diameter; whereas the light wavelength used, ranges from the ultraviolet $\sim 266 \text{ nm}$ (for PLIF measurements) to the near-infrared $\sim 800 \text{ nm}$. Note, however, that X-ray or infrared light are also employed in some techniques (see

section 3.2.2 and 3.2.3). The LMT has been generalized by Gouesbet and Grehan (1982) in order to consider the Gaussian intensity profile of the incident laser beam. The generalized LMT is used when the dimension of the probed particles are on the order of the size of the beam diameter. An example of polar Mie scattering phase functions is given Fig.4.17 for a $20\ \mu\text{m}$ fuel droplet, assuming different state of light polarization.

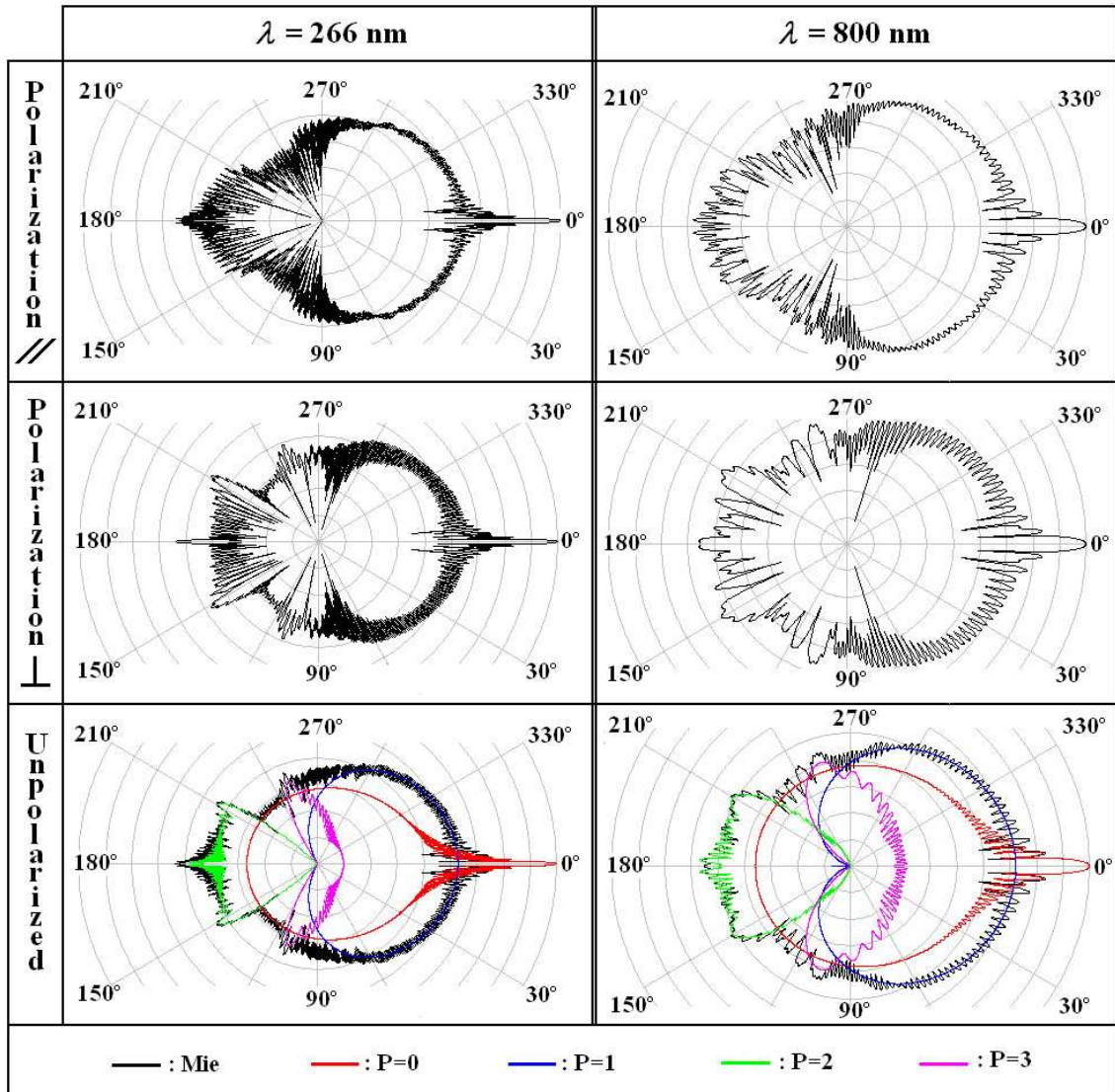


Figure 4.17: Polar Mie scattering phase function of a $20\ \mu\text{m}$ spherical fuel droplet ($n = 1.4 + 0.0i$) at 266 and 800 nm for the perpendicular polarization, parallel polarization and unpolarized light (logarithmic scale). The representation of the scattering modes are also given in terms of Debye series for the case of unpolarized light (calculated from MiePlot - Laven 2006).

The Debye theory provides an alternative method for summing the Mie terms, and like the LMT theory, it represents an exact solution to the scattering problem. Debye theory splits up the calculations into terms that are easily tied to physical scattering processes such as diffraction, reflection, transmission and surface wave phenomena. The scattering

modes of the Debye series are illustrated from $P=0$ to $P=3$ in subsection 4.2.1 (Fig.4.12) and their individual contribution to the total scattering is highlighted in Fig.4.17 for a $20\ \mu\text{m}$ fuel droplet. Finally, Fig.4.18 shows the scattered intensity in the near field region of a $20\ \mu\text{m}$ water droplet crossing a thin light beam.

The LMT is fully applicable in the dilute spray region, where the liquid droplets are homogeneous and where their small size respects a quasi-perfect sphericity. However, the presence of non-spherical droplets and of irregular liquid elements makes the use of the LMT questionable in the dense spray region. Calculations of light scattering by non-spherical particles might be required to understand the general scattering process occurring in the near injector region. However, most of investigated sprays are, in practice, highly atomized sprays in which small spherical droplets are formed rapidly downstream from the nozzle exit. The presence of many ligaments and large irregular droplets concerns principally “poorly” atomized sprays which contain low number densities of droplets and which do not suffer from multiple scattering issues.

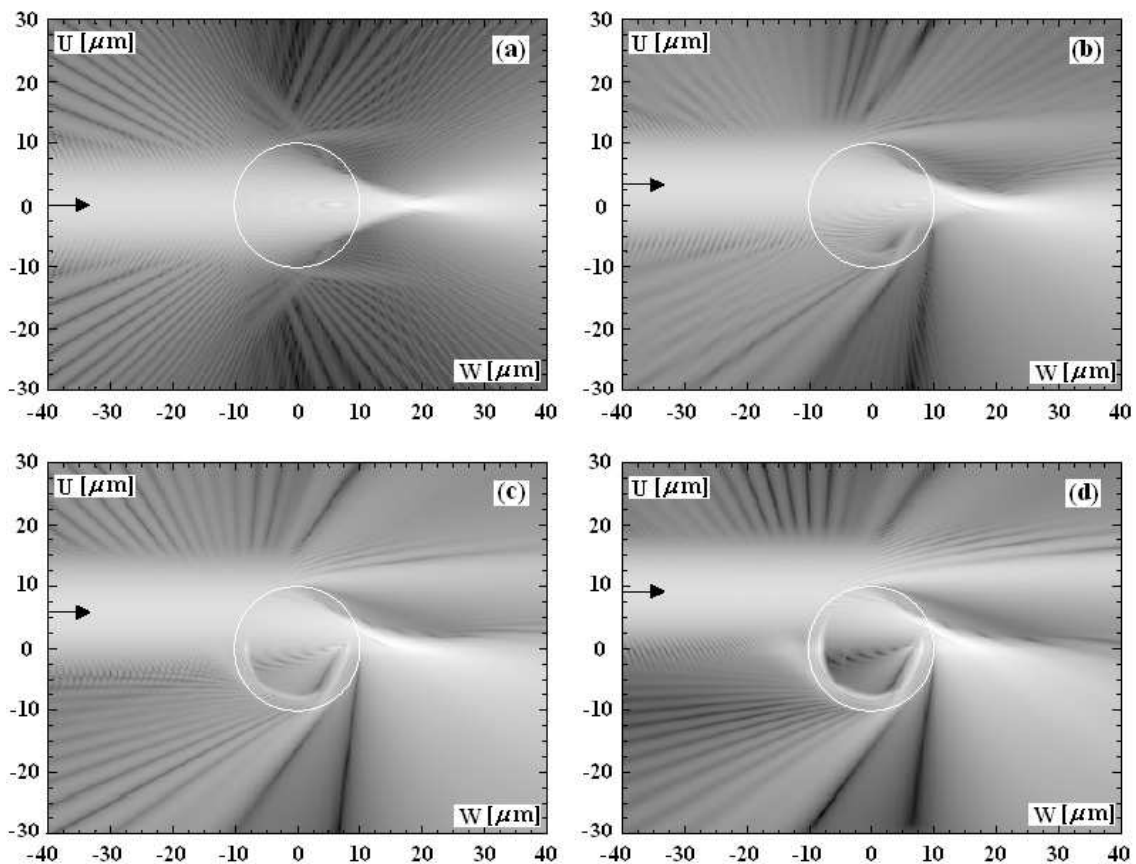


Figure 4.18: Scattered intensity in the near field of a $20\ \mu\text{m}$ water droplet ($n = 1.33 + 0.0i$). The respective distances between the droplet centre and the centre of the light beam along the axis U are $0\ \mu\text{m}$ in (a), $3\ \mu\text{m}$ in (b), $6\ \mu\text{m}$ in (c) and $9\ \mu\text{m}$ in (d) (Albrecht 1999).

4.2.4 Scattering of laser light with a collection of droplets

The propagation of laser beams through a collection of droplets such as sprays is subject to attenuation and multiple scattering phenomena (see illustration in Fig.4.19). Attenuation and multiple scattering introduce errors in the measurement of droplet size and concentration (as seen in sections 3.1.4 and 3.2.5) particularly in the intermediate scattering regime (as explained in section 4.1.2). In spray diagnostics, three processes can be noticed.

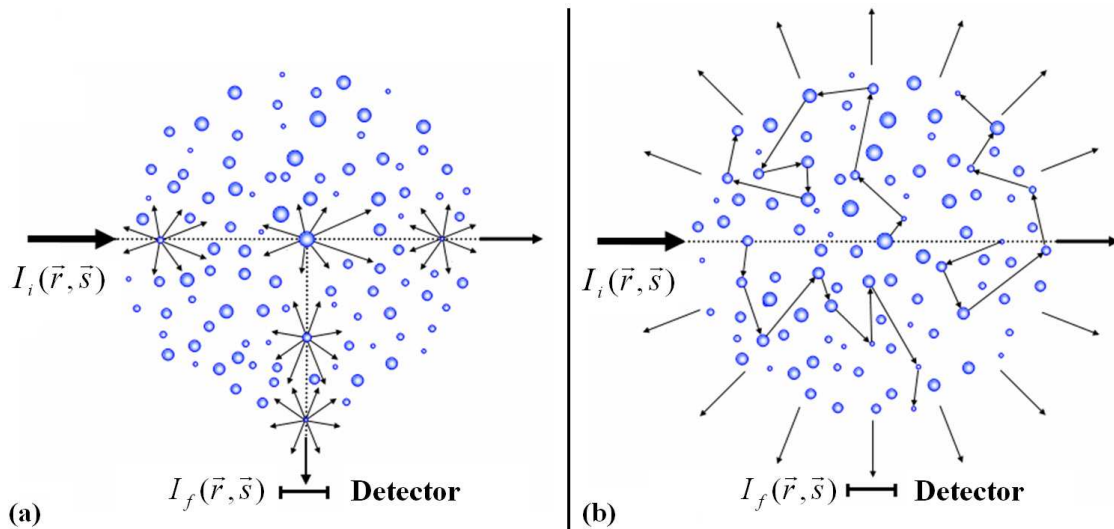


Figure 4.19: Illustration of attenuation (a) and multiple scattering (b) processes when probing a spray with a laser beam.

- *Attenuation along the incident direction:*

The probe beam is attenuated as it traverses the spray due to both scattering and absorption. Depending on position along the laser line-of-sight, not all droplets are illuminated with the same intensity which is reduced exponentially (see the equation of the Beer-Lambert law Eq.4.1.3).

- *Off-axis attenuation:*

This attenuation occurs between the incident laser line-of-sight (or sheet) and the detector (called also out-of-plane attenuation). It corresponds to “secondary scattering” from droplets lying between the probe beam and the detector

- *Multiple scattering:*

Extraneous light is detected after being multiply scattered by a number of the surrounding droplets. Multiple scattering occurs both along the light sheet and between the light sheet

and the detector. Both cause undesirable errors in the detected signal if it is processed with the single scattering assumption.

Multiple scattering is responsible of the changes in photon trajectories from the desired single scattering as depicted in Fig.4.20. Errors introduced by multiple scattering depends on the average deviation of the trajectory of the detected photons per scatter, and hence on the particle size distribution and the detector acceptance angle. Quantifying multiple scattering can be approximated via the measure of the optical depth.

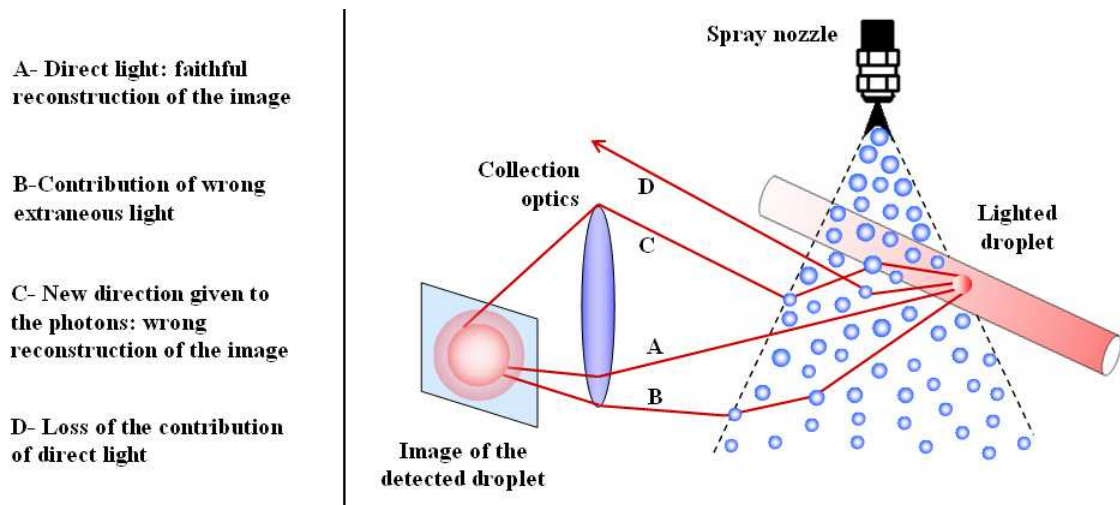


Figure 4.20: Schematic of the light propagation in spray diagnostic with the significant effects produced by multiple scattering.

The magnitude of error introduced by each process varies with position, in a manner dependent on the spray geometry. Corrective solutions are unique for each source-detector configuration and for each spray structure. The most flexible way to understand and quantify multiple scattering and attenuation issues in a given optical diagnostic of a spray, is to simulate the problem as detailed in the next Chapter.

Modelling of Photon Transport

SEVERAL distinct approaches to model light transport within scattering and absorbing media have been developed in the past. These approaches can be separated into two general groups respectively named deterministic and stochastic. The deterministic models include the electromagnetic theory (employed in the Lorenz-Mie theory and in the Rayleigh-Gans approximation) and the radiative transfer theory (applied to a wide range of radiative transfer problems). Stochastic models are based on the calculation of probabilities and include random walk (Weiss and Rubin 1983, Gandjbakhche and Weiss 1995) and Monte Carlo approaches (Sobol 1974, Lux and Koblinger 1991). Many other types of models have also been tested and used. However, they won't be mentioned in this chapter as they do not illustrate the modern tendencies in the modelling of light propagation.

The investigation of photons migration within turbid media is not new and has been numerously applied to a variety of applications. Examples span across disciplines as Astrophysics, Astronomy, Meteorology, Biomedical Optics and Oceanography. In opposition to other commonly investigated scattering media such as skin tissues, atmospheric layers, fogs, and clouds, sprays present particularly strong inhomogeneities in the concentration and distribution of scattering centres with location. Approximations based on homogeneous or layered structures cannot be assumed for spray. This issue makes the problem highly complex and difficult to solve.

In this chapter, a brief overview of the theories and models used for the description of light transport in turbid media is initially given. A particular attention is given to the Monte Carlo technique which is nowadays the most versatile and flexible solution for solving radiative transfer problems. After highlighting the requirements related to the modelling of photon transport within sprays, a complete description of the Monte Carlo codes developed in-house is provided.

5.1 Deterministic and stochastic models

Deterministic and stochastic models are the two main groups for photon transport modelling. In deterministic models light propagation is considered as a whole and the specific light intensity is described by partial differential equations. These equations are derived from the electromagnetic and radiative transport theories. In stochastic model, the light propagation is described locally and the interaction of individual photon with scattering particles are modeled. Even if many stochastic based models can be noticed, only the model of interest, called the Monte Carlo, is described at the end of this section.

5.1.1 Electromagnetic theory

The propagation of electromagnetic waves through a spatially varying medium such as turbid scattering media is classically described by the Maxwell equations (Born and Wolf 1986, Bohren and Huffman 1983). Maxwell's equations treat rigorously the energy transfer of continuous electromagnetic waves and express mathematically the light propagation by wave vectors which are being scattered and absorbed. The most widespread application based on electromagnetic theory is the computations of the LMT. As mentioned in subsection 4.2.3, the LMT is used to describe the scattering of light by single spherical particles suspended into a homogeneous medium of different refractive index. Such computations generally concern the study of light scattering by single liquid droplets in air (see subsection 8.1.1) or by suspended polystyrene microspheres in water (see subsection 8.1.3) which are commonly used for calibration purposes.

For a collection of scattering particles several cases must be considered. If large distance of separation between particles are assumed, the scattering processes of each single particle is independent (see section 4.2.1). In this case and under the single scattering regime the LMT can be used to describe the global scattering of a collection of particles by adding the individual scattering fields together. At high concentration of particles where multiple scattering or independent scattering occurs the final electromagnetic field cannot be approximated by summing each independent field. For dependent scattering, the problem corresponds to light scattering by aggregates and is particularly difficult to solve. Multiple scattering problems can be tackle by employing the idea of perturbed field as a first approximation to the unperturbed scattering theory (Ishimaru 1978). However this approach does not lead to solvable equations to most practical cases of optical diagnostics of spray.

5.1.2 Radiative transfer theory

The radiative transfer theory is derived from the balance of energy between the incoming, outgoing, absorbed, scattered and emitted photons within an infinitesimal volume element (see Fig.5.1).

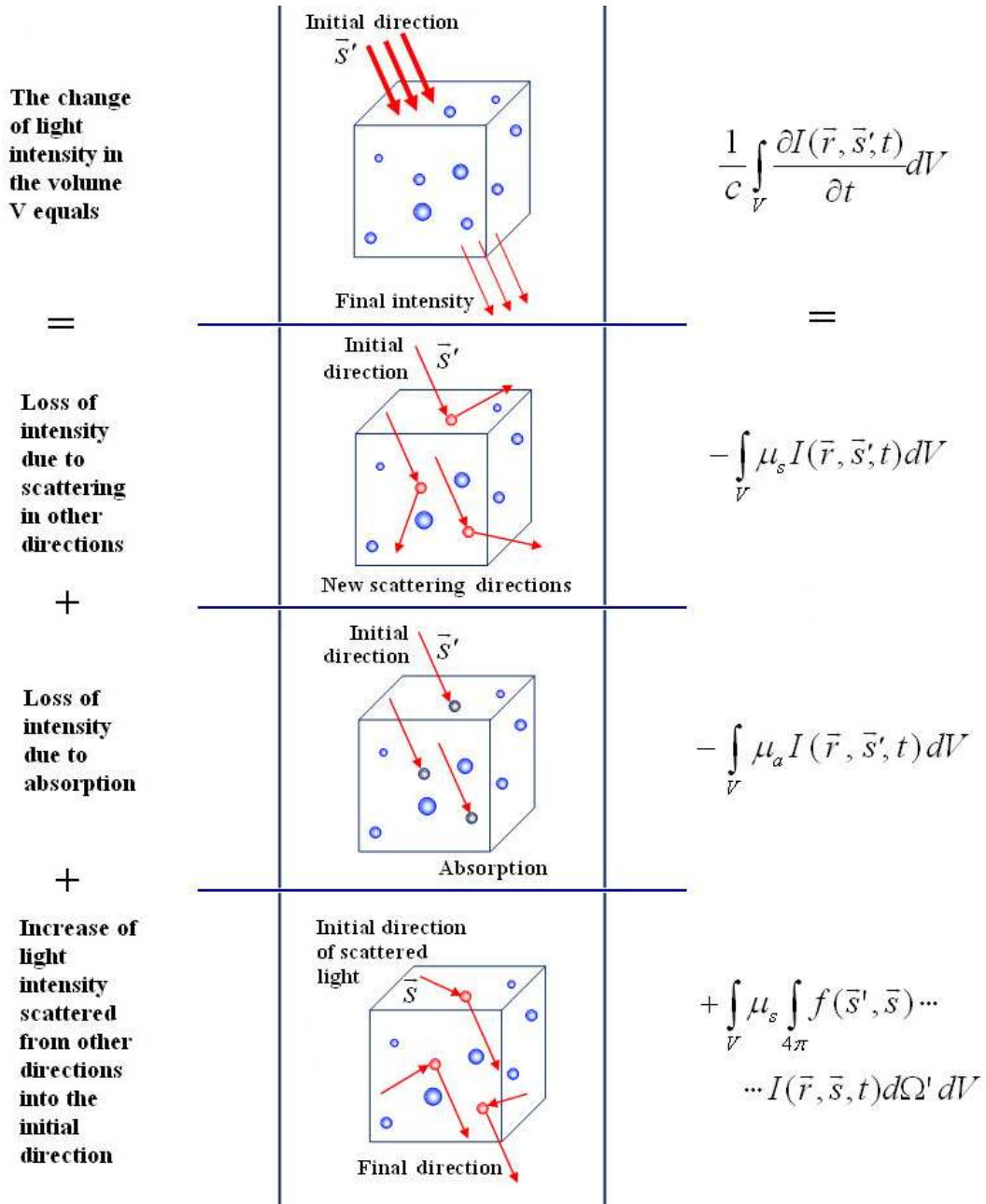


Figure 5.1: Construction of the Radiative Transfer Equation (RTE).

The optical properties of the volume element are assumed homogeneous; the scattering and absorbing events of the confined substructures are then statistically averaged within the medium. The central equation representing the macroscopic balance of energy and

describing the average transport of photons through a turbid medium is the Radiative Transfer Equation (RTE) (or equation of radiative transfer). An illustration describing the RTE is given Fig.5.1. In the RTE only quantities as power or intensity are considered (Ishimaru 1978). Light propagation is envisioned as photons stream and correlations between the radiation fields such as interferences are neglected. Such assumptions can only be assumed if the wavelength of the incident radiation is small when compared to the dimensions of the scattering medium and for well separated scattering centres (independent scattering). For most of turbid media and for the case of laser light propagation in sprays these conditions are respected.

The RTE can be described as follows: The change of radiance along a line of sight corresponds to the loss of radiance due to the extinction of the incident light plus the amount of radiance that is scattered from all other directions into the incident direction. Note that the total extinction equals the loss of radiance due to scattering of the incident light in all other directions, plus the loss of the radiance due to absorption at each light-particle interaction. The RTE is mathematically given as:

$$\frac{1}{c} \frac{\partial I(\vec{r}, \vec{s}', t)}{\partial t} = -\mu_s I(\vec{r}, \vec{s}', t) - \mu_a I(\vec{r}, \vec{s}', t) + \mu_s \int_{4\pi} f(\vec{s}', \vec{s}) I(\vec{r}, \vec{s}, t) d\Omega' \quad (5.1.1)$$

where t is time and c is the speed of the light in the surrounding medium, μ_e , μ_s and μ_a are the respective extinction, scattering and absorbing scattering coefficients and f is the scattering phase function derived from the appropriate scattering theory (e.g. Lorenz-Mie or Rayleigh-Gans scattering). For stationary radiance distribution from continuous wave lasers (or from long laser pulses) the RTE can be derived to:

$$\mu_s I(\vec{r}, \vec{s}') + \mu_a I(\vec{r}, \vec{s}') = \mu_s \int_{4\pi} f(\vec{s}', \vec{s}) I(\vec{r}, \vec{s}) d\Omega' \quad (5.1.2)$$

Note that only one wavelength is most of the time considered in order to make the resolution of the RTE more accessible.

5.1.3 The Monte Carlo (MC) technique

The transport of light in turbid media can be predicted by the solution of the RTE coupled with an appropriate scattering theory. However, due to the complex geometries and range of particle sizes encountered in practical applications it is rarely possible to find an analytical solution to the RTE. Instead, numerical solution schemes are used via stochastic models. It exists many stochastic models based on random walks (Weiss and Rubin

1983), photon path-integral formalism (Jacques and Wang 1997, Wilson and Wang 2001) or Monte Carlo (Sobol 1974, Kandidov 1996) approaches. In random walk models photon motion is strongly restricted by a finite number of directions. For realistic simulation, all possible photon paths must be considered making this restriction impossible to assume. The path-integral method is based on the calculation of most probable photon paths. The main advantage of the technique is the save of computational time by making systematic search of photon path rather than random. However, even if the averaged description of photon trajectory is extracted from this method, an accurate description of the light intensity distribution cannot be obtained. Finally, the Monte Carlo (MC) technique presents the most popular and versatile approach for photon transport within 3D complex structures. The MC simulation allows quantifying the differences between the ideal theoretical approach and the experiment with its imperfections (e.g. imperfectly monodisperse or spherical particles, divergence of a laser beam, finite apertures, *etc*). Examples of MC models are extensive and it can be noticed that the development and improvement of novel realistic MC codes is still a domain of intense activity (Bilenca *et al* 2005, Ramella-Roman *et al* 2005a, 2005b, Boas *et al* 2002 and Berrocal *et al* 2005b). MC photon transport simulation is well established in biomedical (Prahl 1988, Keijzer 1993 and Churmakov 2005) astronomical (Hogerheijde 2000), maritime (Piskozub 2004) and meteorological applications (Bucher 1973, Lavigne 2001). More recently the technique has been applied to the propagation of a laser sheet within a hollow cone spray (Berrocal *et al* 2005a - see section 7.1).

As for the radiative transfer theory the MC technique requires initial optical parameters such as the scattering and absorption coefficients and the scattering phase function. These parameters are used to determine the probability for the photons to interact with the scattering centres (like droplets), the probability to be either absorbed or scattered at each photon-particle interaction and the probability to propagate along a new direction if scattering occurs. The principle any of MC models is based on the sampling of random variables using random numbers with adequate Probability Density Functions. Uniformly distributed (between 0 and 1) random numbers are employed to exact each variables from PDF which have been cumulated (CPDF - Cumulative Probability Density Function). This process is depicted Fig.5.2.

The advantages of MC models over analytical approaches are numerous. First, they allow simulations within 3D complex scattering structures. Second, they are flexible and can handle various geometries. Third, MC simulations gives exacts solutions as long as random numbers are correctly generated and that the physics of photon propagation and scattering employed is exact. Fourth different optical phenomena as inelastic scat-

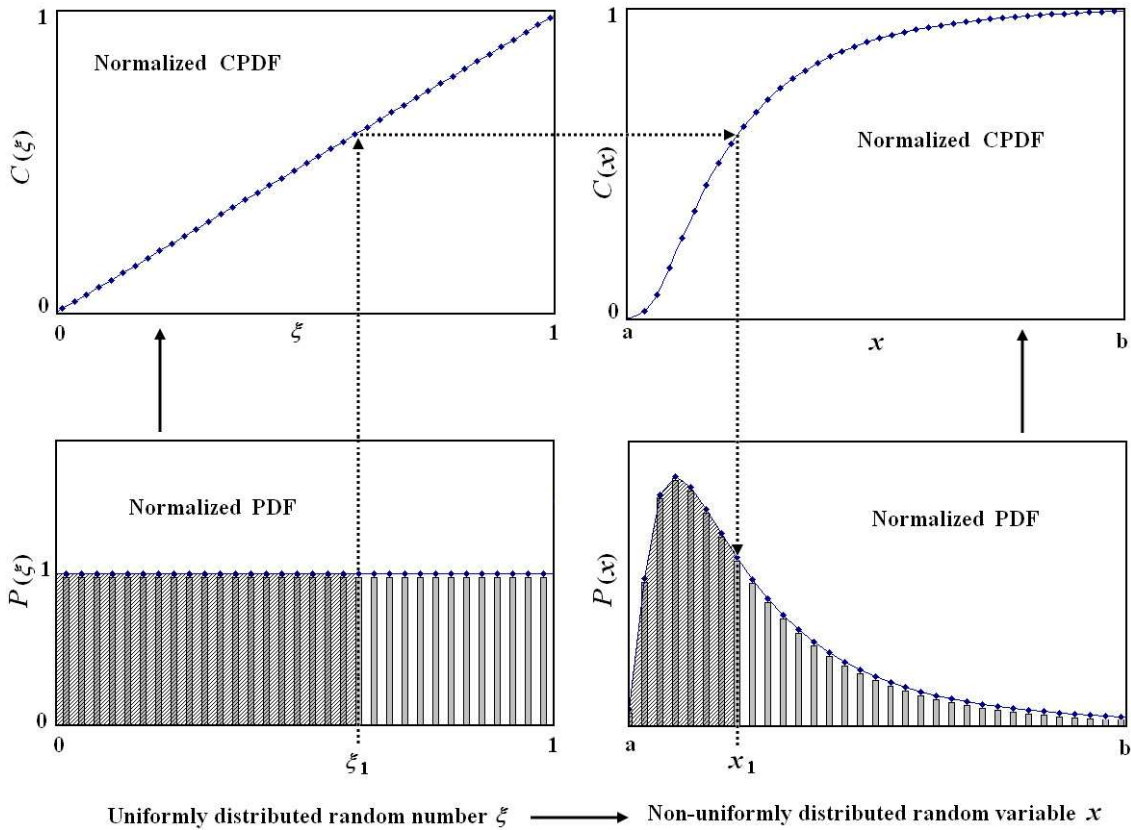


Figure 5.2: Sampling of random variables x from random numbers ξ which are uniformly distributed between 0 and 1. The total area under the curve $P(x)$ and $P(\xi)$ each equal unity and the probability for ξ_1 to be in $[0, \xi_1]$ equals the probability that x is in $[a, x_1]$.

tering, absorption, and polarization effects can be incorporated in MC models. Finally, many quantities like the spatial intensity distributions and the photon time-of-flights can be measured for different detection acceptance angles and source-detector configuration. MC simulations usually describe only the trajectory of the scattered radiation, but polarization changes inside/outside the medium can be also taken into account based on the Stokes-Muller formalism (Bartel *et al* 2000, Wang *et al* 2003) or the Jones formalism (Gangnus *et al* 2004).

5.1.4 Modelling requirements

The appropriate modellings of photon transport in sprays must match with a number of requirements. These requirements are oriented especially to the application of modern optical spray diagnostics and are listed below:

- The model must be flexible and able to consider any spray geometry, structure and

dimension.

- Due to the highly scattering nature of the dense spray region the model has to cope with multiple scattering.
- The model must also be adaptable to any type of source-detector configuration and any specific experimental arrangement.
- Strong variations of both droplet size distribution and droplet concentration must be taken into account within a 3D based structure.
- Several distinct anisotropic scattering phase functions representing the scattering process of different droplet size have to be introduced within the model.
- Several optical quantities of importance must be measured by the model. These quantities are the spatial distribution of light intensity, the number of scattering events occurring, the photon time-of-flight and the measurement of the single light scattering intensity.
- Finally, reliable and accurate predictions have to be generated by the model.

5.2 Development of the MC model

In MC methods, light propagation within scattering media is described locally and not considered as a whole. This chapter discusses initially the validity of MC approximations and assumptions. In a second subsection, the implementation and principle steps of MC simulations are given. Finally, different types of turbid media are identified and for each of them an appropriate MC code has been developed and is described at the end of this section.

5.2.1 Assumptions

- *Droplets sphericity:*

In the MC model described next, droplets are assumed perfectly spherical and respect the Lorenz-Mie scattering conditions. Droplet sphericity allows important simplifications as the scattering process occurring does not depend on the orientation of the droplet with the incident light wave. As seen in section 4.2.4 this corresponds to secondary atomized droplets situated downstream from the liquid core. Due to the surface tension forces,

small droplets tend to be more spherical than large droplets. Light scattering by liquid cores, ligaments and other irregular individual liquid elements are not considered within the MC models developed. Sprays generated from fast and fine atomization generate small round droplets at high speed rates. Diesel sprays and air-blast atomizers are two examples of such sprays and are suitable for realistic MC simulations.

- *Independent scattering:*

The second assumption concerns the independent scattering of the light (see section 4.2.1). In a spray environment, the droplets are well separated after the successive breakups. The complete scattering generated is then the result of the scattering by several individual droplets. For independent scattering with randomly positioned scattering centre, interference effects between the scattered waves can be neglected. This is an important feature as in MC codes light is described by photon packets (not electromagnetic waves) and interferences cannot be considered.

- *Incoherence:*

Incoherence occurs when the phase information is lost after several scattering events. This is generally the case for independent scattering where no regular periodic structures in the position of the scattering centres can be observed. In spray, droplets are generated from instable and chaotic processes. Droplets are finally randomly distributed within a 3D environment without any periodic structures making assumption of incoherence valid.

- *Homogeneity of elementary volumes:*

In the most advanced MC code developed (MC code 3), the entire scattering medium is segregated into a multiplicity of elementary cubic volume when dealing with inhomogeneous media (see section 5.2.3). One restriction consists to assume that these elementary cells have homogeneous optical properties.

- *Unpolarized and monochromatic light source:*

In all presented MC results, the incident and scattered light beams have been assumed unpolarized and monochromatic. The source of light employed in spray diagnostics are generated from lasers. As laser radiation is characterized by high degree of monochromaticity and narrow wavelength spectrums, this assumption is then valid. After a scattering event, the state of polarization state varies and the assumption of unpolarized in which

multiple scattering undergoes remains acceptable. Note however that many MC models deduce the polarization state of photons exiting a scattering medium (Ramella-Roman 2005a, 2005b and Cote 2004).

- *Random position of scattering centres:*

The position of the droplets within the simulated medium is not initially fixed within the input data but calculated randomly during each photon journey. The random number generator used must not then repeat the same series of numbers, in order to avoid identical photon paths.

5.2.2 Implementation of the MC simulations

Before describing the implementation of MC simulations, important remarks regarding the generation of random number should be mentioned. As MC models are based on probabilistic approaches, a true random number is ideally required. However, for computer efficiency, a pseudo random number is used in all MC programs. The major problem with pseudo-random number generator is the periodicity of the number series generated from a seed. However, the problem becomes insignificant by making this period as large as possible. In our model, the random number generator employed has been developed by L'Ecuyer (1998) (*ran2*) and has a period of $\approx 2.3 \cdot 10^{18}$ (Press *et al* 2002).

The general implementation of the MC simulations for light transport can be summarized as follows: Photons start their journey from a light source. The angular and spatial distribution of the light source is modelled according to the purpose of the simulation. Photon history is traced until it gets scattered or absorbed in the medium. Random samples are taken from probability distribution which governs the various transitions, interactions that they undergo. The parameters of interest are extracted from the photon history when photons are absorbed or exit the simulated volume. All these steps are repeated a large number of time until sufficient statistics are cumulated.

- *Photons source:*

Light sources are constructed within MC simulations by defining the initial photon positions and directions of propagation in a manner that the angular and spatial distributions of the desired source is respected. Assuming that a large amount of photons is sent, almost any type of light source can be modelled via MC simulation. Three examples of sources have been employed.

The first example, the simplest, is the point source. In this case all photons start their journey from a unique position. If the initial direction of propagation is constant for all photons, one ray of light only is simulated. This is of use for the study of light scattering with single particles (section 8.1).

The second example concerns flat light beams. For such sources, the photon starting point is uniformly distributed within a predefined surface. If the source is a flat cylindrical beam, this surface is a disk (section 6.3.2) and if the source is a flat laser sheet, this surface is a thin rectangle (section 7.1.2).

For non-uniform distribution profiles of light intensity the distribution of the initial photon position can be deduced from mathematical functions such as Gaussian functions. However, the modelling of complex and non-symmetrical light sources (generally encountered experimentally) must be performed from a matrix array. Each element of the matrix defines the number of photons sent per position from an initial plane. Such technique is used in section 6.2.1 (see Fig.6.10) and allows the exact reconstruction of an experimental laser beam. The transfer of images of objects through scattering media can also be investigated using such techniques (section 8.2).

- *Free path length determination:*

The free path length l_{fp} is the distance of photon propagation between two scattering and/or absorbing particles. The probability density function of a photon to be scattered and/or absorbed after traveling the distance l_{fp} is given as:

$$P(l_{fp}) = \mu_e \cdot e^{-\mu_e \cdot l_{fp}} \quad (5.2.1)$$

Following the process of random sampling illustrated in Fig.5.2, and assuming that $P(l_{fp}) = P(x)$ and $l_1 = x_1$ it is deduced that:

$$\int_a^{l_1} P(l_{fp}) \cdot d(l_{fp}) = \xi_1 \quad (5.2.2)$$

for $\xi_1 \in (0, 1)$

$$\int_a^{l_1} \mu_e \cdot e^{-\mu_e \cdot l_{fp}} \cdot d(l_{fp}) = \xi_1 \quad (5.2.3)$$

with $a = 0$

$$1 - e^{-\mu_e \cdot l_1} = \xi_1 \quad (5.2.4)$$

Finally,

$$l_1 = -\frac{\ln(1 - \xi_1)}{\mu_e} \quad (5.2.5)$$

However, as $(1 - \xi_1) = \xi_1$ for random numbers uniformly distributed between 0 and 1, it is deduced from Eq.5.2.5 that the free path length l_{fp} between two light-particle interactions is calculated from a sampled random number as:

$$l_{fp} = -\frac{\ln \xi}{\mu_e} \quad (5.2.6)$$

By knowing the distance l_{fp} and the initial direction of propagation, the next centre where the photon will interact with a particle can be calculated within the absolute coordinate system.

- *Determination of a scattering or absorption event at each light–particle interaction:*

At each interaction light-particle the photon is either absorbed or scattered. A random number is drawn to decide for this event, by comparison with the albedo. As previously described in Eq.4.1.8, the albedo A corresponds to the ratio between the scattering coefficient and the extinction coefficient and is thus, comprised between 0 and 1. If the random number generated, ξ , is inferior than A , scattering occurs. If on the contrary ξ is superior than A , absorption occurs and the photon stop its journey and a new photon is generated from the light source.

- *Determination of the new direction of propagation after a Scattering event:*

When a scattering event is assumed to occur a new direction of photon propagation must be specified. The direction of photon propagation before a scattering is define by the vector \vec{S}' and with the angles Θ_i and Φ_i within the absolute coordinate system (XYZ). The direction of propagation after a scattering event is define by the vector \vec{S} and with the angles Θ_f and Φ_f within the absolute coordinate system (XYZ). The transformation from \vec{S}' to \vec{S} is performed using the polar and azimuthal scattering angles θ_s and φ_s defined within a local coordinate system (UVW). such transformation is illustrated in Fig.5.3 and mathematically expressed as:

$$\begin{pmatrix} S_x \\ S_y \\ S_z \end{pmatrix} = \begin{bmatrix} \frac{S'_x S'_z}{(1-S_z'^2)^{1/2}} & -\frac{S'_y}{(1-S_z'^2)^{1/2}} & S'_x \\ \frac{S'_y S'_z}{(1-S_z'^2)^{1/2}} & -\frac{S'_x}{(1-S_z'^2)^{1/2}} & S'_y \\ -(1-S_z'^2)^{1/2} & 0 & S'_z \end{bmatrix} \begin{pmatrix} \sin \theta_s \cos \varphi_s \\ \sin \theta_s \sin \varphi_s \\ \cos \varphi_s \end{pmatrix} \quad (5.2.7)$$

The scattering angles θ_s and φ_s are calculated from the scattering phase function. For the simple case of isotropic scattering, the scattering angles are calculated from random numbers ξ such as $\theta_s = \cos^{-1}(2\xi - 1)$ and $\varphi_s = 2\pi\xi$.

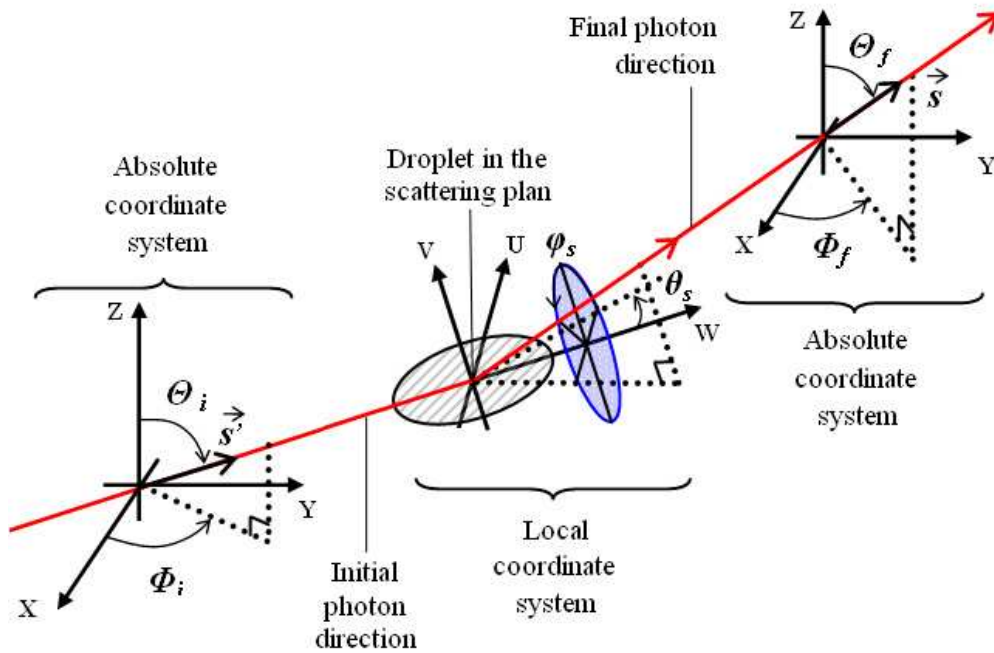


Figure 5.3: Trajectory of a photon scattered by a droplet.

For spherical spray droplets, the scattering process is derived from the LMT (see section 4.2.1). The change in polar angle θ_s is then determined from its inverse cumulative probability density function such as $\theta_s = CPDF^{-1}\xi$. The $CPDF(\theta_s)$ is calculated by integrating the scattering phase function $f(\theta_s)$ over the solid angle $d\Omega'$ between 0 and 4π .

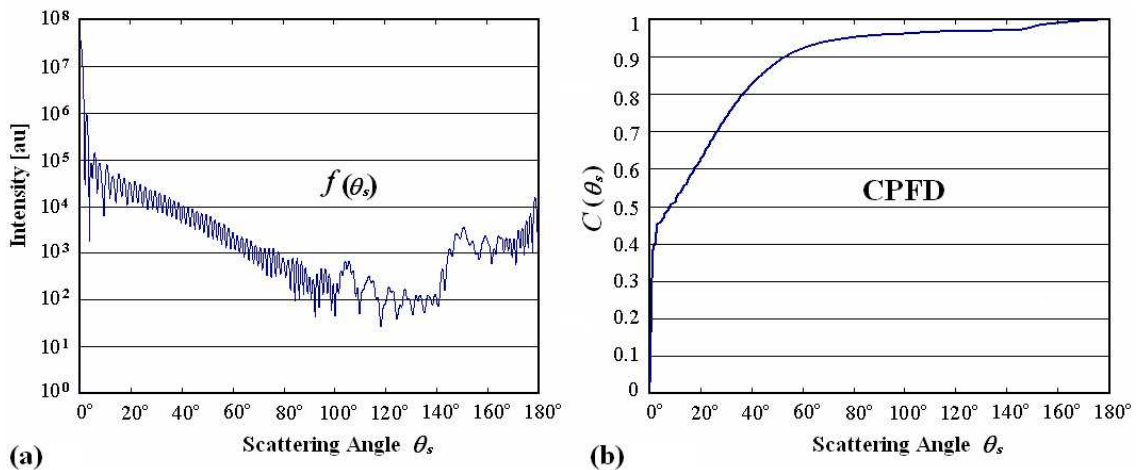


Figure 5.4: Scattering phase function (a) with the corresponding scattering CPDF (b) for a spherical $20\ \mu\text{m}$ fuel droplet ($n = 1.4 + 0.0i$) lighted at 532 nm.

As the analytical form of the inverse CPDF is not available, the CPDF is stored in a look-up table and the inverse transformation is performed at each scattering event using a random number. An example of scattering CPDF is illustrated in Fig.5.4(b) with the

corresponding scattering phase function in Fig.5.4(a). The polar scattering angle is determined with 0.1° resolution. Due to the axis-symmetry of the Mie phase function, the azimuthal angle φ_s is deduced from $\varphi_s = 2\pi\xi$ as for isotropic scattering.

- *Termination of photons journey:*

When photons exit the simulated volume, their direction of propagation and position are known. If they match with the conditions of detection applied (photons must reach the desired area with an incidence angle less than the detection acceptance angle) they are recorded to disk with their own characteristics. Parameters as number of scattering event occurred, distance traveled, and photon time-of-flight are calculated for the selected photons. Note that photons can also be selected as a function of their scattering order and/or depending on the distance traveled within the scattering medium.

5.2.3 Classification of the MC codes

The complexity of the structure of a turbid medium has a direct bearing on the complexity of the MC model required for the simulation. Turbid media are characterized by the concentration of droplets (or other scattering particles), their distribution in space and by the number of different particle sizes or types present.

Five cases of turbid media are identified Table 5.1 depending on the homogeneity of droplet size (or particle type) and on their spatial distribution within the 3D. By definition, homogeneous media are described by a constant number density N of particles in every single point of the sample. Homogeneous media can be either monodisperse or polydisperse.

- *Homogeneous monodisperse scattering medium:*

This is the simplest case for MC simulation. As only one type of particle is considered, only a single scattering CPDF and a single extinction coefficient (defined by a single scattering and absorption cross-section) are required.

- *Homogeneous polydisperse scattering medium:*

If a homogeneous medium is polydisperse, the scattering CPDF used must be deduced from the phase function averaged over the total distribution of droplet sizes (see Eq.4.1.14).

Optical properties	Scattering turbid medium				
	Homogeneous		Inhomogeneous		
	Mono-disperse	Poly-disperse	Mono-disperse	Uniformly polydisperse	Poly-disperse
Single σ_e	×		×		
Single $\bar{\sigma}_e$		×		×	
Single CPDF from f	×		×		
Single CPDF from \bar{f}		×		×	
Single N	×	×			
Several σ_e or several $\bar{\sigma}_e$					×
Several CPDF from f or several CPDF from \bar{f}					×
Several N			×	×	×

MC code 1
MC code 2
MC code 3

Table 5.1: Scattering turbid media types and required optical properties.

The extinction coefficient is in this second case calculated from the average extinction cross-section. Homogeneous monodisperse and polydisperse media can be both simulated by an identical MC code (MC code 1).

When the number density of particles varies from place to place the medium becomes inhomogeneous. In this case, both the extinction coefficient and the scattering CPDF change with location. Working with an inhomogeneous structure requires the scattering medium to be decomposed into elementary volumes in which the optical properties are homogenous. In the presented model these elementary volumes are cubic cells of constant size (Fig.5.5). The size and the number of the cells are chosen based on the accuracy required and on the geometry of the medium. The path length between scattering events of a photon transferring from one cell to another is corrected proportionally to the ratio between the extinction coefficients of the “last cell” crossed and the extinction coefficient of the “new cell” encountered. If $\mu_e(\text{new cell}) < \mu_e(\text{last cell})$, the free path-length l is increased, and if on the contrary $\mu_e(\text{new cell}) > \mu_e(\text{last cell})$, l is decreased. Inhomogeneous media can be monodisperse, uniformly polydisperse or polydisperse.

- *Inhomogeneous monodisperse scattering medium:*

In inhomogeneous monodisperse media (only one size of droplet/particle present) the scattering process and hence the related CPDF is assumed identical in every cell. The

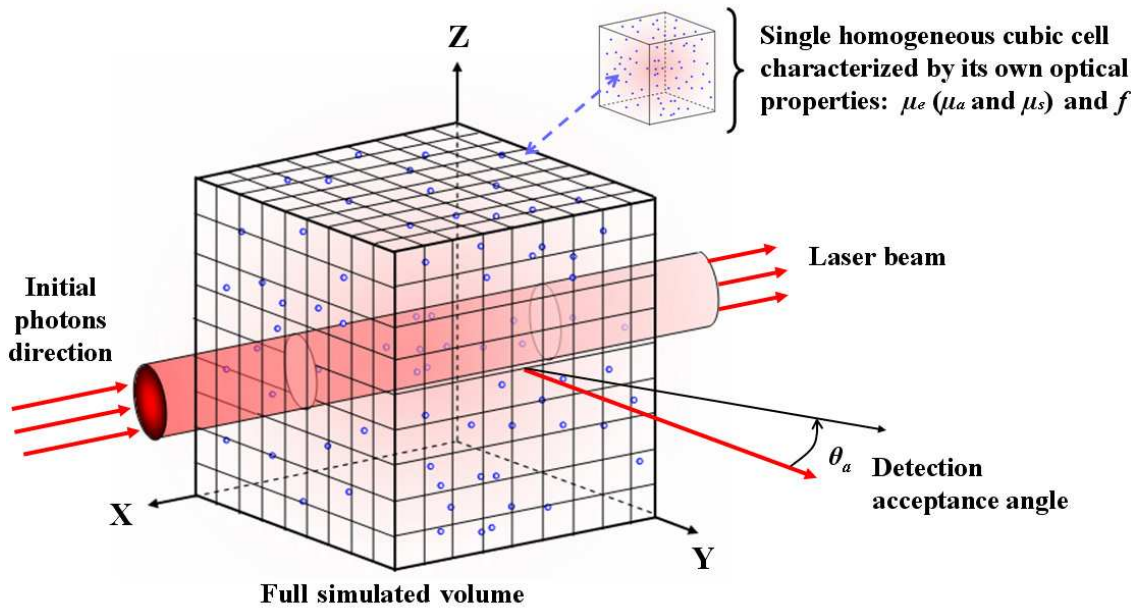


Figure 5.5: Simulation illustration of light propagation within an inhomogeneous polydisperse turbid medium.

variation of the extinction coefficient μ_e is simply related to the variation of the number density of scattering particles (the extinction cross-section is constant) and is introduced in each single cell.

- *Inhomogeneous uniformly polydisperse scattering medium:*

In uniformly polydisperse media the distribution of particle size is constant with location. The averaged scattering phase function and averaged extinction cross-section are both initially calculated in a same manner than for homogeneous polydisperse media. Once again only one scattering CPDF is used by the model and the variation of the scattering coefficient is taken into account using many elementary cubic cells. The same MC code can tackle both monodispersity and uniform polydispersity within inhomogeneous media (MC code 2).

- *Inhomogeneous polydisperse scattering medium:*

For inhomogeneous polydisperse media, both number density of droplets and droplet size distribution vary with location. The extinction cross-section and the scattering CPDF must therefore be defined in each cell (Fig.5.5). This constitutes the most complex scattering case. In the developed model 25 different scattering phase functions can be considered within a medium segregated into 100 X 100 X 100 cubic cells (MC code 3 - see Appendix D).

When a photon enters a cubic cell, the temporary length l traveled for crossing the cell, is calculated assuming that no scattering/absorbing event occurs. This length depends upon the initial direction of the photon, the coordinates of the entry point, and the dimension of the cell. Then, the probability of the photon to be scattered/absorbed along l is performed. If the distance of light-particle interaction is smaller than the temporary length, then, scattering (or absorption) occurs within the cell. If on the contrary, the distance of light-particle interaction is bigger than l , the tracked photon cross the cell without being scattered. Finally, the photon enters a new cell and the calculation process is repeated.

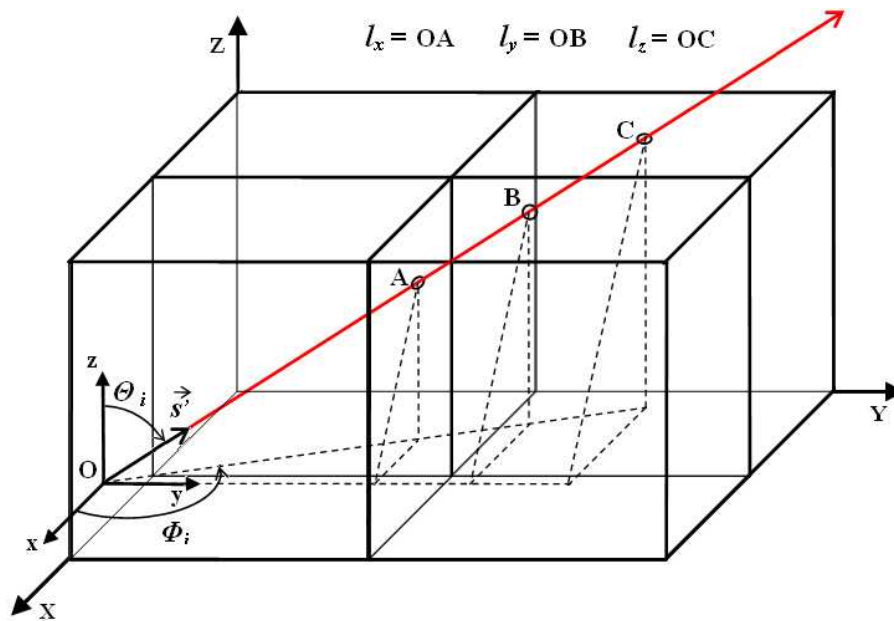


Figure 5.6: Determination of the temporary length l , for a photon crossing a single cubic cell, without being scattered. In the presented example, the photon exit the cell through a (xz) plan and l equals l_x (which is the smallest distance when compared to l_y and l_z).

The major problem in the determination of the temporary distance l , is to know on which face of the cubic cell the photon is supposed to exit. The technique employed in the presented model, consists in calculating the three distances l_x , l_y , and l_z corresponding to the respective distances traveled by the photon between its entry point to the local closest (xz), (yz) and (xy) plans encountered. Finally, the smallest l is found to be the correct length and the exit point is deduced. The scheme of the process is illustrated in Fig.5.6.

Verification and Validation of the Monte Carlo Model

THE comparison procedures against the analytical and experimental results present a crucial stage in the development of any computational models. Depending on the resultant divergences, a MC code can either be fully or partially validated.

In the first section, analytical calculations of scalar intensity for the double light scattering is compared to the MC results for a crossed source-detector geometry. In order to reach solvable analytical equations, isotropic scattering has been assumed within a homogeneous scattering volume.

In the second section, the scattering and multiple scattering of a 800 nm laser beam is investigated within diverse samples of known optical properties. Light intensity distributions are detected on the forward and side face of the sample cells using an Electron Multiplying CCD camera. Experimental and simulated images are compared for a range of different scattering phase functions, optical depths, and detection acceptance angles.

In the last section, polydispersity within inhomogeneous media is investigated. A method to estimate various scattering phase functions is suggested and verified. The capabilities of the technique to approximate the scattering process of any droplets from 2 up to 200 μm (when illuminated at 512 nm) is demonstrated by employing a series of 25 specific averaged scattering phase functions.

6.1 Comparison against analytical results

A theoretical study of laser radiation propagation within a turbid medium is presented and compared with the simulated MC results. A crossed source-detector geometry is used in this analysis in order to separate the the intensity of single scattering from higher scattering orders. The detection of the light intensity for low scattering orders (1st and 2nd orders) is described analytically considering the simplest case of isotropic scattering. The results demonstrate good agreement between analytical and MC techniques. Details of these results can be found in Meglinski *et al.* (2004) and Berrocal *et al.* (2004).

6.1.1 Analytical description of low scattering orders

As described in section 4.1.2 (see Fig.4.5), the intensity of optical radiation propagation in a randomly inhomogeneous scattering volume may be presented as a finite series of scattering orders. The convergence of this series depends on the mean square of the permittivity fluctuations and the characteristic size of the scattering medium. To separate these scattering terms from each other, we apply an idea originally suggested by Kuzmin *et al* (1994) in the study of critical phenomena and second order phase transition.

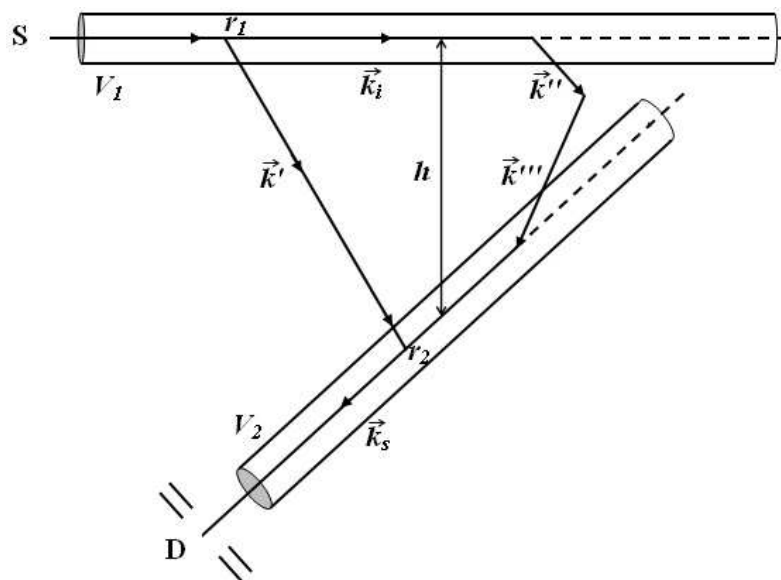


Figure 6.1: Crossed source-detector geometry used to account for low scattering orders.

Schematically, this idea is represented in Fig.6.1. The laser source, S, illuminates the medium with a thin cylindrical laser beam. Detector D is confined by series of small aperture diaphragms so that the detected radiation is localized in a cylindrical volume, V_2 , which is equal to the volume filled by incident the laser beam V_1 . In Fig.6.1, single

scattering occurs at the points r_1 and r_2 and the volumes are separated by a distance h . The vectors \vec{k}_i , \vec{k}' and \vec{k}_s are the wave-vectors of the incident, intermediate and detected double-scattered light, respectively. \vec{k}'' and \vec{k}''' are the intermediate wave vectors for the triple scattered light. If V_1 and V_2 do not intersect, photons must experience at least two scattering events in order to be detected. Similarly, for singly scattered photons to reach the detector, the volumes must intersect (i.e. h must be smaller than the cylinders diameter). When the characteristic diameter of the scattering volume, is much less than the distance to the observation point, the intensity of single scattering light, I_1 , takes the form (Kuzmin and Romanov 1996):

$$I_{(1)} = \frac{I_0 V}{r^2} \frac{k_0^4}{(4\pi)^2} \left(\delta_{\alpha\beta} - \frac{k_{s\alpha} k_{s\beta}}{k^2} \right)^2 G(\vec{q}) \cdot e^{-\mu_e(l_1+l_2)} \quad (6.1.1)$$

I_0 is the intensity of the incident light, r is the distance to the observation point, $k_0 = \omega/c$ where ω is the cycle frequency and c is the speed of light in a vacuum. The exponential multiplier describes attenuation along a path l_1 before and a path l_2 after the scattering event; $\vec{q} = \vec{k}_s - \vec{k}_i$ is the scattering wave vector and \vec{k}_i and \vec{k}_s are the wave vectors of the incident and scattered light, respectively. A factor $\left(\delta_{\alpha\beta} - \frac{k_{s\alpha} k_{s\beta}}{k^2} \right)^2$ accounts for the transverse nature of the scattered electromagnetic wave where α and β are the indices of polarization and $G(\vec{q})$ is the correlation function of the permittivity fluctuations.

The intensity of double scattering, I_2 , is described as:

$$I_{(2)} = \frac{I_0 k_0^8}{r^2 (4\pi)^4} \int_{V_1} dr_1 \int_{V_2} dr_2 F_{\alpha\beta}(\vec{k}_s, \vec{k}_i, \vec{k}') \frac{1}{|\vec{r}_2 - \vec{r}_1|^2} \cdot G(\vec{k}' - \vec{k}_i) \cdot G(\vec{k}_s - \vec{k}') \cdot e^{-\mu_e(l_1+l_2+|\vec{r}_2-\vec{r}_1|)} \quad (6.1.2)$$

where

$$F_{\alpha\beta}(\vec{k}_s, \vec{k}_i, \vec{k}') = \left(\delta_{\alpha\eta} - \frac{k'_\alpha k'_\eta}{k^2} \right) \left(\delta_{\alpha\nu} - \frac{k'_\alpha k'_\nu}{k^2} \right) \left(\delta_{\beta\eta} - \frac{k'_\beta k'_\eta}{k^2} \right) \left(\delta_{\beta\nu} - \frac{k'_\beta k'_\nu}{k^2} \right) \quad (6.1.3)$$

is the polarization factor, and V_1 is the illuminated volume while the scattered light is collected by the detector from the volume V_2 . Summation occurs over the indices (except α and β) when a quantity has more than one index. Equation 6.1.2 describes the intensity of doubly scattered light reaching the detector (i.e. singly scattered light entering volume V_2 and being scattered into the direction \vec{k}_s with a wave vector $\vec{k}_s - \vec{k}'$. Note, all first order scattering events occur in the volume V_1 with a wave-vector $\vec{k}_s - \vec{k}'$ where \vec{k}' is the intermediate wave-vector.

If \vec{k}_i and \vec{k}_s lie in the (xz) plane of the electromagnetic field (collinear vectors - $k_{iy}=k_{sy}=0$)

and if polarization vectors $\vec{e}_\alpha = \vec{e}_i = \vec{e}_\beta = \vec{e}_s = \vec{e}_s$, then in single scattering:

$$\left(\delta_{\alpha\beta} - \frac{k_{s\alpha} k_{s\beta}}{k^2} \right)^2 = 1 \quad (6.1.4)$$

and the double scattering polarization factor becomes:

$$F_{\alpha\beta}(\vec{k}_s, \vec{k}_i, \vec{k}') = \left(1 - \frac{k_y^2}{k^2} \right)^2 \quad (6.1.5)$$

The comparison of the single and the double light scattering permits us to extract information about the scattering media. To illustrate this, let consider a weakly scattering medium of spherical particles with the correlation function, $G(\vec{q})$, described by the Rayleigh-Gans approximation formula:

$$G(\vec{q}) = N \left(\frac{4\pi\Delta\varepsilon}{q^3} [\sin(qD) - qD \cos(qD)] \right)^2 \quad (6.1.6)$$

where N is the number density, $\Delta\varepsilon$ is the difference of permittivities between the particles and the the host medium and D is the particle diameter. If the diameter of the particle is less than the wavelength of incident radiation, $G(\vec{q})$ are described as:

$$G(\vec{q}) \approx \left(\frac{2\pi\Delta\varepsilon}{3} \right) D^6 N \quad (6.1.7)$$

Hence, using the relations presented in Eq.6.1.4, Eq.6.1.5 and Eq.6.1.7, the intensities of single and double light scattering can be respectively approximated to:

$$I_{(1)} = \frac{I_0 V}{r^2} k_0^4 \left(\frac{\Delta\varepsilon}{6} \right)^2 D^6 N \cdot e^{-\mu_e(l_1+l_2)} \quad (6.1.8)$$

and

$$I_{(2)} = \frac{I_0 k_0^8}{r^2} \left(\frac{\Delta\varepsilon}{6} \right)^4 \int_{V_1} dr_1 \int_{V_2} dr_2 \frac{1}{|\vec{r}_2 - \vec{r}_1|^2} \cdot \frac{k_y'^2}{k^2} \left(1 - \frac{k_y'^2}{k^2} - \frac{(\vec{k}_s \vec{k}')^2}{k^4} \right) \cdot D^1 2N^2 \cdot e^{-\mu_e(l_1+l_2+|\vec{r}_2-\vec{r}_1|)} \quad (6.1.9)$$

From the two last equations, it can be easily seen that the ratio $I_{(2)}/I_{(1)}$ depends on the factor $(\Delta\varepsilon)^2 D^6 N$. This factor provides a description of the optical properties of the medium. Thus, the ratio of measured $I_{(2)}$ and $I_{(1)}$ gives the values of the optical parameters of the medium. However, to ensure reliable results, higher orders of scattering should be taken into account. The evaluation of analytical expressions for the scattering orders $I_{(3)}$, $I_{(4)}$, $I_{(5)}$, etc is an extraordinary complex mathematical problem requiring the calculation of

multi-fold integrals. A simplified form of $I_{(2)}$ is given below:

$$I_{(2)} = C \int_{-L_1/2}^{L_1/2} dl_1 \int_{-L_2/2}^{L_2/2} dl_2 \int_0^{R_1} r_1 dr_1 \int_0^{R_2} r_2 dr_2 \int_0^{2\pi} d\Phi_1 \int_0^{2\pi} d\Phi_2 \cdot \frac{1}{|\vec{r}_2 - \vec{r}_1|^2} \cdot e^{-\mu_e(l_1+l_2+|\vec{r}_2-\vec{r}_1|)} \quad (6.1.10)$$

where C is a constant, L_1, L_2 are the lengths and R_1, R_2 the radius of the respective cylinders V_1 and V_2 . The cylinder V_1 is directed along the Z axis and the V_2 along the X axis. It is seen that the double scattering intensity calculation requires cumbersome computation of the six-fold integral (Eq.6.1.10) whereas $I_{(3)}$ requires calculation of a nine-fold integral, $I_{(4)}$ a twelve-fold integral and so on. To avoid these complex calculations, the numerical MC technique is employed to calculate the higher-order scattering terms.

6.1.2 Description of the MC simulation

The MC scheme presented here is suitable for the geometry described in Fig.6.1 and possesses the following characteristics. The scattering volume is defined by a cube of $L = L_1 = L_2 = 50$ mm in a 3D coordinate system. The medium is assumed non-absorbing, and homogeneous. The source S is defined by a cylindrical laser beam of 1 mm diameter (i.e. $R_1 = R_2 = 0.5$ mm) which enters through a face of the sampling cube with an angle, β , corresponding to the source-detector angle. This angle, β , ranges between 0° (forward scattering detection) and 180° (back scattering detection) so that the laser beam always passes through the central point, O , of the cube, illuminating a cylindrical volume, V_1 , through the scattering medium (Fig.6.2). The detector, D, is represented by a square aperture of 1 mm located on the top face of the cube and positioned at different distances h from the central vertical axis of the cube. For simplicity, the cylindrical, volume V_2 , described in section 6.1.1 is assumed in the simulation as a long rectangular cuboid (see Fig.6.2). The scattering coefficient, μ_s , ranges between 0.04 and 0.18 mm^{-1} . In the presented geometry, this range allows the transition from single to multiple scattering to be investigated in the given geometry with an optical depth between $2 \leq OD \leq 9$.

Isotropic scattering is considered in the MC simulation. In this case, the number of considered parameters is reduced and θ_s is obtained from $\cos(\theta_s) = (2\xi - 1)$ and φ_s is obtained from $\varphi_s = 2\pi\xi$ where ξ is a random number uniformly distributed between 0 and 1.

Photon packets are assumed to have been detected if they reach the detector, D, with an incident angle θ_i less than detector acceptance angle θ_a ($\theta_i < \theta_a$). We will note this

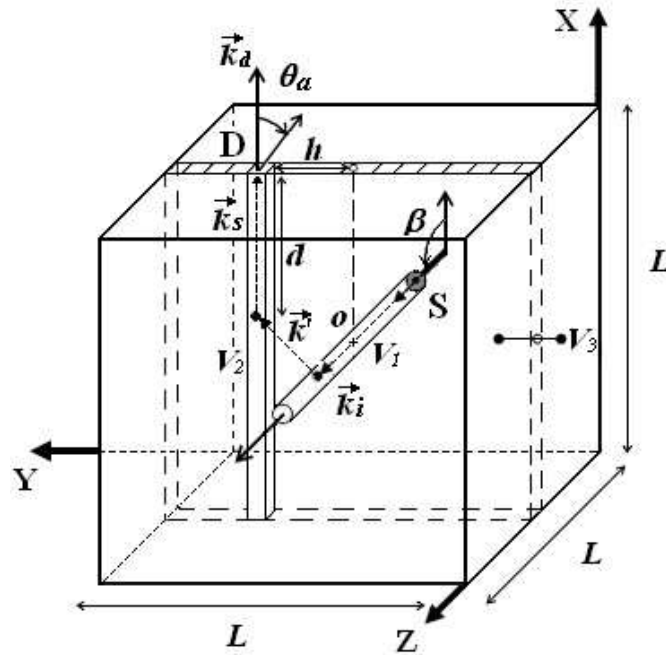


Figure 6.2: Computational geometry: The scattering volume is a cube of $L = 50$ mm defined in a 3D coordinate system. One of the corners of the cube corresponds to the (XYZ) frame.

approach as the “*standard MC*” scheme. If the detector acceptance angle is very small ($\theta_a < 2^\circ$), the number of photon packets detected is low and the data shows strong statistical fluctuations. To obtain less noisy results for the small acceptance angle ($\theta_a \sim 2$), a “*semi-analytical MC*” scheme is used. This scheme employs the probability, W , that the scattered photon packet strikes the detector at normal incidence:

$$W = f(\vec{k}_d - \vec{k}') \Omega_d e^{\mu_e d} \quad (6.1.11)$$

Here, \vec{k}_d is the normal vector towards the detector, Ω_d is the elementary solid angle spanning a line normal to the detector and d is the distance between the photon scattering event and detector. $f(\vec{k}_d - \vec{k}')$ is the scattering phase function, constant for isotropic scattering: $f(\vec{k}_d - \vec{k}') = 1/4\pi$. Thus the total intensity of the scattering orders is obtained by calculation of the probability for all scattering events occurring within the volume V_3 (see Fig.6.2). This approach significantly reduces the computational time required for a given noise level (by a factor of ~ 100) and allows accurate comparisons between the MC and the analytical approach.

6.1.3 Comparison and discussion

MC results and analytical calculations of I_2 are presented as a function of the distance h in Fig.6.3. The black circles represent the results of the standard MC when considering an acceptance angle of 2° . The white circles represent the results of the semi-analytical MC simulation assuming $\theta_a = 0^\circ$. The solid line corresponds to the exact analytical calculation described in Eq.6.1.10. The scattering coefficient is fixed to $\mu_s = 0.04 \text{ mm}^{-1}$ ($OD = 2$). It is seen from Fig.6.3, that the analytical results agree well with the MC results, especially those described by the semi-analytical MC scheme. As the standard MC simulation assumes a detection acceptance angle bigger than 0° , the amount of intensity detected is globally found to be higher than when calculated from the other two methods. It is also seen that the semi-analytical MC method offers better statistics than the standard one. The distance h ranges, here, from 0 to 25 mm.

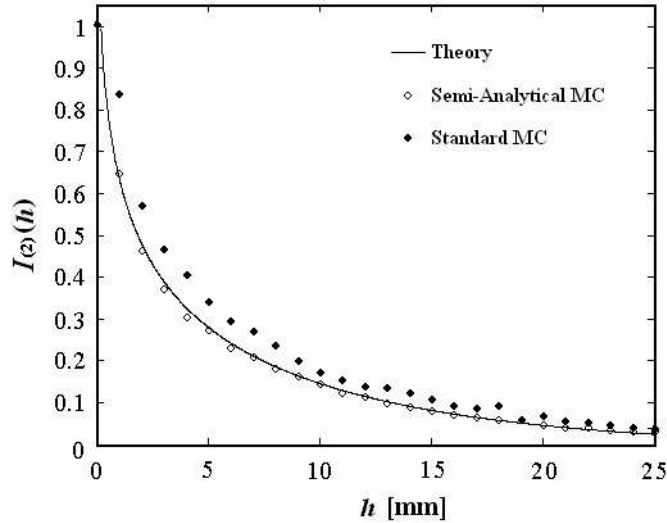


Figure 6.3: Double light scattering intensity I_2 with respect to the distance h between V_1 and V_2 . Isotropic scattering is assumed with $OD = 2$.

As decreasing $I_2(h)$ is important for small h , accurate calculations have been performed in the range $0 < h < 5$ mm using the semi-analytical MC scheme and the analytical approach. Results of $I_2(h)$ are presented in Fig.6.4 for $\mu_s = 0.04 \text{ mm}^{-1}$ in (a) and $\mu_s = 0.16 \text{ mm}^{-1}$ in (b). To calculate the intensity of double scattering by Eq.6.1.10, the cylindrical coordinate frames (l_1, r_1, Φ_1) and (l_2, r_2, Φ_2) is introduced:

$$\vec{r}_1 = (r_1 \cos \Phi_1, r_1 \sin \Phi_1, l_1) \quad (6.1.12)$$

$$\vec{r}_2 = (l_2, h + r_2 \cos \Phi_2, r_2 \sin \Phi_2) \quad (6.1.13)$$

If $h \gg R_1$ and R_2 , and the source-detector angle $\beta = 90^\circ$, Eq.6.1.10 is significantly

simplified and can be written as:

$$I_{(2)}(h) = A\pi^2 R_1^2 R_2^2 \int_{-L_1/2}^{L_1/2} dx \int_{-L_2/2}^{L_2/2} dz \frac{1}{x^2 + z^2 + h^2} \cdot e^{[-\mu_e(L+z-x+(x^2+z^2+h^2))^{1/2}]} \quad (6.1.14)$$

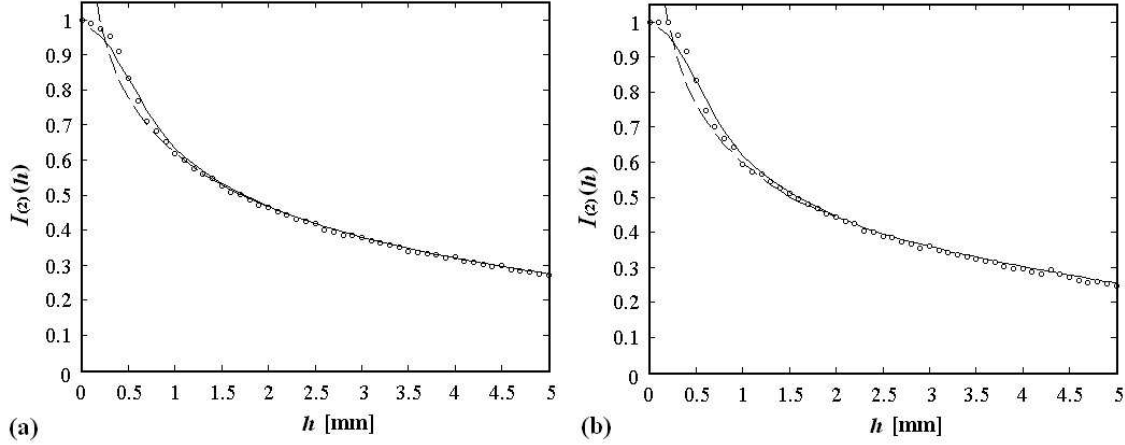


Figure 6.4: Double light scattering intensity $I_{(2)}$ with respect to the distance h between V_1 and V_2 . Isotropic scattering is assumed with $OD = 2$ in (a) whereas $OD = 8$ in (b). The solid curve represents the results of calculation using the exact Eq.6.1.10, the dotted curve using the approximation Eq.6.1.14 and (\circ) are the results of the semi-analytical MC scheme.

For low scattering in the medium ($OD = 2$), the MC results and analytical calculation agree reasonably well (see Fig.6.4(a)). Similar agreement is obtained for higher scattering in the medium ($OD = 8$) especially at $h > 2$ mm (see Fig.6.4(b)).

The agreement is not complete as the analytical results neglect scattering orders higher than 2; whereas, the MC calculations consider these higher orders. The dashed lines show the analytical calculation results with the approximate form of $I_{(2)}$ as described Eq.6.1.14. This equation reduces to $I_{(2)}(h) \sim |\ln(h)|$ for $h \rightarrow 0$ and predicts that the intensity of scattering tends to infinity. The discrepancy between the exact Eq.6.1.10 (solid line in Fig.6.4) and approximate Eq.6.1.14 formulas begins at $h = 1.2$ mm; this is close to the diameter of the cylinders.

Analytical expressions for higher scattering orders (i.e. $I_{(3)}$, $I_{(4)}$, etc.) differ from the expressions for $I_{(1)}$, $I_{(2)}$ (see Eqs. 6.1.1 and 6.1.2) and involve multi-order integrals. This is due to the presence of intermediate integration over the total scattering volume. However, using the MC technique, it is possible to evaluate these higher scattering orders. The 3rd, 4th, 5th and 10th scattering orders calculated by the MC technique are presented in Fig.6.5 for the low scattering medium ($OD = 2$). The intensity of second order, $I_{(2)}(h)$, is also included for comparison. All the calculated intensities are normalized to the value of the single light scattering intensity $I_{(1)}$ at $h = 0$ (where $I_{(1)}$ dominates all other scattering

orders). It is worth mentioning that the high-order integrals (for $n > 3$) do not possess a logarithmic singularity as predicted by Eq.6.1.14, and return smooth functions of h (see Fig.6.5).

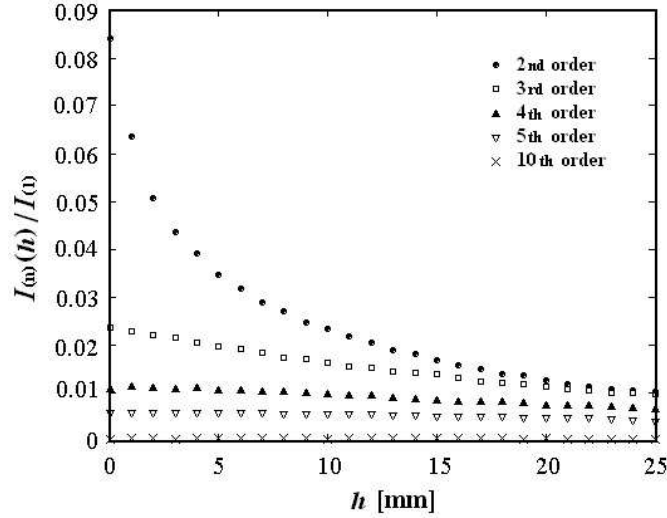


Figure 6.5: Intensity of various scattering orders I_n as a function of h . The intensity of each scattering order is normalized to the intensity of single scattering at $h = 0$. Isotropic scattering is assumed with $OD = 2$.

The intensity of the higher scattering orders falls with increasing the distance h . When varying h from 0 to 25 mm, $I_{(3)}$ decreases by 2.5, $I_{(4)}$ decreases by 1.4, $I_{(5)}$ decreases by 1.1, and $I_{(10)}$ remains equal to zero due to the low optical depth of the medium. For comparison, $I_{(2)}$ is reduced by a factor of 9 in the same interval.

A good agreement between the analytical and MC technique is demonstrated for the study of the double light scattering. Both analytical and MC calculations show a strong logarithmic dependence of $I_{(2)}$ with the distance h between the illuminating and the collecting volumes. This logarithmic dependence is weaker on higher scattering orders and can be considered constant when compared with the single scattering order.

To conclude, the MC model is verified for the simple case of isotropic scattering within a homogeneous volume. Such results validate the use of the MC code for the study of more complex cases where the analytical method does not provide solvable equations. An investigation involving anisotropic scattering processes and larger detection acceptance angles is given in section 7.2.3 for the same crossed source-detector geometry presented in Fig.6.2.

6.2 Comparison against experimental results

In this section, the results of the MC simulations are experimentally validated by using several homogeneous sample cells containing a solution of monodisperse polystyrene spheres in distilled water. Various particle sizes and concentrations are considered such that the complete scattering process resulting from each sample remains comparable with that occurring either in the dilute or dense spray region. The two-dimensional distributions of light intensity is recorded experimentally and calculated from the simulation for both the side and forward scattering. The influence of the size and the concentration of spheres on the entirety of the resultant scattering process is shown. Furthermore, the effects of the detection acceptance angle on the detected images are demonstrated.

6.2.1 Experimental setup and MC simulation description

- *Experimental setup* :

The experiment is based on the transmission of a laser beam through a homogeneous monodisperse scattering medium of known optical properties and the detection of the intensity profiles of the scattered light. The incident laser light is produced by a Spectra-Physics Tsunami Ti:Sapphire mode-locked laser. Light pulses with ~ 80 fs duration (FWHM ~ 11 nm centered at ~ 800 nm) and 10 nJ energy were transmitted through a 10 mm X 10 mm X 45 mm optical glass cell containing a suspension of polystyrene spheres immersed in distilled water. Several solutions are prepared by varying the concentration and the size of the polystyrene spheres.

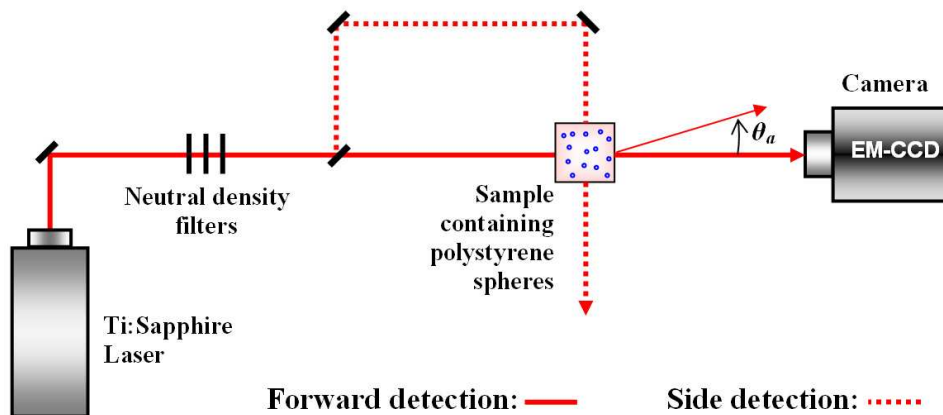


Figure 6.6: Experimental configuration. Two optical paths are independently considered for both forward and side detection.

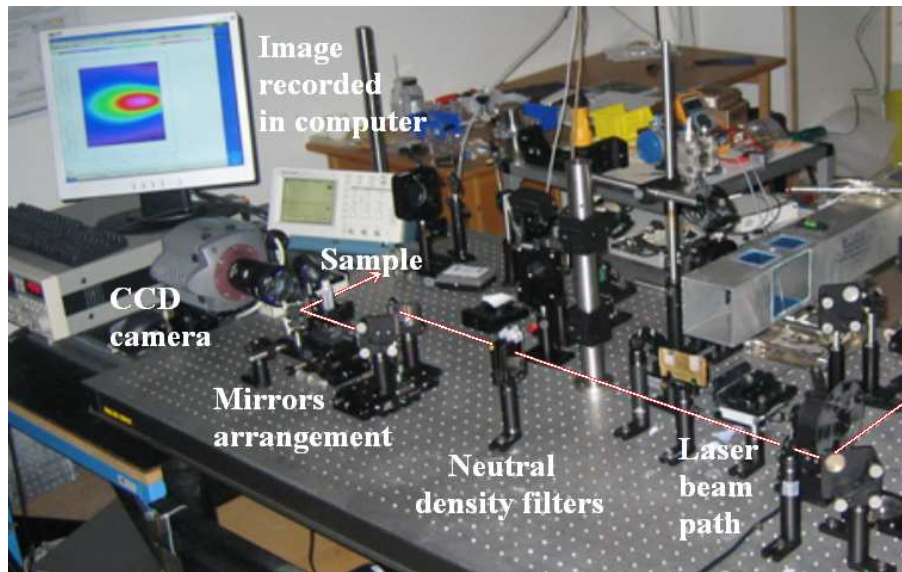


Figure 6.7: Picture of the experimental setup.

The number density of spheres in each cell was adjusted to provide optical depths of 2, 5 and 10 for two cases of sphere diameter, D , equal to $1\ \mu\text{m}$, $2\ \mu\text{m}$, $5\ \mu\text{m}$ and $20\ \mu\text{m}$. The initial concentrations of polystyrene spheres were diluted with distilled water. The calculations of these dilutions are summarized for 5 ml of final solution in Table 6.1. The value of the optical depth was verified from the Beer-Lambert law by measuring the transmission of the incident light for each sample with a photodiode and a lock-in amplifier. A smaller cell (5 mm wide instead of 10 mm) was employed in order to check the concentration of polystyrene spheres at the highest optical depth, corresponding to $OD = 10$ (the concentration of particles for $OD = 10$ in a 10 mm cell equals that of $OD = 5$ in a 5 mm cell). The attenuation measurements confirmed the correct concentration of polystyrene spheres for each sample with a maximum error of $\pm 5\%$.

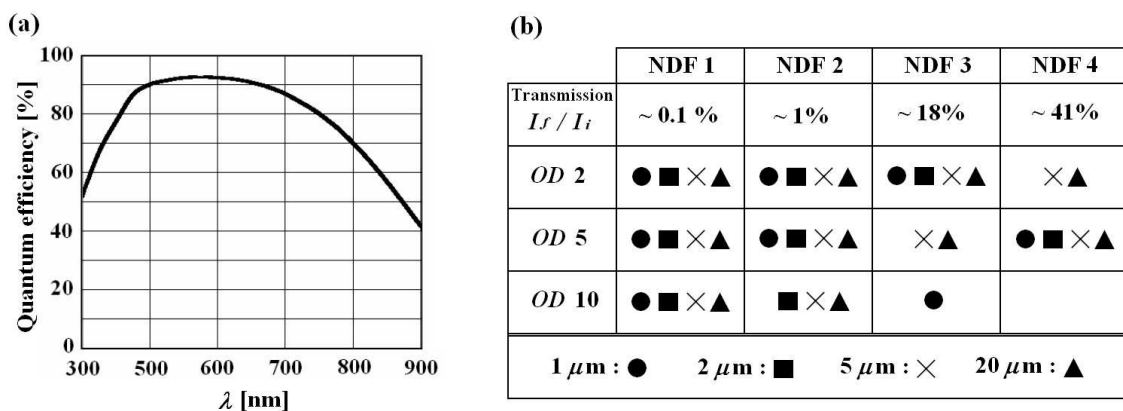


Figure 6.8: (a) Quantum efficiency for the iXon DV887 camera at -20° thermoelectric cooling. For $\lambda = 800\ \text{nm}$, 70% of quantum efficiency is reached. (b) Association of the neutral density filters at each optical depth for forward detection.

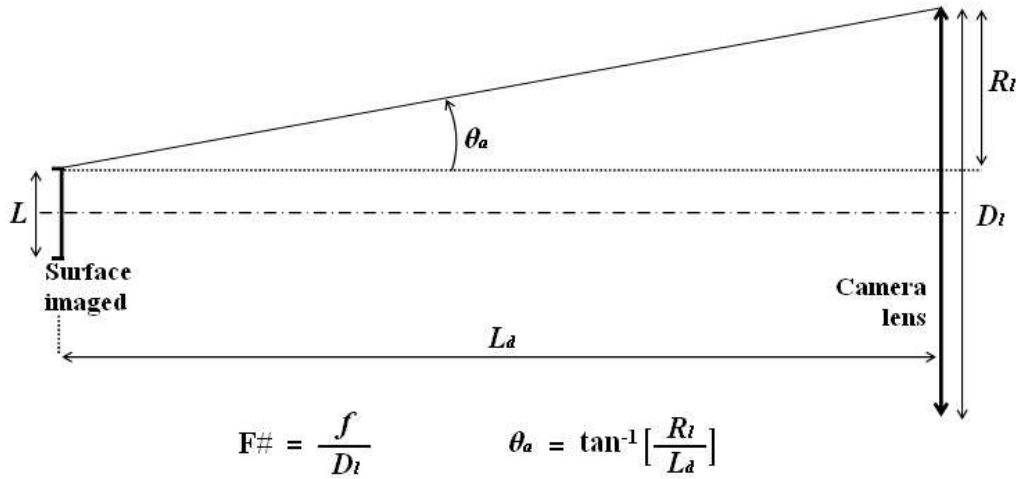
D [μm]	Initial N of spheres	σ_e [cm^{-1}]	Length [cm]	OD [au]	μ_e [cm^{-1}]	Final N of spheres	Initial N Final N	Volume wanted [ml]	Volume to take [ml]	I initial I final
1.01	1.77E+11	1.33E-08	1	2	2	1.50E+08	1180.12	5	4.24E-03	0.1353353
1.95	2.35E+10	1.13E-07	1	2	2	1.76E+07	1335.06	5	3.75E-03	-
5.01	4.86E+07	4.83E-07	1	2	2	4.14E+06	11.74	5	4.26E-01	-
20.9	2.72E+06	6.25E-06	1	2	2	3.20E+05	8.50	5	5.88E-01	-
1.01	1.77E+11	1.33E-08	1	5	5	3.76E+08	472.05	5	1.06E-02	0.0067379
1.95	2.35E+10	1.13E-07	1	5	5	4.41E+07	534.02	5	9.36E-03	-
5.01	4.86E+07	4.83E-07	1	5	5	1.04E+07	4.69	5	1.06E+00	-
20.9	2.72E+06	6.25E-06	1	5	5	8.00E+05	3.40	5	1.47E+00	-
1.01	1.77E+11	1.33E-08	1	10	10	7.52E+08	236.02	5	2.12E-02	0.0000454
1.95	2.35E+10	1.13E-07	1	10	10	8.82E+07	267.01	5	1.87E-02	-
5.01	4.86E+07	4.83E-07	1	10	10	2.07E+07	2.35	5	2.13E+00	-
20.9	2.72E+06	6.25E-06	1	10	10	1.60E+06	1.70	5	2.94E+00	-

initial wanted deduced

Table 6.1: Characteristics of the initial solution of polystyrene spheres, and dilution with distilled water.

The light intensity scattered from the cell was detected using an Andor iXon DV887 Electron Multiplying CCD camera. This camera has single photon detection capability without an image intensifier due to its multiplication gain feature which can be varied from unity up a thousand. At 800 nm, the quantum efficiency reaches 70% when using thermoelectric cooling set to -20°C as seen in Fig.6.8 (a).

The intensity profiles of the scattered light were detected on both the front and side face of the cell. A 10 X 10 mm surface is imaged onto 200 X 200 CCD pixels, resulting in an image resolution of 50 μm . Two F/#'s, equal to 1.8 and 5.6 were successively employed. The focal distance, f , of the camera lens equals 10 cm. The distance, L_d , between the surface of the sample and the camera lens was equal to 15.2 cm. From these parameters, the detection acceptance angle of the collection optics is equal to $\theta_a = 8.5^\circ$ for F/# = 1.8 and $\theta_a = 1.5^\circ$ for F/# = 5.6 (as shown in Fig.6.9). Due to the high pulse repetition rate (82 MHz) and the long detection aperture time (0.015s), the laser source is perceived by the camera as a continuous laser source. For each measurement, 10 images were recorded and averaged. Both illustration and photograph of the experiment are shown in Fig.6.6 and Fig.7.2. For each measurement, an appropriate selection of several Neutral Density Filters (NDF) was used in order to detect the maximum number of photons on the CCD chip while avoiding saturation. Four NDF have been initially characterized. The



	L [cm]	f [cm]	L_d [cm]	D_l [cm]	R_l [cm]	θ_a [$^\circ$]
$F\# = 1.8$	1	10	15.2	5.555	2.277	~ 8.5
$F\# = 5.6$	1	10	15.2	1.786	0.393	~ 1.5

Figure 6.9: Determination of the detection acceptance angle θ_a of the collection optics for the two $F\#$ considered.

measurement of the transmission for each NDF is approximated in the table presented in Fig.6.8 (b) with the selection for each sample. The Full Width at Half Maximum (FWHM) of the initial laser beam intensity profile was measured along the vertical axis Z , at $X = 5$ mm and is found to be equal to $d_a = 2.55$ mm when $\theta_a = 8.5^\circ$ and $d_b = 2.61$ mm when $\theta_a = 1.5^\circ$.

- *MC Simulation:*

In the simulation, the laser wavelength is assumed to be monochromatic and equal to 800 nm. The dimensions of the experimental cell are assumed by considering a cubic volume of 10 mm length. The intensity profile of the source, S , is modeled from the experimental matrix of the incident laser beam as illustrated in Fig.6.10. This matrix is obtained from the EM-CCD camera by imaging the surface of a cell containing only distilled water (without polystyrene spheres). Using this technique, the exact experimental source is considered and any irregularity in the laser beam profile is accounted for within the modelling, allowing a more realistic MC simulation. Computed photons are recorded at the exit position, provided detection conditions are met. This implies that the angle

between the vector normal to the detection face (front face or side face) and the vector direction of the photons must be within the acceptance angle, θ_a (see Fig. 3).

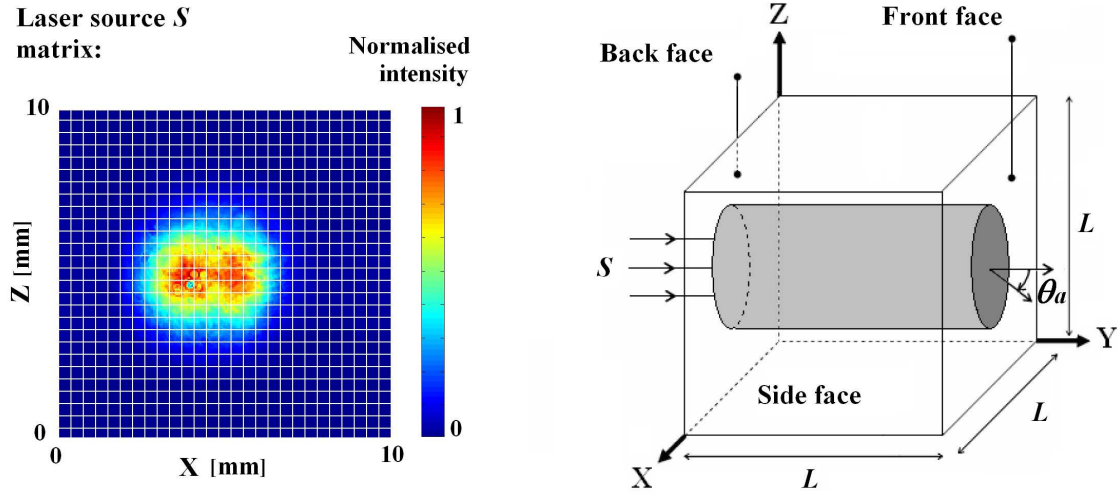


Figure 6.10: Simulation configuration: The laser source S is modeled from the experimental image matrix (200 X 200 pixels). Photons are sent from S into a scattering single cubic cell of $L = 10$ mm.

According to Ma *et al.* (2003), polystyrene spheres illuminated at 800 nm have a refractive index of $n = 1.578 - 0.0007i$ (see Fig.B.1 in Appendix A). The wavelength dependence of the real part of the refractive index n_r is expressed by the Cauchy dispersion relation (Matheson and Saunderson 1952 and Nikolov and Ivanov 2000):

$$n_r(\lambda) = A + \frac{B}{\lambda^2} + \frac{C}{\lambda^4} \quad (6.2.1)$$

Based on a least-squares fit of experimental results (see fig. B.1), Ma *et al.* found each coefficient equal to: $A=1.5725$, $B=0.0031080$ and $C=0.00034779$. Due to the negligible part of the absorbing component when comparing to the scattering component (the albedo Λ tends to 1), the spheres have been assumed non-absorbing in the model, with $n = 1.578 + 0.0i$. The refractive index of the surrounding medium is for distilled water: $n = 1.33 + 0.0i$.

The resulting Lorenz-Mie phase functions used in the model for $D = 1 \mu\text{m}$, $D = 2 \mu\text{m}$, $D = 5 \mu\text{m}$ and $D = 20 \mu\text{m}$ are illustrated in section 8.1.3 Fig.8.12. For each simulation, 3 billions of photons are sent through the scattering medium and the resultant computational time is ~ 7.5 hours at optical depth $OD = 2$ and ~ 25 hours at $OD = 10$, when using a Intel(R) Core(TM) 2 CPU 6600 at 2.40 GHz processor. The relative speed of computation is then on the order of $9 \mu\text{s}/\text{photon}$ (at $OD = 2$) and $30 \mu\text{s}/\text{photon}$ (at $OD = 10$).

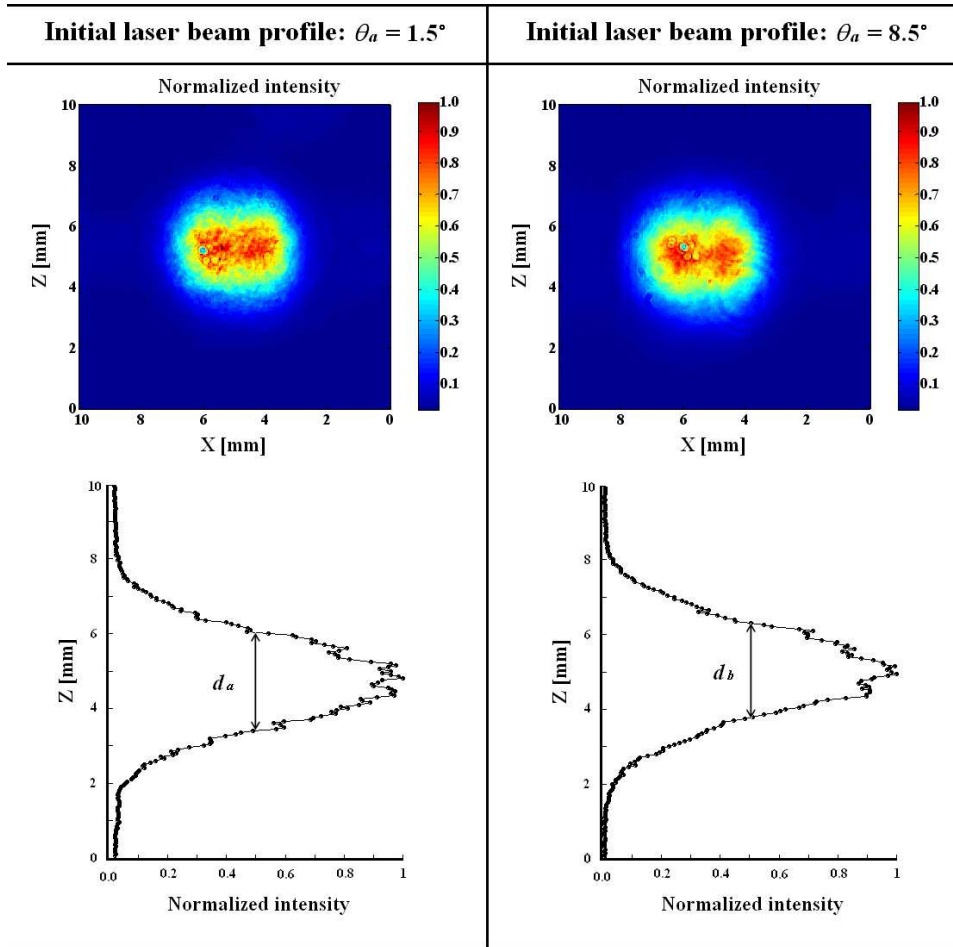


Figure 6.11: 2D initial intensity profiles of the laser beam imaged experimentally and implemented within the MC simulations for the two cases of detection acceptance angle 1.5° and 8.5° . The 1D profiles along the Z axis at $X = 5$ mm are also illustrated above the respective images. The corresponding FWHM are $d_a = 2.55$ mm for $\theta_a = 8.5^\circ$ and $d_b = 2.61$ mm for $\theta_a = 1.5^\circ$.

6.2.2 Forward scattering detection

The first set of comparisons shows the forward scattering detection with polystyrene spheres of $1 \mu\text{m}$ diameter. The 2D intensity distribution is shown on the front face for the large detection acceptance angle $\theta_a = 8.5^\circ$ in Fig.6.13. By increasing the optical depth from $OD = 2$ to $OD = 10$, the light intensity transmitted through the scattering sample is reduced and the laser beam profile diffuses. At $OD = 2$, the amount of light crossing the sample reaches a maximum value of 19% of the initial intensity. This result is found both experimentally and in the simulation. The Beer-Lambert law predicts a lower transmission of 13.5% in the same conditions. A such optical depth, the laser beam does not diffuse and its FWHM remains fairly constant. At $OD = 5$, the simulated results diverge smoothly from the experimental results (the maximum light transmission equals 2.2% experimentally against 2.8% for the simulation) and the differences with the

Beer-Lambert prediction ($I_f/I_i = 0.67\%$) becomes significant. It is also seen that the laser beam starts to diffuse and its FWHM is 1.28 times wider from its original value.

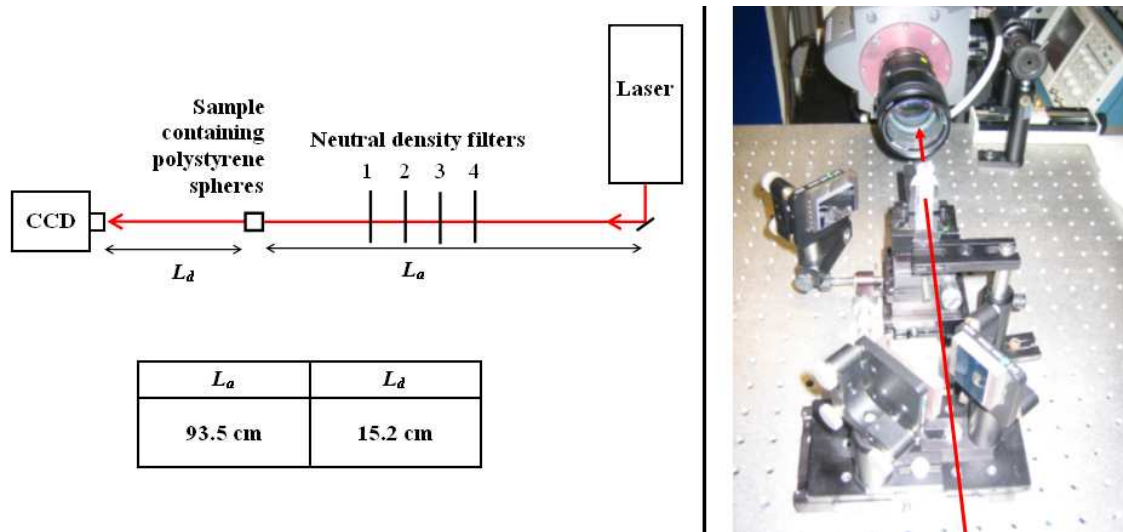


Figure 6.12: Experimental configuration for the forward scattering detection.

At $OD = 10$, the laser beam is now highly diffused with a FWHM equals to $1.85 d_a$. The maximum transmission corresponds to 0.18% experimentally, 0.52% with the simulation and the Beer-Lambert law predicts only 0.0045%. These results show the considerable divergences between the Beer-Lambert calculations, which neglect the effects of multiple scattering, and the results from both the experiment and from the MC simulation where a large detection acceptance angle is assumed.

By reducing the detection acceptance angle to $\theta_a = 1.5^\circ$, it is observed from Fig.6.14 that the detected light intensity reduces while the incident laser beam profile tends to diffuse less. At $OD = 2$, the maximum amount I_f/I_i of light intensity recorded is equal now to only 14% both experimentally and via simulation (the Beer-Lambert law predicts 13.5%). At $OD = 5$ this value is 1% experimentally and 0.75% with the simulation (the Beer-Lambert law predicts 0.67%). Finally, at $OD = 10$ the light transmission value is 0.027% experimentally and 0.025% with the simulation (the Beer-Lambert law predicts 0.67%). It is deduced that, for the small detection acceptance angle $\theta_a = 1.5^\circ$, the transmitted light intensity recorded becomes closer to the one from the Beer-Lambert law.

At $\theta_a = 1.5^\circ$ the laser beam tends, then, to keep its initial profile when increasing OD . The increase of the FWHM is observed only at $OD = 10$ and equals $1.61 d_b$. It is also apparent that at smaller detection acceptance angles, the number of photons detected is significantly reduced, resulting to a deterioration of the spatial resolution in the MC image.

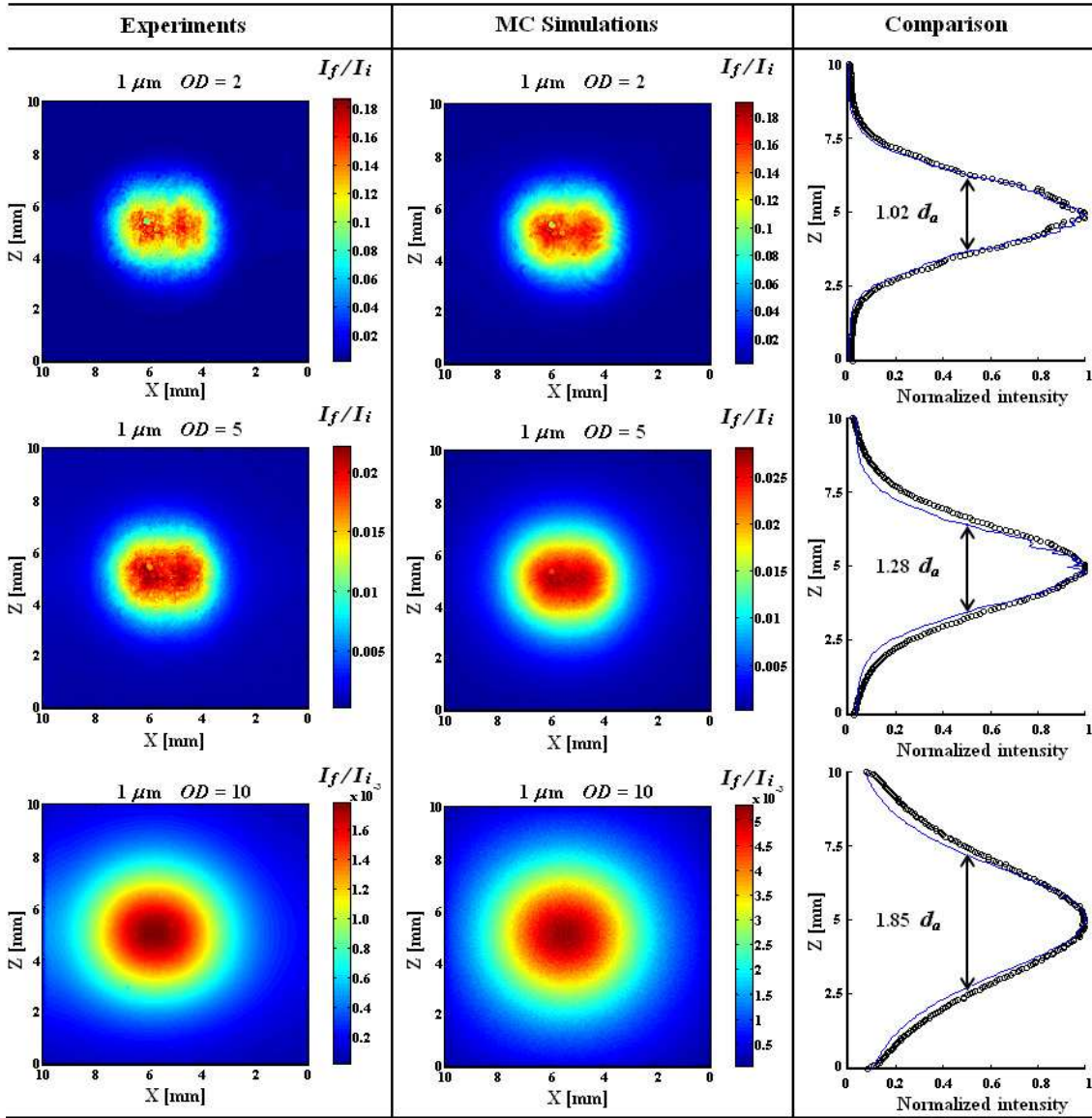


Figure 6.13: Comparison between the front face experimental and simulated images at detection acceptance angle $\theta_a = 8.5^\circ$. Solutions of 1 μm polystyrene spheres are considered at optical depths $OD = 2$, $OD = 5$ and $OD = 10$. The intensity scale of the images corresponds to the final light intensity, I_f , detected per pixel divided by the maximum value of the incident light intensity I_i . A comparison of the intensity profile along the vertical axis at $X = 5$ mm is also shown on the right side of the figure. The solid line corresponds to the experimental results and the circles are the results from simulation. Three billion of photons have been launched for the MC simulations.

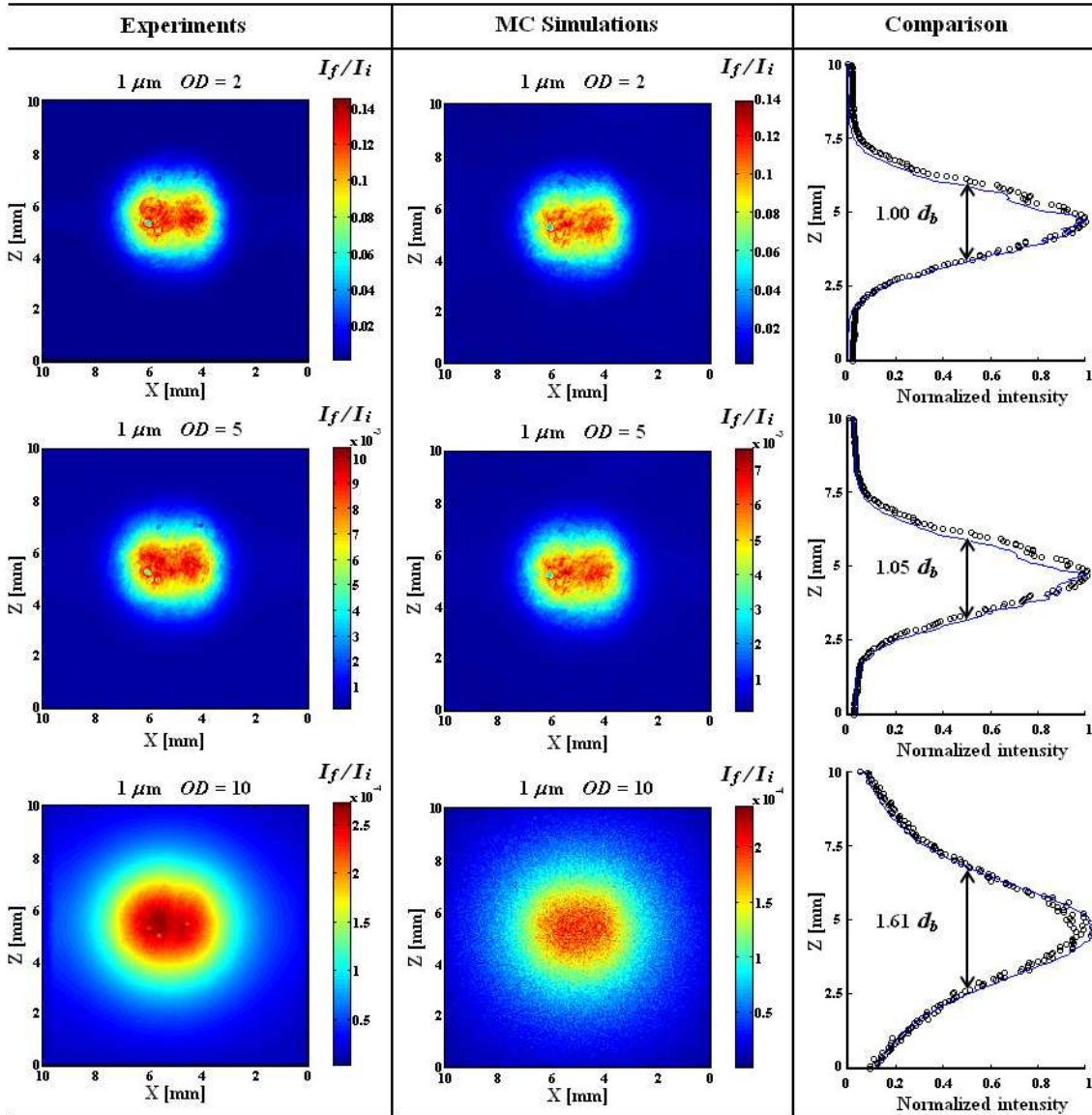


Figure 6.14: Comparison between the front face experimental and simulated images at detection acceptance angle $\theta_a = 1.5^\circ$. Solutions of 1 μm polystyrene spheres are considered at optical depths $OD = 2$, $OD = 5$ and $OD = 10$. The intensity scale of the images corresponds to the final light intensity, I_f , detected per pixel divided by the maximum value of the incident light intensity I_i . A comparison of the intensity profile along the vertical axis at $X = 5$ mm is also shown on the right side of the figure. The solid line corresponds to the experimental results and the circles are the results from simulation. Three billion of photons have been launched for the MC simulations.

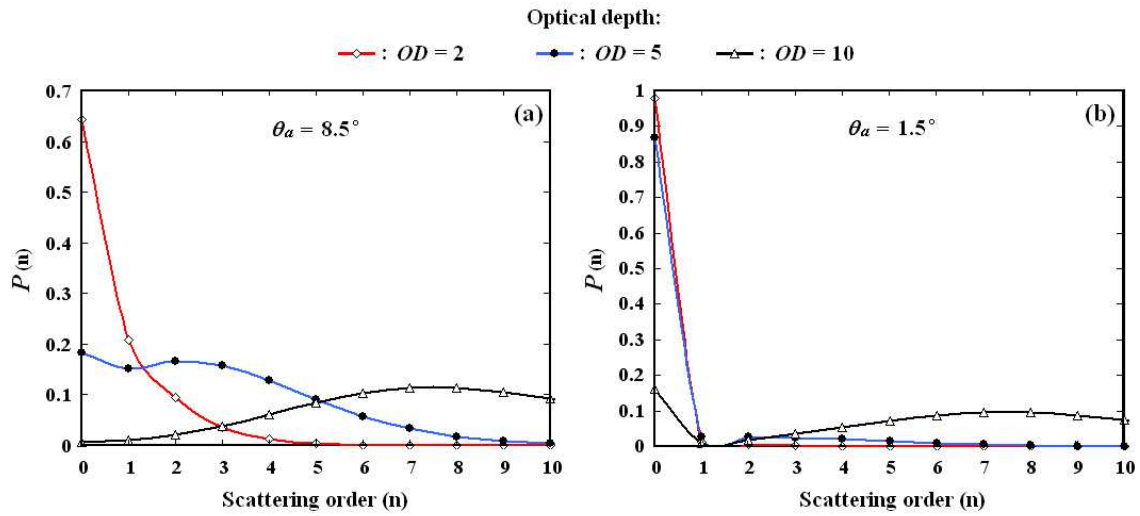


Figure 6.15: Distribution of the scattering orders at the various optical depths, for the polystyrene spheres of 1 μm diameter. All simulated photons exiting the scattering medium through the front face and within the indicated acceptance angle θ_a are recorded.

The amount of light intensity detected for each scattering order from $n = 0$ to $n = 10$ is plotted in Fig.6.15. At scattering order $n = 0$, photons cross the scattering sample without being scattered. This non-scattered light, generally termed ballistic light, corresponds to the ballistic photons which traverse the scattering medium without encountering any scattering or absorption events. The influence of the optical depth and of the detection acceptance angle on the contribution $P(0)$ of the ballistic photons can be observed by comparing Fig.6.15(a) and 6.15(b). At the acceptance angle $\theta_a = 8.5^\circ$ $P(0)$ equals 65%, 18% and 0,6% for the respective optical depths $OD = 2$, $OD = 5$ and $OD = 10$. By reducing the detection acceptance angle to $\theta_a = 1.5^\circ$, the amount of multiply scattered light detected is reduced and $P(0)$ increases significantly, reaching 98%, 87% and 16% (for $OD = 2$, $OD = 5$ and $OD = 10$ respectively). At the same time, the contribution of the high scattering orders ($n > 4$) increases smoothly with increasing OD while the contribution of the low scattering orders ($n < 3$) is reduced abruptly. These results demonstrate the divergence between the experimental/simulated results and the Beer-Lambert predictions at the large detection acceptance angle $\theta_a = 8.5^\circ$, and their agreement at the small angle $\theta_a = 1.5^\circ$ where the amount of ballistic light detected, $P(0)$, is closer to 100%.

The second set of comparisons is based on forward scattering detection with polystyrene spheres of 2 μm diameter. The intensity distribution profile is shown on the front face for the large detection acceptance angle $\theta_a = 8.5^\circ$ in Fig.6.16. At $OD = 2$ the light transmission reaches a maximum value of $\sim 30\%$. This is observed both experimentally and via simulation. At $OD = 5$, this maximum equals 6% experimentally and 7.5% via simulation. At $OD = 10$, I_f/I_i equals 0.7% experimentally and 1.7% via simulation.

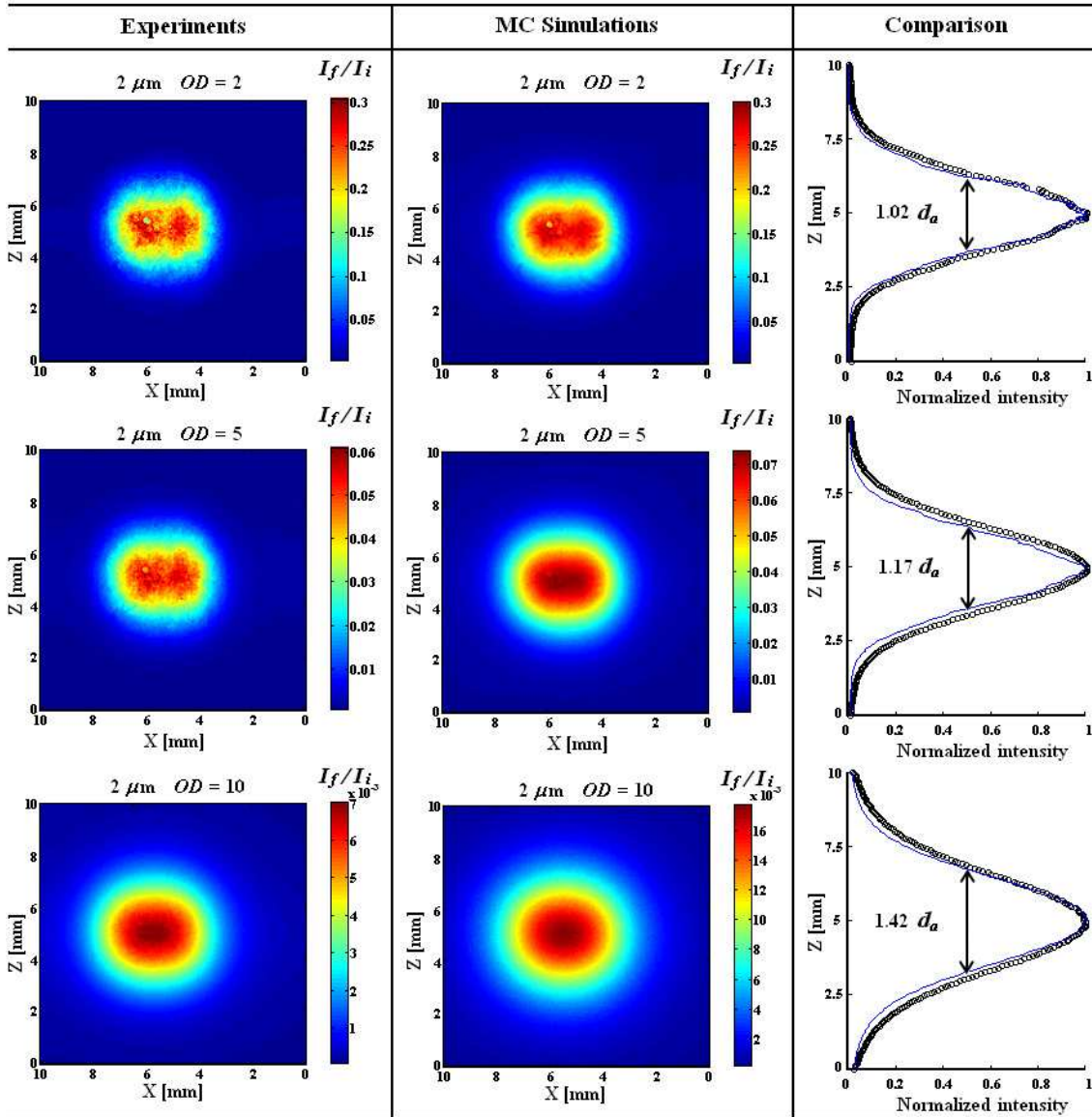


Figure 6.16: Comparison between the front face experimental and simulated images at detection acceptance angle $\theta_a = 8.5^\circ$. Solutions of 2 μm polystyrene spheres are considered at optical depths $OD = 2$, $OD = 5$ and $OD = 10$. The intensity scale of the images corresponds to the final light intensity, I_f , detected per pixel divided by the maximum value of the incident light intensity I_i . A comparison of the intensity profile along the vertical axis at $X = 5$ mm is also shown on the right side of the figure. The solid line corresponds to the experimental results and the circles are the results from simulation. Three billion of photons have been launched for the MC simulations.

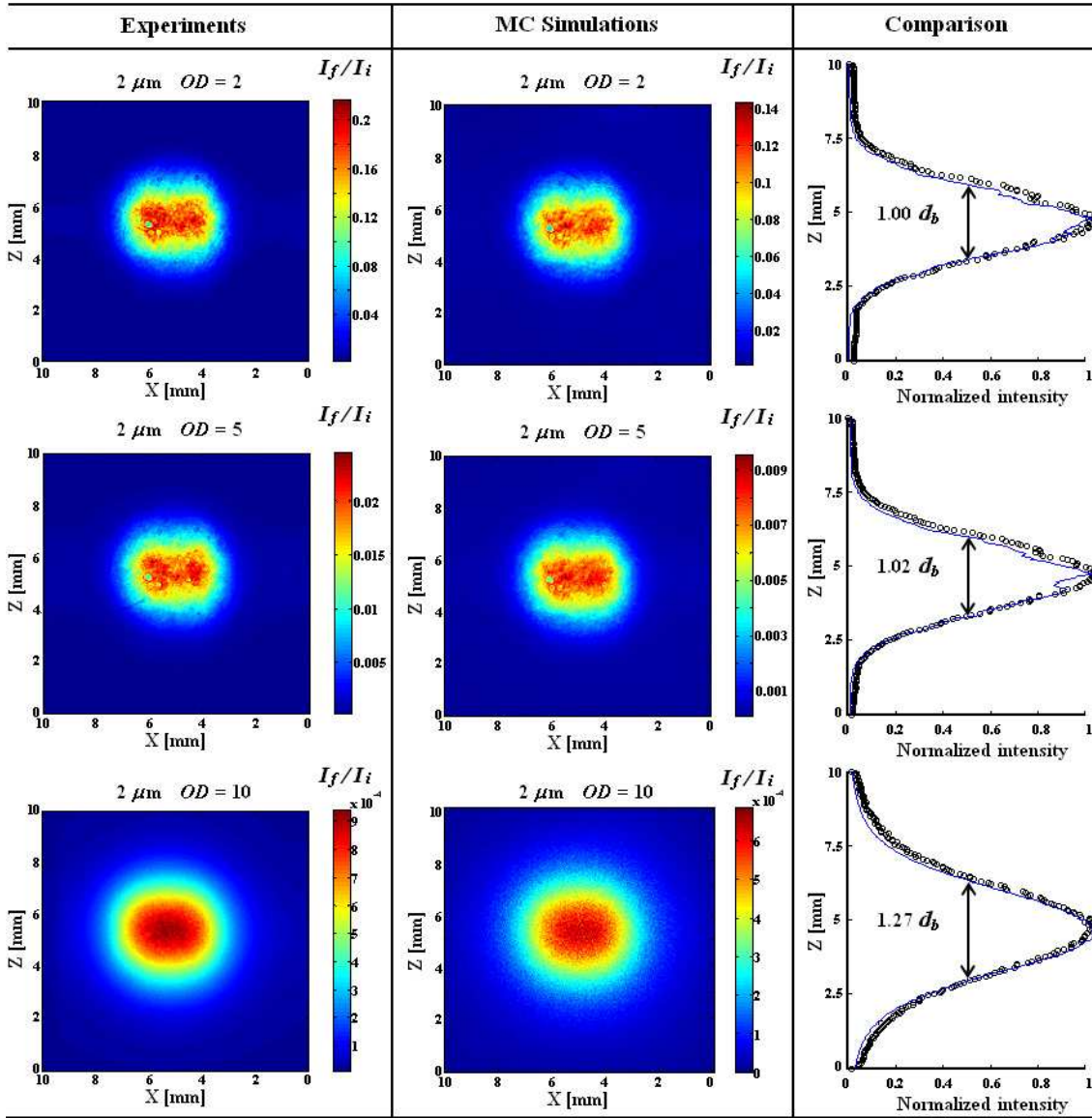


Figure 6.17: Comparison between the front face experimental and simulated images at detection acceptance angle $\theta_a = 1.5^\circ$. Solutions of 2 μm polystyrene spheres are considered at optical depths $OD = 2$, $OD = 5$ and $OD = 10$. The intensity scale of the images corresponds to the final light intensity, I_f , detected per pixel divided by the maximum value of the incident light intensity I_i . A comparison of the intensity profile along the vertical axis at $X = 5$ mm is also shown on the right side of the figure. The solid line corresponds to the experimental results and the circles are the results from simulation. Three billion of photons have been launched for the MC simulations.

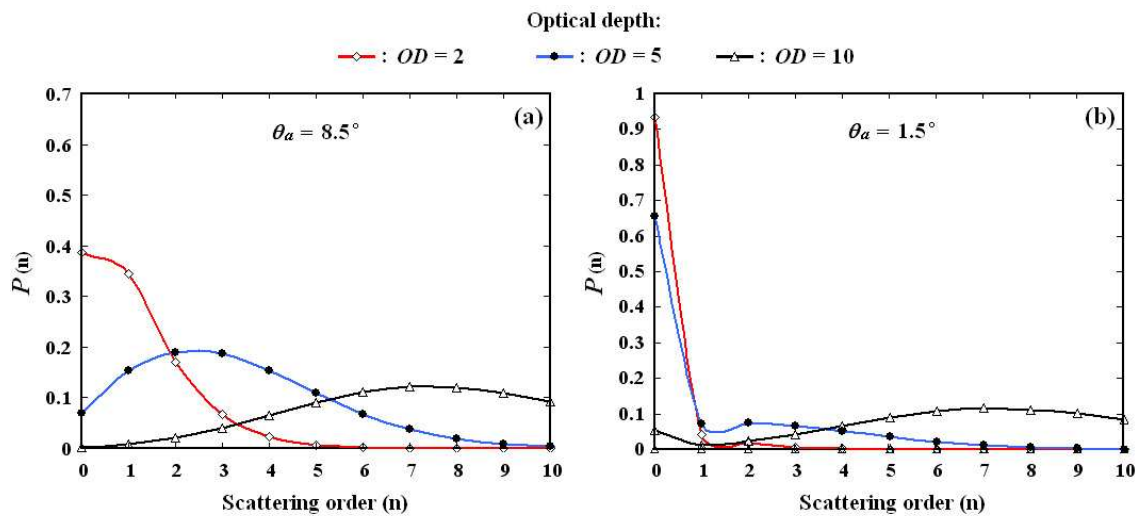


Figure 6.18: Distribution of the scattering orders at the various optical depths, for the polystyrene spheres of $2 \mu\text{m}$ diameter. All simulated photons exiting the scattering medium through the front face and within the indicated acceptance angle θ_a are recorded.

For the $2 \mu\text{m}$ particles, the laser beam does not diffuse as much as for the spheres of $1 \mu\text{m}$ diameter. The FWHM of the laser beam intensity profile is equal, here, to $1.17 d_a$ and $1.42 d_a$ at the respective optical depths $OD = 5$ and $OD = 10$.

For the small detection acceptance angle $\theta_a = 1.5^\circ$ (as seen in Fig.6.17), the FWHM equals $1.17 d_a$ and $1.42 d_a$ for the respective $OD = 5$ and $OD = 10$. Furthermore, the light intensity detected is reduced while the shape of the incident laser beam remains well conserved. Experimental and simulated images agrees well qualitatively but diverges quantitatively. At $OD = 2$ the maximum amount of light transmitted equals 20% experimentally and 14% with the simulation. At $OD = 5$, 2.5% is obtained experimentally against 0.9% via simulation. Finally, at $OD = 10$ the light transmission value is 0.09% experimentally and 0.07% with the simulation.

The amount of light intensity detected for each scattering order from $n = 0$ to $n = 10$ is plotted in Fig.6.18. For $\theta_a = 8.5^\circ$, the contribution of higher scattering orders is important even for the low optical depth $OD = 2$. By decreasing θ_a from 8.5° to 1.5° , the detection of ballistic photons is largely improved: From 38.6% to 93.3% at $OD = 2$, from 6.9% to 65.4% at $OD = 5$ and from 0.19% to 5.35% at $OD = 10$.

The third set of comparison is based on forward scattering detection with polystyrene spheres of $5 \mu\text{m}$ diameter. The intensity distribution profile is shown on the front face for the large detection acceptance angle $\theta_a = 8.5^\circ$ in Fig.6.19. At $OD = 2$ the light transmission reaches a maximum value of $\sim 30\%$. This is observed both experimentally and via simulation.

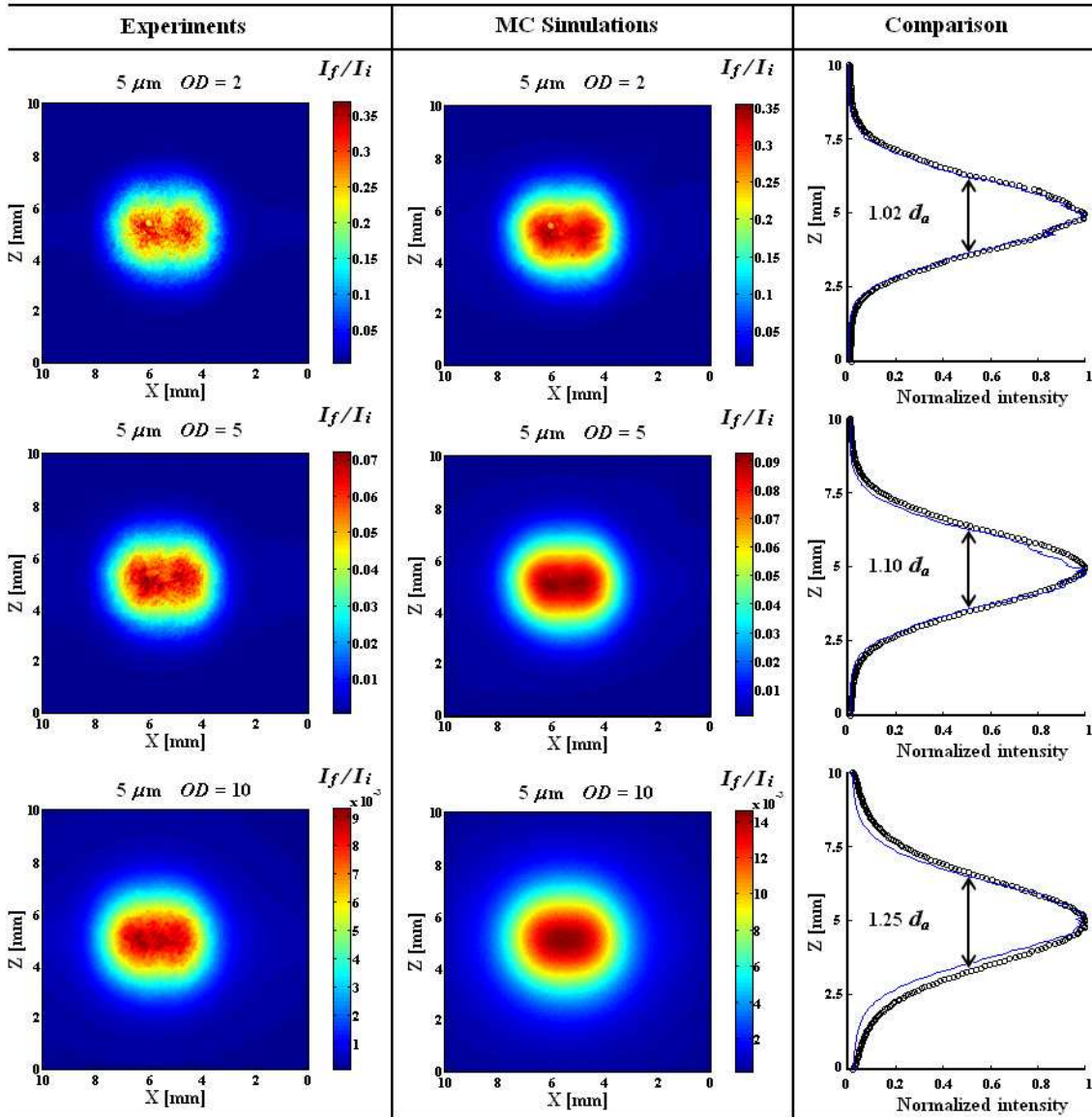


Figure 6.19: Comparison between the front face experimental and simulated images at detection acceptance angle $\theta_a = 8.5^\circ$. Solutions of 5 μm polystyrene spheres are considered at optical depths $OD = 2$, $OD = 5$ and $OD = 10$. The intensity scale of the images corresponds to the final light intensity, I_f , detected per pixel divided by the maximum value of the incident light intensity I_i . A comparison of the intensity profile along the vertical axis at $X = 5$ mm is also shown on the right side of the figure. The solid line corresponds to the experimental results and the circles are the results from simulation. Three billion of photons have been launched for the MC simulations.

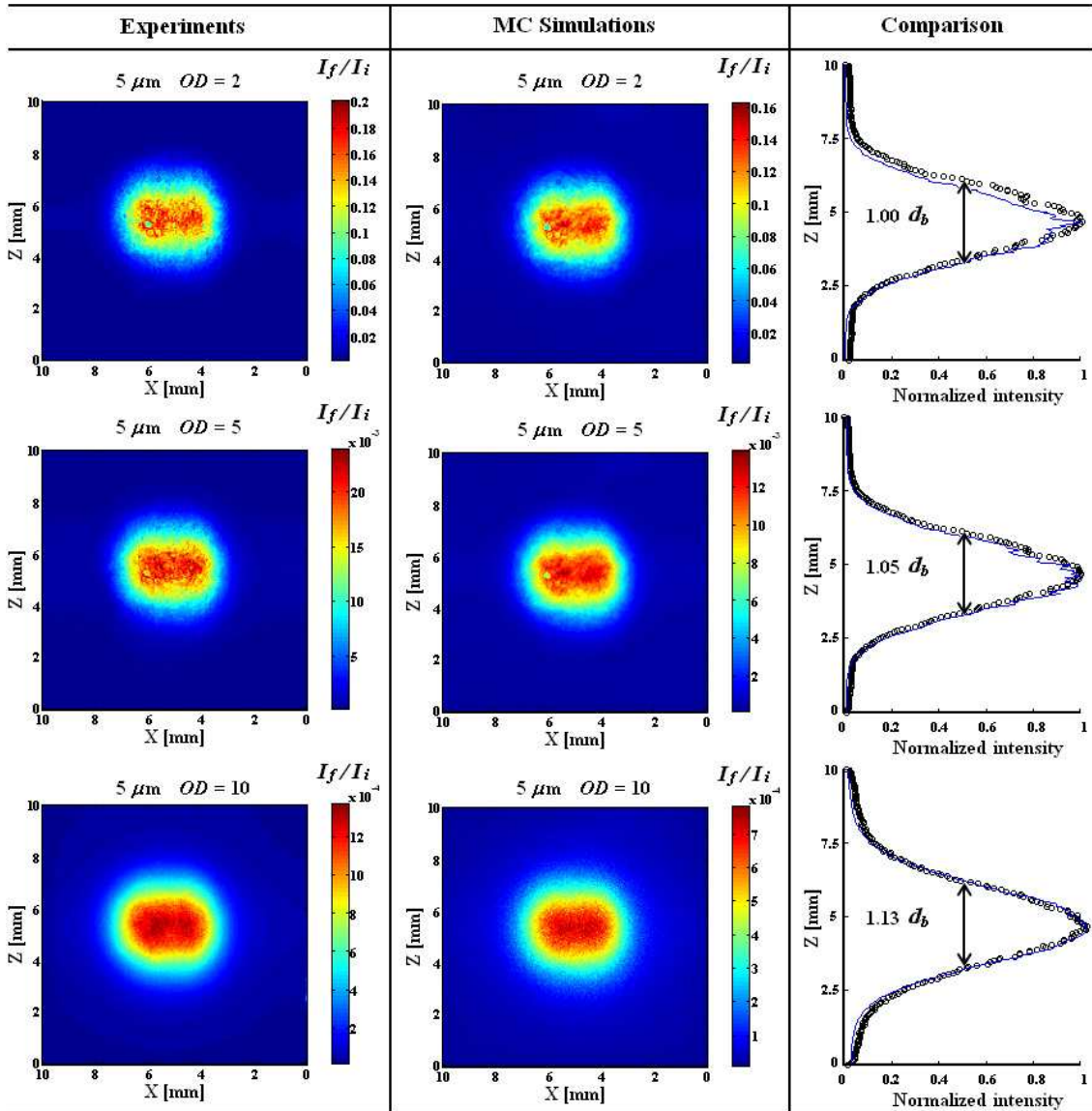


Figure 6.20: Comparison between the front face experimental and simulated images at detection acceptance angle $\theta_a = 1.5^\circ$. Solutions of 5 μm polystyrene spheres are considered at optical depths $OD = 2$, $OD = 5$ and $OD = 10$. The intensity scale of the images corresponds to the final light intensity, I_f , detected per pixel divided by the maximum value of the incident light intensity I_i . A comparison of the intensity profile along the vertical axis at $X = 5$ mm is also shown on the right side of the figure. The solid line corresponds to the experimental results and the circles are the results from simulation. Three billion of photons have been launched for the MC simulations.

At $OD = 5$, the maximum I_f/I_i equals 7% experimentally and 9% via simulation. Finally, at $OD = 10$, I_f/I_i equals 0.9% experimentally and 1.4% via simulation.

For the 5 μm particles, the laser beam does not diffuse as much as for spheres of 1 and 2 μm diameter. The FWHM of the laser beam intensity profile is, here, equal to 1.10 d_a and 1.25 d_a at respective $OD = 5$ and $OD = 10$.

For the small detection acceptance angle $\theta_a = 1.5^\circ$ (as seen in Fig.6.20), the FWHM equals 1.05 d_a at $OD = 5$ and 1.13 d_a at $OD = 10$. Furthermore, the light intensity detected is reduced while the shape of the incident laser beam remains well conserved. Experimental and simulated images agrees well qualitatively but diverges quantitatively. At $OD = 2$ the maximum amount of light transmitted equals 20% experimentally and 16% with the simulation. At $OD = 5$, 2.5% is obtained experimentally against 1.4% via simulation. Finally, at $OD = 10$ I_f/I_i equals 0.14% experimentally and 0.075% via simulation.

The fourth set of comparison is based on forward scattering detection with polystyrene spheres of 20 μm diameter. The intensity distribution profile is shown on the front face for the large detection acceptance angle $\theta_a = 8.5^\circ$ in Fig.6.21. At $OD = 2$ the light transmission reaches a maximum value of 60% and 40% for the experiment and for the simulation respectively. At $OD = 5$, this maximum equals 12% both experimentally and via simulation. Finally, at $OD = 10$, I_f/I_i equals 0.8% experimentally and 2.5% via simulation. The qualitative and quantitative divergences are found to be more important here, than for any other investigated size of polystyrene spheres. At 20 μm the dimension of the scattering particles reaches the resolution of the EM-CCD camera and leads to the detection of laser speckles. Closer results could be found with the simulation, by averaging a larger number of experimental images (which is only equal to 10 here). The FWHM of the laser beam intensity profile is 1.05 d_a and 1.26 d_a at respective $OD = 5$ and $OD = 10$ and remains close to the values find for the 5 μm spheres.

For the small detection acceptance angle $\theta_a = 1.5^\circ$ (as seen in Fig.6.22), the FWHM equals 1.06 d_a at $OD = 5$ and 1.13 d_a at $OD = 10$. Furthermore, the light intensity detected is reduced while the shape of the incident laser beam remains well conserved. Experimental and simulated images agrees well qualitatively but diverges quantitatively. At $OD = 2$ the maximum amount of light transmitted equals 42% experimentally and 30% with the simulation. At $OD = 5$, 6% is obtained experimentally against 4.5% via simulation. Finally, at $OD = 10$ I_f/I_i equals 0.16% experimentally and 0.27% via simulation.

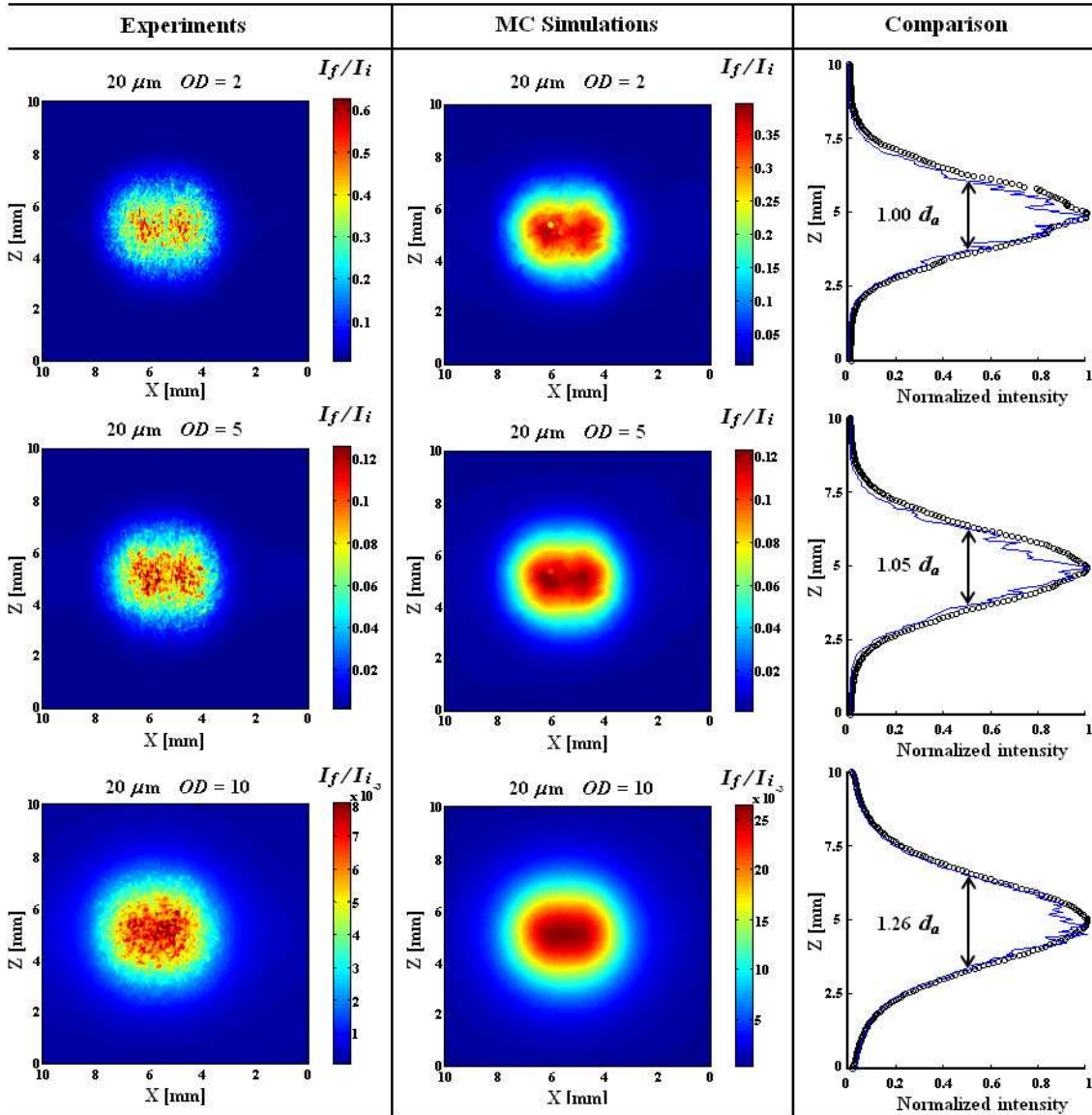


Figure 6.21: Comparison between the front face experimental and simulated images at detection acceptance angle $\theta_a = 8.5^\circ$. Solutions of 20 μm polystyrene spheres are considered at optical depths $OD = 2$, $OD = 5$ and $OD = 10$. The intensity scale of the images corresponds to the final light intensity, I_f , detected per pixel divided by the maximum value of the incident light intensity I_i . A comparison of the intensity profile along the vertical axis at $X = 5$ mm is also shown on the right side of the figure. The solid line corresponds to the experimental results and the circles are the results from simulation. Three billion of photons have been launched for the MC simulations.

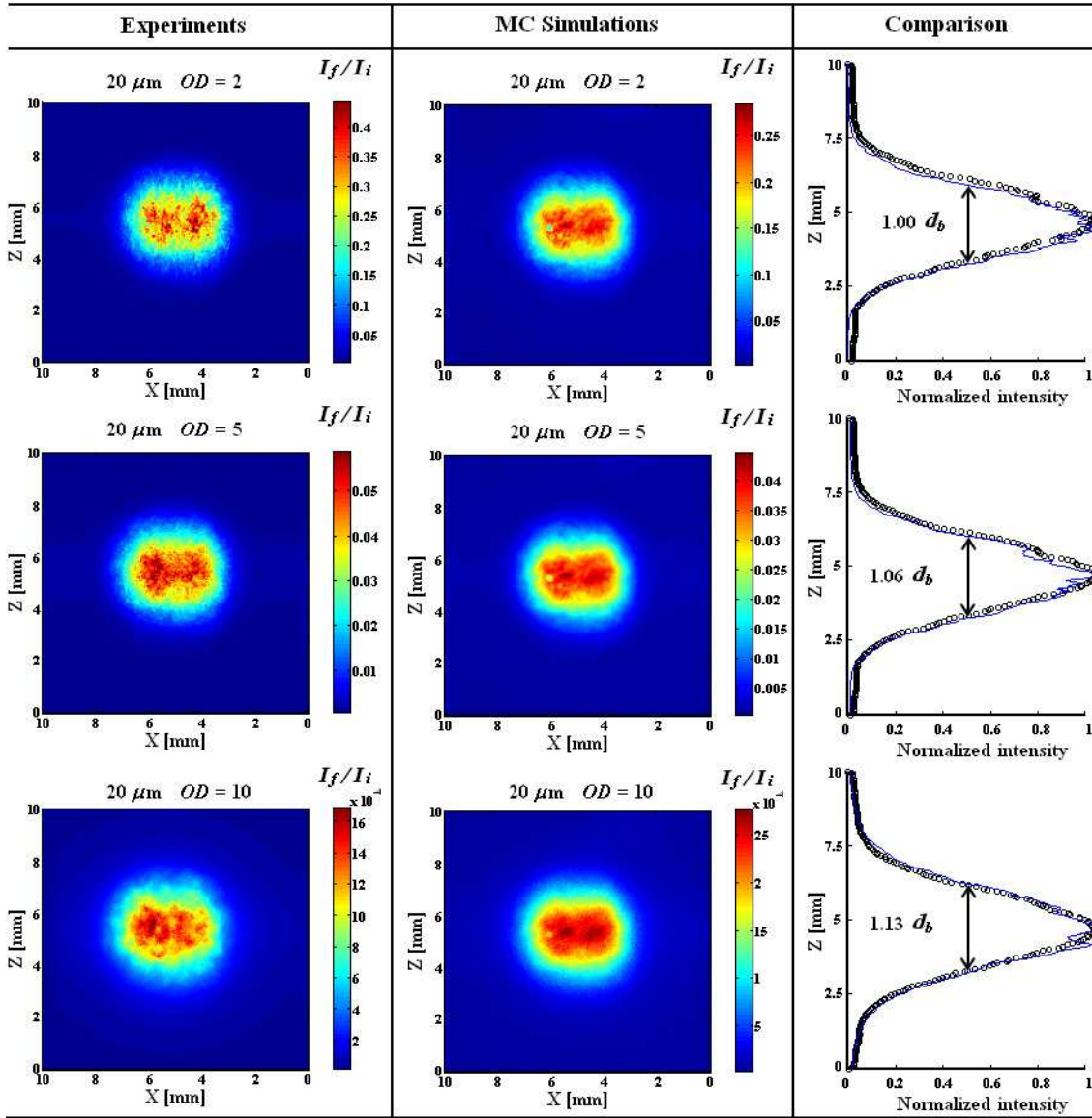


Figure 6.22: Comparison between the front face experimental and simulated images at detection acceptance angle $\theta_a = 1.5^\circ$. Solutions of 20 μm polystyrene spheres are considered at optical depths $OD = 2$, $OD = 5$ and $OD = 10$. The intensity scale of the images corresponds to the final light intensity, I_f , detected per pixel divided by the maximum value of the incident light intensity I_i . A comparison of the intensity profile along the vertical axis at $X = 5$ mm is also shown on the right side of the figure. The solid line corresponds to the experimental results and the circles are the results from simulation. Three billion of photons have been launched for the MC simulations.

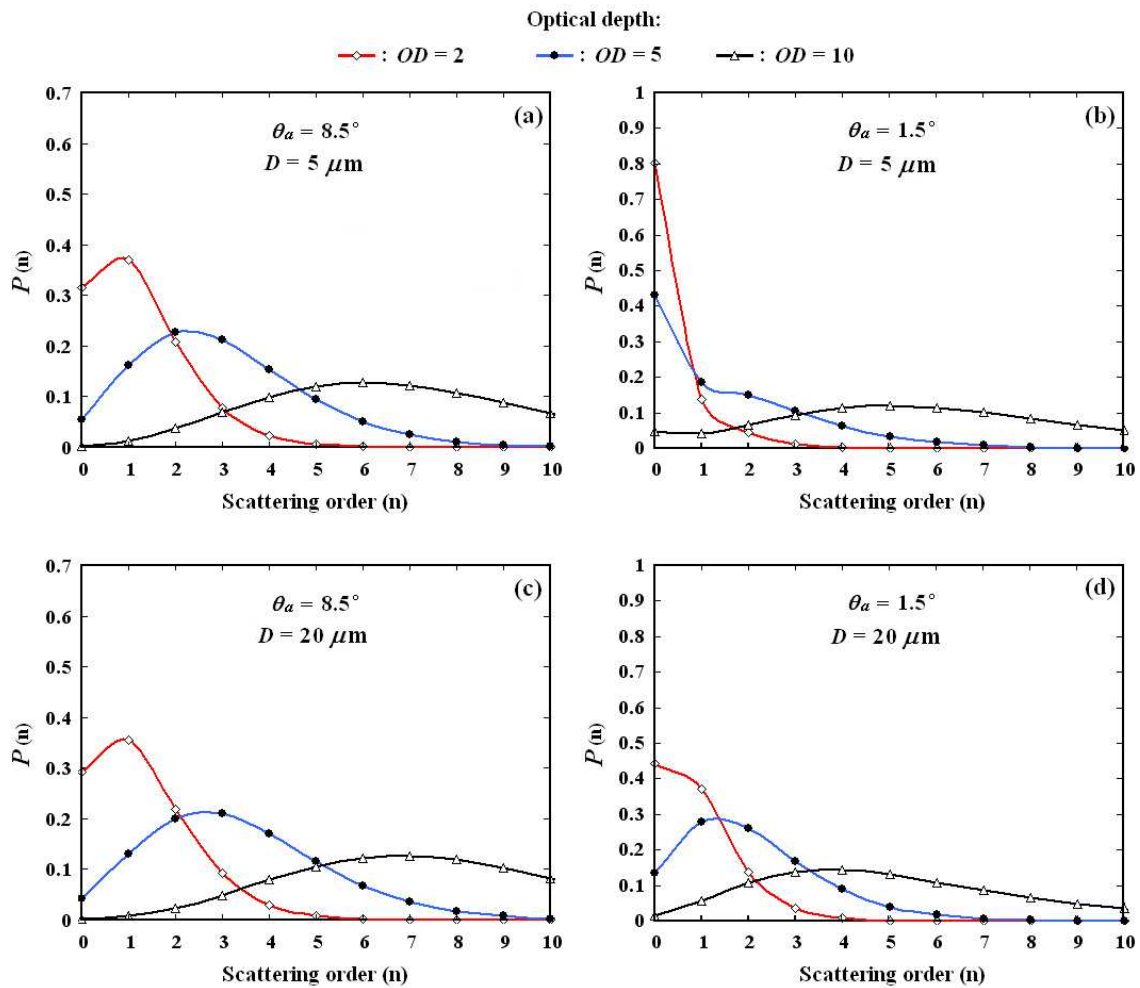


Figure 6.23: Distribution of the scattering orders at the various optical depths, for the polystyrene spheres of 5 and 20 μm diameter. All simulated photons exiting the scattering medium through the front face and within the indicated acceptance angle θ_a are recorded.

The amount of light intensity detected for each scattering order from $n = 0$ to $n = 10$ is plotted in Fig.6.23 for both cases of 5 and 20 μm polystyrene spheres. The influence of the optical depth and of the detection acceptance angle on the contribution $P(0)$ of the ballistic photons can be observed.

For the 5 μm particle and for the acceptance angle $\theta_a = 8.5^\circ$, $P(0)$ equals 31.6%, 5.6% and 0.23% at respective optical depths $OD = 2$, $OD = 5$ and $OD = 10$. By reducing the detection acceptance angle to $\theta_a = 1.5^\circ$, the amount of multiply scattered light detected is reduced and $P(0)$ increases significantly, reaching now 80.1%, 43.2% and 4.8% (for $OD = 2$, $OD = 5$ and $OD = 10$ respectively).

For the 20 μm particles and for the acceptance angle $\theta_a = 8.5^\circ$, $P(0)$ equals 29.2%, 4.3% and 0.13% at respective optical depths $OD = 2$, $OD = 5$ and $OD = 10$. By reducing the detection acceptance angle to $\theta_a = 1.5^\circ$, the amount of multiply scattered light detected is

reduced and $P(0)$ increases significantly, reaching now 44.4%, 13.4% and 1.4% (for $OD = 2$, $OD = 5$ and $OD = 10$ respectively).

For the larger particles, the resultant statistics on the forward face becomes sufficient for good spatial resolution in the MC image, even at the low detection acceptance angle $\theta_a = 1.5^\circ$. The scattering phase function of larger particles is characterized by a more significant forward scattering lobe (as seen in subsection 8.1.3). This scattering feature is responsible for the increase of the light intensity scattered and multiply scattered in the forward direction. As a result, the divergences with the Beer-Lambert predictions are increased, whereas the broadening effect of the incident laser beam is reduced.

- *Conclusions for the forward scattering detection :*

- Results from the MC simulations agree very well with the experimental images both qualitatively and quantitatively for $OD \leq 5$. The simulated images are generated, here, with an identical spatial resolution as in the experiment.
- These agreements are found for various scattering particle size (polystyrene microspheres of $1 \mu\text{m}$, $2 \mu\text{m}$, $5 \mu\text{m}$ and $20 \mu\text{m}$) at both large ($\theta_a = 8.5^\circ$) and small ($\theta_a = 1.5^\circ$) detection acceptance angle.
- Discrepancies appears qualitatively at high optical depth when $OD = 10$ with more photons detected in the simulation than experimentally. Despite these quantitative divergences, the spatial distribution of the simulated light intensity is comparable to the experimental one.
- At high OD , errors due to low statistics are introduced in the simulated results for the forward scattering detection.
- When the detection acceptance angle is reduced, the amount of light intensity transmitted is reduced until it matches with the Beer-Lambert predictions. This occurs when 100% of the detected signal corresponds to non-scattered light (ballistic photons).
- When the optical depth is increased, the amount of scattered and multiply scattered photons detected increases consequently and must be added to the Beer-Lambert prediction. This amount depends directly on the value of the detection acceptance angle.
- For a constant OD and θ_a , the divergences between the Beer-Lambert prediction and the experimental/simulated results are also related to the forward scattering nature of the particles. These divergences are more important for highly forward scattering phase function

(big particles) than for phase function characterized by a smaller factor of anisotropy g (small particles).

- The amount of light intensity detected (experimentally and via simulation) differs considerably from that predicted by the Beer-Lambert law. These divergences increase when increasing OD and for large θ_a due to the important contribution of the multiply scattered light detected. An effective corrective procedure to the Beer-Lambert law is proposed in subsection 8.4 based on MC calculation of the ballistic photons contribution to the total detected signal.

6.2.3 Side scattering detection

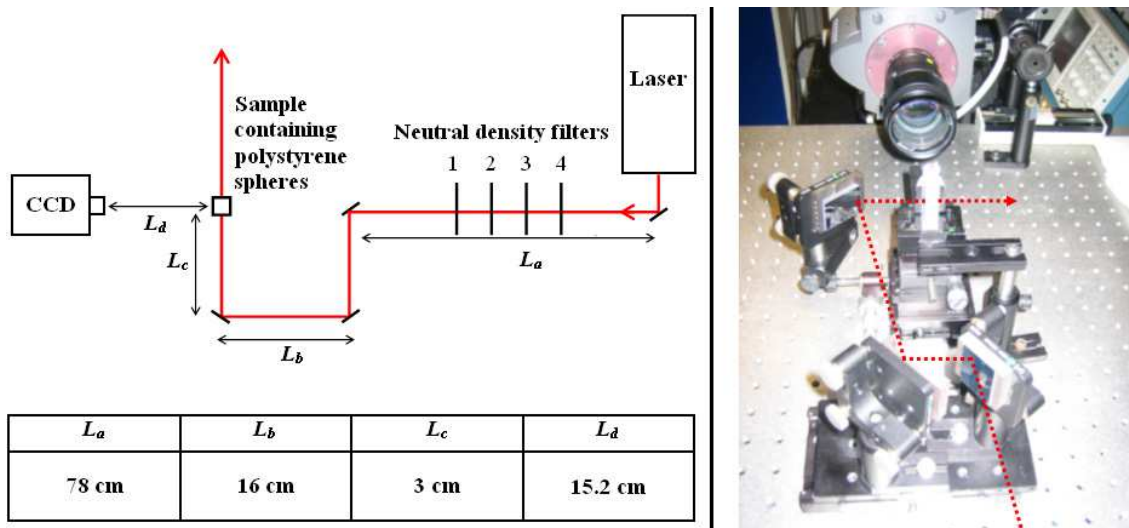


Figure 6.24: Experimental configuration for the side scattering detection.

The first set of comparisons is based on the side face detection with polystyrene spheres of $1 \mu\text{m}$ diameter. Fig.6.25 shows the intensity distribution profile on the side face for a large detection acceptance angle $\theta_a = 8.5^\circ$ at the optical depths $OD = 2$, $OD = 5$ and $OD = 10$. By increasing the OD , it can be seen that the cylindrical shape of the incident beam is wider. This broadening of the incident light source operate in an identical manner for the experimental and simulated results. The detected light intensity is increased and the photon penetration distance in the scattering medium is reduced at high OD . The increasing of light intensity detected leads to better statistics in the MC simulation, due to the higher number of photons recorded. Thus, contrary to the forward scattering detection, MC simulation shows better agreement with experimental results at $OD = 10$ than at $OD = 2$.

The second set of comparisons concerns the detection of the side scattered light through polystyrene spheres of $2 \mu\text{m}$ diameter. Fig.6.26 shows the intensity distribution profile on the side face for the large detection acceptance angle $\theta_a = 8.5^\circ$ at the optical depths $OD = 2$, $OD = 5$ and $OD = 10$. Similarly than the previous presented results (see Fig.6.25), the amount of light transmitted through the sample is reduced and the laser beam diffuses more with increasing OD . However, these phenomena are not as significant as it was found with $D = 1 \mu\text{m}$. By the same token, both experimental and simulated results demonstrate, that for a more forward scattering phase function (here for $D = 2 \mu\text{m}$), the light tends to penetrate further into the scattering medium and to conserve the initial shape. The relative light intensity is also reduced and equal 8.10^{-4} here against 12.10^{-4} for $D = 1 \mu\text{m}$ at $OD = 10$.

The third set of comparisons concerns the detection of the side scattered light through polystyrene spheres of $5 \mu\text{m}$ diameter. Fig.6.27 shows the intensity distribution profile on the side face for the large detection acceptance angle $\theta_a = 8.5^\circ$ at the optical depths $OD = 2$, $OD = 5$ and $OD = 10$. Once again, a very good agreement is found between the experimental and simulated results for the three cases of optical depth investigated. It is also seen that the amount of light intensity recorded on the side face is mainly dependant on the value of OD but does not change significantly with the features of the scattering phase functions.

The last set of comparisons concerns the detection of the side scattered light through polystyrene spheres of $20 \mu\text{m}$ diameter. Fig.6.28 shows the intensity distribution profile on the side face for the large detection acceptance angle $\theta_a = 8.5^\circ$ at the optical depths $OD = 2$, $OD = 5$ and $OD = 10$. At this particle size, the forward scattering lobe is very significant and increases the amount of light scattered in the forward direction, while reducing the amount of light scattered in the off-axis. The amount of detected light at low optical depth is inferior than for the other considered diameter. For $OD = 2$ the maximum amount of detected light is twice less than for $D = 1 \mu\text{m}$. However, when considering $OD = 10$ the amount of detected light on the side face remains fairly constant for all particle size assumed (contrary to the forward scattering detection).

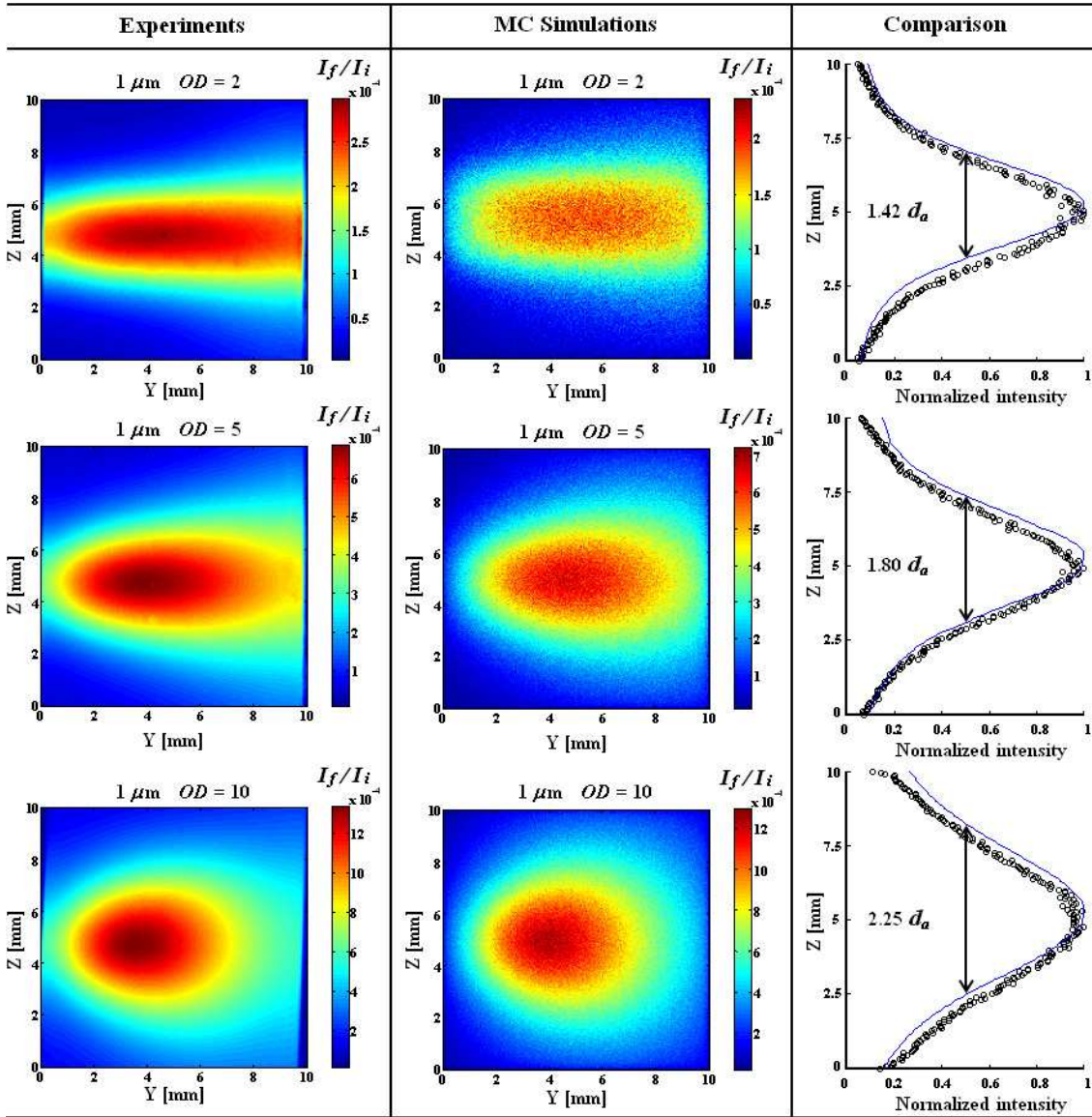


Figure 6.25: Comparison between the side face experimental and simulated images at detection acceptance angle $\theta_a = 8.5^\circ$. Solutions of polystyrene spheres of $1 \mu\text{m}$ diameter are considered at optical depths $OD = 2$, $OD = 5$ and $OD = 10$. The intensity scale of the images corresponds to the final light intensity, I_f , detected per pixel divided by the maximum value of the incident light intensity I_i . A comparison of the intensity profile along the vertical axis at $X = 5 \text{ mm}$ is also shown on the right side of the figure. The solid line corresponds to the experimental results and the circles are the results from simulation. Three billion of photons have been launched for the MC simulations.

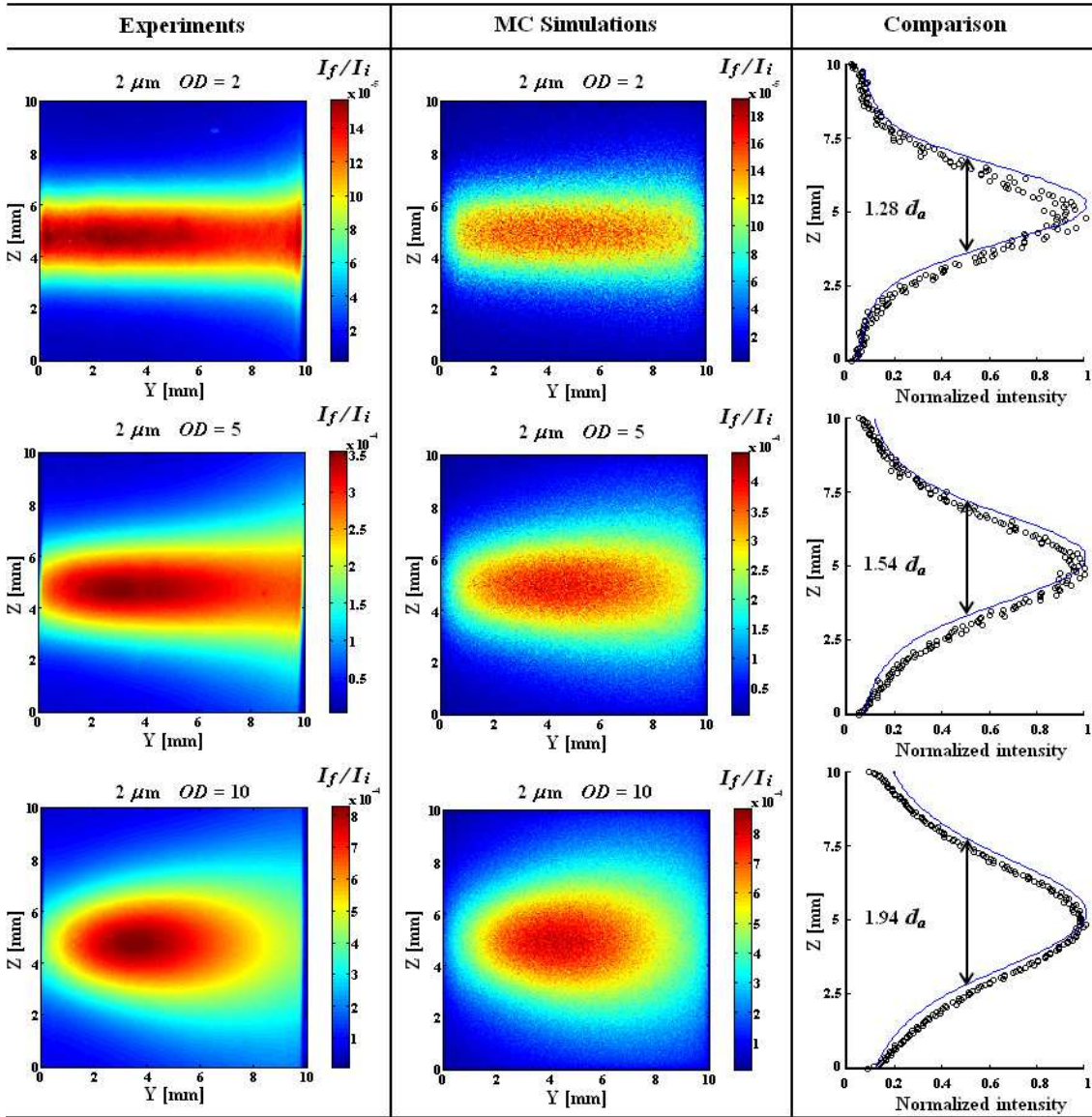


Figure 6.26: Comparison between the side face experimental and simulated images at detection acceptance angle $\theta_a = 8.5^\circ$. Solutions of polystyrene spheres of $2 \mu\text{m}$ diameter are considered at optical depths $OD = 2$, $OD = 5$ and $OD = 10$. The intensity scale of the images corresponds to the final light intensity, I_f , detected per pixel divided by the maximum value of the incident light intensity I_i . A comparison of the intensity profile along the vertical axis at $X = 5 \text{ mm}$ is also shown on the right side of the figure. The solid line corresponds to the experimental results and the circles are the results from simulation. Three billion of photons have been launched for the MC simulations.

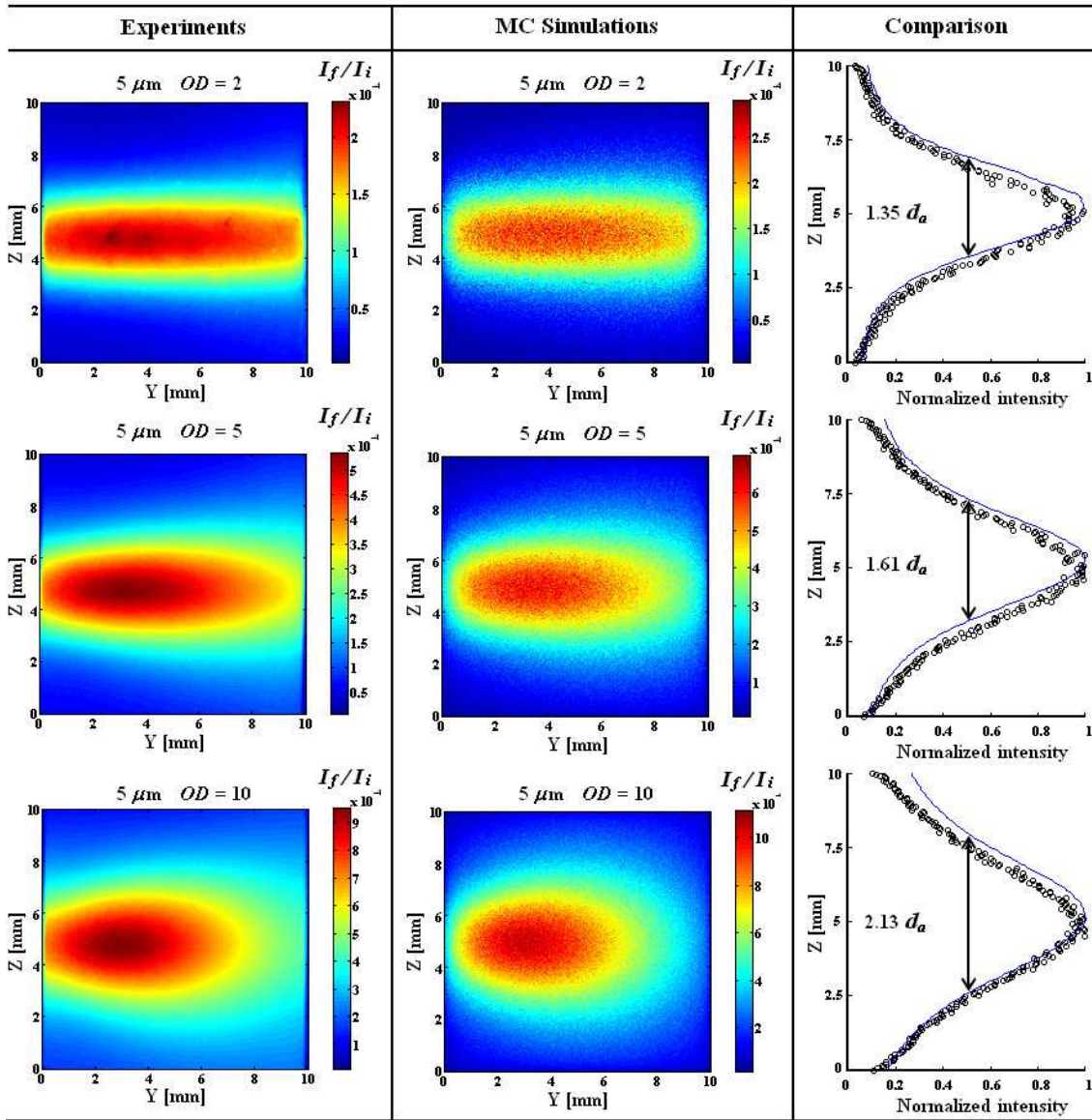


Figure 6.27: Comparison between the side face experimental and simulated images at detection acceptance angle $\theta_a = 8.5^\circ$. Solutions of polystyrene spheres of $5 \mu\text{m}$ diameter are considered at optical depths $OD = 2$, $OD = 5$ and $OD = 10$. The intensity scale of the images corresponds to the final light intensity, I_f , detected per pixel divided by the maximum value of the incident light intensity I_i . A comparison of the intensity profile along the vertical axis at $X = 5 \text{ mm}$ is also shown on the right side of the figure. The solid line corresponds to the experimental results and the circles are the results from simulation. Three billion of photons have been launched for the MC simulations.

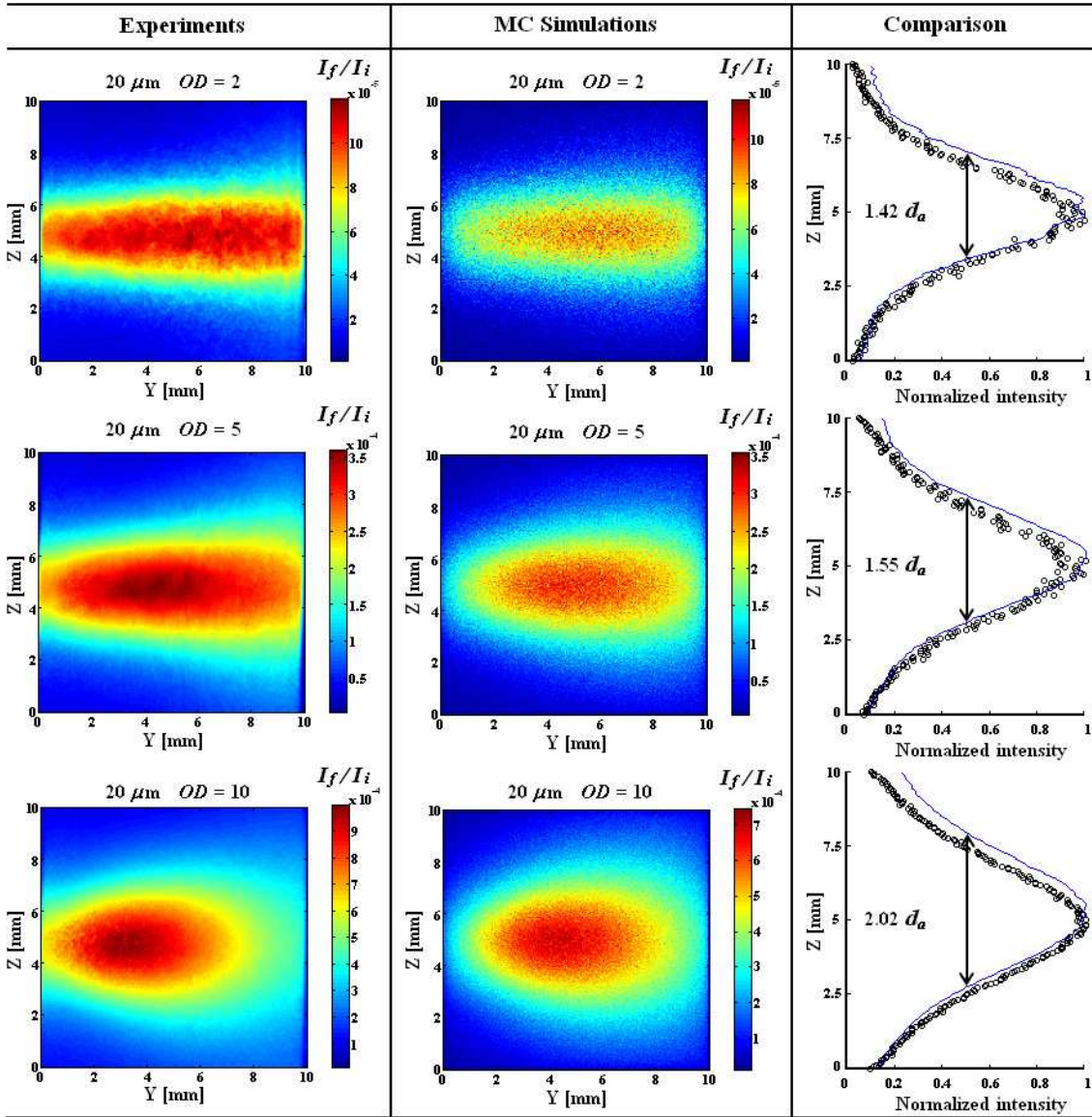


Figure 6.28: Comparison between the side face experimental and simulated images at detection acceptance angle $\theta_a = 8.5^\circ$. Solutions of polystyrene spheres of $20 \mu\text{m}$ diameter are considered at optical depths $OD = 2$, $OD = 5$ and $OD = 10$. The intensity scale of the images corresponds to the final light intensity, I_f , detected per pixel divided by the maximum value of the incident light intensity I_i . A comparison of the intensity profile along the vertical axis at $X = 5 \text{ mm}$ is also shown on the right side of the figure. The solid line corresponds to the experimental results and the circles are the results from simulation. Three billion of photons have been launched for the MC simulations.

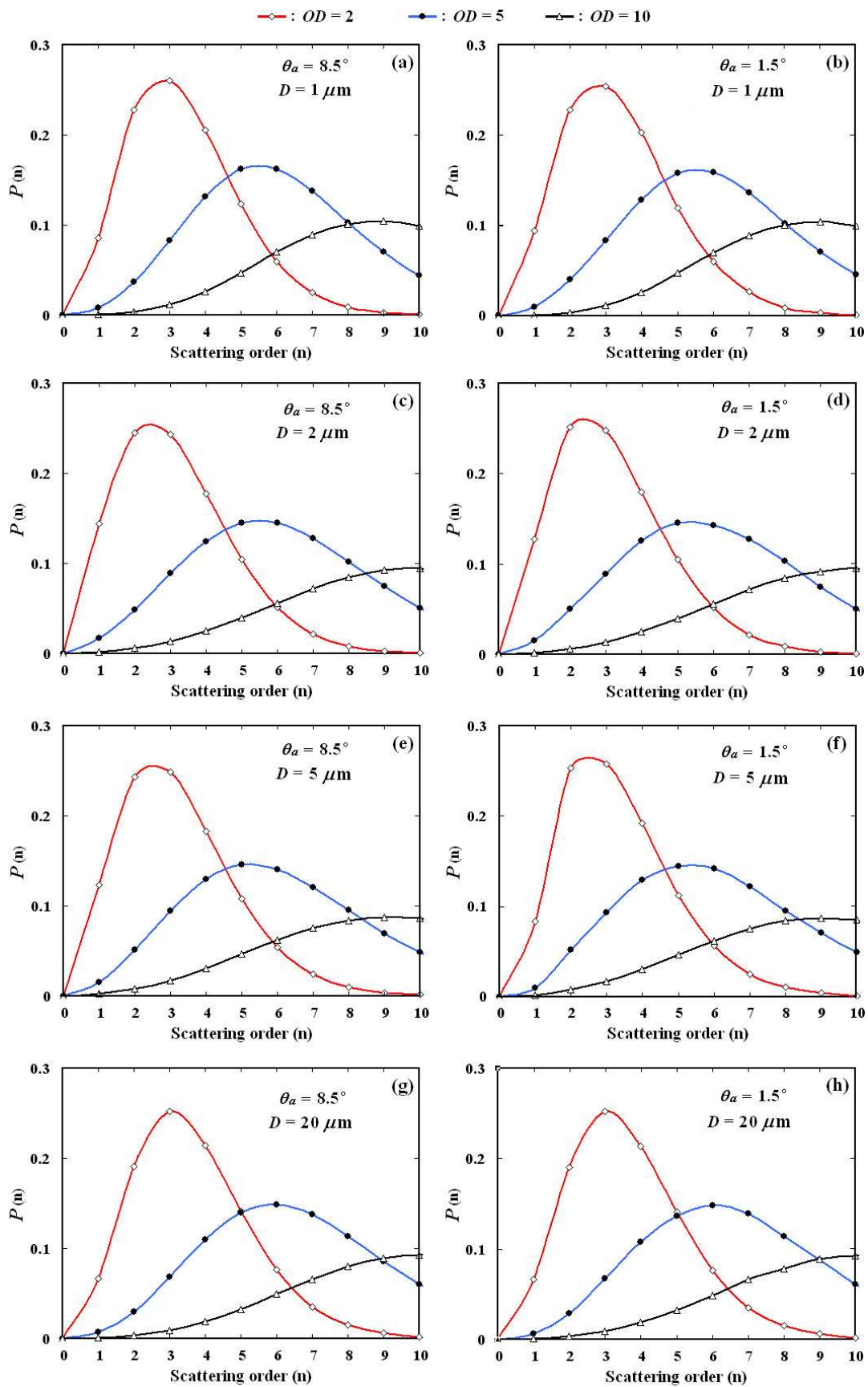


Figure 6.29: Distribution of scattering orders for the side face detection.

The amount of light intensity detected for each scattering order from $n = 0$ to $n = 10$ is plotted in Fig.6.29 for each size of polystyrene sphere. Contrary to the forward scattering detection, it is seen here, that the detection acceptance angle and the scattering phase function have both a minor influence on the contribution of each scattering order. At equal OD , Fig.6.29(a) to (h), show a similar contributions. For all cases of study, it can also be noticed that the value of OD remains always close or equal to the dominant scattering order. It is deduced from these results that the optical depth is the only parameter affecting consequently the contribution of the scattering orders when detecting on the side.

- *Conclusions for the side scattering detection :*

- Results from the MC simulations agree very well with the experimental images both qualitatively and quantitatively for $OD \geq 5$. The simulated images are generated, here, with an identical spatial resolution as in the experiment.
- These agreements are found for various scattering particle size (polystyrene microspheres of $1 \mu\text{m}$, $2 \mu\text{m}$, $5 \mu\text{m}$ and $20 \mu\text{m}$) at large detection acceptance angle ($\theta_a = 8.5^\circ$). Results from MC simulation at low acceptance angle $\theta_a = 1.5^\circ$ have demonstrated insufficient statistic to generate 2D images with high spatial resolution.
- At low OD , errors due to low statistics are introduced in the simulated results for the side scattering detection. When, however, the optical depth is increased, the amount of scattered and multiply scattered photons reaching the side face is increased and a higher light intensity detected. This increase of light intensity seems to be "linearly" related to the value of the optical depth. Thus, the optimum qualitative and quantitative comparison between the MC and experimental results are observed at $OD = 10$, whereas; discrepancies occur principally at $OD = 2$.
- By increasing the optical depth, the distance of photon penetration along the incident direction is reduced. Furthermore, the cylindrical shape of the incident laser beam becomes wider due to an increase of the diffuse photons within the cell.

6.3 Verification of the phase function approximation

When dealing with inhomogeneous polydisperse media each unitary cubic cell requires its own optical properties (see section 5.2.3). Introducing a scattering CPDF for each cell requires a large amount of input data, particularly if the medium is represented with a large number of cells. Generating the correct scattering CPDF at each scattering event dramatically increases the running time. One solution to this problem uses several averaged scattering CPDF (stored in lookup tables), each one representing either the scattering of a set of droplets of similar size, or representing a particular size distribution. This approximation is verified against the rigorous approach in this section (published in Berrocal *et al* 2005b).

6.3.1 Calculation method

Four Log-Normal distributions of droplets size typically encountered in sprays have been chosen using different values of average diameter \bar{D} and standard deviation σ . The equation describing Log-Normal distributions has been given previously section 2.2.3 in Eq.2.2.3. The distributions tested are based on mean diameters $\bar{D} = 5 \mu\text{m}$ and $\bar{D} = 40 \mu\text{m}$ with standard deviations σ equal to 10% and 80% of \bar{D} (Fig.6.30). The bin width equals $0.4 \mu\text{m}$. Distribution (a) is representative of an automotive fuel injector spray, distribution (c) of a medical nebulizer spray, and the other distributions are included to show the effect of standard deviation.

Two methods for representing the local scattering phase function in polydisperse homogeneous media were tested. The method one (M_1) is based on the determination of the average phase function \bar{f} over the complete distribution of drops size (see Eq.2.2.3). \bar{f} has been calculated for the four particle distributions described above and the scattering CPDF of \bar{f} is deduced for each of these distributions. Only one scattering CPDF representative of the complete drops distribution is used in the MC simulations with the method M_1 . In the case of infinitesimal size bin width of the drops size distribution M_1 would give the exact mathematical solution of the global scattering process that occurs in a homogeneous polydisperse turbid media. The calculations of the averaged scattering phase functions have been performed from Eq.4.1.14 given in section 4.1.3.

In method two (M_2), 25 different scattering CPDF are defined such as each CPDF is representative of the scattering by particles belonging to a class of drop sizes. Even if several approaches can be employed to determine these CPDF, only one has been found valid. The first approach takes into account only the phase function corresponding to the

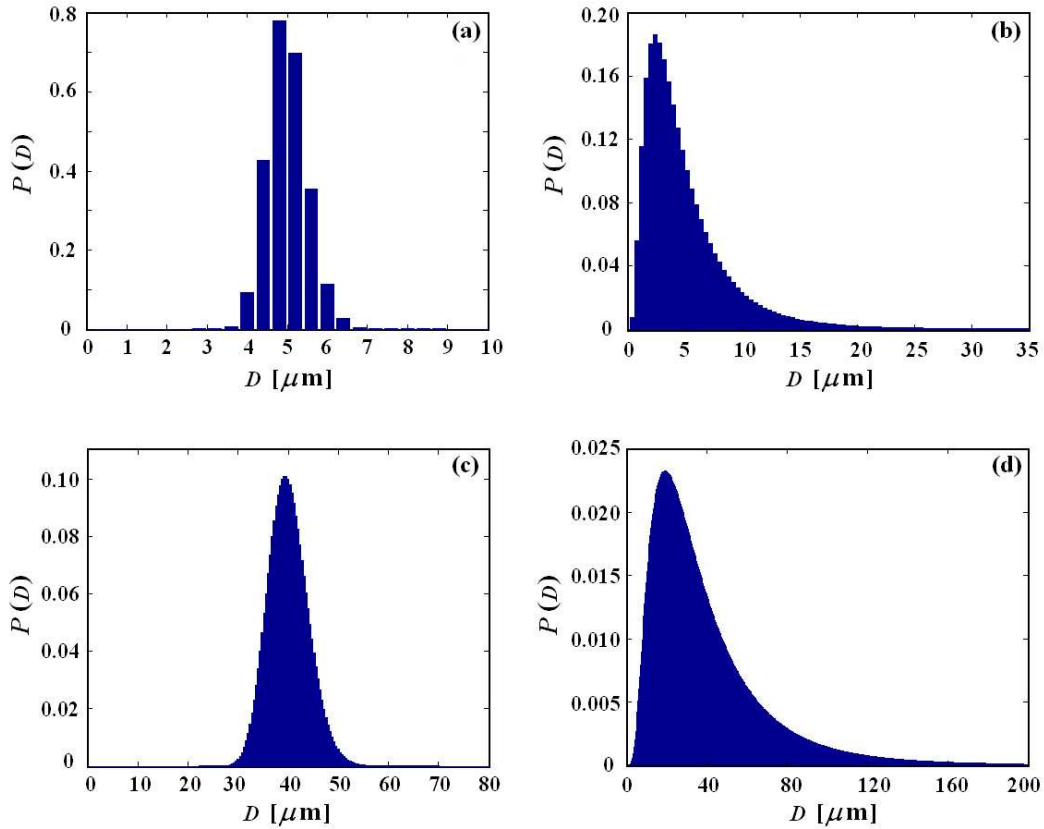


Figure 6.30: Normalized Log-Normal distributions of droplets size for different \bar{D} and σ . (a) $\bar{D} = 5 \mu\text{m}$ and $\sigma = 0.5 \mu\text{m}$ (10% of \bar{D}), (b) $\bar{D} = 5 \mu\text{m}$ and $\sigma = 4 \mu\text{m}$ (80% of \bar{D}), (c) $\bar{D} = 40 \mu\text{m}$ and $\sigma = 4 \mu\text{m}$ (10% of \bar{D}) and (d) $\bar{D} = 40 \mu\text{m}$ and $\sigma = 32 \mu\text{m}$ (80% of \bar{D}).

middle drop size of the class bin. As the scattering phase functions do not change linearly with the drops diameter this method has been rejected. The second approach consists in adding the phase function of the minimum value of the bin to the one corresponding to the maximum value and to divide the result by 2. Once again this approximation has been rejected due to the non-linear changes of the phases function with droplet sizes. Finally the appropriate method is based on calculation of the phase function averaged over the range of particle size, with an equal number of drops for each given size but weighted with the corresponding scattering cross-section (Eq.2.2.3 with $n(D)$ equals 1 for every D). When a scattering event occurs, the diameter of the particle encountered is determined with the distribution of droplet size and a random number. The probability $P(D_1)$ of a drop of diameter D_1 being encountered by a photon packet is given by:

$$P(D_1) = \frac{n(D_1) \cdot \sigma_e(D_1)}{\sum_{D=0}^{\infty} n(D) \cdot \sigma_e(D)} \quad (6.3.1)$$

Once the diameter of the particle encountered is found, the correct approximate scattering

CPDF can be chosen. Note that if the exact phase function (corresponding to the drops size reached) was chosen (instead of the approximated one), method M_2 would be equal to method M_1 . The accuracy of M_2 is then directly related to the difference between the real scattering CPDF of the droplet encountered and the approximate CPDF chosen. Reducing the size range over which scattering CPDF are averaged increases the accuracy of the technique. In the present work 25 classes of drop size are used and the range of sizes for each class is varied according to the rate of change of scattering CPDF with droplet size. The boundaries between each size class are selected by hand to minimize the difference between the CPDF on neighboring classes.

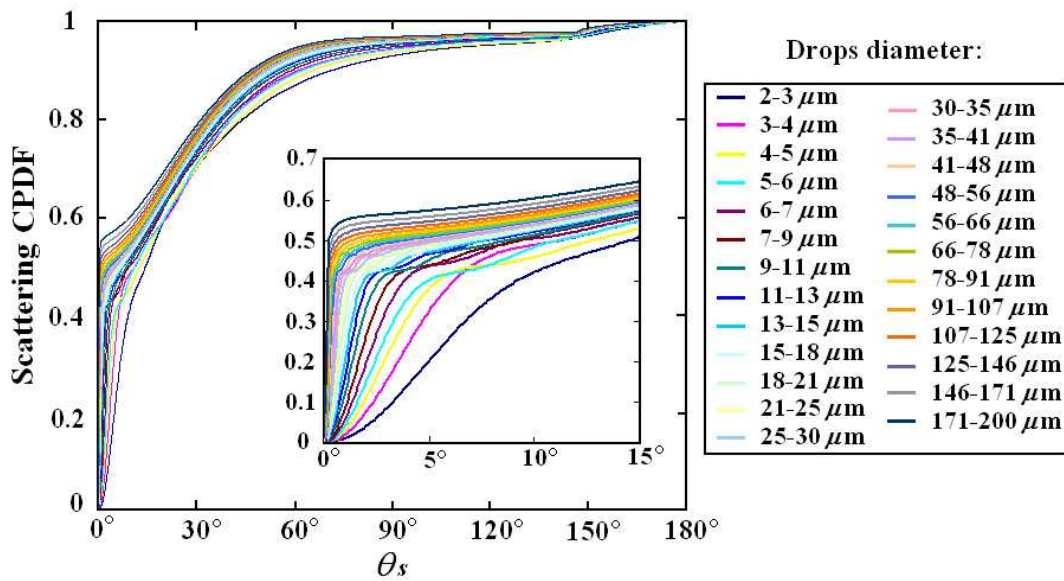


Figure 6.31: Representation of 25 scattering Cumulative Probability Density Function calculated from the Lorenz-Mie Theory. Scattering particles diameters range from 2 to 200 μm .

It is seen Fig.6.31 that for small particles neighboring scattering CPDF diverge strongly and overlap at small angles θ_s when $D \leq 15 \mu\text{m}$. For large particles, the scattering CPDF do not overlap and remain close one to each other even when the particle size interval is large. Thus to maximize the accuracy of the technique while minimizing the memory requirements, the range of sizes is kept small for small droplets ($\sim 1 \mu\text{m}$) and large (up to 29 μm) for large droplets. Further reducing the particle size increases the accuracy of the technique at the expense of greater memory requirements.

6.3.2 Description of the simulation

Each droplet size distribution in Fig.6.30 has been used. The droplets are contained in a homogeneous single cubic cell of dimension $L = 50 \text{ mm}$. A cylindrical flat laser beam S

of 20 mm diameter enters through the scattering sample crossing perpendicularly the $Y = 0$ plane (back face) and exiting through the $Y = L$ plane (front face) (Fig.6.32).

The source wavelength λ is 532 nm and the light is assumed unpolarized. Intensity profiles on the back face (back scattering) and on the front face (forward scattering) are recorded for different detector acceptance angles θ_a . In each simulation 100 millions photons are sent. The surrounding medium is air (refractive index equals $1+0.0i$). The droplets are spherical and non-absorbing with refractive index $1.4+0.0i$ and the scattering CPDF are calculated from the Lorenz-Mie theory. Scattering and extinction coefficients are then equal and the simulations are run with fixed to 0.12 and 0.24 mm^{-1} . The resulting optical depths are respectively 6 and 12, corresponding to the intermediate single-to-multiple scattering regime. The range of particle size is $2 \mu\text{m} - 200 \mu\text{m}$ (typical of droplet sizes in fuel sprays) and the resulting size parameter x is: $11.81 \leq x \leq 1181.05$.

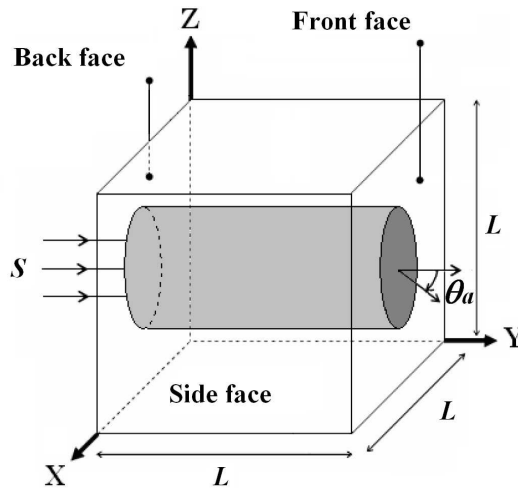


Figure 6.32: The scattering medium is a single homogeneous cube of $L = 50$ mm. The source S is a cylindrical laser beam characterized by a flat light intensity distribution.

6.3.3 Results and comparison

Results obtained from M_2 are compared to the results obtained from M_1 by analyzing quantitatively the light intensity distribution on the front and back face of the scattering medium (Fig.6.32). Note the intensity scale is different for each image. The images presented are obtained using M_1 for a single dropsize distribution with an average diameter of $40 \mu\text{m}$ and a standard deviation of $32 \mu\text{m}$ (Fig.6.33(a)). The scattering coefficient μ_s is fixed to $\mu_s = 0.12 \text{ mm}^{-1}$ and 0.24 mm^{-1} giving respectively an average number of scatters per photon of ~ 6 and ~ 12 scatters.

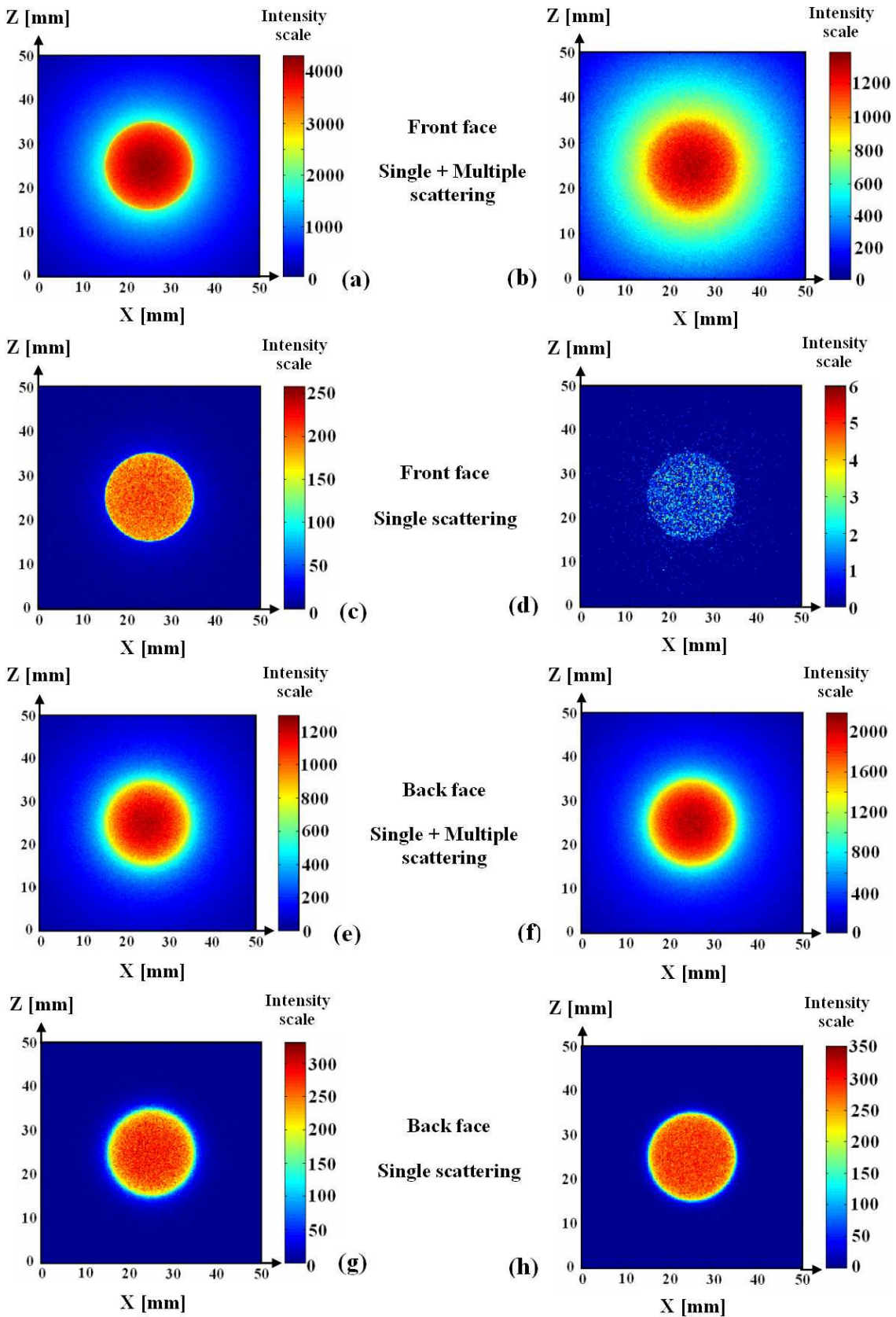


Figure 6.33: Intensity distribution for forward and backward light scattering at different scattering coefficient, $\mu_s = 0.12 \text{ mm}^{-1}$ for (a) (c) (e) (g) and $\mu_s = 0.24 \text{ mm}^{-1}$ for (b) (d) (f) (h). The detection acceptance angle $\theta_a = 90^\circ$ and 100 millions of photons are launched. The intensity scale represents the number of photons detected per pixel (of $25 \mu\text{m}$ side).

Figure 6.33(a) ($\mu_s = 0.12 \text{ mm}^{-1}$) and (b) ($\mu_s = 0.24 \text{ mm}^{-1}$) demonstrate the broadening of the beam on the front face as the optical depth increases (for $\mu_s = 0.12 \text{ mm}^{-1}$ $OD = 6$ and for $\mu_s = 0.24 \text{ mm}^{-1}$ $OD = 12$). The images illustrate the quantitative distribution of the forward and backward scattered light considering all scattering orders (Fig. 6.33(a), (b), (e) and (f)) and with the detector filtered to detect single scattering only (Fig. 6.33(c), (d), (g) and (h)). Figure 6.33(a) and (b) show that doubling μ_s the forward light intensity is strongly attenuated (by a factor of ~ 3.3) and that the shape of the laser beam is no longer clearly defined. On the contrary for back scattering (Fig. 6.33(e) and (f)), as increases the detected intensity increases also but the pattern of scattered radiation does not change significantly.

Single scattering detected in the forward direction shows a faithful reconstruction of the laser beam for $\mu_s = 0.12 \text{ mm}^{-1}$ (Fig. 6.33(c)). However the intensity of single scattering is weak compared to the amount of multiple scattering for $\mu_s = 0.24 \text{ mm}^{-1}$ (Fig. 6.33(d)). It can be seen from Fig. 6.33(g) and (h) that single back scattered signal remains relatively constant for both scattering coefficients. The effects of the detection acceptance angle are also investigated. In Fig. 6.33 all photons reaching the detection areas are detected (acceptance angle $\theta_a = 90^\circ$). As found in other simulations (section 7.2), the acceptance angle can be used to optimize the ratio of singly to multiply scattered photons detected.

In Fig. 6.34 the detection acceptance angle θ_a is reduced to 5° . $\mu_s = 0.12 \text{ mm}^{-1}$ in Fig. 6.34(a) and (c), corresponding to Fig. 6.33(a) and (c), and $\mu_s = 0.24 \text{ mm}^{-1}$ in Fig. 6.34(b) and (d), corresponding to Fig. 6.33(b) and (d). The total intensity on the front face is strongly reduced but the boundaries of the laser beam appear clearly (Fig. 6.34(a) and (b)). The single scattering intensity detected per pixel remains close for both acceptance angles $\theta_a = 90^\circ$ Fig. 6.33(c) and (d) and $\theta_a = 5^\circ$ Fig. 6.34(c) and (d). This indicates that most of single scattered photons propagate with a polar scattering angle θ_a less than 5° and shows the high intensity of scattering in the forward direction in Mie scattering processes. The scattering coefficient, the geometry of the sample and the scattering phase function all influence the number of scattering events n occurring and the total path length L of the photon packets. Slice differences in the scattering phase functions (between the exact one and the approximated one used in the simulations M_2) do not affect significantly the parameters n and L , but can modify the final intensity distribution. The images presented in the two last figures have been obtained from method M_1 . Corresponding images have been generated by applying M_2 . Due to the symmetry of the images, only the intensity profile along a line passing from the centre of the laser beam $X = 25 \text{ mm}$ until the edge of the image $X = 50 \text{ mm}$, is considered with Z fixed to 25 mm at $Y = 0$ or $Y = L$. The comparison between the two methods is made by calculating the ratio of intensities

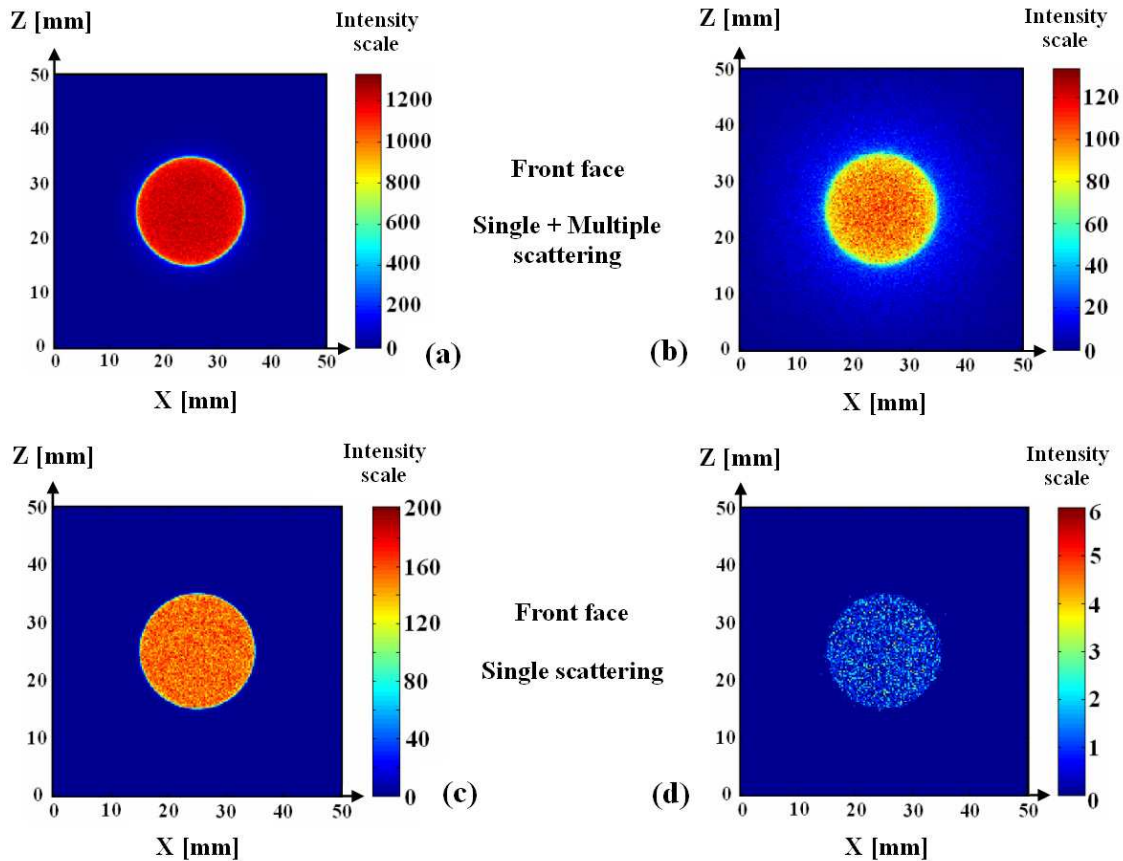


Figure 6.34: Intensity distribution for forward light scattering. $\mu_s = 0.12 \text{ mm}^{-1}$ for (a) (c) and $\mu_s = 0.24 \text{ mm}^{-1}$ for (b) (d). The detection acceptance angle $\theta_a = 5^\circ$. 100 millions of photons are sent. The intensity scale represents the number of photon detected per pixel. Each pixel is square with $25 \mu\text{m}$ sides.

along this line of the image generated with M_1 to the image generated with M_2 . This ratio is plotted Fig.6.35 for $\mu_s = 0.12 \text{ mm}^{-1}$ and $\mu_s = 0.24 \text{ mm}^{-1}$ using once again the log-normal droplet size distribution defined by $\bar{D} = 40 \mu\text{m}$ and $\sigma = 32 \mu\text{m}$ (Fig.6.30(a)). Total intensity (single and multiple scattering taken together) are detected on the front face and the back face of the scattering cube with a detection acceptance angle $\theta_a = 90^\circ$. It is seen from Fig.6.35 that the ratio M_1 / M_2 (Image method one / Image method two) remains equal to ~ 1 (0.02) for both forward and back light scattering. These results show the very good agreement between the two methods at large detection acceptance angles.

Figure 6.37 shows the same data, but this time with a detection acceptance angle θ_a of 5° . In Fig.6.34 it is seen that with this restricted acceptance angle the number of detected photons is very low outside of the projected area of the incoming beam. This low photon count makes the M_1 / M_2 intensity ratio noisy in Fig. 6.37 at $X > 35 \text{ mm}$. At $X < 35 \text{ mm}$ the greater number of detected photons give a better defined ratio. Here it is seen

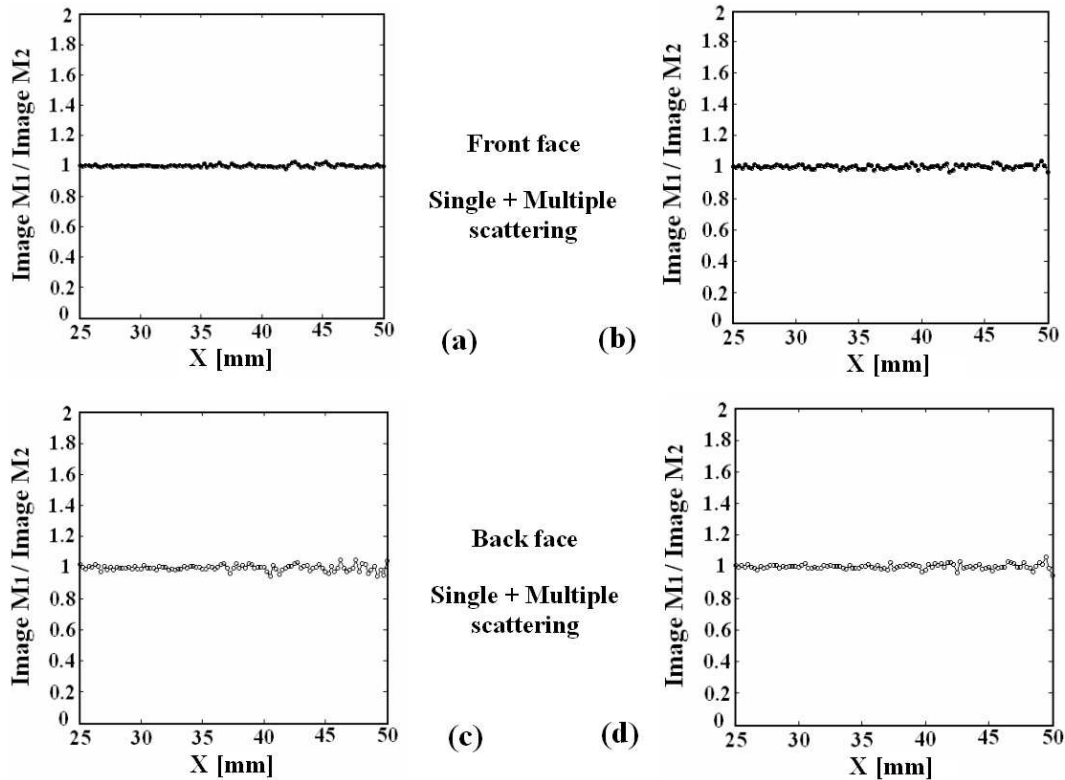


Figure 6.35: Intensity ratio, along a beam profile, between the 2 MC methods. Forward scattering is in (a) and (b) and backscattering in (c) and (d). Both single and multiple scattering are detected together. Detector acceptance angle $\theta_a = 90^\circ$. $\mu_s = 0.12 \text{ mm}^{-1}$ for (a) (c) and $\mu_s = 0.24 \text{ mm}^{-1}$ for (b) (d).

that the results from M_2 match the results from M_1 for small detection acceptance angles as well as for large. Doubling the scattering coefficient from 0.12 mm^{-1} to 0.24 mm^{-1} significantly reduces the number of photons reaching the front face and making the M_1/M_2 intensity ratio noisier for $\mu_s = 0.24 \text{ mm}^{-1}$ (Fig. 6.37(b)) than for $\mu_s = 0.12 \text{ mm}^{-1}$ (Fig. 6.37(a)).

In Fig.6.36 the comparison is performed for single scattering detection with $\mu_s = 0.12 \text{ mm}^{-1}$. It is seen that for both acceptance angles $\theta_a = 5^\circ$ and $\theta_a = 90^\circ$ the ratio fluctuates equally either side of 1 when $X < 35 \text{ mm}$. At large distance from the laser beam centre ($X > 35 \text{ mm}$) results diverge between the two detection apertures: If $\theta_a = 90^\circ$ (Fig.6.37(a)), few photons are detected giving strong statistical fluctuations in the resulting ratio M_1/M_2 . If however $\theta_a = 5^\circ$ (Fig.6.37(b)), no singly scattered photons are detected for either method and a flat line is plotted for $X > 40 \text{ mm}$. A small number of photons are detected at the edge of the laser beam at the intermediate distance $35 \text{ mm} < X < 40 \text{ mm}$ giving a noisy interval.

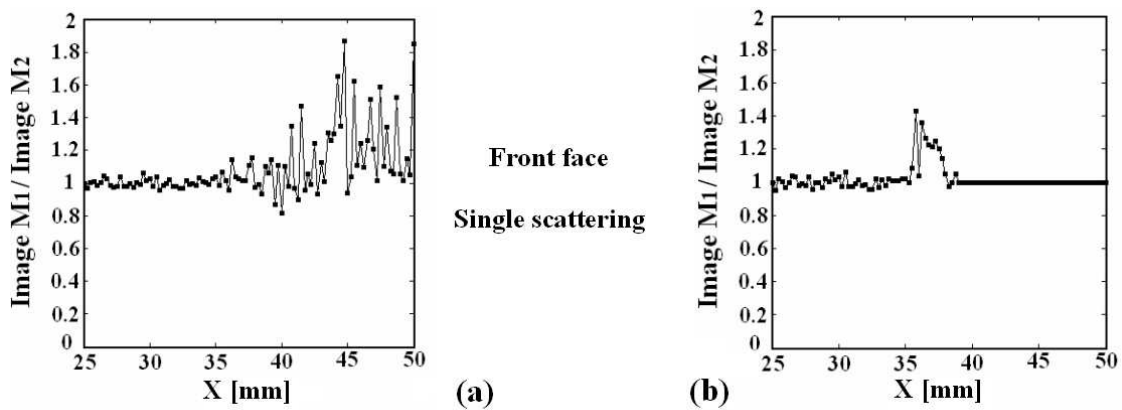


Figure 6.36: Intensity profile ratio between the 2 MC methods for the forward scattering with $\mu_s = 0.12 \text{ mm}^{-1}$. Single scattering only, is detected with an acceptance angle $\theta_a = 90^\circ$ in (a) and $\theta_a = 5^\circ$ in (b). No singly scattered photons are detected at $X > 40 \text{ mm}$ when $\theta_a = 5^\circ$.

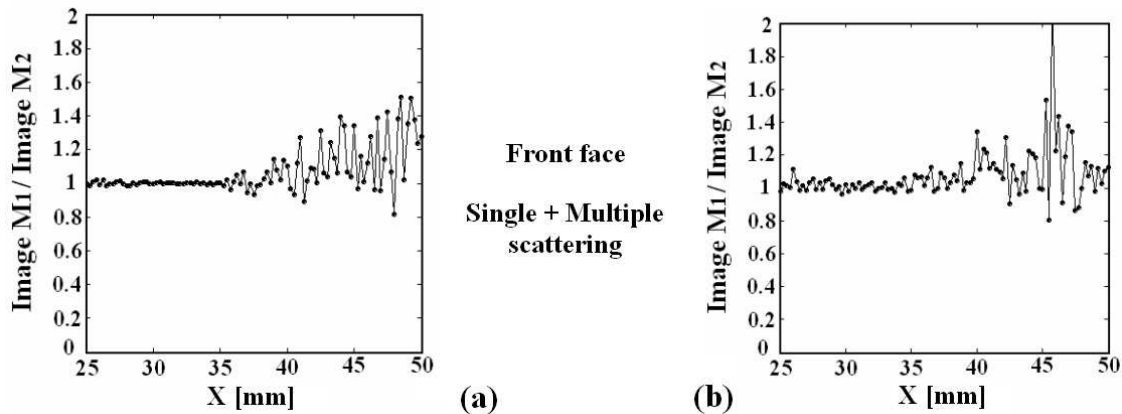


Figure 6.37: Intensity profile ratio between the 2 MC methods for forward light scattering. Single and multiple scattering are detected with an acceptance angle $\theta_a = 5^\circ$. $\mu_s = 0.12 \text{ mm}^{-1}$ for (a) (c) and $\mu_s = 0.24 \text{ mm}^{-1}$ for (b) (d).

These comparisons show that the divergences between the two methods are only observed when the detected signal is weak. These differences are caused by the strong statistical fluctuations which occur when the amount of collected data resulting from probability laws is too low. However where these fluctuations are strong, the ratio is biased to values greater than one. More photons are then detected with M_1 than M_2 on the front face when the signal is weak. It is deduced that the weight given to the scattering phase function of large particles (with large forward scattering lobe) is then more important in M_1 than in M_2 . These results demonstrate that apart from very small differences in the number of detected photons scattered at high angles when the signal is weak, the results obtained with the phase function approximation used in method M_2 are in excellent agreement with the rigorous method M_1 , for droplet sizes over the range $2 - 200 \mu\text{m}$ of particle size, for different $\theta_a = 5^\circ$ and $\theta_a = 90^\circ$ and with varying over a factor of 2. It remains to verify

method two for other particle size distributions. Figure 6.38 shows the results for the three other log-normal distributions, defined respectively by $\bar{D} = 40 \mu\text{m}$ with $\sigma = 4 \mu\text{m}$ (Fig.6.36(a)), $\bar{D} = 5 \mu\text{m}$ with $\sigma = 4 \mu\text{m}$ (Fig.6.36(b)) and $\bar{D} = 5 \mu\text{m}$ with $\sigma = 0.5 \mu\text{m}$ (Fig.6.36(c)). Photons from all scattering orders have been detected with an acceptance angle $\theta_a = 90^\circ$ on the front face, assuming a scattering coefficient of 0.12 mm^{-1} .

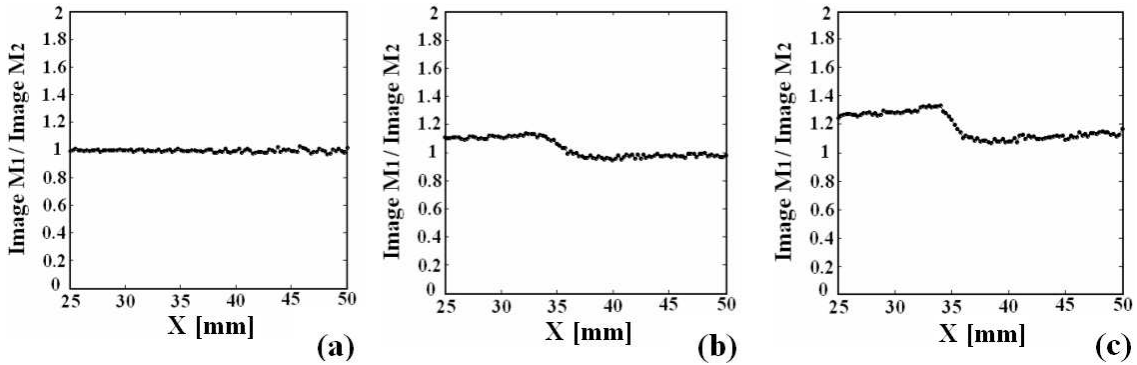


Figure 6.38: Intensity profile ratio between the 2 MC methods for $\mu_s=0.12 \text{ mm}^{-1}$. Single and multiple light scattering are detected on the front face with an acceptance angle $\theta_a = 90^\circ$. The log-normal distributions of particle size are characterized by: (a): $\bar{D} = 40 \mu\text{m}$ with $\sigma = 4 \mu\text{m}$ (10% of \bar{D}), (b): $\bar{D} = 5 \mu\text{m}$ with $\sigma = 4 \mu\text{m}$ (80% of \bar{D}), (c): $\bar{D} = 5 \mu\text{m}$ with $\sigma = 0.5 \mu\text{m}$ (10% of \bar{D}).

When the average diameter is $40 \mu\text{m}$ with $4 \mu\text{m}$ standard deviation (Fig.6.38(a)) the ratio of intensities from the two methods is once again ~ 1 (0.02). This result verifies the use of method two for distributions of particles based on large mean diameters with small relative standard deviation. Greater differences between method two and method one appear when small drops are considered. It is seen that the ratio M_1/M_2 is greater than 1 and reaches a maximum of ~ 1.2 when $\bar{D} = 5 \mu\text{m}$ with $\sigma = 4 \mu\text{m}$ (Fig.6.36(b)). If the standard deviation is reduced to $0.5 \mu\text{m}$ (Fig.6.36(c)) the differences between the two methods are increased with a ratio lying between $1.15 < M_1/M_2 < 1.4$. It is deduced from this results that method one gives more forward light scattering than method two when only small particles are considered. These results were expected from Fig.6.31 due to the differences in the averaged scattering CPDF for small drop sizes which result from the averaging used in the two methods. Referring to the size distributions plotted in Fig.6.30, the comparison above demonstrates that the phase function approximation used in method two gives accurate results for any distribution of spherical drops comprised between 10 and 200 microns, except for very small differences in the number of photons scattered at high angles where the singly scattered signal is weak. For particles smaller than $10 \mu\text{m}$, discrepancies in the global light intensity distribution appear between the exact and the approximated solution. These differences can be corrected by reducing the particle size interval used for small drops ($D < 10 \mu\text{m}$) in method two (see Fig.6.31).

Particles from 2 to 200 μm have been considered with a step of 0.4 μm . The exact approach would require using a total of ~ 500 phase functions (if not averaged). The use of only 25 phase functions presents a reduction in memory requirement by ~ 20 times. This study finally demonstrates that the appropriate use of approximated phase functions in a MC code can produce results reaching the one obtained if the exact phase functions were considered. The method M_2 can be now applied in the case of inhomogeneous turbid media assuming that most of the drops considered are bigger than 10 μm in diameter.

Applications of Monte Carlo Simulations to Spray Diagnostics

IN Chapter 6, the MC model has been verified with the theoretical approach and validated against a large set of experimental data. The capability of the MC code to generate realistic images with high spatial resolution has also been shown. Furthermore, the investigation of polydispersity within inhomogeneous media has demonstrated the possibility of using 25 appropriate scattering phase functions in order to represent the scattering process of droplets from 2 up to 200 μm (when illuminated at 532 nm). From these considerations, the MC model can now be applied to practical cases of spray diagnostic.

In the first section of this chapter, a typical hollow cone water spray is experimentally studied using laser sheet imaging. Mie and LIF signals are recorded simultaneously and the spray is imaged when running at various injection pressure. Effects of multiple scattering are qualitatively shown on the resultant experimental images. The droplets size (around 25 μm) is characterized via PDA measurements. From these experiments, a two-dimensional mapping of the extinction coefficient and droplet size is deduced at 7 bars pressure of injection. These data are introduced within the MC model and a comparison between experimental and simulated images is provided.

The second section is devoted to the analysis of a classical cross-source-detector geometry. The aim of this investigation is to deduce the optimum optical configuration for the detection of the singly scattered light. The detector is located at various position from the light source and several detection acceptance angles are employed. Both isotropic and anisotropic scattering are considered within a homogeneous cubic volume. The optimization of single light scattering detection is deduced from various geometrical configurations and conditions of detection.

7.1 Optical measurements and MC simulations of a hollow cone spray

A hollow cone water spray is characterized experimentally using planar Mie and LIF imaging techniques. The pressure of the water injected through the pressure-swirl atomizer is set to several values and increased progressively until reaching very fine atomization. Images obtained from both techniques are compared and the attenuation of the laser sheet is quantified for each injection pressure. The effect of multiple scattering on the resultant images is also described. From the resultant experimental data, MC simulations are performed to estimate the amount of singly scattered photons detected. Finally, the experimental and simulated images are compared for the case of 7 bars pressure of injection.

7.1.1 Experiments

The nozzle employed in the experiment is a *Delavan* pressure-swirl nozzle type, producing a hollow cone with nominal 70° cone angle. Deionized water is sprayed for injection pressures comprised from 1.5 bars up to 28 bars into an optical chamber set to the atmospheric pressure. The laser light which illuminates the spray is produced by a Continuum Surelite II Nd:YAG laser. Nd:YAG laser generates coherent light pulses of 5-7 ns at fundamental wavelength 1064 nm. Using a second harmonic generator, a 532 nm laser source is commonly produced and widely applied in spray diagnostics. In our experiment, the fourth harmonic is selected and $\lambda = 266$ nm. At this harmonic, the laser light energy equals ~ 70 mJ per pulse. Laser harmonics were spatially separated with a lithium fluoride prism and a set of dichroic mirrors. The laser sheet is formed by the association of a semi-convergent and a semi-divergent lens positioned at a respective distance equal to the sum of their focal distance. The laser sheet dimension is ~ 1 mm wide in the middle of the spray and 30 mm high.

The fluorescence signal is obtained by diluting sodium salicylate at 0.058 g/l, in deionized water. Sodium salicylate is known as the sodium salt of salicylic acid (an active ingredient of aspirin) and emit in average at 409 nm when excited at 308 nm.

Both Mie and LIF images are detected simultaneously by a LaVision SprayMaster-3 CCD camera fitted with a LaVision IRO image intensifier. The Mie signal is separated from the LIF signal using two 266 nm mirrors on two separated optical channels.

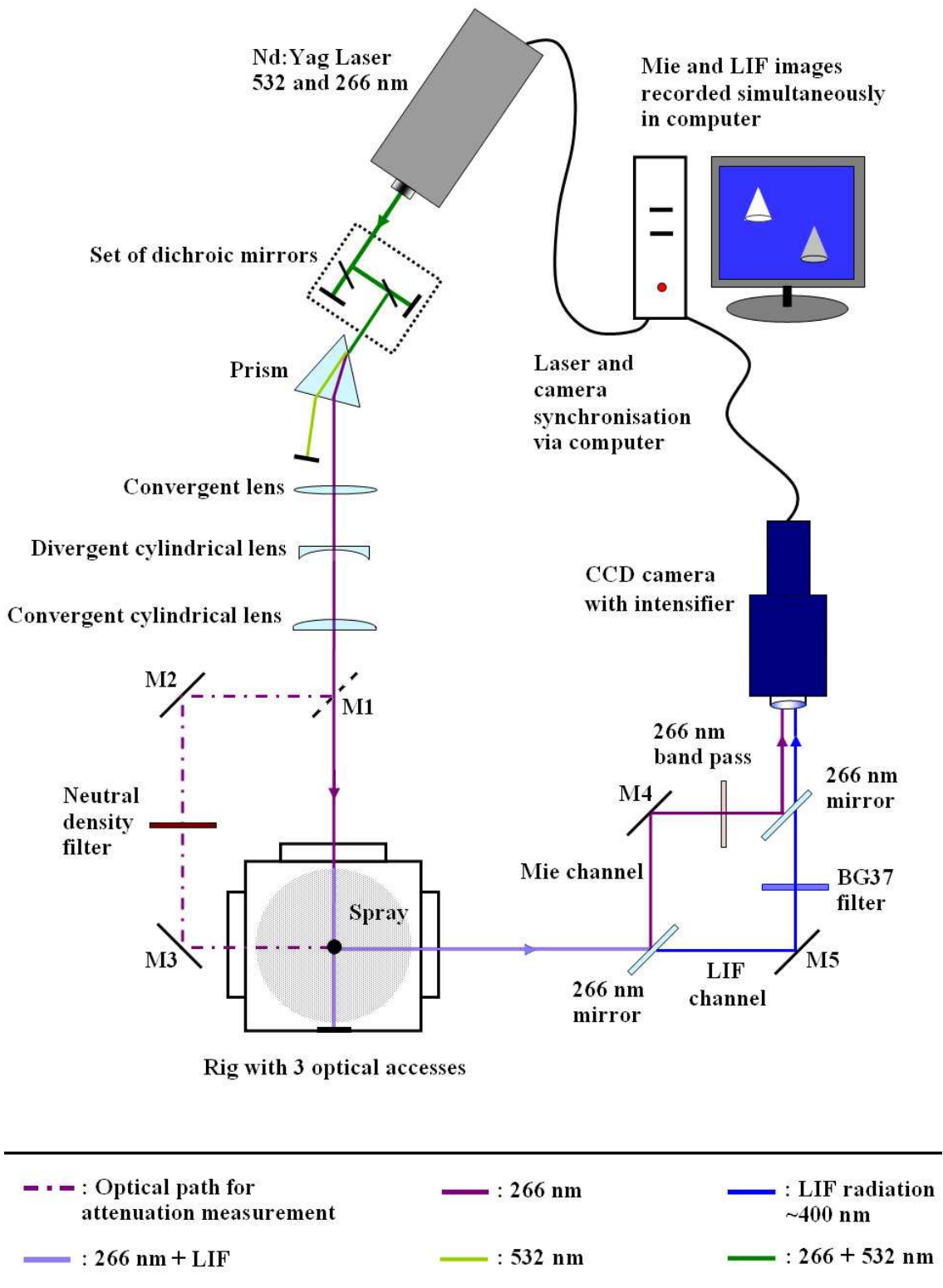


Figure 7.1: Mie and LIF dual imaging setup. Only one camera records both images which are separated using two independent channels. By positioning the mirror M1, a second optical path for is used for measuring the laser light intensity transmission.

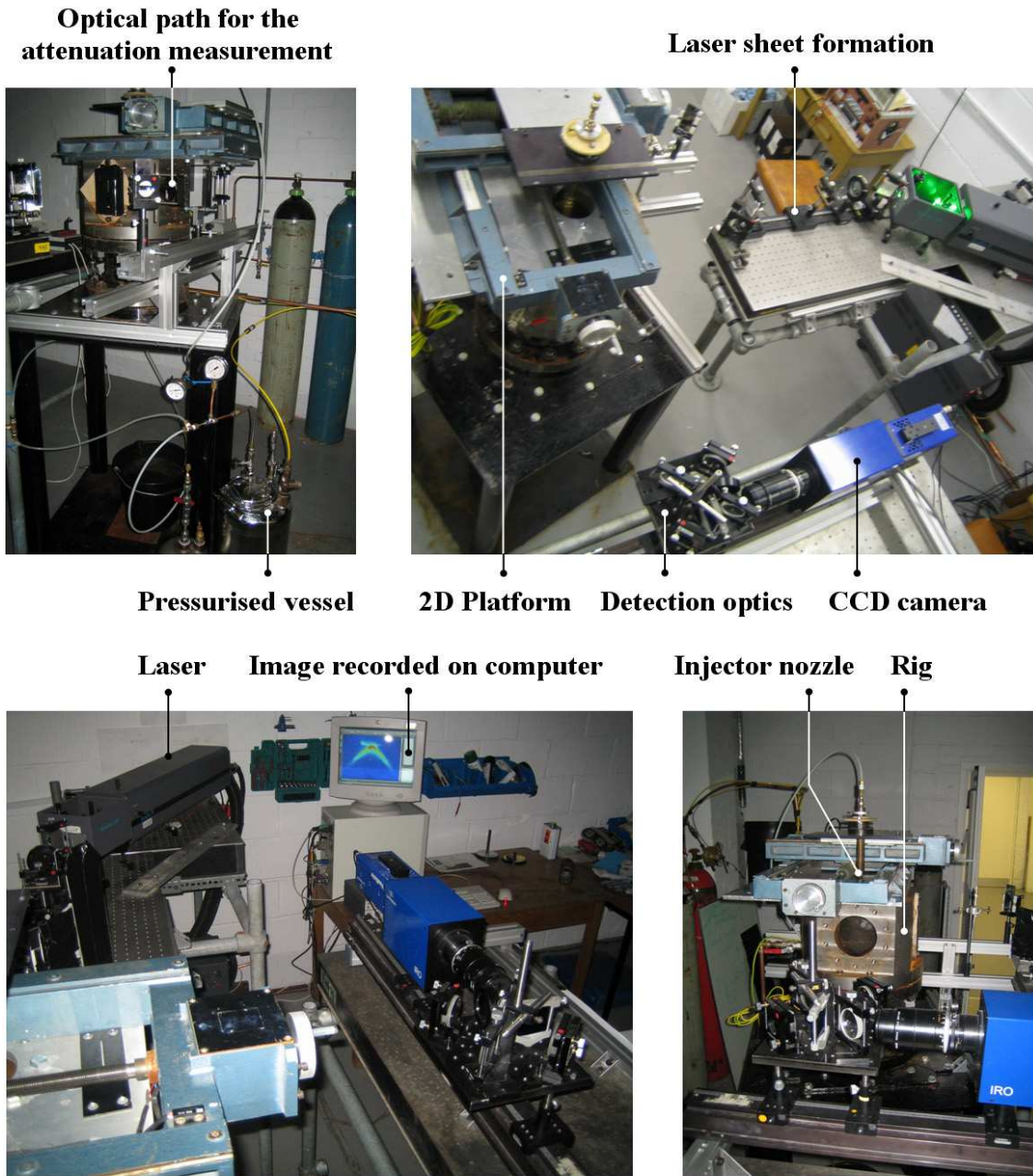


Figure 7.2: Photograph of the experimental setup.

A BG37 filter (no transmission for $\lambda < 300$ nm) is applied in the LIF channel, whereas, in the Mie channel a 266 nm band pass filter is used. The gain of the intensifier is fixed to 8. Images are spatially separated (to avoid overlapping issues of the Mie and LIF images simultaneously detected) by adjusting accurately the orientation of the mirrors M4 and M5 (see Fig.7.1). The detection acceptance angle of the collection optics equals 2.5° . This dual imaging set up was originally presented by Le Gal (1999) an illustration is given in Fig.7.1 with a photography in Fig.7.2.

A second optical path is also installed (by positioning the mirror M1 on the initial laser sheet path) to measure the intensity transmission of the laser sheet through the spray (for this measurement, the nozzle is rotated around its vertical axis with an angle of 90° from its original position). Figure 7.3 shows the intensity profile of the laser sheet before and after crossing the spray along the central axis. It is seen from Fig.7.3(a) that the light intensity is reduced with increasing the water pressure of injection from 1.5 to 28 bars. The transmission of light is lower in the near nozzle region and reaches a minimum value of ~ 0.2 at $p_i = 28$ bars (Fig.7.3(b)). The relatively large detection acceptance angle ($\theta_a = 2.5^\circ$) and the forward nature of the droplets ($g=0.87$) introduces errors in the deduction of the optical depth. From the Beer-Lambert law, a transmission I_f/I_i of 0.2 gives an optical depth of 1.6. In fact, due to the multiple scattering contribution, this value can be estimated to be over 2. The scattering of light within the presented spray falls then in the early intermediate single-to-multiple scattering regime. Explanation regarding the correction of Beer-Lambert predictions are provided in subsection 8.4.

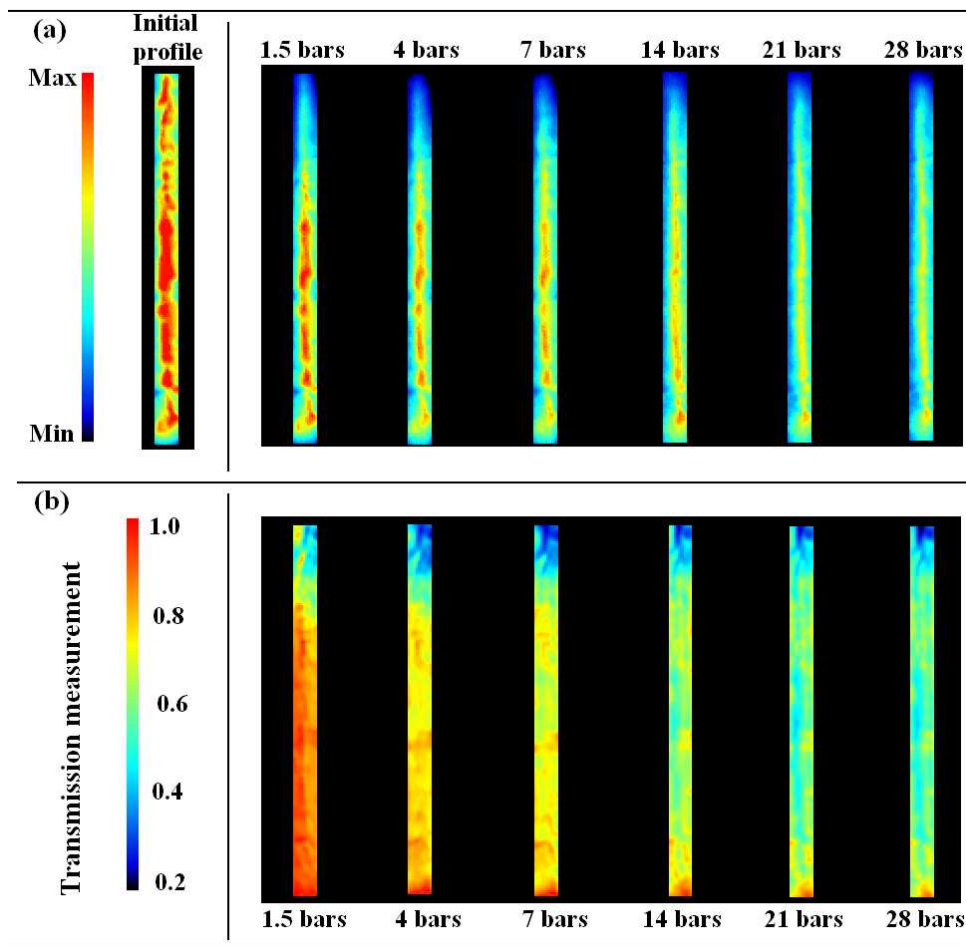


Figure 7.3: Measurement of the intensity transmission of the laser sheet. (a) shows the vertical profile of the laser sheet and (b) is the transmission ratio I_f/I_i .

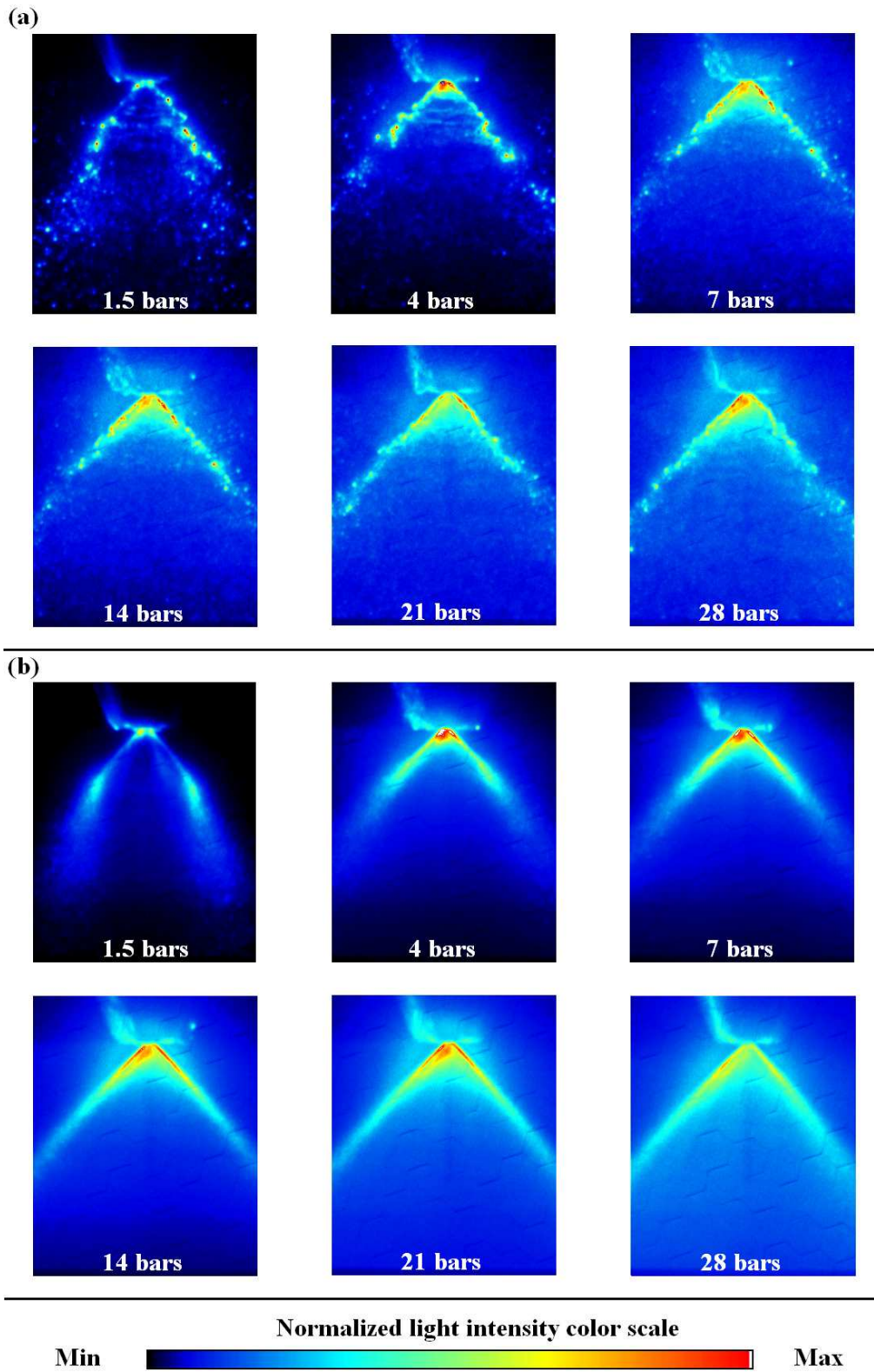


Figure 7.4: Mie images at various pressure of injection. (a) are single shots whereas (b) corresponds to the averaged images of 100 single shots.

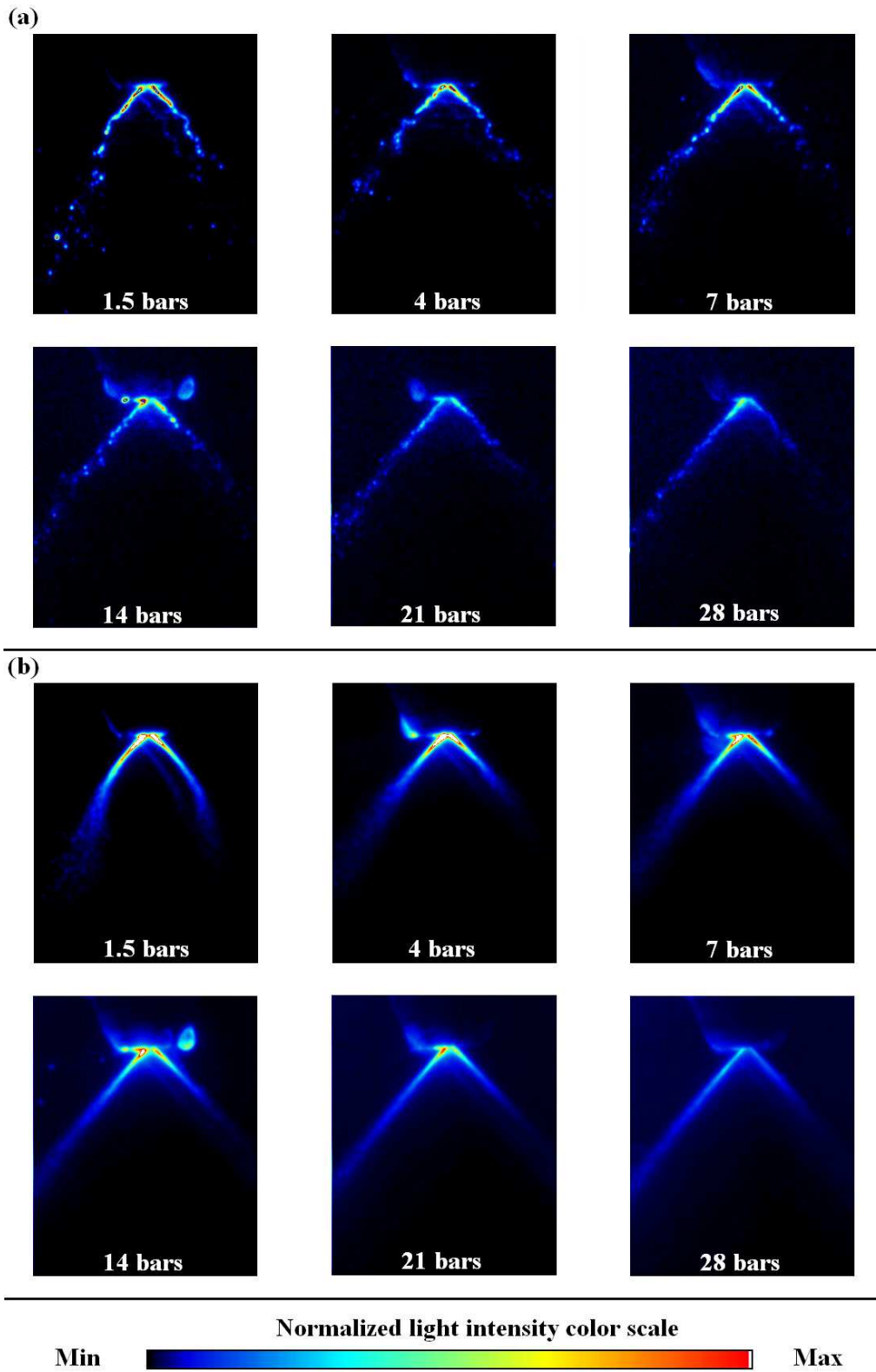


Figure 7.5: LIF images at various pressure of injection. (a) are single shots whereas (b) corresponds to the averaged images of 100 single shots.

The experimental Mie images are presented in Fig.7.4 at various water pressure of injection (between $p_i=1.5$ bars and $p_i=28$ bars). In Fig.7.4(a) single shot images are shown whereas in Fig.7.4(b) averaged images of 100 shots are shown. By increasing p_i the size of droplets decreases, whereas their concentration increases. The spray becomes denser making multiple scattering stronger. The image details becomes blurred. The surrounding brightness on each images gives an indication to the amount of multiply scattered light detected. It is also seen that below 4 bars the breakup of the conical liquid sheet occurs a few millimeters from the nozzle tip; above this pressure it occurs promptly on exit.

Figure 7.5 shows the LIF experimental images obtained at different water pressure (between $p_i=1.5$ bars and $p_i=28$ bars). In Fig.7.5(a) single shot images are shown whereas in Fig.7.5(b) averaged images of 100 shots are presented. As the LIF signal is volume dependant, the maximum light intensity is detected in the near nozzle region at low injection pressure, due to the presence of large liquid elements. The brightness of the diffused light observed on the Mie images at high p_i does not occur here. The LIF images are, then, less affected by the presence of multiply scattered photons. However, the light intensity is strongly attenuated along the laser sheet path when increasing p_i . The LIF images present better contrast when compared to the Mie images, with distinct separation between the liquid and gas phases. However, the LIF light intensity detected is much lower, resulting into a lower SNR.

The Root Mean Square (RMS) of the averaged Mie and LIF images is given in appendix C, Fig.C.3. RMS images offer a measurement of the light intensity fluctuations. They highlight the variations of droplets position, and in the same time, they remove the fairly constant intensity detected from multiple scattering. RMS images present, then, interesting features which probably should be further investigated and applied to laser sheet imaging.

7.1.2 Monte Carlo simulation

The data required for the MC simulation is the the extinction coefficient μ_e and the droplets diameter D . A two-dimensional mapping of the extinction coefficient is approximated using the experimental LIF images combined with the measurement of the light sheet intensity transmission. The process is illustrated in Fig.7.6 and explained as follows.

Two averaged (over 100 single shots) LIF images are considered. In the first image the

initial horizontal axis of the spray is orientated at 0° angle with the axis of the laser sheet; whereas, in the second case this orientation is 180° . In other words, the spray is illuminated from one side on the first image and from the other side and the second image. The two images are added and averaged (see Fig.7.6(a)). This bidirectional illumination technique, which was presented by Sick and Stojkovic (2001) and Talley *et al* (1996), allows correcting partially the images from attenuation issues along the laser path. From the LIF corrected images, the number of photons $k_{(n)}$ recorded per pixel is assumed to be proportional to the LVF. Assuming that a medium contains only droplets of identical extinction cross-section (all droplets are of same size), the light intensity recorded becomes then proportional to the number density of droplets and to the extinction coefficient. From these assumptions, it is considered that the 2D light intensity mapping of the corrected LIF images gives intensity values linearly related to the value of the extinction coefficient. If all pixels have the same extinction coefficient $\bar{\mu}_e$ along the horizontal axis, the value of $\bar{\mu}_e$ is deduced from the transmission I_f/I_i as:

$$\frac{I_f}{I_i} = e^{-\bar{\mu}_e \cdot L} \implies \bar{\mu}_e = -\frac{\ln(I_f/I_i)}{L} \quad (7.1.1)$$

where L is the total distance crossed by the laser sheet. If now pixels are characterized by various extinction coefficients as illustrated Fig.7.6(c) for 3 pixels, it is deduced that the transmission equals:

$$\frac{I_f}{I_i} = \frac{I_1}{I_i} \cdot \frac{I_2}{I_1} \cdot \frac{I_f}{I_2} = e^{-\mu_{e1} \cdot l_p} \cdot e^{-\mu_{e2} \cdot l_p} \cdot e^{-\mu_{e3} \cdot l_p} = e^{-(\mu_{e1} + \mu_{e2} + \mu_{e3}) \cdot l_p} \quad (7.1.2)$$

The sum of the extinction coefficients becomes then:

$$\sum_{n=1}^{n=3} \mu_{e(n)} = -\frac{\ln(I_f/I_i)}{l_p} \propto \sum_{n=1}^{n=3} k_{(n)} \quad (7.1.3)$$

where l_p is the length of a single pixel. From the previous considerations, the sum of the extinction coefficients $\mu_{e(n)}$ is finally assumed to be proportional to the sum of the number of photon per pixel $k_{(n)}$ of the corrected LIF image.

By measuring the transmission I_f/I_i along the light sheet (see Fig.7.6(b) and Fig7.3) the value of the scattering coefficient can then be redistributed within each pixel. A 2D mapping of μ_e is finally extracted and results are presented in Appendix C, Fig.C.1 at low and high water pressure of water injection.

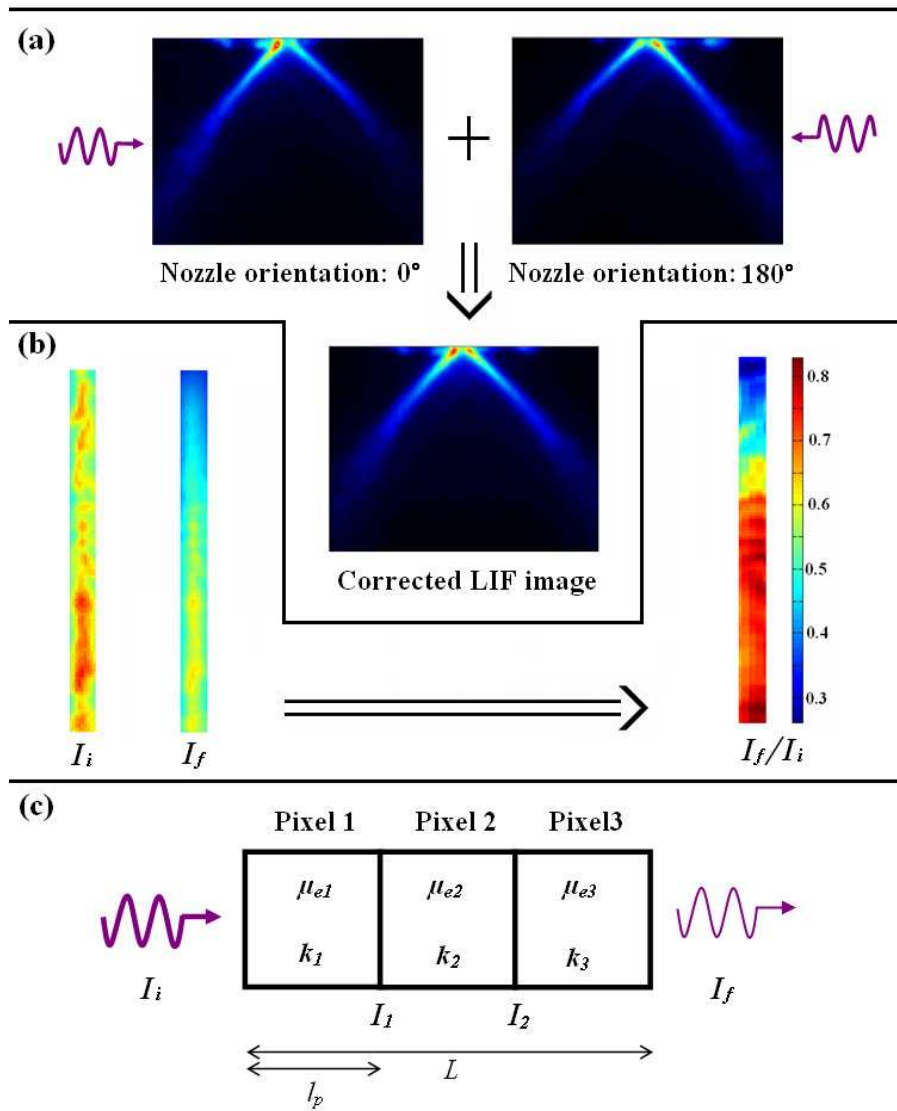


Figure 7.6: Two-dimensional deduction of the extinction coefficient: First the LIF images are corrected from attenuation (a), then the measurement of the transmission is performed (b) and finally $\mu_{e(n)}$ is deduced for each pixel n as a function of the light intensity $k_{(n)}$.

The deduction of the droplet diameters for the MC simulation is performed from PDA experimental data. At $p_i=7$ bars, the concentration of droplet remains relatively low, allowing reliable measurements. The geometrical mean diameter of the droplets is measured every 2 mm vertically and horizontally, downstream the nozzle tips using a 3-component Dantec PDPA system. The setup is configured to operate in 30° forward scatter mode. The launch optics are adjusted for a focal length of 600 mm and positioned so that the beams crossed over the centre of the rig. The 2D surface probed corresponds to the one crossed by the laser sheet during the dual Mie/LIF imaging experiment. It is found that the mean droplets diameter ranges from 5 μm up to 38 μm with position within the spray (Fig.data2(b)). The global mean diameter, averaged over the full plane, is 25 μm (assum-

ing a 266 nm wavelength the resulted anisotropy factor g equals 0.87 - see Fig.4.9). Due to the lack of spatial resolution, these data have been redistributed using a 2D mapping of SMD previously measured by Le Gal (1999) for the same injector running under same operating conditions. Even if this approach is not exact, it provides a high spatial resolution required for the MC simulation. The 2D mapping of the estimated droplet diameters is given in Fig.7.7(b) with the 2D mapping of the extinction coefficient in Fig.7.7(a).

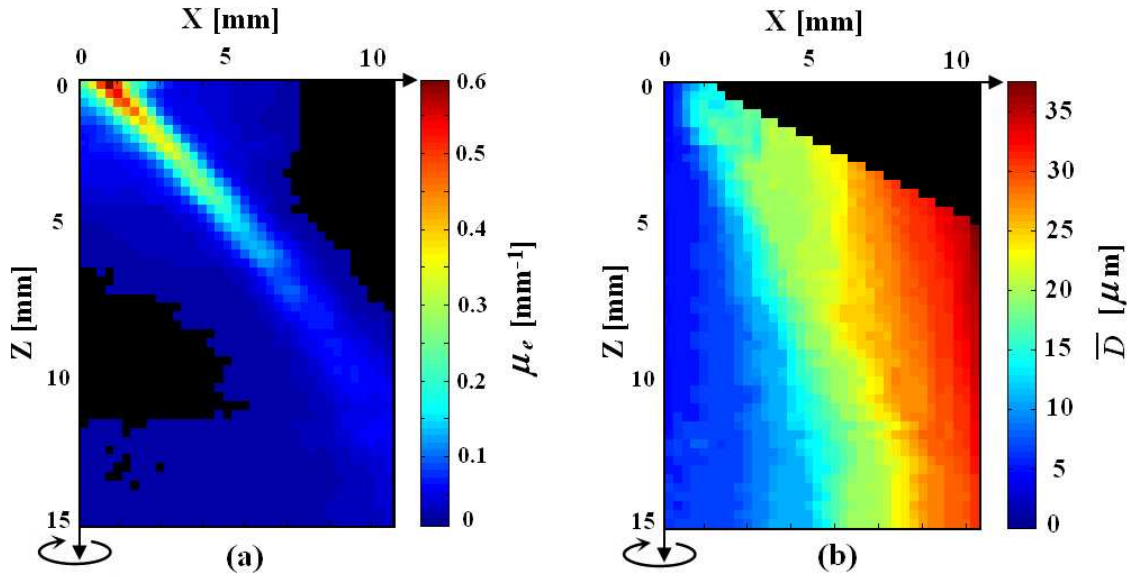


Figure 7.7: Spatial distribution of the extinction coefficient (a) and of the geometrical mean droplet diameter (b) through the central plane of the hollow cone spray. By rotating the data around the central vertical axis MC input data are generated in 3D.

The data used in the computational model is in the form of a 2D half plane as shown in Fig.7.7. The spray is assumed symmetrical and the full 3D structure is initially constructed in the model by rotating the data around the vertical axis. The final 3D simulated volume is divided into cubic cells characterized by a given μ_e and \bar{D} . Each pixel on Fig.7.7 represents a square area with $220 \mu\text{m}$ side and the cubic cells assumed in the MC model have the same side length. Figure 7.8 is a schematic of the MC simulation. The dimensions of the full simulated volume are 20 mm X 20 mm X 15 mm. The laser sheet is assumed monochromatic at 266 nm and crosses the scattering medium in the middle of the spray.

In the simulation, the laser sheet is 1 mm wide and 15 mm high with a flat distribution of light intensity. Droplets are considered spherical and non-absorbing with a refractive index of $1.4+0.0i$. The detection area is one of the faces of the scattering volume parallel to the laser sheet (Fig.7.8). The detector acceptance angle is set to $\theta_a = 2.5^\circ$. With this angle a large number of photons are required to obtain good statistics and 5 billion photons are sent. In each cell of the simulated volume, the average diameter of drops

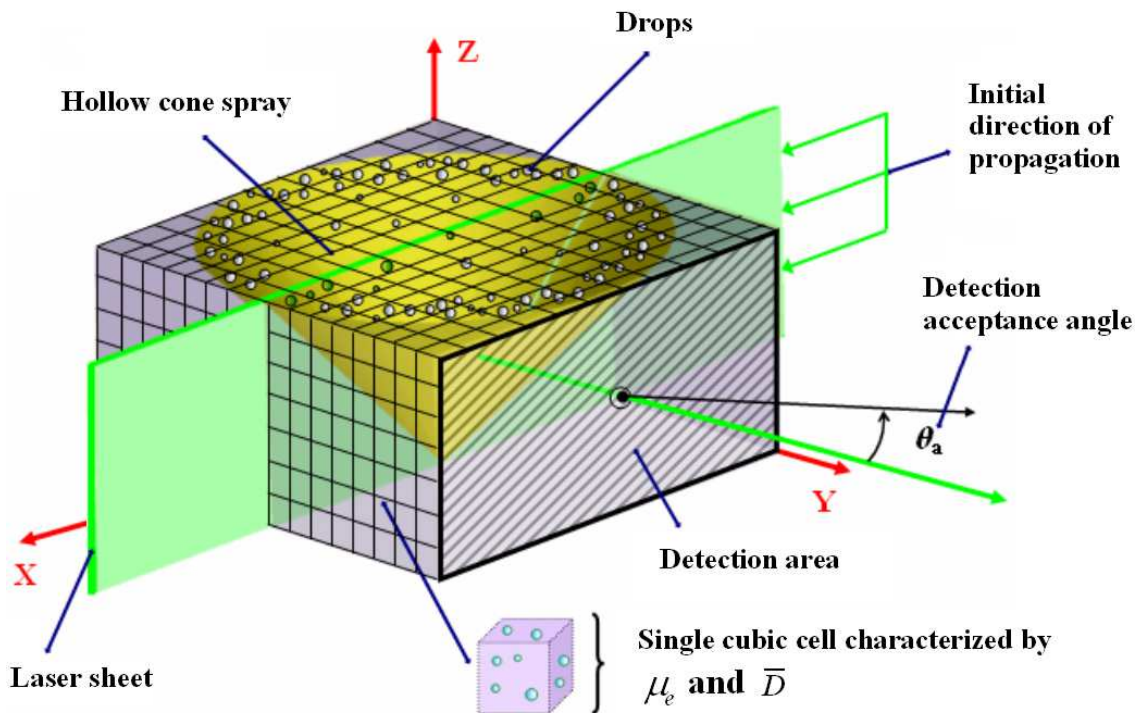


Figure 7.8: Illustration of the MC simulation. The optical properties of the spray are distributed within the 3D using homogeneous elementary cubic cells.

is given. Instead of taking the exact scattering phase function related to this average diameter, an approximate phase function is chosen using the method M_2 described and verified in section 6.3. However in the present case, the incident light wavelength is 266 nm (instead of 532 nm) and the droplet size ranges between 1 and 100 μm (instead of 2-200 μm).

7.1.3 Comparison discussion

Figure 7.9 shows the divergences between the experimental Mie image and the simulated MC image. The laser light sheet enters on the left hand side of the image and leaves on the right. It can be seen that when all detected photons are included (Fig.7.9(a)), the basic spray structure of the simulated image agrees well with the experimental image (Fig.7.9(b)) even if some differences on the light intensity distribution can be noticed. These differences are explained by several factors: Firstly the restricted number of photons computed compromises the definition of the MC image. Secondly data used in the simulation are symmetrical around the spray axis, whereas real sprays of this type are known to be asymmetric by up to 15% in mass flow rate. Thirdly, input MC data of both the scattering coefficient and the droplet size have been approximated. The lack of ac-

curacy in the input data does not allow reaching a simulated image with a light intensity distribution equals to the experimental image as presented in section 6.2.1. Finally the experimental intensity profile distribution has been approximated in the simulation to a flat laser sheet. By considering the real laser sheet profile (see Fig.6.10, section 6.2.1) more realistic simulation would be obtained.

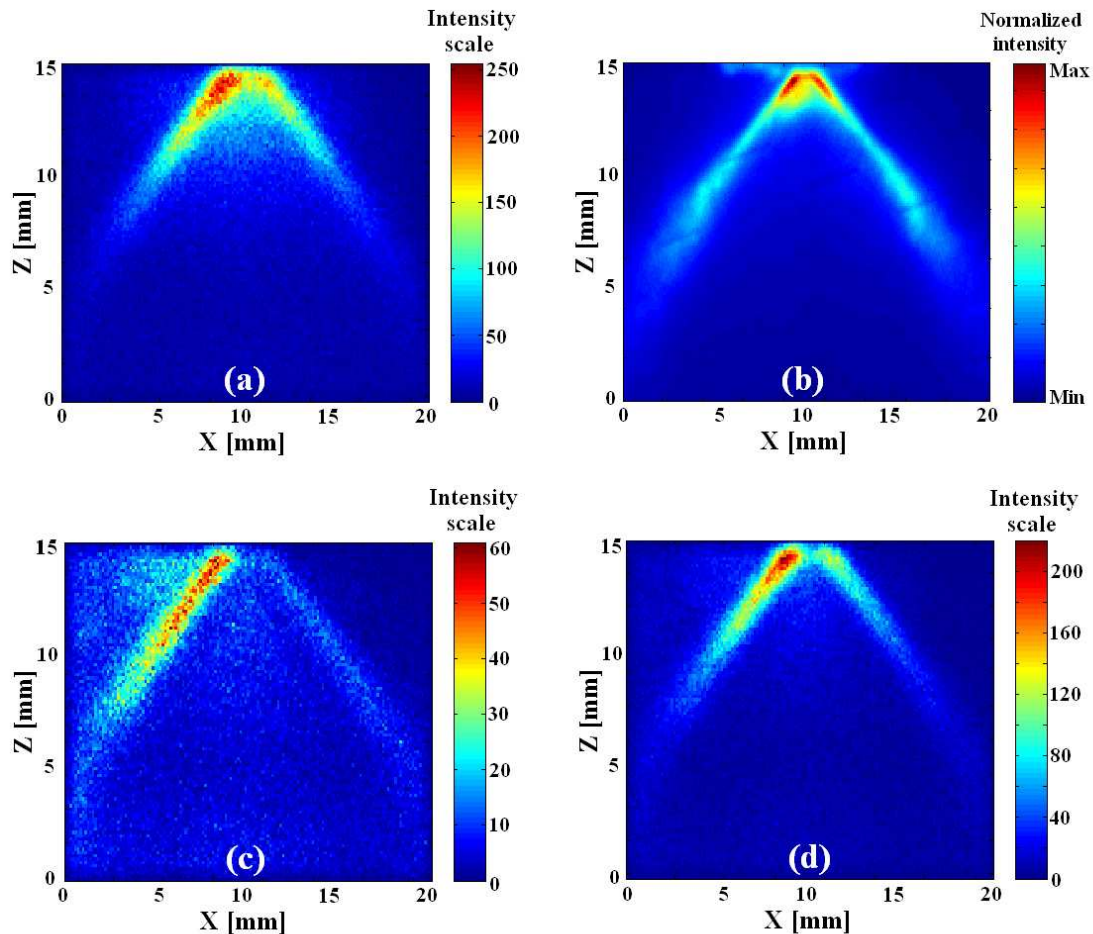


Figure 7.9: Comparison between the simulated (a) and experimental (b) images for the planar Mie imaging of a hollow cone water spray. (c) and (d) are also results of MC simulation: (c) is generated from the singly scattered detected photons only and (d) is generated by removing the multiply scattered light outside of the laser sheet plane.

By taking into account all these factors the spatial resolution of MC images will reach the one obtain in experimental images allowing an accurate comparison of both images. Figure 7.9(c) is an image generated by numerically filtering Fig. 7.9(a) to include only singly scattered photons. It is seen that most of the detected photons are positioned on the left hand side of the spray (the side on which the laser sheet enters). Singly scattered light intensity is strongly reduced on the right edge of the spray image. However, as many of the scattering events are forwards scattering events with low angular deviations,

the structure and direction of the light sheet is largely preserved, and the right part of the spray can be clearly observed in Fig.7.9(a) and (b). It is seen that for single scattering the maximum number of detected photons per pixel is ~ 60 counts/pixel; whereas, with both single and multiple scattering the maximum is ~ 250 counts/pixel. Only 24% of the total number of detected photons has been singly scattered. The traditional assumption that all detected photons have been scattered only once, and carry information about single droplets only, is questionable. Multiple scattering occurring is dominant (76%) even for a spray assumed dilute and in which PDA measurements are possible.

The experimental Mie images compared to the simulated results clearly introduce influence of multiple scattering in the detection (only $\sim 30\%$ of the detected photons correspond to single light scattering intensity). From these results, it is deduced that the quantitative analysis and post processing of input data can be performed for the further reverse MC modelling. However, it is admitted from the results obtained in section 6.2.3 that if the exact input data could be incorporated within the MC mode, the distribution of the intensity profile would be equal to the distribution found in the experimental images in a same manner that results found in section 6.2.

7.2 Crossed source-detector geometry analysis for spray diagnostics

The aim of this study is to describe the variation of light intensity of several scattering orders, depending on the value of fundamental parameters. These parameters are the detection acceptance angle, the optical depth, the scattering process (isotropic or anisotropic) and the source-detector geometry. From this investigation, the deduction of the most efficient source-detector configurations for the detection of single light scattering intensity is presented. Such optimization is an initial and fundamental step in the development and improvement of new optical spray diagnostics.

7.2.1 Description of the MC simulations

The geometry of the simulations is previously presented and investigated analytically in section 6.1. An illustration is given in Fig.7.10: (a) is the source-detector configuration in 3D; (b) and (c) present a 2D view from the (XY) plan with respectively $h > 0$ and $h = 0$. The view from the (XZ) plan is seen in (d) with $\beta = 0^\circ$ and in (e) with $\beta < 0^\circ$. The scattering medium is considered as a cubic and homogeneous volume of dimension

$L = 50$ mm. For each detected photon the scattering order and the distance h from the incident beam is stored in a data file. The intensity of different scattering orders is then determined by the number of photons recorded and can be plotted as a function of h . It is demonstrated in section 6.1, that the MC code agrees very well with the analytical approach for the measurement of $I_{(2)}(h)$ considering isotropic scattering and an angle β of 90° .

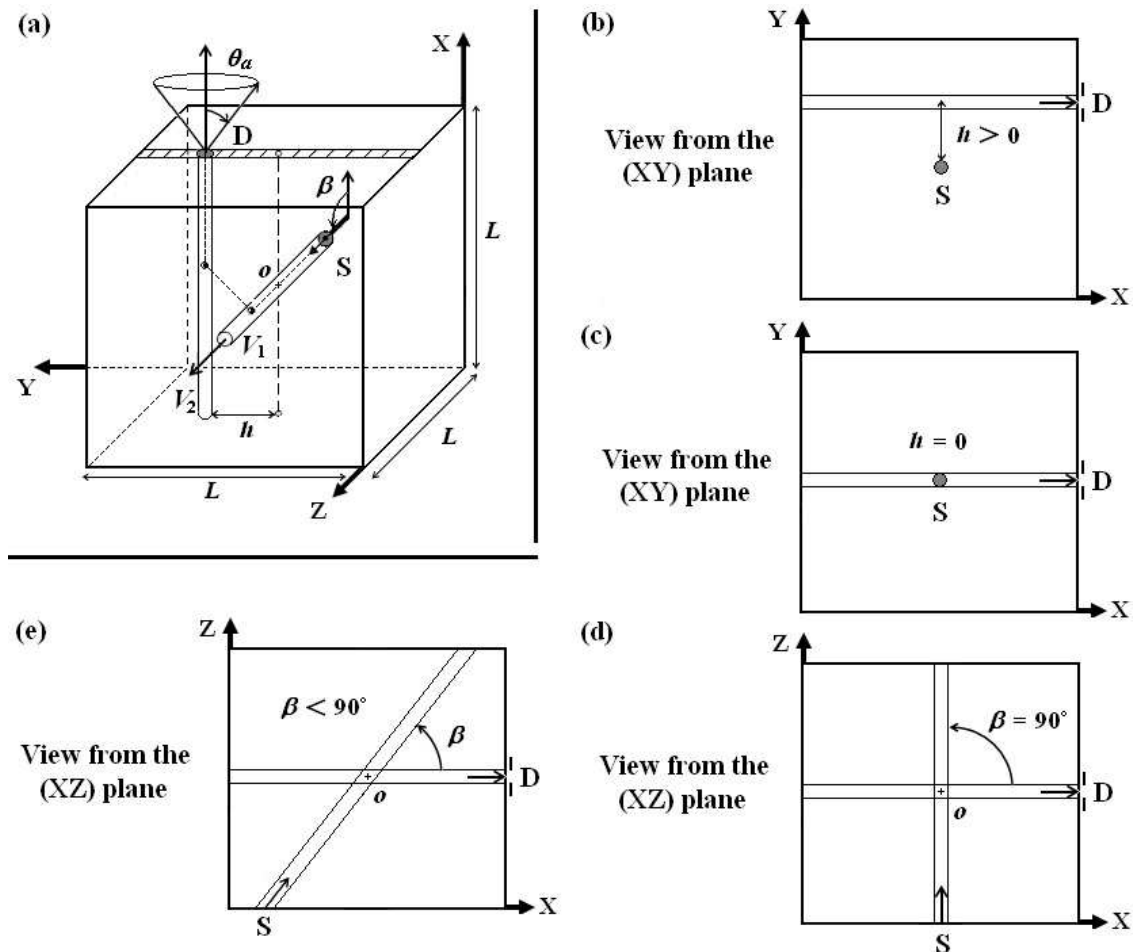


Figure 7.10: Geometry of the simulation: (a) is the 3D configuration, (b)-(c) are seen from the (XY) plane showing the variation of h and (d)-(e) present a view from the (XZ) plane for different values of β .

In this section, fundamental optical parameters are investigated with their effects on the detection of the light intensity at various scattering order n . These parameters are:

- The optical depth OD .
- The scattering process: isotropic or anisotropic.
- The detection acceptance angle θ_a .
- The source-detector angle β .

The first part of the section concerns only the isotropic scattering case. In the second part the MC simulations are performed with an anisotropic phase function based on spherical droplets of $15 \mu\text{m}$ diameter. This phase function was deduced from the Lorenz-Mie Theory considering a realistic spray problem. Detailed information is provided in section 7.2.3. Different scattering coefficient have been considered ranging from $\mu_s = 0.04 \text{ mm}^{-1}$ to $\mu_s = 0.18 \text{ mm}^{-1}$. Considering the dimension of the cube (50 mm side), the resulting optical depth ranges then from from 2 to 9 which is characteristic of the intermediate scattering regime.

7.2.2 Results and analysis for isotropic scattering

In all results presented here, the crossed source-detector geometry is based on an angle β of 90° and the scattering process is assumed isotropic.

Fig.7.11 shows the effect of the detection acceptance angle on the total detected intensity as a function of h . For each detection acceptance angle, the intensity has been normalized to 1 at the maximum value of $I_{(tot)}$ found at $h = 0$. Two optical depths have been considered: In (a) $OD = 2$ and in (b) $OD = 8$. In both case, the decreasing of the light intensity with respect to the distance h is more important for small θ_a than large θ_a .

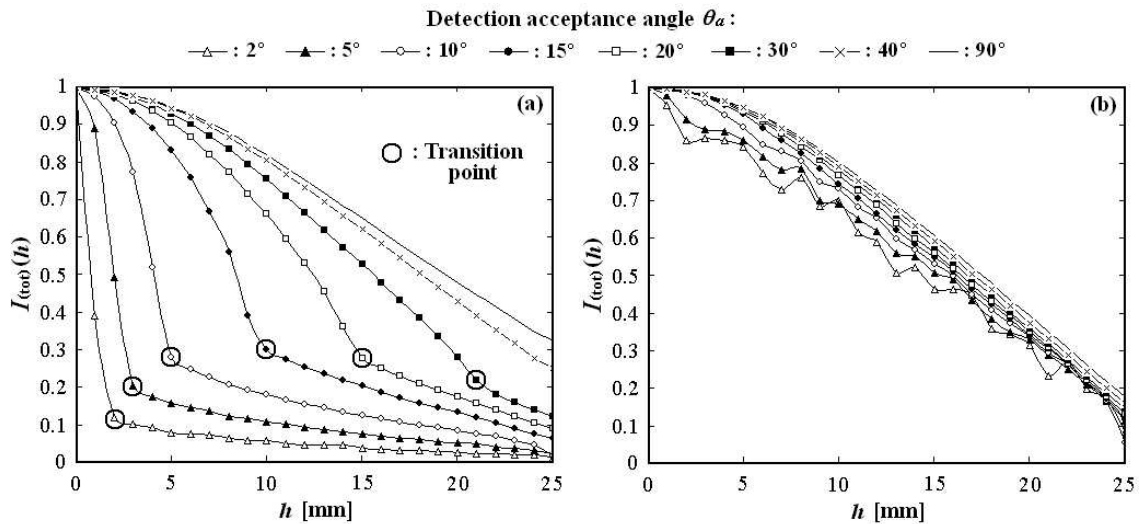


Figure 7.11: Normalized total intensity versus h . The symbols represents different values of the detector numerical aperture. In (a) the optical depth is fixed to 2; whereas, in (b) the optical depth equals 8. The source-detector angle, β , is fixed to 90° .

When $OD = 2$ (Fig.7.11 (a)), the total intensity reduces quickly (at small θ_a) for the first values of h where the first and the second scattering order both dominate the detected signal. By increasing h , the single scattering is, at some point, not detected and

the contribution of large scattering orders appears more clearly, making the curve decrease suddenly though smoothly. The transition point where the single light scattering is no longer detected can be visualized on the graph where the curves start to decrease smoothly. This feature appears to be less evident at large θ_a where the single scattering is still detected for large h .

When $OD = 8$ (Fig.7.11 (b)), the single scattering no longer dominates the signal and the transition point from which the single light intensity is not detected cannot be seen. The effect of the detection acceptance angle on the variation of the total light intensity detected becomes insignificant and the decrease of $I_{(tot)}$ as a function of h is found to be continuously smooth even for small θ_a .

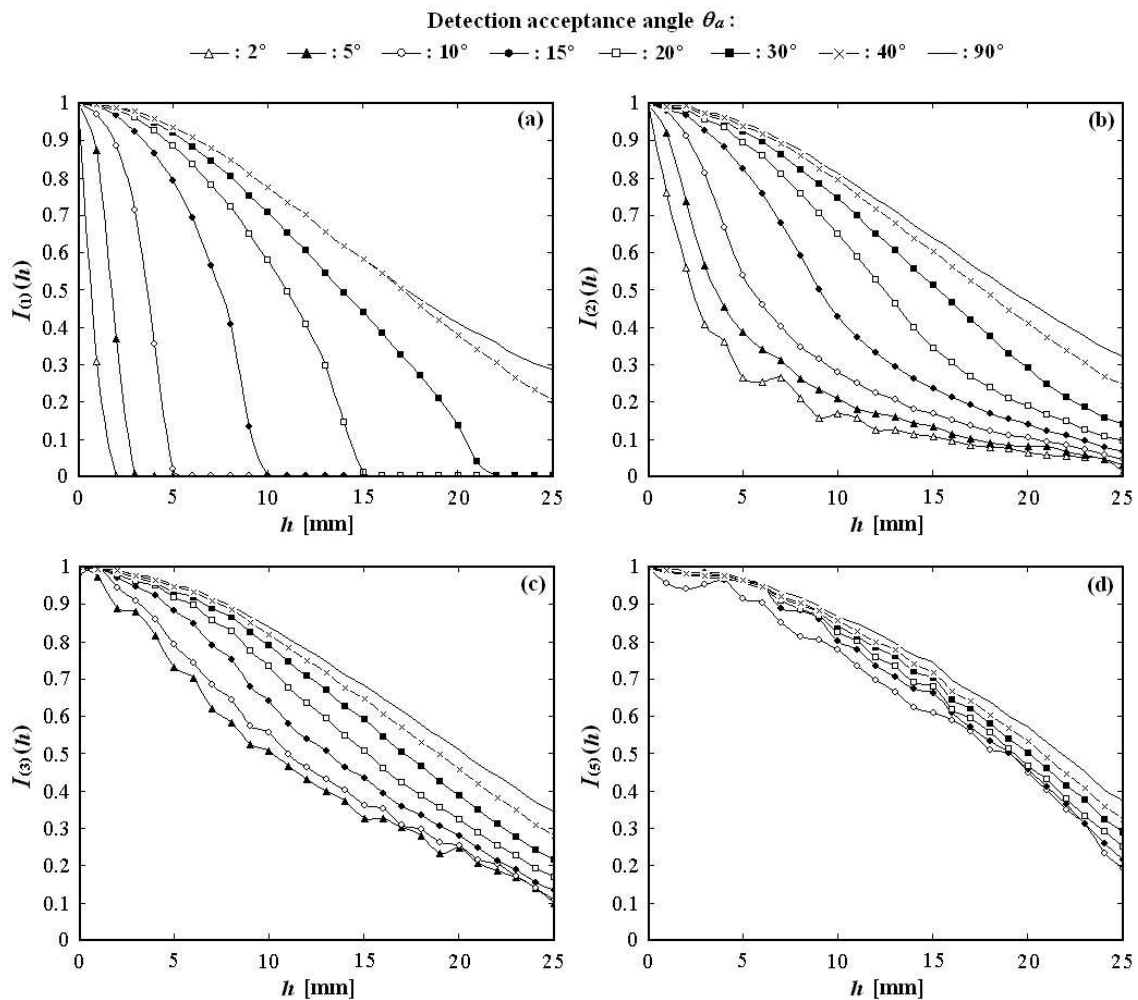


Figure 7.12: Normalized intensity of different scattering orders versus h : (a) single light scattering, (b) double scattering, (c) triple scattering, (d) fifth-order scattering. The symbols represents different values of the detector numerical aperture. The source-detection angle, β , is fixed to 90° and the optical depth equals 2.

In Fig.7.12, the independent contribution of the first, second, third and fifth scattering orders are depicted. The effect of the detection acceptance angle on the detected intensities of different scattering orders was investigated at $OD = 2$. Once again, each intensity curve is normalized.

In Fig.7.12 (a) and (b) it can be seen that single and double light scattering are strongly dependent on acceptance angle. The reduction of $I_{(1)}$ and $I_{(2)}$ in respect with the distance h is considerably more important for small θ_a than for large θ_a . On the contrary, for higher scattering order such as $I_{(3)}$ (Fig.7.12 (c)) and $I_{(5)}$ (Fig.7.12 (d)), the effect of the detection acceptance angle is clearly reduced. This can be explained by considering the trajectories of the photons packets between the source and detector. For single and double scattering, in order to enter a detector with a small acceptance angle these trajectories are clustered into a compact locus. The locus of trajectories with high orders of scattering will be less compact.

The relative intensity $I_{(n)}/I_{(tot)}$ contributed by different scattering orders n is plotted as a function of detector acceptance angle in Fig.7.13. The distance $h = 0$ and the optical depth equals 2 in (a) and 8 in (b).

For $OD = 2$ (Fig.7.13 (a)), single scattering dominates at small θ_a and reaches a maximum value of 83% for $\theta_a = 2^\circ$. By extrapolating the curve to the ideal case $\theta_a = 0^\circ$, it can be approximated that $I_{(1)}$ equals ~ 92 of the total detected signal. As expected, the contribution of single scattering decreases with increasing detector aperture. This decrease is important at small θ_a , becomes smooth for $\theta_a > 20^\circ$ and reaches a minimum value of $I_{(1)} = 32\%$ at $\theta_a = 90^\circ$. The contribution of single and multiple (double plus higher orders) scattering becomes equal at a detector acceptance angle of 15° . For $\theta_a > 15^\circ$ multiple scattering dominates the detected signal. With increasing θ_a , the detector collects scattered light from an increasing volume of the medium outside the cylindrical source beam where only multiple scattering occurs. The respective scattering order 2,3 and 5 all increase with θ_a . The light intensity of the 10th scattering order almost equals zero and is insignificant in the graph. The effects of acceptance angle becomes more and more negligible as larger scattering orders are considered. Finally, these results demonstrate that even at relatively low optical depth the amount of multiply scattered light detected can dominate if the acceptance angle is large.

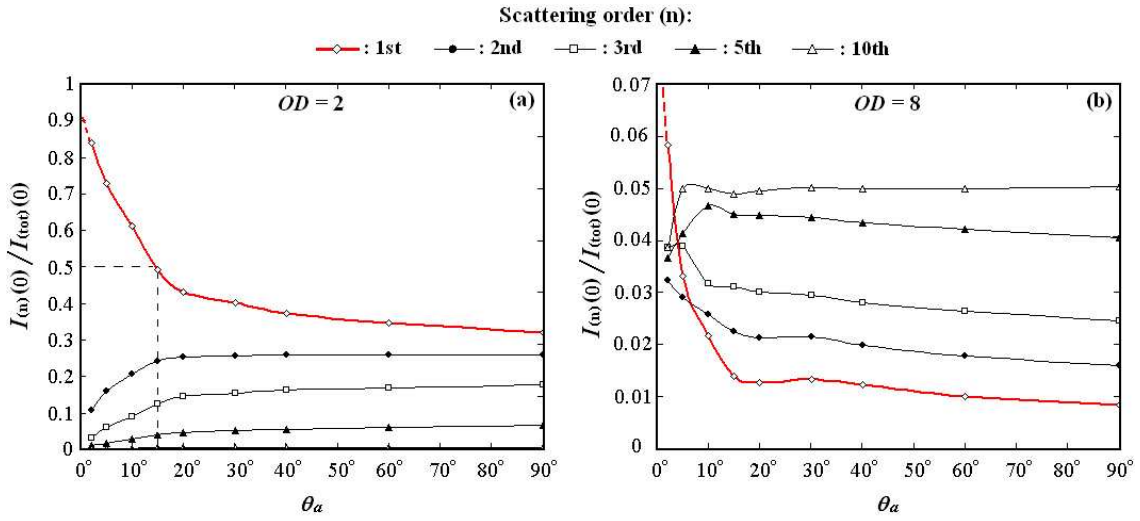


Figure 7.13: Relative intensity of each scattering order as a function of the detection acceptance angle at $h = 0$ and $\beta = 90^\circ$. In (a) the optical depth is fixed to 2; whereas, in (b) the optical depth equals 8.

For $OD = 8$ (Fig.7.13 (b)), it can be seen that the contribution of the single scattering no longer dominates and reaches a maximum value of 6% for $\theta_a = 2^\circ$. By extrapolating the curve to the ideal case $\theta_a = 0^\circ$, $I_{(1)}$ can be approximated as reaching $\sim 12\%$ of the total detected signal. It is thus deduced that slight changes of small acceptance angles ($\theta_a < 10^\circ$) have a major effect on the amount of detected single scattering. On the contrary, a change of θ_a for $\theta_a > 20^\circ$ does not affect the ratio $I_{(1)}/I_{(tot)}$ which remains equals to $\sim 1.3\%$. The scattering orders 2 and 3 decrease smoothly with θ_a . The 5th scattering order increase until $\theta_a = 10^\circ$ and then decrease for larger acceptance angles. The dominant scattering order seen on the graph corresponds to $n = 10$. It is deduced that even for an ideal detection case, the amount of single scattering detected remains very poor when assuming such optical depth.

The influence of the optical depth on the detection of different scattering orders n where $n = \{1, 2, 3, 5, 10\}$ is illustrated in Fig.7.14 using the semi-analytical MC approach (see section 6.1.2). The ratio of the intensity of the (n^{th}) order of scattering to the total light intensity is plotted at $h=0$ for the perfect case of the detection where $\theta_a = 0^\circ$. For $n = 1$, this ratio decreases monotonically with increasing OD . At $OD=2$, the amount of single scattering detected reaches $\sim 90\%$. This result agrees well with those previously presented in Fig.7.13 demonstrating good agreement between the standard and semi-analytical MC codes. The contribution of multiple scattering dominates for $OD > 5.3$ when the single scattering is less than 50%. At $OD = 8$, the intensity orders from 2 to 10 becomes very similar. This illustrates the transition from the intermediate to the multiple scattering regime where the light transport can be described by the diffusion approximation. Such

results agree well with the ones given by Bizheva *et al*(Bizheva 1998).

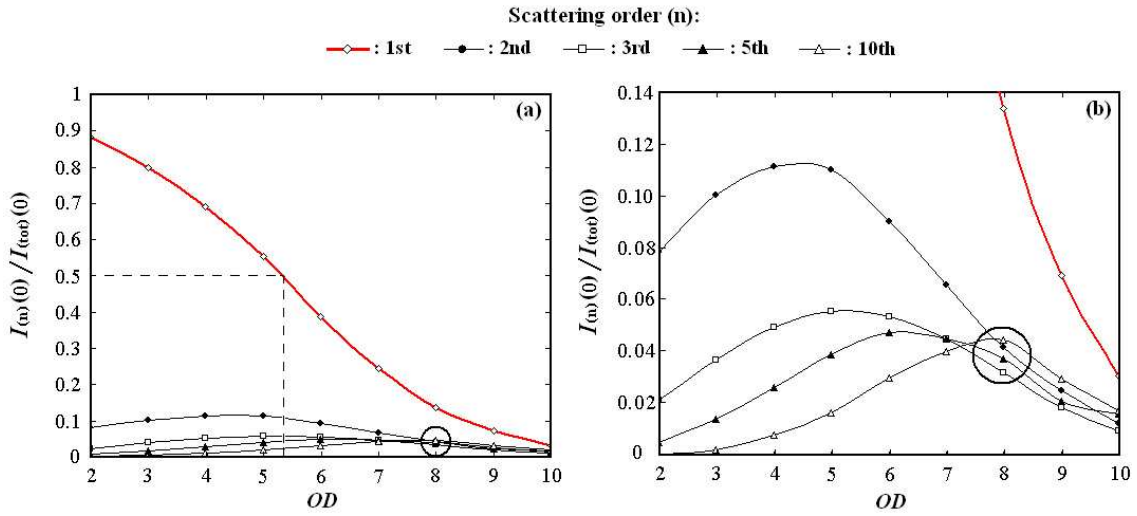


Figure 7.14: Relative intensity for different scattering orders as a function of the optical depth at $h = 0$ and $\beta = 90^\circ$. Results are produced via the semi-numerical MC code assuming the perfect case of detection with $\theta_a = 0^\circ$. In (b) the maximum value of the ratio $I_{(n)}/I_{(tot)}$ is set to 0.14 in order to highlight the contribution of the higher scattering orders.

- *Conclusions for isotropic scattering with $\beta = 90^\circ$:*

- At low optical depths, the contribution of $I_{(1)}$ to the total detected light intensity is important. Small acceptance angles increase this contribution in an important manner (Fig.7.13).
- By increasing h , the contribution of $I_{(1)}$ tends to be null. For large θ_a , this contribution becomes null at large h and for small θ_a this contribution becomes null at small h (7.12 (a)).
- The transition point where $I_{(1)}$ is no longer detected is noticeable only at low optical depth (Fig.7.11).
- The detection acceptance angle has a crucial effect on the detection of the single and double light intensity at different distances, h , (Fig.7.12 (a) and (b)). For higher scattering orders, the value of θ_a does not contribute consequently to the variation of the light intensity as a function of h (Fig.7.12 (c) and (d)).
- At high optical depths all scattering orders give an “equal” contribution to the total signal detected (Fig.7.14). In this case, the variation of the total light intensity is not governed by the first two scattering orders and the changes of the total light intensity with h are not affected anymore by θ_a (Fig.7.11 (b)).

- Single scattering remains the dominant scattering order even at high optical depths when assuming a perfect case of detection with $\theta_a = 0^\circ$. However when $OD > 5.3$, 50% of the signal becomes altered by multiple scattering (Fig.7.14).

7.2.3 Results and analysis for anisotropic scattering

In the next presented simulations, the scattering phase function is deduced from spherical droplets of $15 \mu\text{m}$ in diameter. This phase function is calculated using the LMT from a realistic case of spray diagnostic: The source wavelength (assumed monochromatic) is 532 nm , the refractive index of the droplet is $1.4+0.0i$, and the refractive index of the surrounding medium is $1+0.0i$. The resultant factor of anisotropy, g , of the phase function equals 0.818 . Such scattering properties are representative of droplets found within sprays of hydrocarbon fuel in air. Similarly to the results presented previously for the isotropic scattering, the crossed source-detector geometry is, in this subsection, based on an angle β of 90° .

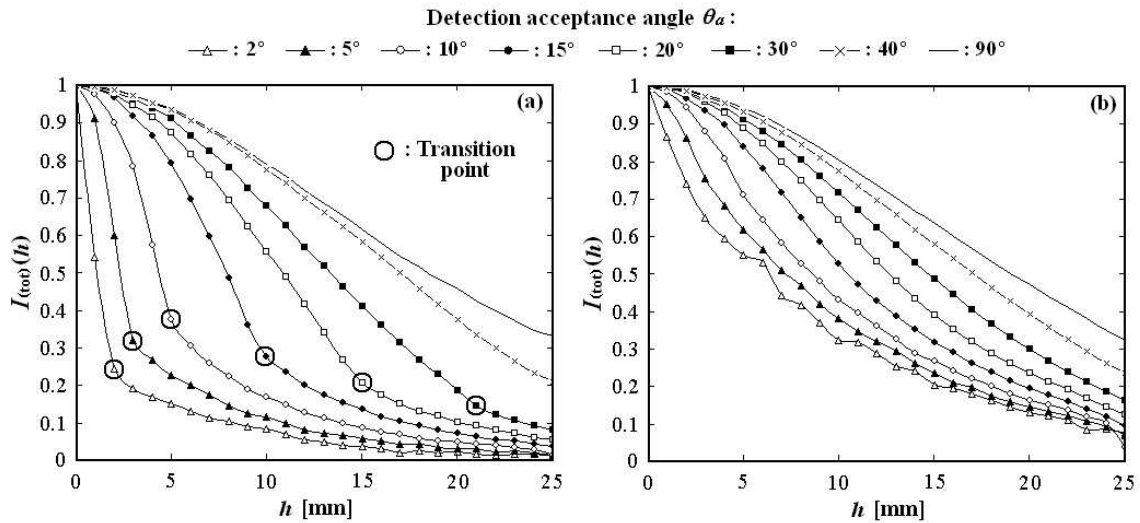


Figure 7.15: Normalized total intensity versus h . The symbols represents different values of the detector numerical aperture. In (a) $OD = 2$; whereas, in (b) $OD = 7$ (β is fixed to 90° in (a) and (b)).

Fig.7.15 shows the effect of the detection acceptance angle on the total detected intensity as a function of h . For each detection acceptance angle, the intensity is normalized to 1 at the maximum value of $I_{(tot)}$ found at $h = 0$. Two optical depths have been considered: In (a) $OD = 2$ and in (b) $OD = 7$. In both cases, the decrease in the light intensity with respect to distance h is more important for small θ_a than large θ_a .

When $OD = 2$ (Fig.7.15 (a)), the total intensity is attenuated quickly for the first values

of h and at small θ_a . In these conditions, both the first and the second scattering order dominate the detected signal.

The transition point where the single light scattering is no longer detected, can once again be visualized on the graph where the curves suddenly decrease smoothly. This smooth decreasing corresponds to the contribution of the higher scattering orders only. However, the transition is not as evident as for the isotropic scattering (see Fig.7.11 (a)).

When $OD = 7$ (Fig.7.15 (b)), the higher scattering orders (between 5 and 9) dominate. The transition point from which the single light intensity is no longer detected cannot, then, be observed on the curves. The effect of the detection acceptance angle is here less important than for $OD = 2$.

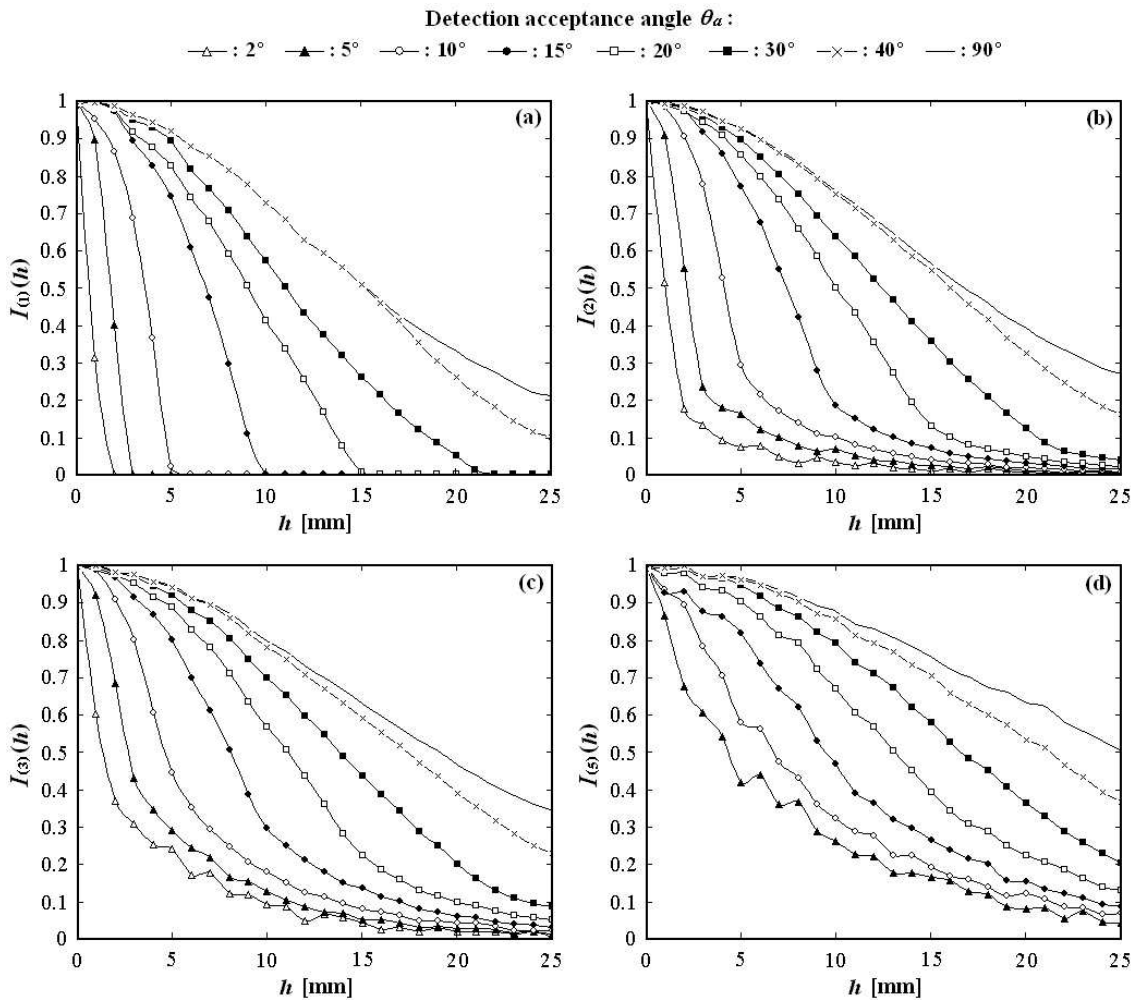


Figure 7.16: Normalized intensity of different scattering orders versus h : (a) single light scattering, (b) double scattering, (c) triple scattering, (d) fifth-order scattering. The symbols represents different values of the detector numerical aperture with β fixed to 90° and $OD = 2$.

In Fig.7.16, the independent contribution of the first, second, third and fifth scattering

orders are depicted. The effect of the detection acceptance angle on the normalized intensities of different scattering orders are investigated at $OD = 2$.

It is observed from Fig.7.16 that the first, second, third and fifth scattering orders are all dependent on the detection acceptance angle. However, this dependence reduces gradually by increasing the scattering order n . When comparing the Fig.7.16 (c) with Fig.7.12 (b), it is noticed that the behaviour of $I_{(3)}$, for anisotropic scattering, is similar to $I_{(2)}$, for isotropic scattering. Fig.7.16 (d) shows that even for the fifth scattering order, the light intensity ($I_{(5)}$) as a function of h remains strongly dependant on θ_a . Note that for isotropic scattering, the detection of $I_{(5)}$ as a function of h is, on the contrary, unaffected by the value of θ_a (as shown in the last subsection in Fig.7.12 (d)).

The relative intensity $I_{(n)}/I_{(tot)}$ contributed by different scattering orders n is plotted as a function of the detector acceptance angle in Fig.7.17. The distance h equals 0 and the optical depth ranges from 2 to 7. It can be seen that the intensities $I_{(2)}$, $I_{(3)}$ and $I_{(5)}$ dominates the detected signal at respective $OD = 2$, $OD = 3$ and $OD = 5$ (Fig.7.17 (a), (b) and (d)). This characteristic seems to be caused by the highly forward scattering property of the phase function.

For isotropic scattering, the contribution of single scattering intensity decreases continuously when increasing the optical depth and/or the detection acceptance angle (see Fig.7.13). For anisotropic scattering a more complex behaviour can be noticed:

By increasing the optical depth and keeping a constant value of θ_a , the intensity of each scattering order, such as $n > 2$, increases until a maximum value and then decrease continuously (see also Fig.7.18). A good example is the contribution of the third and the fifth scattering order which both initially increase and then decrease with OD . The single and double light scattering both decrease when OD is successively set from 2 to 7. This is explained by the fact that the double light scattering has already reached his maximum contribution at $OD = 2$; whereas, for the singly scattered light, its maximum contribution occurs when OD tends to zero.

When $I_{(n)}$ decreases with OD the effect of the acceptance angle is described as follows:

In the range $2^\circ < \theta_a < 15^\circ$, the contribution of $I_{(n)}$ decreases with increasing θ_a . In the range $15^\circ < \theta_a < 40^\circ$, the contribution of $I_{(n)}$ increases (even for $n = 1$). Finally at $\theta_a > 40^\circ$, the amount of $I_{(n)}$ becomes constant.

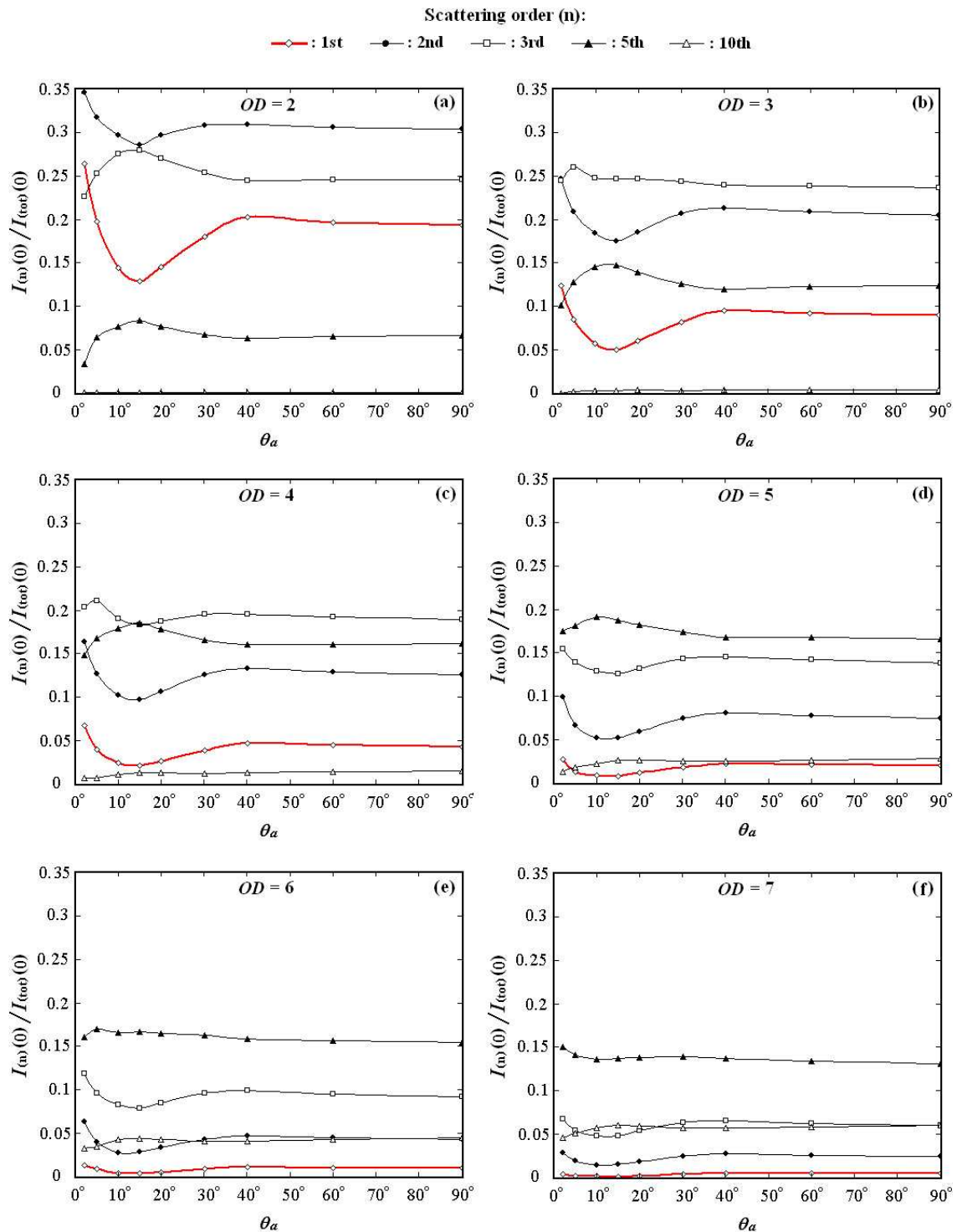


Figure 7.17: Relative intensity of each scattering order as a function of the detection acceptance angle at $h = 0$ and $\beta = 90^\circ$. The optical depth ranges from 2 (in (a)) to 7 (in (b)).

When $I_{(n)}$ increases with OD , the effect of the acceptance angle is inverted:

In the range $2^\circ < \theta_a < 15^\circ$, the contribution of $I_{(n)}$ increases with increasing θ_a . In the range $15^\circ < \theta_a < 40^\circ$, the contribution of $I_{(n)}$ decreases. Finally, at $\theta_a > 40^\circ$, the amount of $I_{(n)}$ becomes constant.

The influence of the optical depth on the detection of different scattering orders where $n = \{1, 2, 3, 5, 10\}$ is illustrated in Fig.7.18 for the acceptance angles $\theta_a = 2^\circ$ in (a) and $\theta_a = 10^\circ$ in (b). For an acceptance angle of 2° , it is seen that the amount of single scattering detected equals 27% at $OD = 2$ and reduces monotonically to 0.4% at $OD = 7$ (Fig.7.18 (a)). By increasing the acceptance angle to $\theta_a = 10^\circ$, the amount of single scattering detected at $OD = 2$ is divided by 2 and reaches $\sim 14\%$ (Fig.7.18 (b)). It is also noticed that, similarly to the first scattering order, the contribution of the second scattering order intensity is also reduced. Only the contribution of greater orders, for $n = 3, 5$ and 10 , increases when θ_a is equals to 10° .

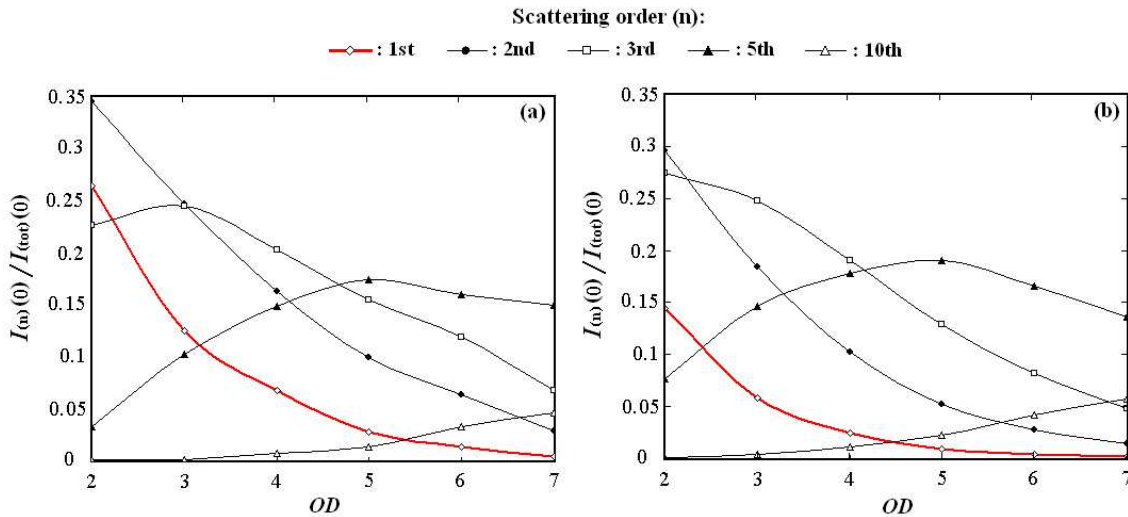


Figure 7.18: Relative intensity of each scattering order as a function of the optical depth at $h = 0$ and $\beta = 90^\circ$. In (a) $\theta_a = 2^\circ$ and in (b) $\theta_a = 10^\circ$.

For the anisotropic scattering case, the single scattering intensity reaches a maximum of 27% compared to 83% for isotropic scattering in the same conditions (Fig.7.13 (a)). This clearly demonstrates the impact of the phase function on the detection geometry. The diameter of the particles considered here, is $D = 15\mu\text{m}$, and the Mie phase function for these conditions shows a strong forward scattering lobe. As a consequence, the probability for a photon to remain in the same direction after a scattering event is high. At very narrow acceptance angles, the light intensity detected comes mainly from multiple scattering events occurring mainly within the volumes V_1 or V_2 (see Fig.7.10); similarly, the single scattering light detected takes place only at the intersection of V_1 with V_2 .

If a photon is initially scattered in the direction of the detector, it is unlikely that any other scattering events occurring between this first scatter and the detector will deviate the photon's trajectory enough to prevent detection due to the high probability of forward scattering. Thus, intensity of double and triple scattering detected increases.

- *Conclusions for anisotropic scattering with $\beta = 90^\circ$:*
- At low optical depths, the contribution of $I_{(1)}$ to the total detected light intensity reaches a maximum value of 27% for $\theta_a = 2^\circ$, compared to 35% for the double light scattering intensity (Fig.7.17 (a)).
- By increasing the distance h , the contribution of $I_{(1)}$ tends to null. Similarly to isotropic scattering, for large θ_a , this contribution becomes null at large h and for small θ_a this contribution becomes null at small h (Fig.7.16 (a)).
- The transition point where $I_{(1)}$ is no longer detected can be only noticed at low optical depth (Fig.7.15). However, this transition is not as clearly defined than as for isotropic scattering (Fig.7.11 (a)).
- The acceptance angle contributes to the variation of both the low (first, second) and high (third, fifth) scattering orders with h even if this contribution reduces with increasing scattering order n (Fig.7.16).
- When increasing the optical depth, each scattering order becomes successively dominant (Fig.7.17 and Fig.7.18).
- Single scattering is never the dominant scattering order for any OD superior or equal to 2. The detection of $I_{(1)}$ is optimized for θ_a close to 0. For $\theta_a = 15^\circ$ the amount of $I_{(1)}$ detected is the least.
- For an anisotropic scattering process with high factor of anisotropy (close to 1), the geometry proposed with $\beta = 90^\circ$, is not appropriated for the optimum detection of the single light scattering intensity.

7.2.4 Comparisons and discussion

A comparison between isotropic and anisotropic scattering is presented in Fig.7.19 for the case of a “global” detection and for the perpendicular detection with $\beta = 90^\circ$. The “global” detection corresponds to the detection of all photons exiting the scattering cube.

In other words, all faces of the scattering cube are considered as detectors with an acceptance angle equal to 90° . For the detection with $\beta = 90^\circ$, the acceptance angle θ_a is fixed to 2° on a surface of 1 mm^2 similarly to the previous simulations.

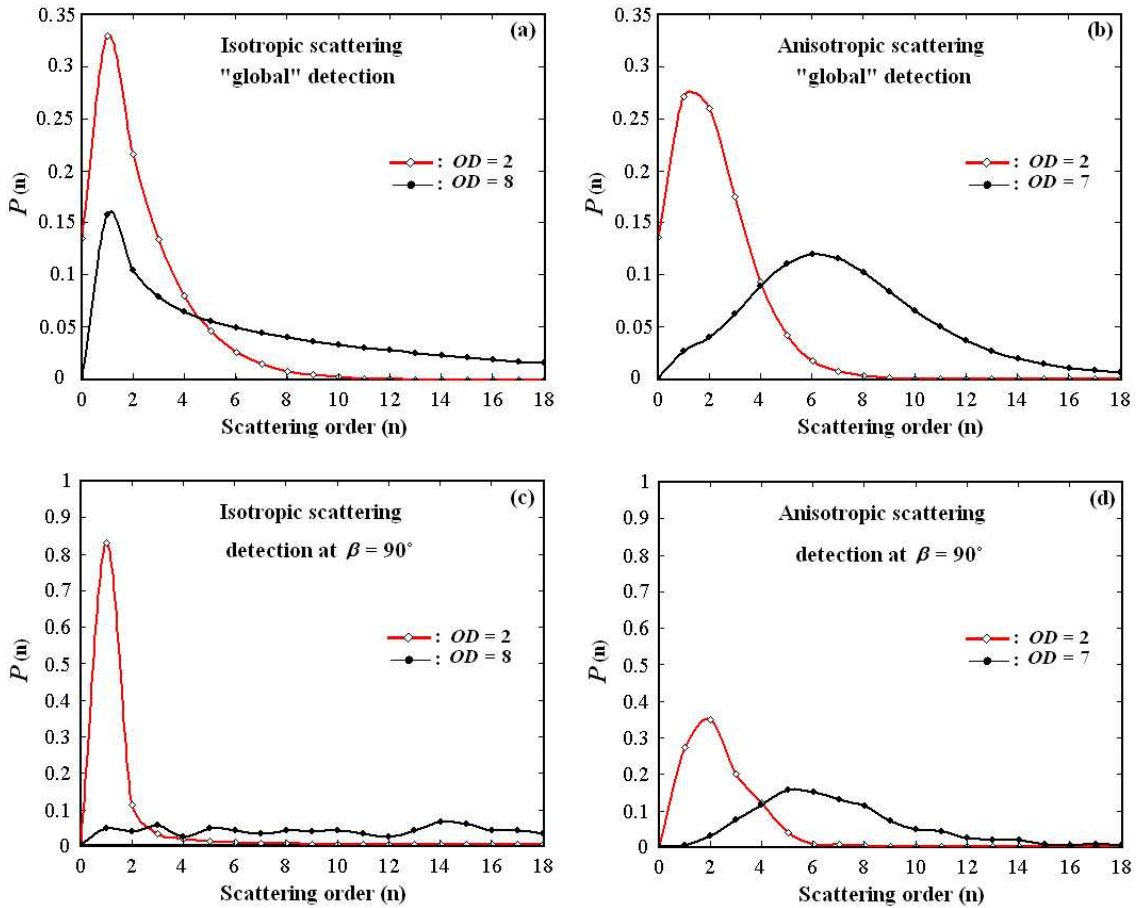


Figure 7.19: Comparison between the "global" detection and the detection at 90° . Isotropic and anisotropic scattering (for fuel droplets of $D = 15 \mu\text{m}$) have both been considered.

In Fig.7.19, (a) the first scattering order remains the dominant order even at high optical depth such as $OD = 8$. This feature seems to be typical of a turbid medium characterized by particles respecting individually an isotropic scattering process.

On the contrary, in Fig.7.19 (b) the first scattering order does not remain dominant and the successive second, third, fourth, *etc* orders becomes successively dominant when increasing OD . For $OD = 7$, it is seen that the major scattering order is equal to 6. This features seems to be typical of a turbid medium characterized by particles respecting individually a highly forward anisotropic scattering process. In our case these particles are fuel drops of $15 \mu\text{m}$.

Contrary to the detection at $\beta = 90^\circ$, ballistic photons are detected in the global detection. It can be thus noticed that the contribution of the scattering order 0 (corresponding

to ballistic photons) is superior than 0 in the global detection, especially at $OD=2$. In Fig.7.19 (c) and (d), ballistic photons cannot be detected due to the perpendicular configuration and $P_{(0)} = 0$. When comparing Fig.7.19 (c) with (a), it can be noticed that the detection of single scattering is largely increased when using the perpendicular crossed source-detector configuration. However, at high OD this configuration does not help the detection of single scattering due to the strong backscattering of the single scattered light at large OD . A comparison between Fig.7.19 (b) and (d) shows that a similar amount of single scattering is detected for both cases of detection. These results demonstrate once again that the geometry used with $\beta = 90^\circ$ does not present any clear advantages for the case of anisotropic scattering.

The effect of the source-detector intersection angle, β , on the detection of single scattering is investigated in Fig.7.20 (a) with an acceptance angle of 2° and $OD = 2$. The results are given for isotropic scattering and for two different anisotropic phase functions based, respectively, on droplets of $1 \mu\text{m}$ and $15 \mu\text{m}$ in diameter. The phase function of the $1 \mu\text{m}$ droplets has been calculated with the same conditions than that deduced for $15 \mu\text{m}$ (the source is 532 nm and the droplet refractive index is $1.4+0.0i$ - see subsection 7.2.3).

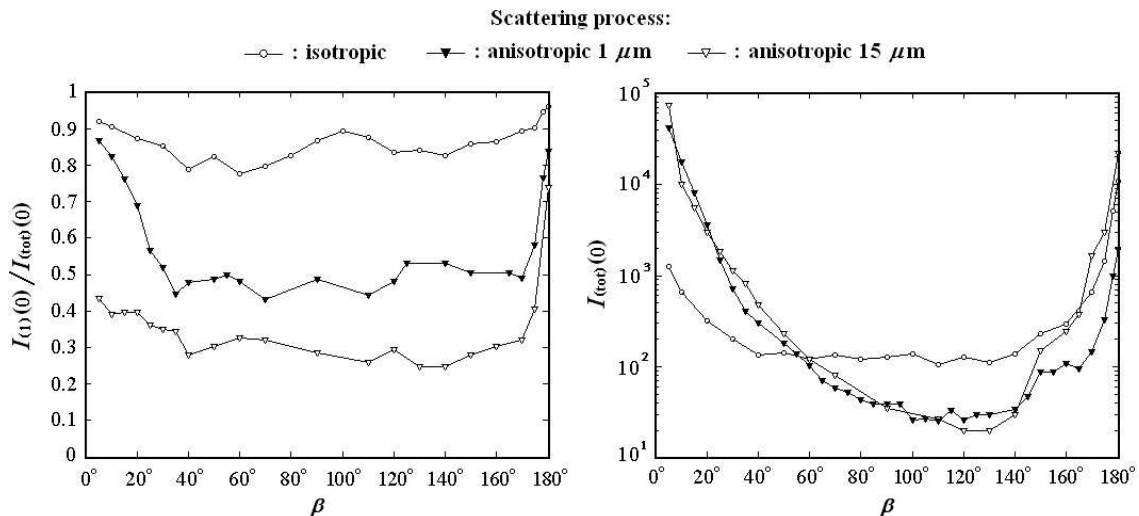


Figure 7.20: Effect of the source-detector angle β on the single scattering detection at $h = 0$ with an acceptance angle θ_a of 2° . (a) is the amount of single scattering, I_1/I_{tot} , detected versus the source detector angle, β , and (b) is the total intensity detected versus β . Both isotropic and anisotropic scattering (for spherical fuel droplets of $1 \mu\text{m}$ and $15 \mu\text{m}$) are considered.

The fraction of the total intensity contributed by single scattering, $I_{(1)}/I_{(tot)}$, as a function of β is plotted Fig.7.20 (a). It can be seen that for isotropic scattering, the fraction of single scattering in the total detected signal is insensitive to β and remains between 80% and 95%. On the contrary, the effect of β on the detection of single scattering is highly significant for anisotropic scattering. It can be seen in this case that forward scattering (β

close to 0°) and back scattering detection (β close to 180°) are most efficient for the detection of single scattering intensity. For particles of $15 \mu\text{m}$ diameter, the single scattering intensity detected reaches 44% for $\beta = 5^\circ$ and 76% for $\beta = 180^\circ$.

The detection of single scattering using a forward detection angle ($\beta = 0^\circ$) is more efficient for small particles (88% of I_1 with $D = 1 \mu\text{m}$) than for big particles (44% of I_1 with $D = 15 \mu\text{m}$). With $\beta = 90^\circ$, single scattering intensity reaches only $\sim 30\%$ for $D = 15 \mu\text{m}$, $\sim 50\%$ for $D = 1 \mu\text{m}$ but $\sim 85\%$ for isotropic scattering. Thus perpendicular detection of the first scattering orders seems more appropriate for scattering processes close to isotropic scattering. However, back scattering detection ($\beta = 180^\circ$) allows detection of a high amount of single scattering for both isotropic and anisotropic cases: 84% of I_1 with $D = 1 \mu\text{m}$ and 74% of I_1 with $D = 15 \mu\text{m}$.

Fig.7.20 (b) shows the total intensity detected as a function of the source-detector angle, β , for $OD = 2$. This total intensity reaches a maximum for the forward detection with both anisotropic scattering processes considered. However, $I_{(tot)}$ is strong for isotropic scattering at $\beta = 90^\circ$ as well as at forward and back scattering. Back scattering intensity is strong for all three scattering processes investigated.

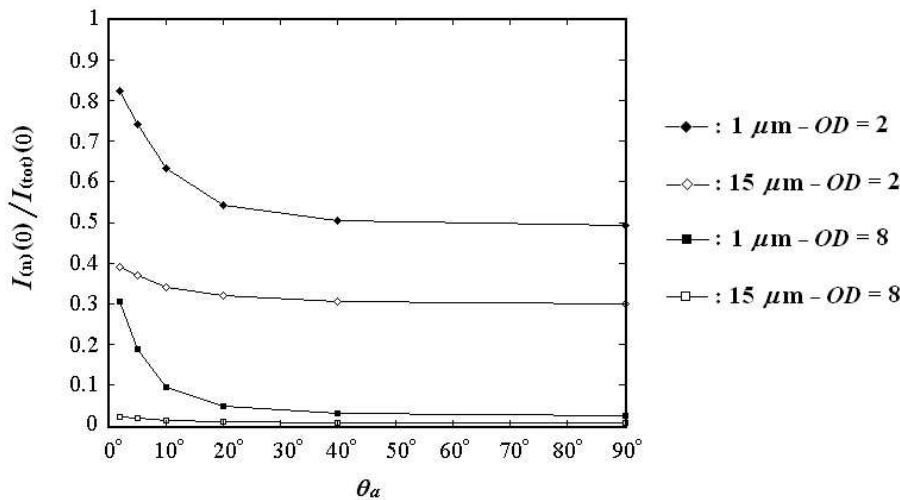


Figure 7.21: Results of I_1/I_{tot} versus the acceptance angle θ_a for anisotropic scattering with $\beta = 10^\circ$ and with the optical depths $OD=2$ and $OD=8$. Spherical fuel droplets of 1 and $15 \mu\text{m}$ are considered.

Considering Fig.7.20 (a) and (b) together, it seems that forward scattering detection allows detection of both a high fraction of single scattering and a strong total scattering signal. It is possible to detect a signal that is very strongly dominated by single scattering at near-forward and near-backward scatter. In the case of forward scattering, keeping β greater than the acceptance angle avoids the detection of unscattered (ballistic) light. From these results, the optimum angle β for the detection of single light scattering seems

to be around 10° when considering scattering fuel droplets of 1 and $15\ \mu\text{m}$.

In Fig.7.21, we show the fraction contributed by single scattering for a low ($OD = 2$) and high ($OD = 8$) scattering medium with anisotropic scattering and a source-detector angle equal to 10° . It can be seen that, if the particles are large the influence of acceptance angle is not as strong. For $OD = 8$, the single scattering detection reaches a maximum of 30% for particles of $1\ \mu\text{m}$ in diameter versus only $\sim 2\%$ for particles of $15\ \mu\text{m}$. These results demonstrate once again the significance of the scattering phase function in the extraction of single scattering.

General Results of Monte Carlo Simulations

THE MC simulation is an effective approach to various radiative problems and has capabilities for a number of applications. In this chapter, four examples are provided.

The first example concerns the scattering of light by a single spherical particle positioned in the middle of an empty cubic volume. Using the adequate scattering phase function of the particle, the light intensity distributions is visualized in the forward, side, and back direction of the far-field scattering region. The interference fringe separations and rings of light, can be observed and analyzed from such simulations.

The second example is the investigation of image transfer within an homogeneous turbid environment. The initial source of light is, here, not a laser beam but an illuminated object. Experimental and simulated results are compared and a strategy of image reconstruction is suggested. Such approach has potential applications to a large number of visibility issues such as seeing through the fog, mist or clouds.

The third section is devoted to the propagation of ultra-short light pulses through various scattering media. Time-resolved calculations of the light intensity exiting a scattering volume on the forward, side and back directions are performed. Effects of optical depth, detection acceptance angle and scattering phase function are shown. Investigations of this type are fundamental in the development of future laser techniques based on time-gating detection.

The final important application of MC simulation is the extrapolation of the Beer-Lambert law for including the multiple scattering contribution. An effective procedure is suggested in the last section.

8.1 3D Investigation of light scattering by single spherical particles

The scattering of light by single spherical particles is investigated based on the LMT and using the MC technique. A unique particle is positioned in the middle of an empty cubic volume and lighted by a monochromatic coherent light source. The intensity profile of the scattered light is recorded and plotted in 2D for the back, side and forward scattering corresponding respectively to the back, side and front face of the cube (see Fig.8.1). This section provide a clear visualization of the single scattering process.

- In the first subsection, four diameters of droplets typically encountered in fuel sprays are considered. These diameters are $D = 1 \mu\text{m}$, $D = 15 \mu\text{m}$, $D = 50 \mu\text{m}$ and $D = 150 \mu\text{m}$.
- In the second subsection, the total scattering representative of a collection of fuel droplets is considered. Calculation of averaged phase functions are performed for the four fuel droplet distributions. These distributions are employed in the investigation of polydisperse scattering media, described in section 6.3, and are represented in Fig.6.30.
- In the last subsection, the four diameters $D = 1 \mu\text{m}$, $D = 2 \mu\text{m}$, $D = 5 \mu\text{m}$ and $D = 20 \mu\text{m}$ of polystyrene microspheres are considered. These polystyrene spheres the ones employed in Chapter 6.2 for the comparison with experimental results.

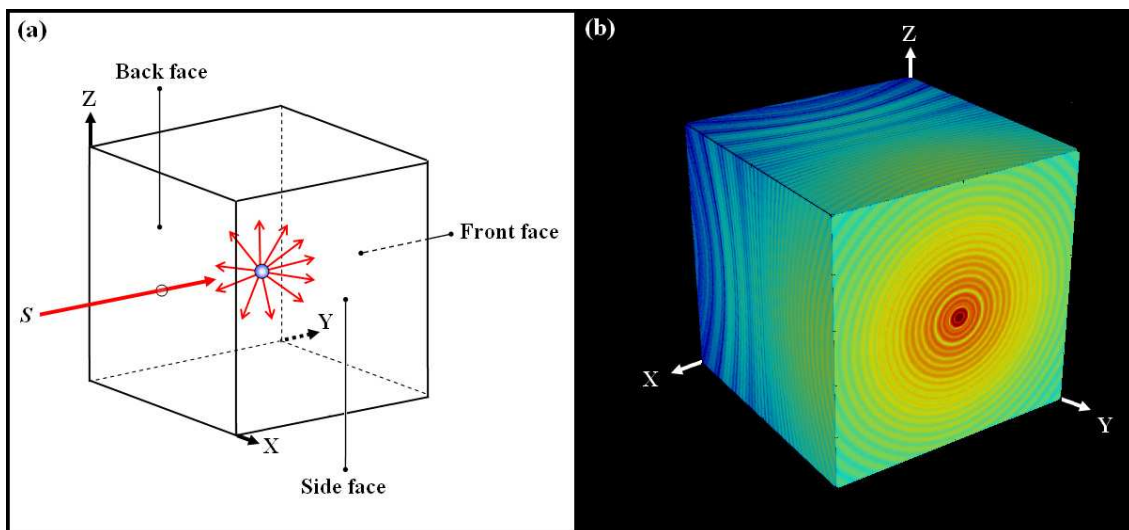
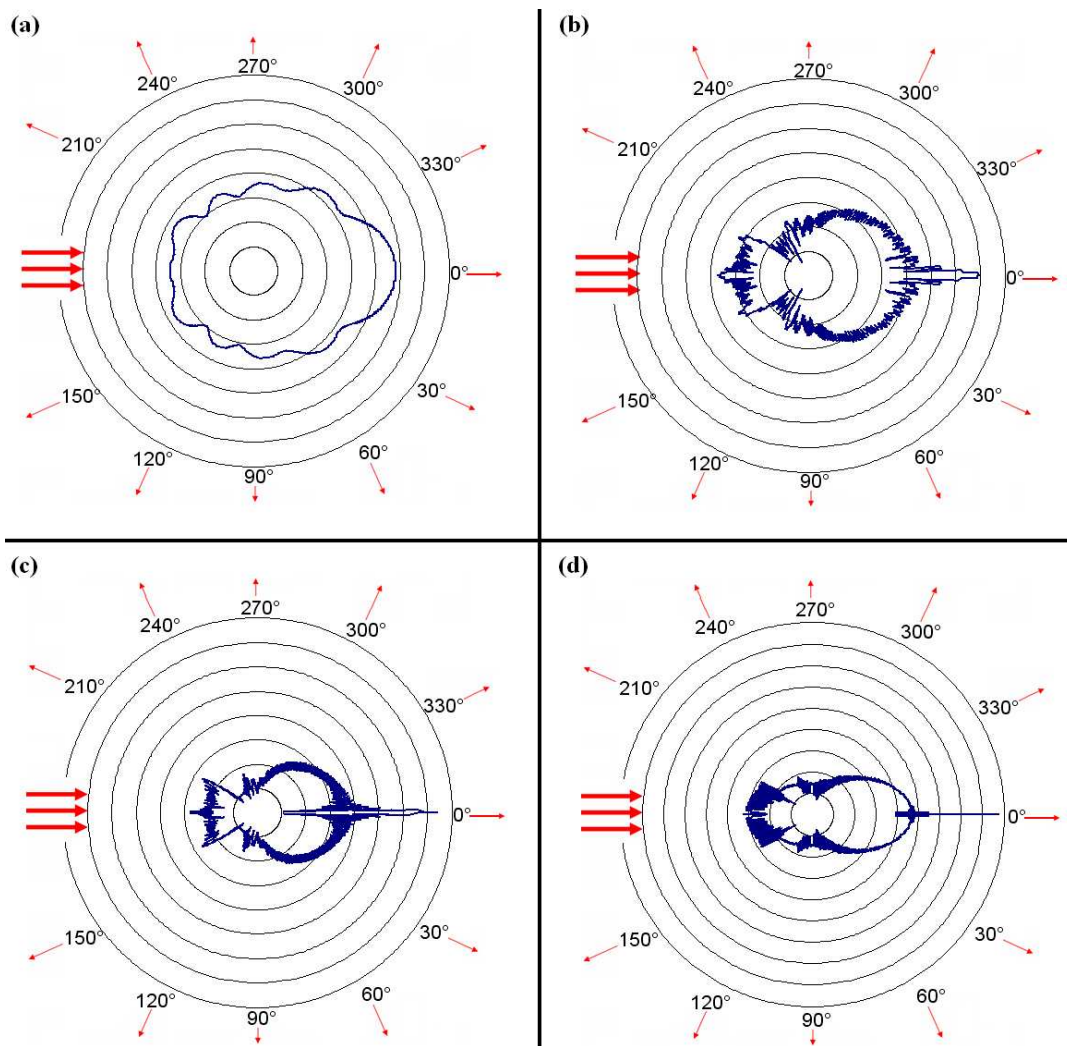


Figure 8.1: A single spherical droplet is positioned and illuminated in the middle of an empty cubic volume. (a) is the schematic of the simulation and (b) is the 3D normalized intensity distribution generated from the MC simulation.

8.1.1 Scattering by a single fuel droplet



	(a)	(b)	(c)	(d)
D [μm]	1	15	50	150
λ [nm]	512	512	512	512
n [au]	$1.4+0.0i$	$1.4+0.0i$	$1.4+0.0i$	$1.4+0.0i$
x [au]	~ 6	~ 88.5	~ 307	~ 920
g [au]	0.78	0.82	0.87	0.92

Figure 8.2: Polar scattering phase functions (logarithmic scale) with related table of optical characteristics for single fuel droplets illuminated at 512 nm. In (a) $D = 1 \mu\text{m}$, in (b) $D = 15 \mu\text{m}$, in (c) $D = 50 \mu\text{m}$ and in (d) $D = 150 \mu\text{m}$.

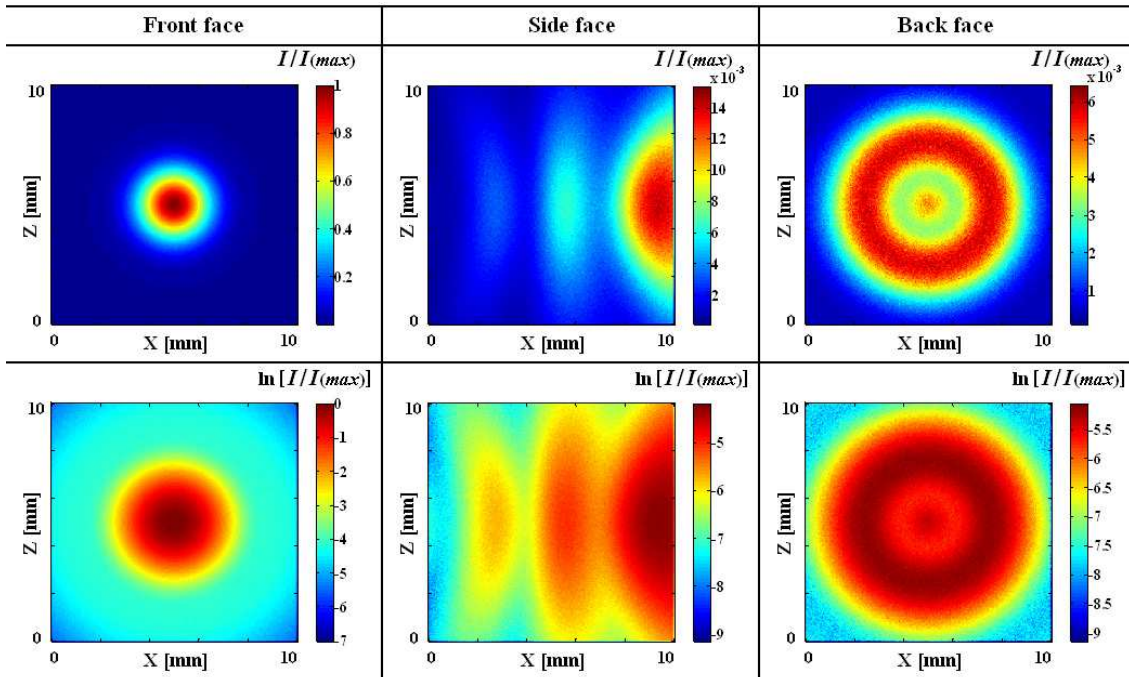


Figure 8.3: Relative intensity profile of the scattered light on the front, side and forward faces for the case (a) where $D = 1 \mu\text{m}$. Due to the large lobes of the scattering phase function, a diffused disc of light is visualized on the front and back face, without any observable interference fringes on the side face.

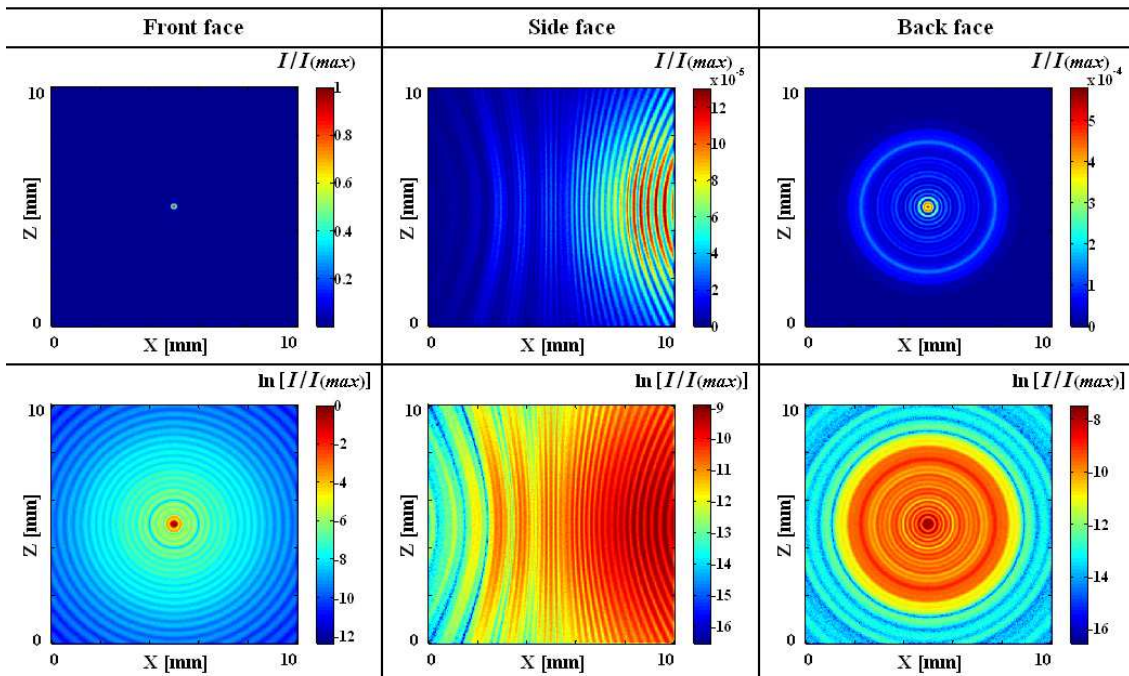


Figure 8.4: Relative intensity profile of the scattered light on the front, side and forward faces for the case (b) where $D = 15 \mu\text{m}$. Due to the narrow lobes of the scattering phase function, light rings can be visualized on both the front and back face, with interference fringes on the side face.

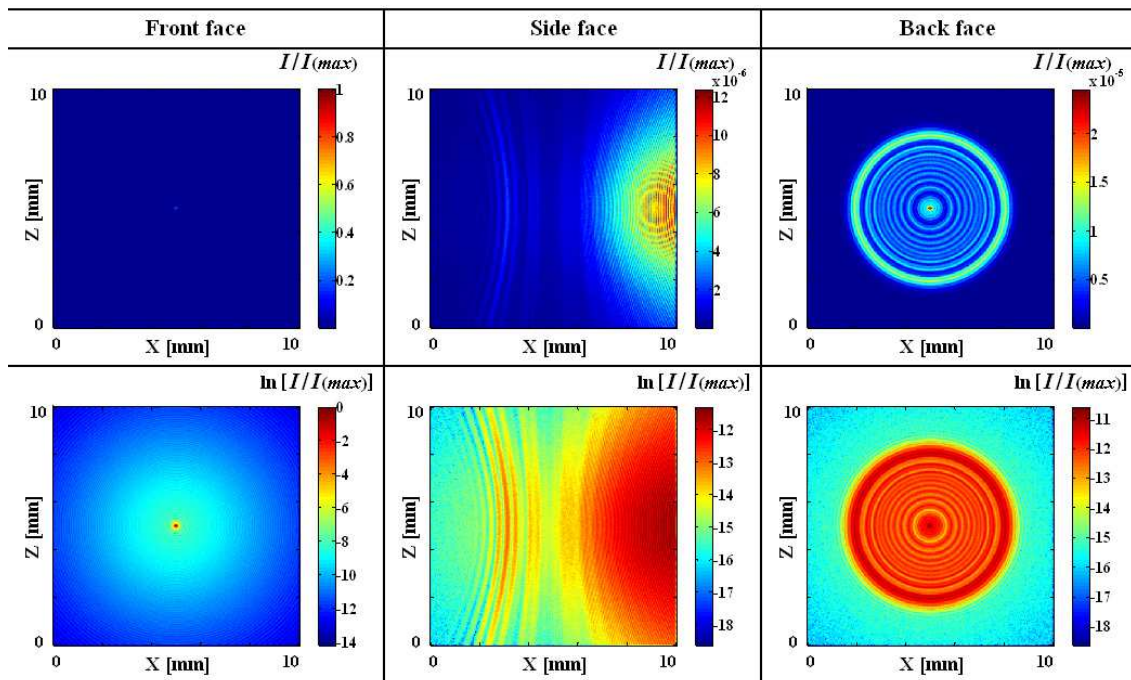


Figure 8.5: Relative intensity profile of the scattered light on the front, side and forward faces for the case (c) where $D = 50 \mu\text{m}$. For such droplet sizes, a significant forward pick is observable on the scattering phase function making the level of light intensity largely superior at $\theta_0=0^\circ$ than for any other direction.

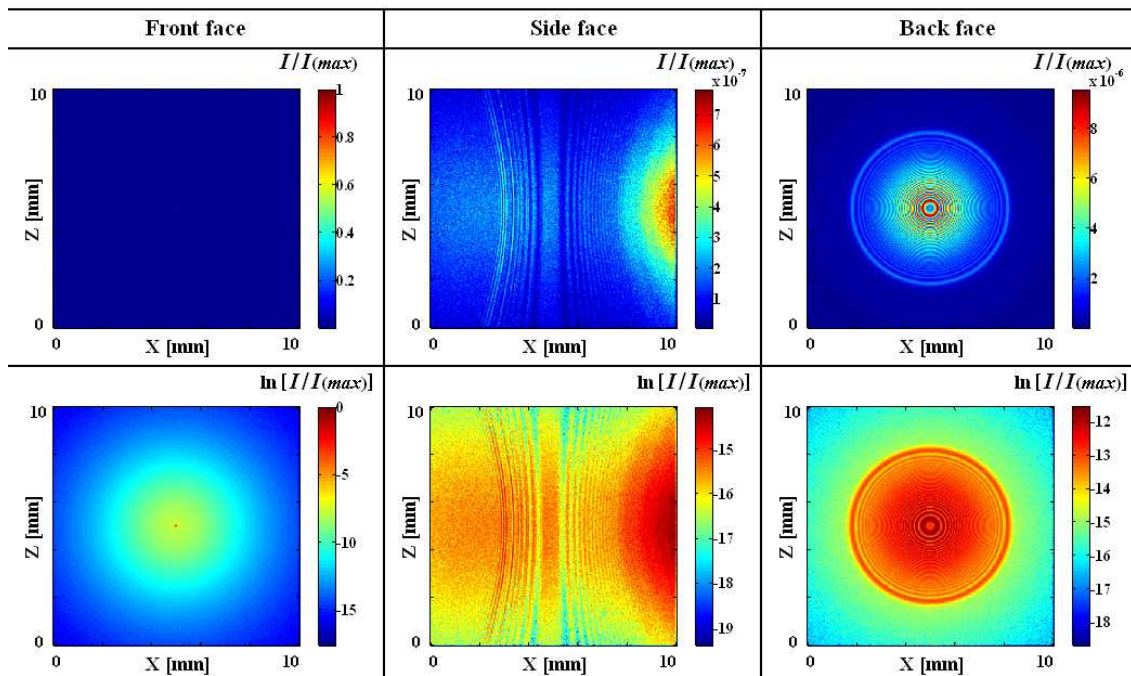
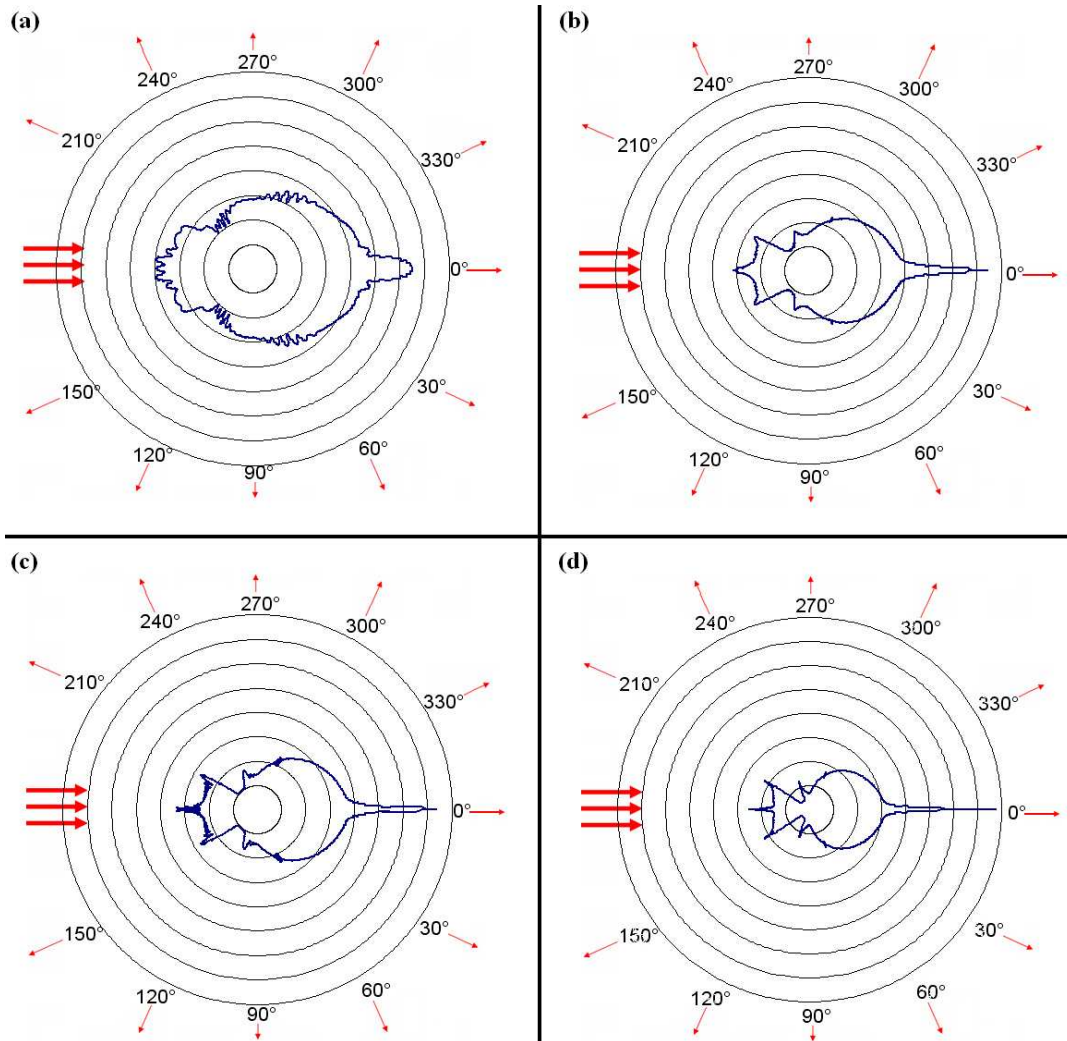


Figure 8.6: Relative intensity profile of the scattered light on the front, side and forward faces for the case (d) where $D = 150 \mu\text{m}$. For such droplet sizes, a significant forward pick is observable on the scattering phase function making the level of light intensity largely superior at $\theta_0=0^\circ$ than for any other direction.

8.1.2 Scattering from an averaged scattering phase-function from various distributions of fuel droplets



	(a)	(b)	(c)	(d)
\bar{D} [μm]	5	5	40	40
σ [μm]	0.5	4	4	32
λ [nm]	532	532	532	532
n [au]	1.4+0.0i	1.4+0.0i	1.4+0.0i	1.4+0.0i
g [au]	0.784	0.845	0.848	0.851

Figure 8.7: Polar scattering phase functions (logarithmic scale) with related table of optical characteristics. The phase functions representative of four Log-Normal droplet distributions are considered. These distributions are illustrated in Fig.6.30.

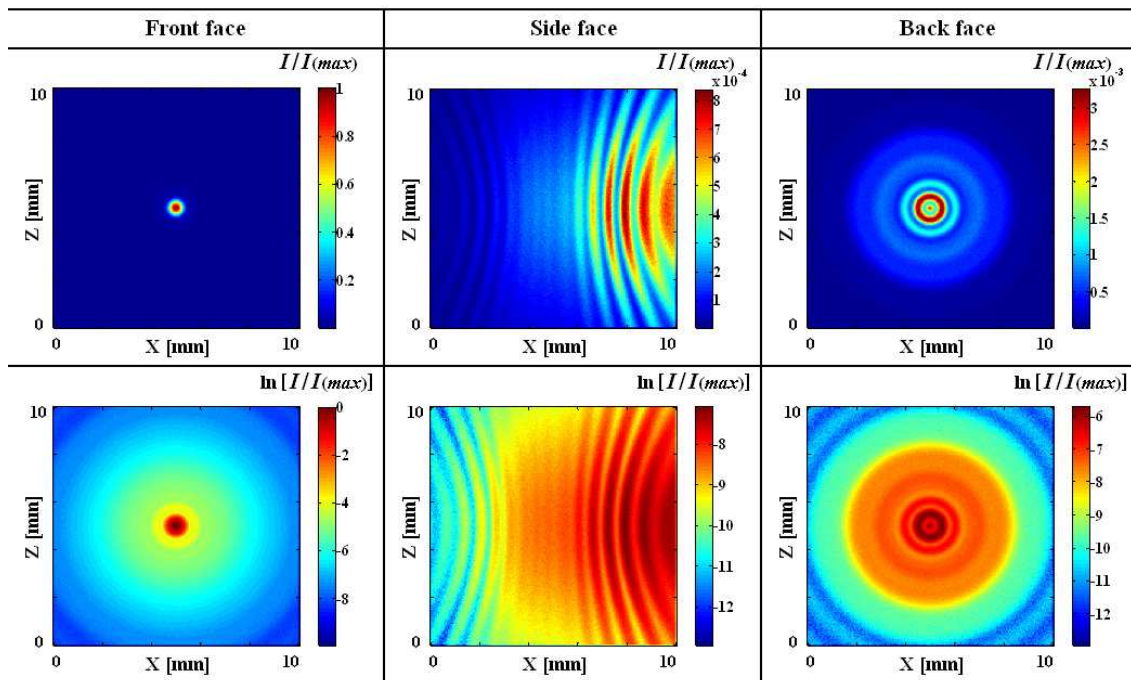


Figure 8.8: Intensity of the scattered light on the front, side and forward faces generated from a single scattering phase function representative of a Log-Normal droplet distribution. $\bar{D} = 5 \mu\text{m}$ and $\sigma = 0.5 \mu\text{m}$ (10% of \bar{D}). The distribution is given in Fig.6.30(a).

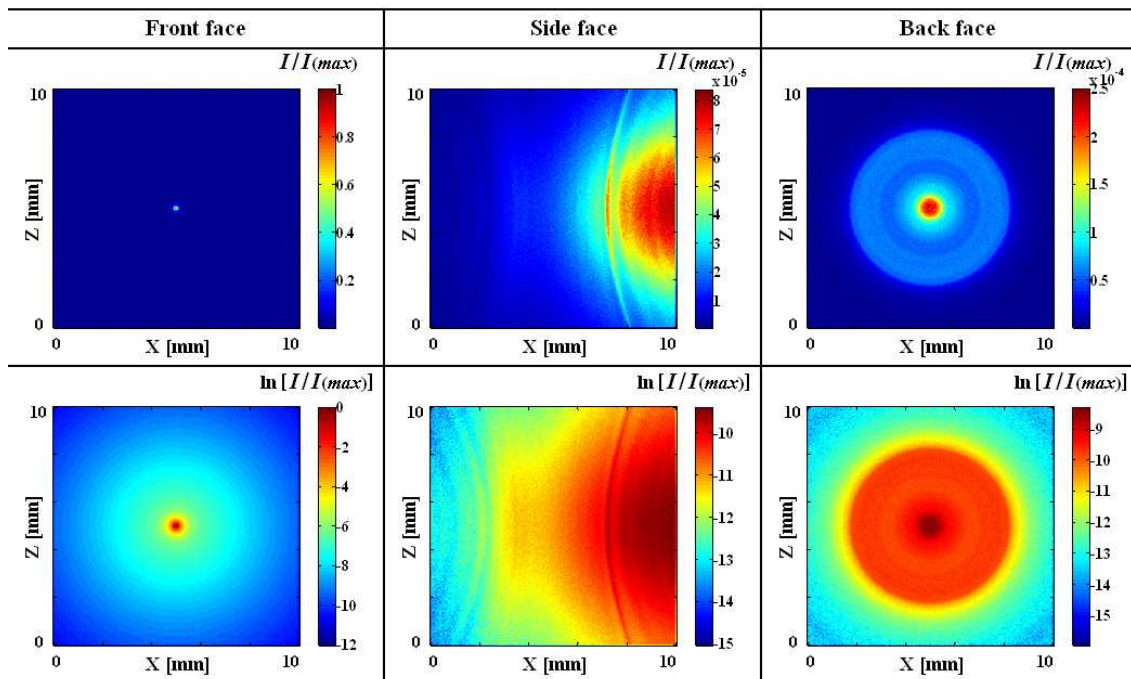


Figure 8.9: Intensity of the scattered light on the front, side and forward faces generated from a single scattering phase function representative of a Log-Normal droplet distribution. $\bar{D} = 5 \mu\text{m}$ and $\sigma = 4 \mu\text{m}$ (80% of \bar{D}). The distribution is given in Fig.6.30(b).

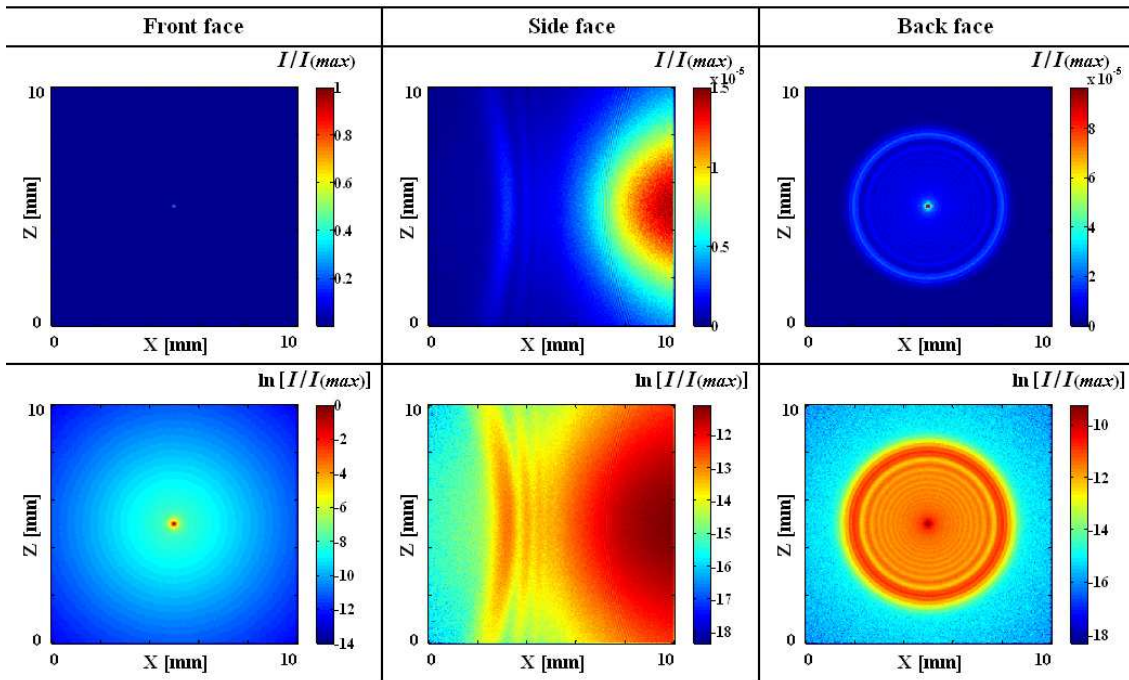


Figure 8.10: Intensity of the scattered light on the front, side and forward faces generated from a single scattering phase function representative of a Log-Normal droplet distribution. $\bar{D} = 40 \mu\text{m}$ and $\sigma = 4 \mu\text{m}$ (10% of \bar{D}). The distribution is given in Fig.6.30(c).

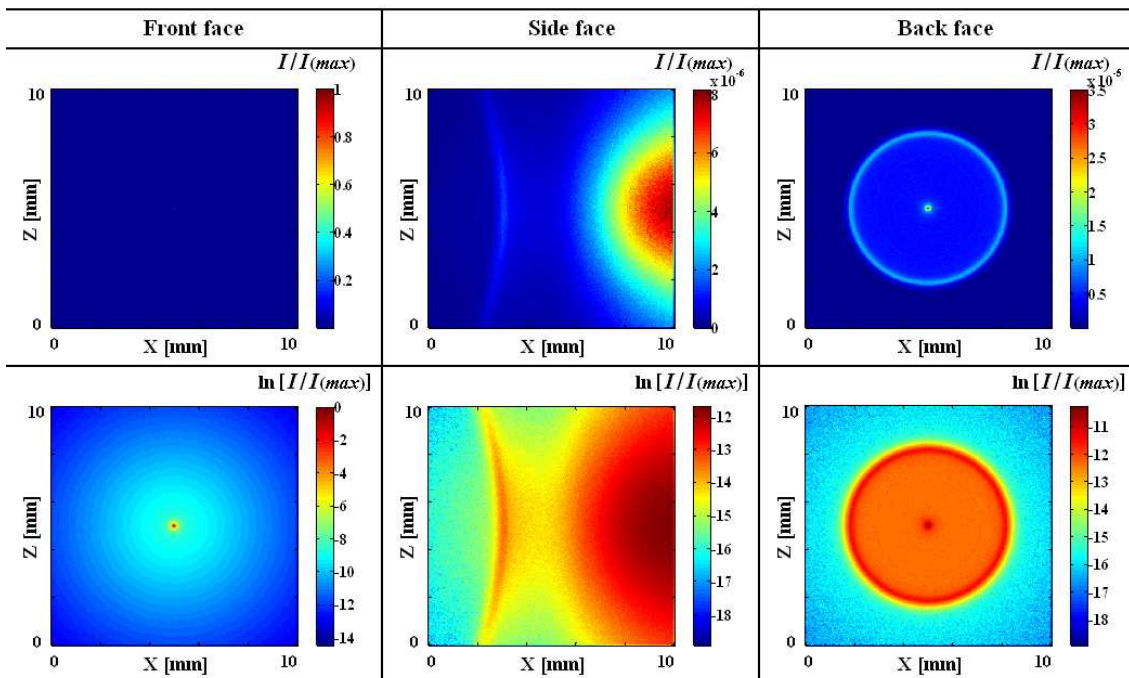
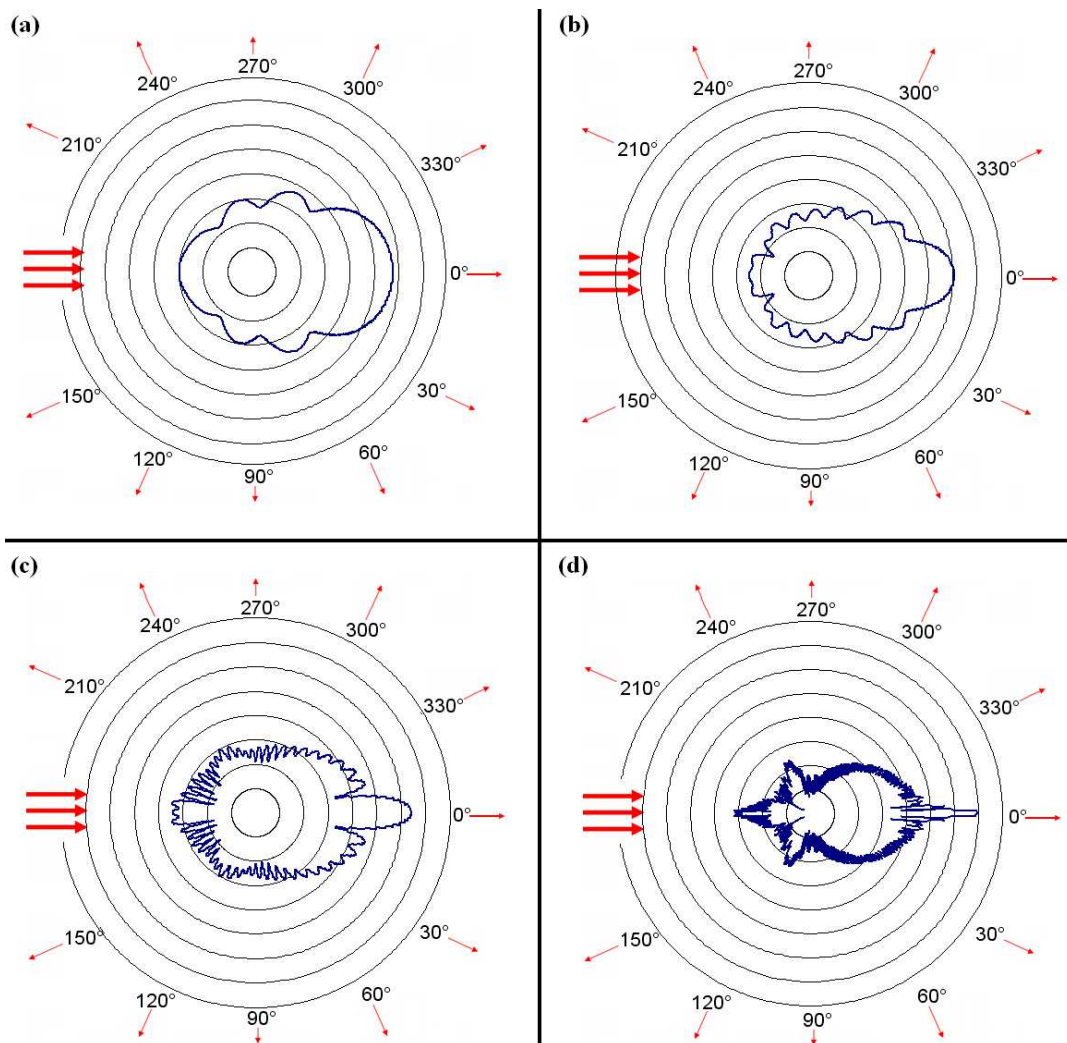


Figure 8.11: Intensity of the scattered light on the front, side and forward faces generated from a single scattering phase function representative of a Log-Normal droplet distribution. $\bar{D} = 40 \mu\text{m}$ and $\sigma = 32 \mu\text{m}$ (80% of \bar{D}). The distribution is given in Fig.6.30(d).

8.1.3 Scattering by a single polystyrene sphere



	(a)	(b)	(c)	(d)
D [μm]	1	2	5	20
λ [nm]	800	800	800	800
n [au]	1.578+0.0i	1.578+0.0i	1.578+0.0i	1.578+0.0i
x [au]	≈ 4	≈ 8	≈ 19.5	≈ 78.5
g [au]	0.90	0.93	0.88	0.93

Figure 8.12: Polar scattering phase functions (logarithmic scale) with related table of optical characteristics for the polystyrene spheres illuminated at 800 nm. In (a) $D = 1 \mu\text{m}$, in (b) $D = 2 \mu\text{m}$, in (c) $D = 5 \mu\text{m}$ and in (d) $D = 20 \mu\text{m}$.

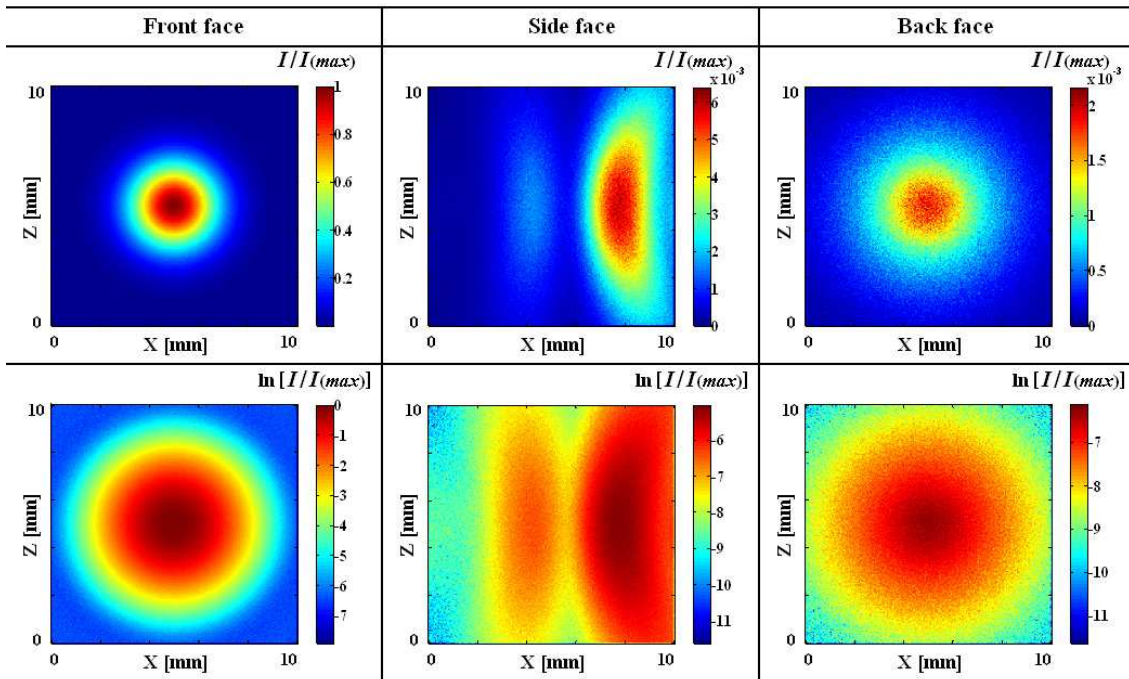


Figure 8.13: Relative intensity profile of the scattered light on the front, side and forward faces for the case (a) where $D = 1 \mu\text{m}$. Due to the large lobes of the scattering phase function, a diffused disc of light is visualized on the front and back face, without any observable interference fringes on the side face.

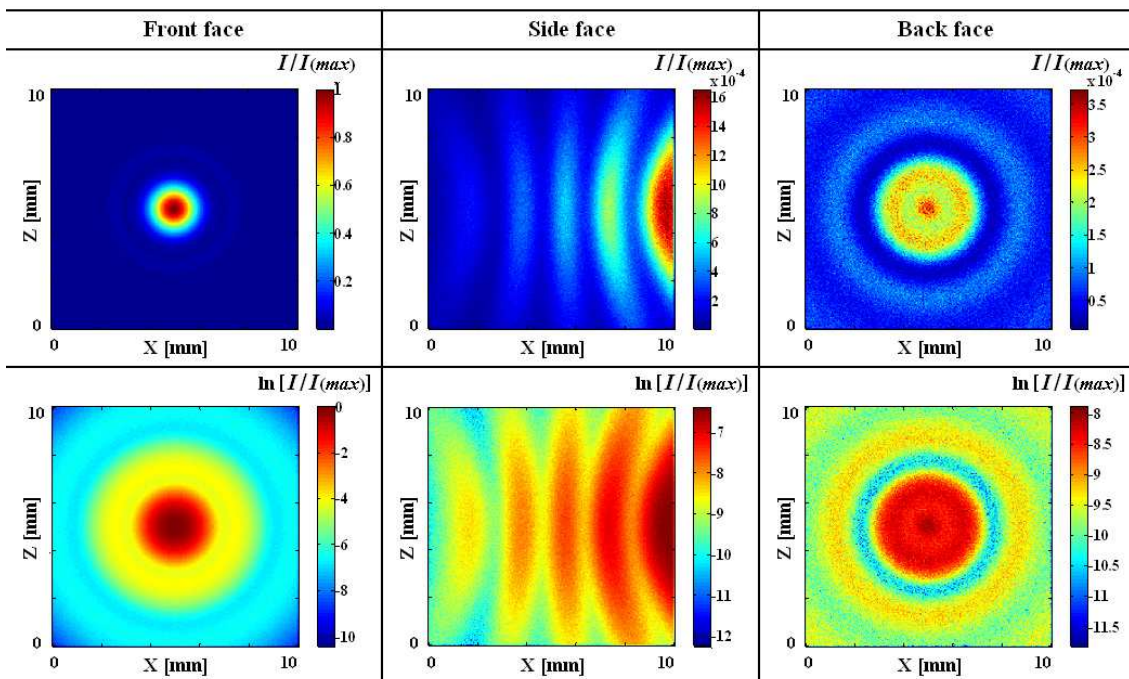


Figure 8.14: Relative intensity profile of the scattered light on the front, side and forward faces for the case (a) where $D = 2 \mu\text{m}$. Due to the large lobes of the scattering phase function, a diffused disc of light is visualized on the front and back face. Some interference fringes can be observed on the side face.

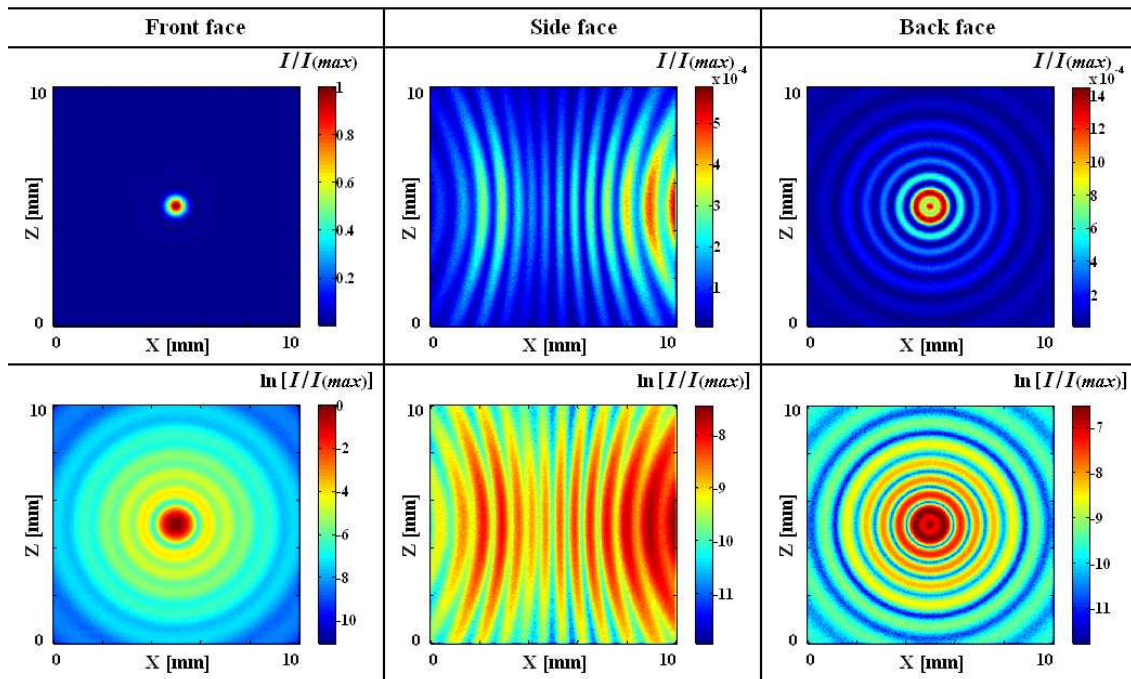


Figure 8.15: Relative intensity profile of the scattered light on the front, side and forward faces for the case (c) where $D = 5 \mu\text{m}$. The forward pick start to be clearly observable on the scattering phase function making the level of light intensity superior at $\theta_0=0^\circ$ than for any other directions.

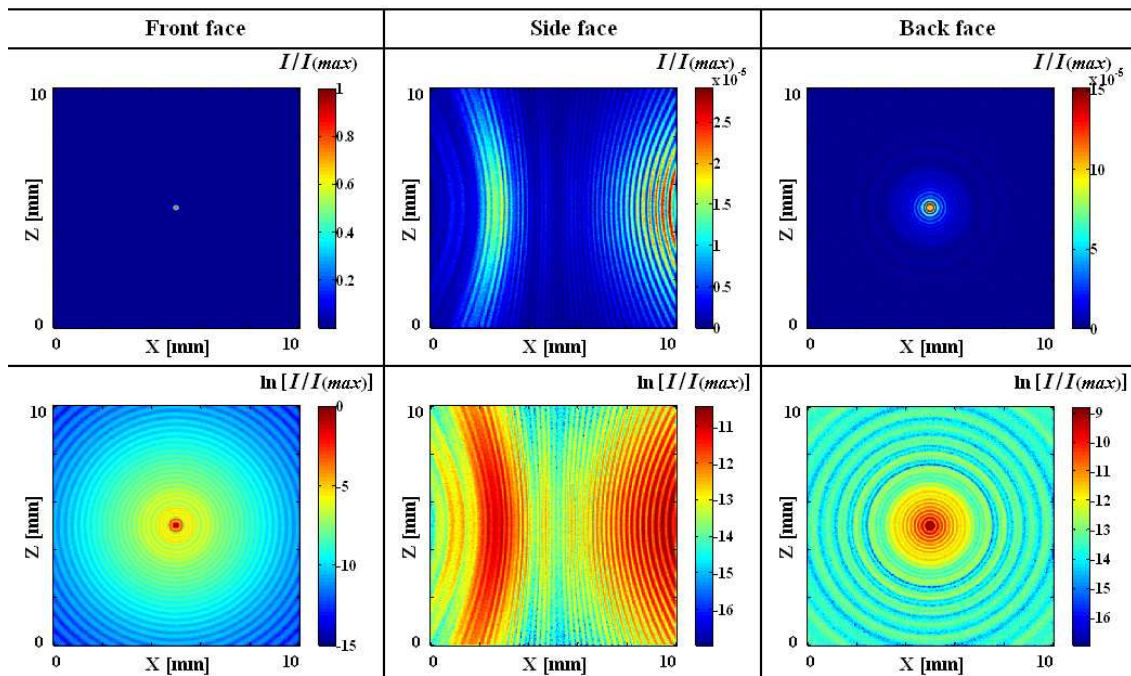


Figure 8.16: Relative intensity profile of the scattered light on the front, side and forward faces for the case (c) where $D = 20 \mu\text{m}$. At this droplet size, a significant forward pick is now observable on the scattering phase function making the level of light intensity largely superior at $\theta_0=0^\circ$ than for any other directions.

8.2 Image transfer through turbid media

In this section, the process of image transfer within a homogeneous monodisperse turbid medium is studied. A blurred image of an object is experimentally recorded and compared to the simulated image. An analysis based on the decomposition of the MC image into a sum of images generated from individual scattering order is provided. Finally, a correction strategy is suggested and applied to the experimental image in order to suppress the blurring effects caused by multiple scattering.

8.2.1 Image analysis

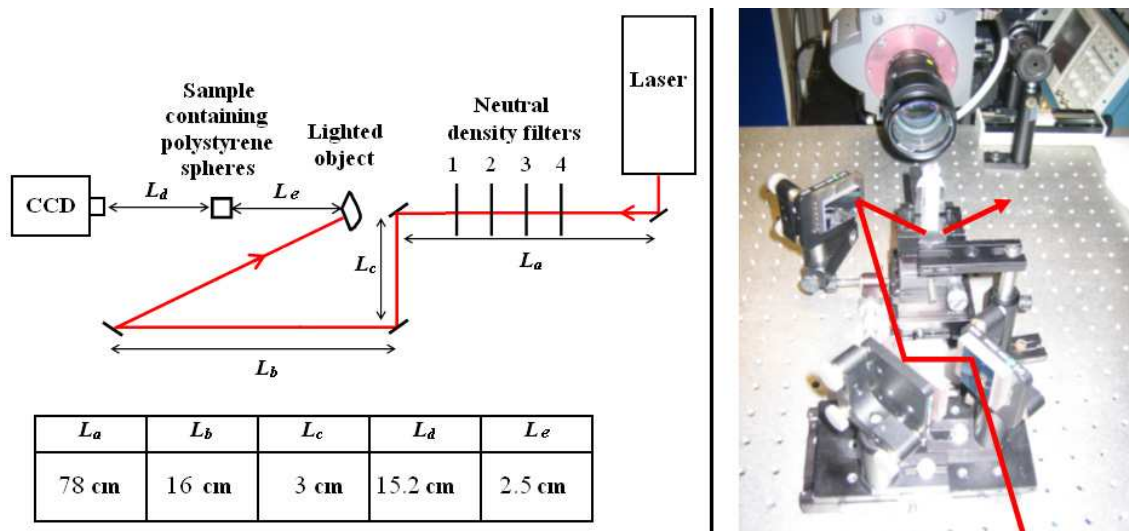


Figure 8.17: Experimental configuration: An object is lighted behind the scattering medium and imaged via a EM-CCD camera.

The basics of the experiment consist in illuminating (at 800 nm) an object, which is positioned behind a sample cell containing an homogeneous solution of monodisperse polystyrene spheres. Similarly to the experiment described in subsection 6.2, the object is imaged using a EM-CCD camera with a detection acceptance angle of the collection optics sets to $\theta_a = 8.5^\circ$. Only one solution of polystyrene spheres, with $OD = 5$ and $D = 20 \mu\text{m}$, is used here. An illustration is provided Fig.8.17. The initial source of light emitted from the object is simulated via the “source matrix method” described in subsection 6.2.1. Figure 8.18 shows a comparison of simulated and experimental images. In the experiment the illuminated object scatters light in all directions. However, in the simulation the incident direction of photons is assumed to be unidirectional. This difference is responsible to a brighter image in the centre of the simulated image; whereas, the

experimental image shows a more homogeneous distribution of light intensity over the full imaged surface.

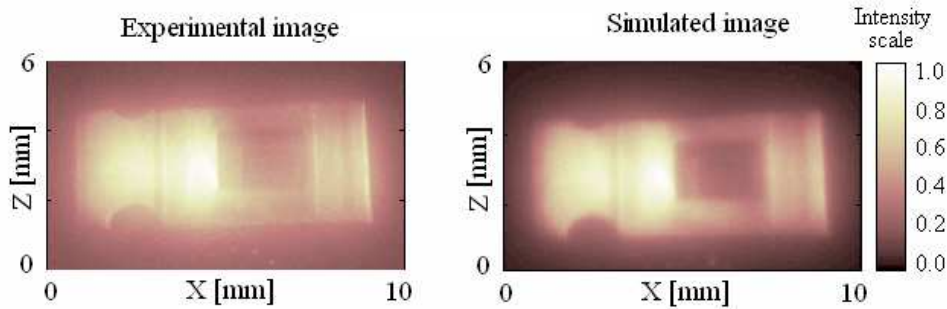


Figure 8.18: Comparison between the experimental and simulated images for an object illuminated behind a scattering medium. The scattering medium is a sample containing a solution of polystyrene spheres ($D = 20 \mu\text{m}$ and $OD = 5$) in distilled water.

The contribution of each scattering order within the detected signal can be calculated from MC simulation. Figure 8.19 shows this contribution from $(n)=0$ up to $(n)=3$. Images from higher scattering orders are seen to be less fidel than images from lower scattering orders. The ideal case of detection corresponds to the detection of ballistic photons only, when no scattering event has occurred. The contribution of ballistic photons is, here, of $\sim 4.3\%$; whereas, the contribution of the third scattering order is of $\sim 17.5\%$.

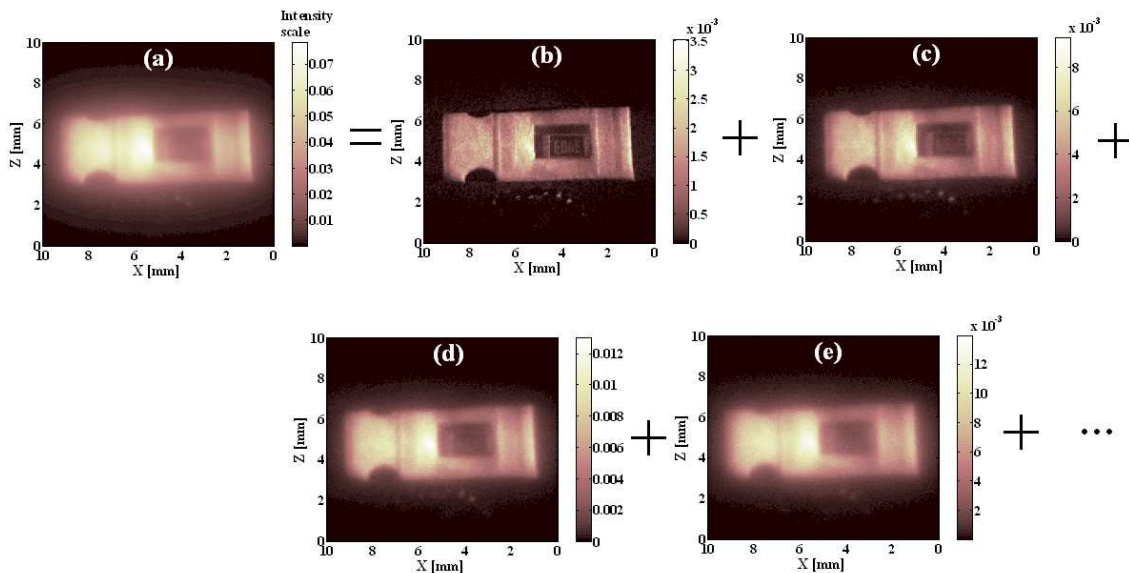


Figure 8.19: Simulated contribution of each scattering order during the transfer. (a) is the image from all detected scattering order, (b) is the ballistic image of the object and (c), (d) and (e) are respectively the single, the second and third scattering orders.

As observed in the previous Chapter, the dominant scattering order remains close to the value of the optical depth, for highly forward scattering particles. In the presented case,

the scattering orders from 3 up to 7 (around 5) present the principal contribution to the resultant image.

8.2.2 Correction procedure

Multiple scattering contribution can be calculated by summing the individual contribution of each scattering order larger or equal to 2. By subtracting this contribution to the simulated image, only ballistic and singly scattered photons are represented. In such case, the new simulated image generated is corrected from blurring effects. This strategy is also applied to the experimental image as seen in Fig.8.20. It is observed that the corrected experimental image shows, after correction, a better contrast especially on the edges of the imaged object. From these results, further investigations are now required to accurately deduce the capability of this technique in removing the blurring effects from experimental images.

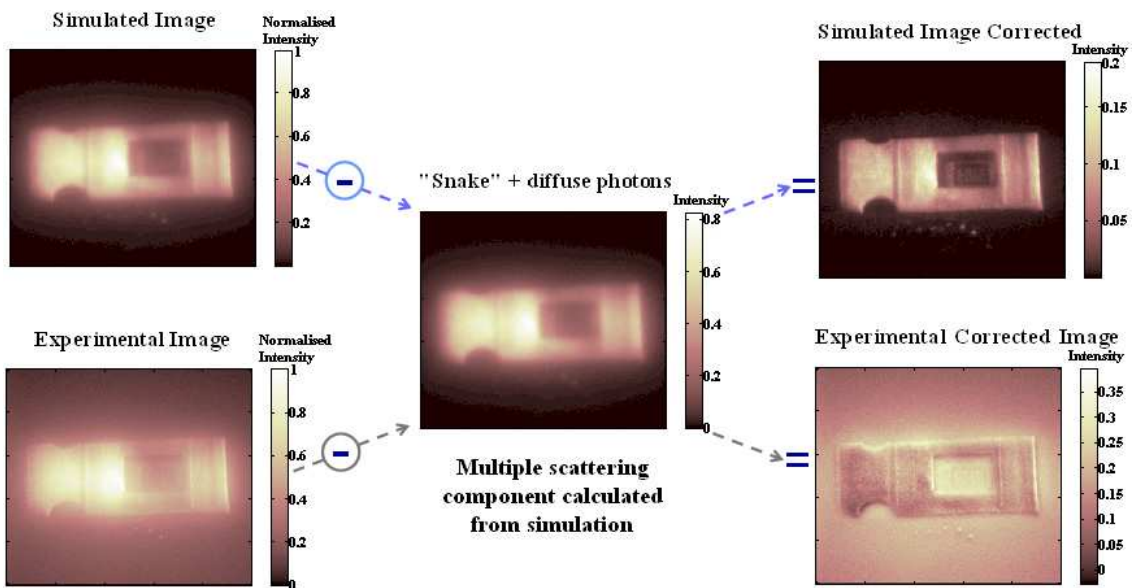


Figure 8.20: Correction procedure to multiple scattering on the recorded experimental and simulated images. The multiple scattering contribution is calculated from MC simulation and subtracted.

8.3 Propagation of ultra-short laser pulses through turbid media

At present, femtosecond laser pulses are employed to a variety of optical measurements. In spray diagnostics, the capability of time-gated detection using ultra-fast pulses has been recently demonstrated (Paciaroni 2004). The use of MC calculation to analyze the propagation of such light pulses within turbid media is, then, of fundamental importance in the optimization of modern instruments. This section is devoted to the simulation of ultra-short pulses within various homogeneous scattering volumes.

8.3.1 MC simulation

In these simulations, polystyrene spheres of diameter $D = 1 \mu\text{m}$ and $D = 20 \mu\text{m}$ are considered. The characteristics of the simulation are identical than those presented in section 6.2.1. However, the detection acceptance angle is, here, of $\theta_a = 11.4^\circ$. Photons exiting the cubic volume through the front, side and back face with an incident angle smaller than θ_a are recorded. The light pulse is assumed as a Dirac pulse and is assumed to be infinitesimally small. Time-resolved measurements for various scattering orders are also performed. A schematic of the simulation is given in Fig.8.21.

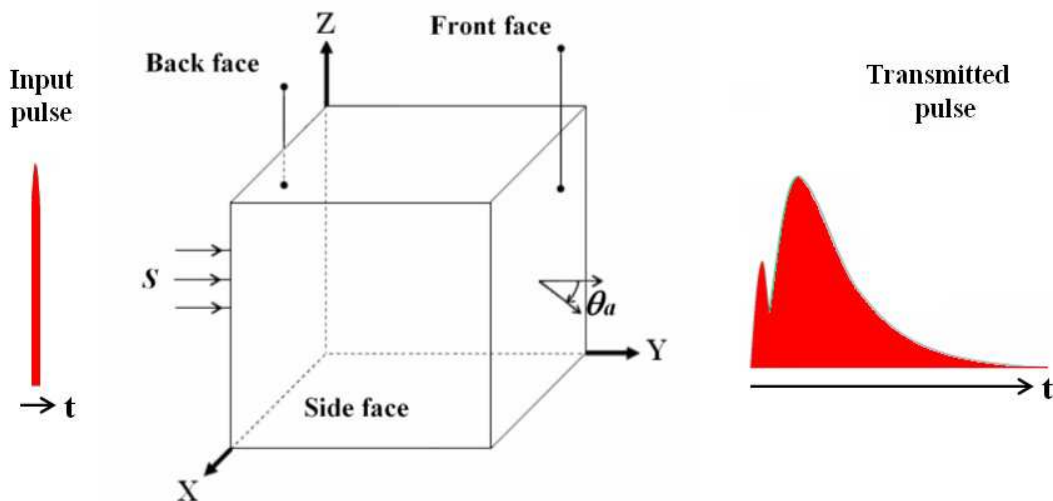


Figure 8.21: Simulated cubic volume of 10 mm length containing a solution of polystyrene microspheres. An ultra-short pulse of light crosses the medium along the Y axis. Time-resolved calculations are performed from MC modelling on the front, back and side face of the face of scattering volume. The detection acceptance angle is set to $\theta_a = 11.4^\circ$.

8.3.2 Results and discussion

Figure 8.22 shows the temporal profile of the pulse when exiting on the front, back and side face of the simulated volume for $1 \mu\text{m}$ particle diameter assuming $OD = 2$ and $OD = 5$. On the front face, at $OD = 2$, the amount of ballistic photons is clearly dominant at the early time detection. By increasing OD to 5, the contribution to snake photons becomes clearly visible, just after the arrival of ballistic photons, broadening the detected signal of ~ 5 ps. On the contrary, for the side and back detection, the increase of OD does not contribute to any increase the width of the detected light pulse.

Figure 8.23 shows identical MC calculations, but for the $20 \mu\text{m}$ particles. Due to the highly forward nature of the scattering phase function, the scattered and multiply-scattered photons do not travel much larger distances than the ballistic photons. As a results, a high pick of light intensity which include various scattering orders is detected on the front face, even at $OD = 5$.

On back face, a constant decrease of photon number as a function of time of arrival can be observed. Once again, the width of the pulse for backward and side detection is not increased when considering larger OD . When comparing results from $D = 1 \mu\text{m}$ with $D = 20 \mu\text{m}$ it is observed that differences occur mainly for the case of forward scattering detection.

Figure 8.24 is a comparison between $1 \mu\text{m}$ and $20 \mu\text{m}$ particle size, for an optical depth $OD = 10$. The effects of the scattering phase function on the temporal profile of the light pulse are illustrated. As predicted, on the front face, a much wider pulse is seen when considering more isotropic scattering phase function. In the same time, the ballistic pulse cannot be visualized anymore for $D = 1 \mu\text{m}$. An interesting feature is seen for the backward detection. For $D = 20 \mu\text{m}$ the temporal curve decrease continuously with the time. However, for $D = 1 \mu\text{m}$, an pick showing an increase of detected photons with the time can be noticed. The temporal profile of the back scattered light pulse (which in our case presented a similar width for $D = 1 \mu\text{m}$ and $D = 20 \mu\text{m}$) gives, then, an indication on the factor of anisotropy of the scattering particles. Finally, the pulse detected on the side face does not show any major qualitative divergences between $D = 1 \mu\text{m}$ and $D = 20 \mu\text{m}$.

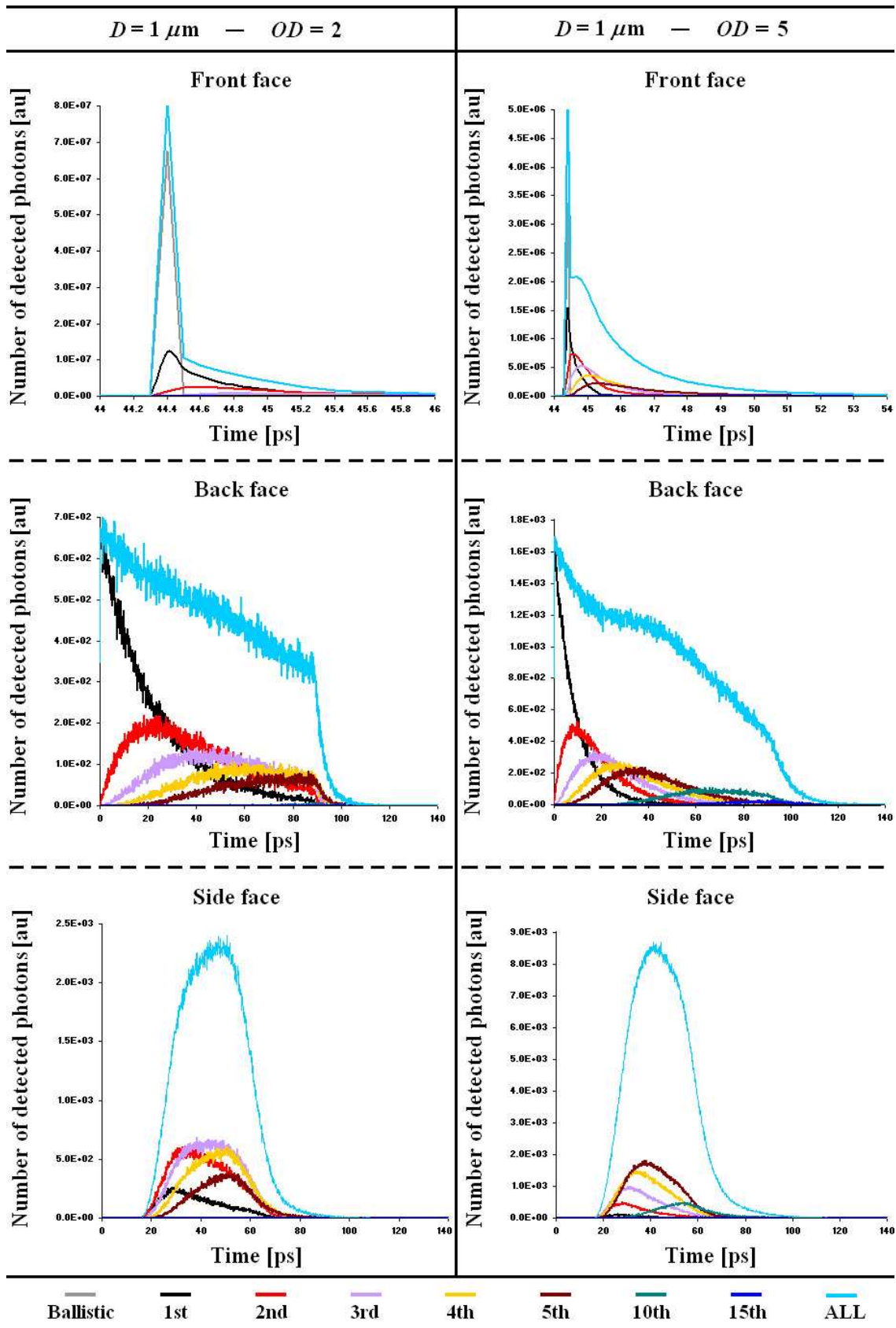


Figure 8.22: Simulated time-resolved calculations of a light pulse exiting on the front, back and side face of the simulated volume for the $1 \mu\text{m}$ spheres at $OD = 2$ and $OD = 5$.

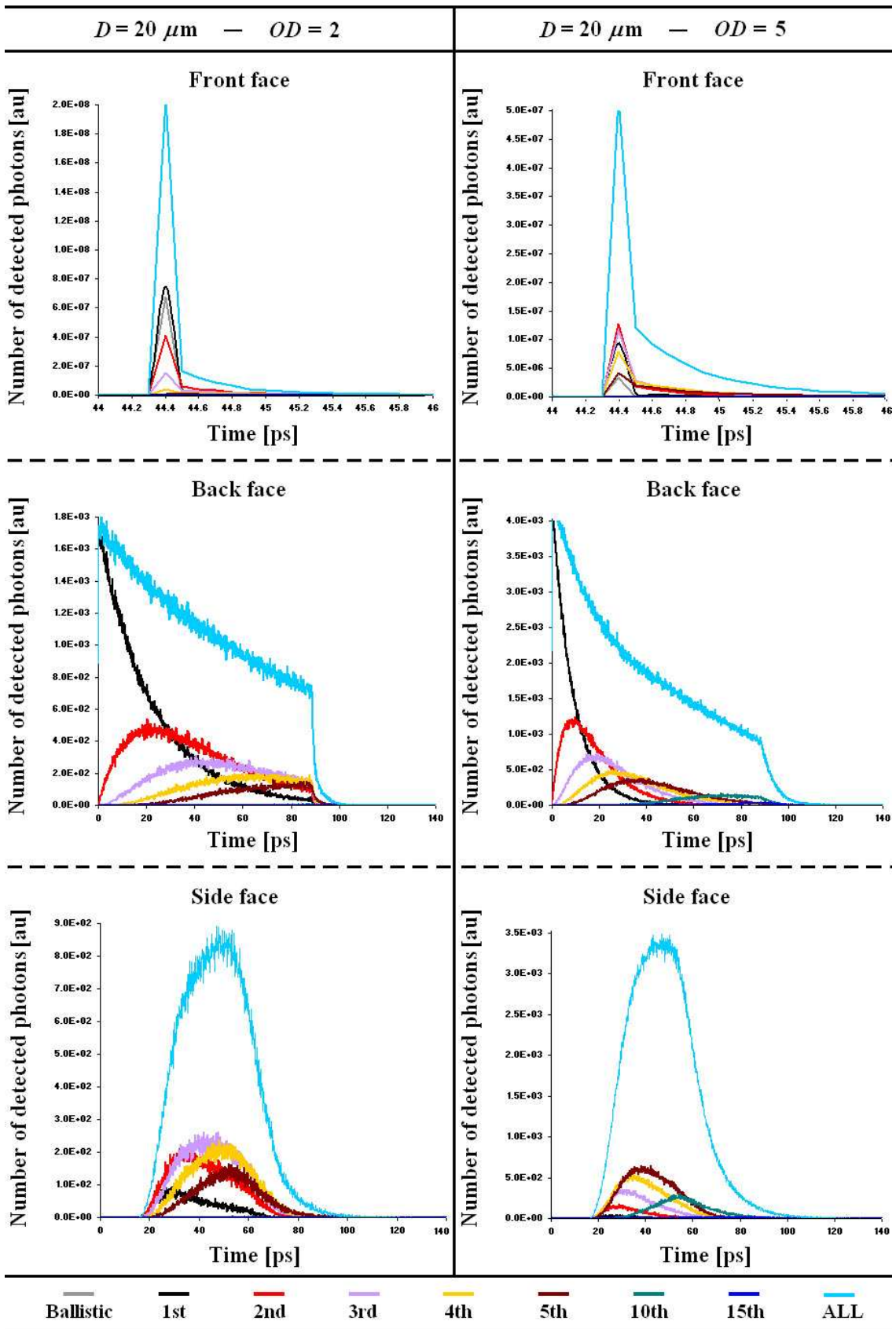


Figure 8.23: Simulated time-resolved calculations of a light pulse exiting on the front, back and side face of the simulated volume the 20 μm spheres at $OD = 2$ and $OD = 5$.

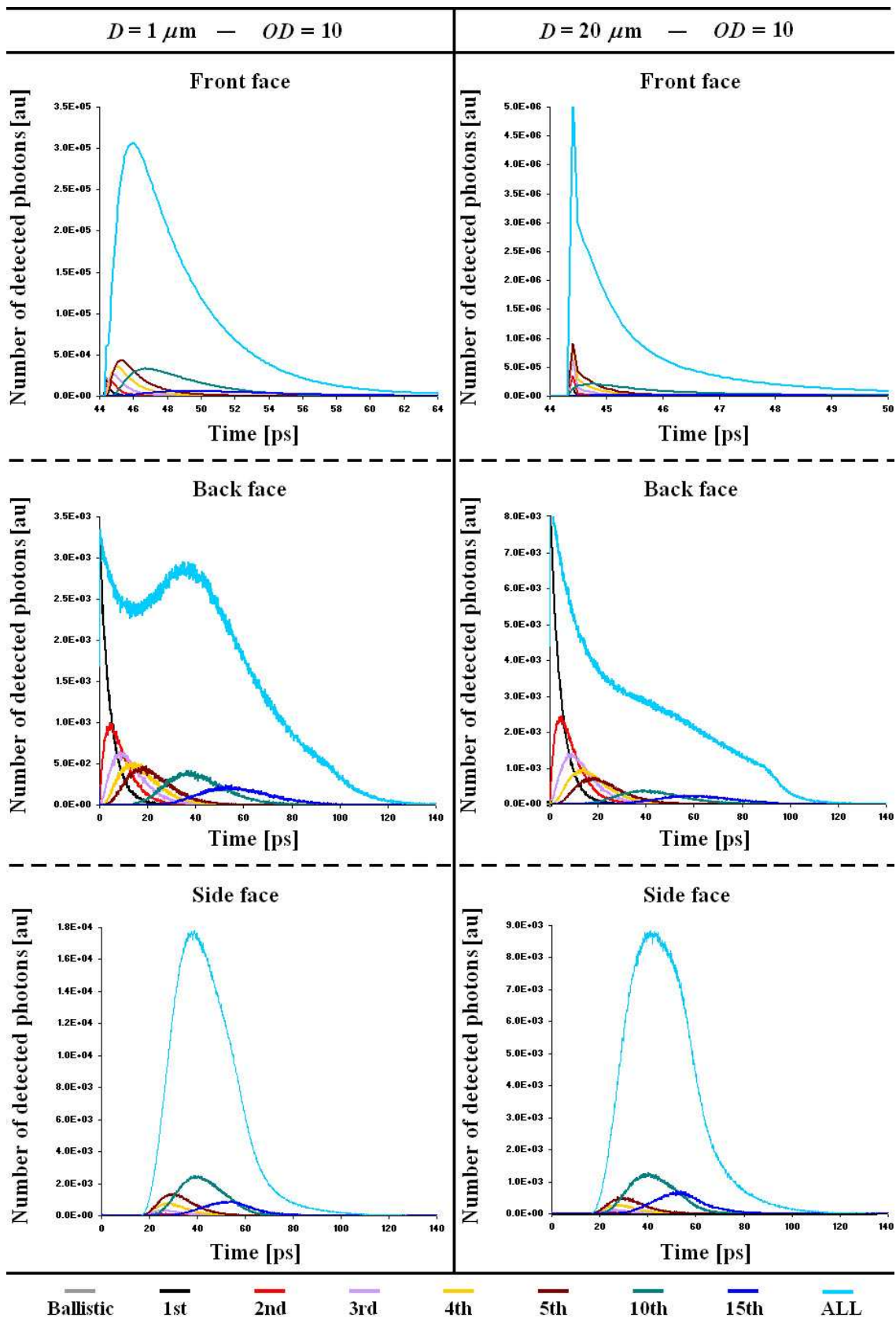


Figure 8.24: Simulated time-resolved calculations of a light pulse exiting on the front, back and side face of the simulated volume the $1 \mu\text{m}$ and $20 \mu\text{m}$ spheres at $OD = 10$.

8.4 Extrapolation of the Beer-Lambert transmission to multiple scattering

When considering a scattering system, the transmitted intensity, I_f , equals the sum of the non-scattered light intensity, I_b , from ballistic photons, plus the light intensity, I_{ms} , from scattered and multiply scattered photons:

$$I_f = I_b + I_{ms} \quad (8.4.1)$$

Assuming that I_{ms} is related to I_b by a coefficient k we have:

$$I_f = I_b + k.I_b \quad (8.4.2)$$

Here, k corresponds to the contribution of scattered and multiply scattered light over the contribution of non-scattered light. The contribution of ballistic photon is defined by $P(0)$ and the contribution of scattered and multiply scattered photons equals $P(tot) - P(0)$. For a normalized distribution where $P(tot) = 1$, the multiply scattered photon contribution becomes, $1 - P(0)$, and the coefficient k equals:

$$k = \frac{1 - P(0)}{P(0)} \quad (8.4.3)$$

From Eq.8.4.3 it follows:

$$I_f = I_b + \frac{1 - P(0)}{P(0)} \cdot I_b \quad (8.4.4)$$

By definition the Beer-Lambert law describes the exponential reduction of an incident light intensity I_i along a line-of-sight, as a function of the optical depth. In highly scattering environments, some photons which are scattered away from the optical axis undergo a succession of scattering events and are eventually redirected along the original path of the incident light. Experimentally, the amount of multiply-scattered light detected increases with the detection acceptance angle. The contribution of I_{ms} is not considered in the Beer-Lambert law, which applies only to the number of ballistic photons crossing the scattering sample, such that:

$$I_b = I_i \cdot e^{-OD} \quad (8.4.5)$$

By including Eq.8.4.5 in Eq.8.4.4 we obtain:

$$I_f = I_i \cdot e^{-OD} + \frac{1 - P(0)}{P(0)} \cdot I_i \cdot e^{-OD} \quad (8.4.6)$$

Finally:

$$I_f = \frac{1}{P(0)} \cdot I_i \cdot e^{-OD} \tag{8.4.7}$$

Here, the final light intensity calculated from the conventional Beer-Lambert law is increased by the factor $1 / P(0)$ which is the inverse probability density of the ballistic photon contribution.

	1 μm polystyrene spheres			2 μm polystyrene spheres		
Optical Depth	2	5	10	2	5	10
1/P(0) at θ _a = 8.5°	1.55	5.45	164.49	2.59	14.54	520.16
1/P(0) at θ _a = 1.5°	1.02	1.15	6.24	1.07	1.53	
Beer-Lambert transmission	0.135	0.0067	0.000045	0.135	0.0067	0.000045
Transmission at θ _a = 8.5°						
Corrected Beer-Lambert	0.210	0.0367	0.007468	0.350	0.0980	0.0236
Simulated data	0.192	0.0282	0.005200	0.298	0.0752	0.0173
Experimental data	0.188	0.0224	0.001800	0.308	0.0615	0.0071
Transmission at θ _a =1.5°						
Corrected Beer-Lambert	0.138	0.0078	0.000283	0.145	0.0103	
Simulated data	0.138	0.0076	0.000237	0.144	0.0096	
Experimental data	0.147	0.0105	0.000274	0.219	0.0248	0.0010

	5 μm polystyrene spheres			20 μm polystyrene spheres		
Optical Depth	2	5	10	2	5	10
1/P(0) at θ _a = 8.5°	3.17	17.96	436.11	3.42	23.39	793.22
1/P(0) at θ _a = 1.5°	1.25	2.31	20.58	2.25	7.48	73.46
Beer-Lambert transmission	0.135	0.0067	0.000045	0.135	0.0067	0.000045
Transmission at θ _a = 8.5°						
Corrected Beer-Lambert	0.429	0.1210	0.019799	0.463	0.1576	0.0360
Simulated data	0.359	0.0934	0.014800	0.401	0.1242	0.0268
Experimental data	0.373	0.0728	0.009400	0.500	0.1267	0.0081
Transmission at θ _a =1.5°						
Corrected Beer-Lambert	0.169	0.0156	0.000934	0.305	0.0504	0.00333
Simulated data	0.165	0.0140	0.000791	0.288	0.0451	0.00280
Experimental data	0.203	0.0230	0.001400	0.350	0.0550	0.00170

Table 8.1: Deduction of the corrective factor $1/P(0)$ from the Monte Carlo calculations. The corrected/modified Beer-Lambert transmission is compared with the simulated results and with the experiment presented in subsection 6.2.2.

The results from the extrapolated Beer-Lambert law are compared in Table 8.1 with the

experimental and simulated results for the transmission of the laser beam at various optical depths and detection acceptance angles. Good agreement is found between the simulated and experimental results for the three optical depth $OD = 2$, $OD = 5$ and $OD = 10$.

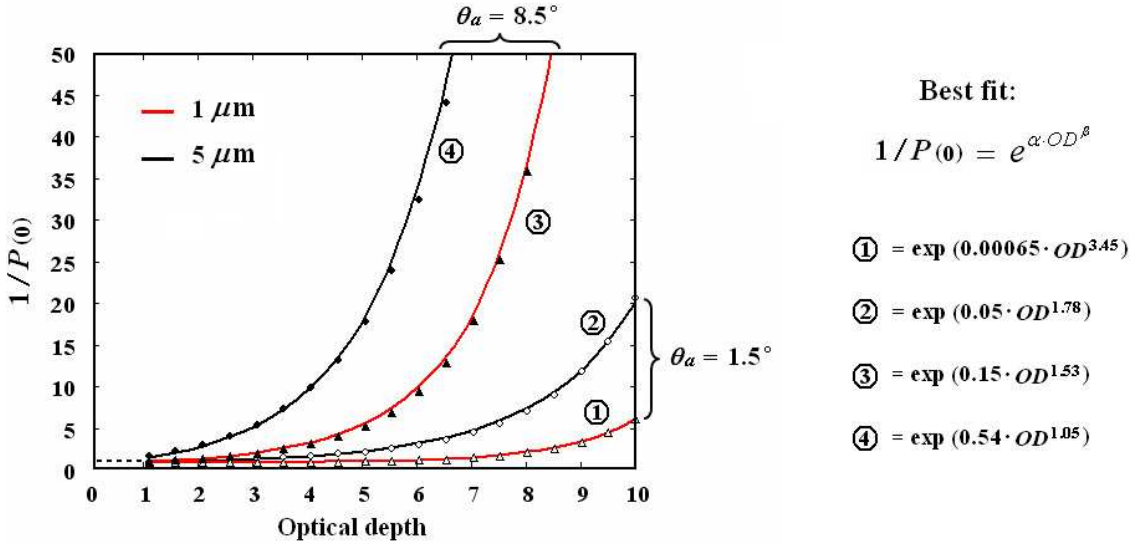


Figure 8.25: Corrective factor $1/P(0)$ as a function of the optical depth. Each value of $1/P(0)$ is deduced via MC calculations for the intermediate scattering regime $1 < OD < 10$. The red and black lines correspond to the best fit of the calculated data.

The factor $1/P(0)$ is plotted in Fig.8.25 as a function of OD for the $1 \mu\text{m}$ and $5 \mu\text{m}$ sphere diameters and for the detection acceptance angles $\theta_a = 1.5^\circ$ and $\theta_a = 8.5^\circ$. The simulation data shows that $1/P(0)$ increases exponentially with $\alpha \cdot OD^\beta$. This increase becomes more apparent at large detection acceptance angles and for scattering particles which exhibit a dominant forward scattering lobe (larger particles). From these results the Beer-Lambert relation can be modified and written such that the light intensity from multiply scattered photons is considered:

$$I_f = I_i \cdot e^{-OD + \alpha \cdot OD^\beta} \quad (8.4.8)$$

The coefficients α and β are related to the detection acceptance angle and to the particle diameter D . The term $-OD + \alpha \cdot OD^\beta$ is always negative implying $\alpha \cdot OD^\beta < OD$.

Summary and Conclusion

MULTIPLE scattering of light within sprays and other complex turbid media has been investigated by means of a computational model developed in-house. The model is based on the MC technique and simulates the propagation of optical radiation within scattering volumes, where both particle concentration and size distribution vary strongly with position. The main results and achievements of this thesis are enumerated as follows:

- A new and flexible MC code for light scattering in inhomogeneous polydisperse turbid media has been designed. The model divides the entire simulated volume into elementary homogeneous cubic cells. From such an approach, high variations of droplets number density within 3D volumes can be taken into account. Both the size and number of cells are flexible, and various spray geometries and structures can be constructed.
- Simulated results have shown excellent agreement with the analytical approach for the case of isotropic scattering and homogeneous media. A source-detector geometry that allows the intensity of single scattering to be measured separately from higher scattering orders has been proposed and tested.
- A method to approximate the scattering phase function from different droplet sizes has been presented and verified. This approach reduces the required memory space by ~ 20 times, and is useful for to the study of inhomogeneous polydisperse media.
- The simulation of the exact experimental light source has been performed using an input matrix array. The procedure is key to the validation of any MC model, where experimental and simulated images have to be accurately compared.
- Comparisons between experimental and simulated results have demonstrated excellent agreements for different solutions of monodisperse polystyrene spheres suspended in distilled water. Various configurations have been investigated by changing the properties of

the scattering medium, (optical depth of 2, 5 and 10 - particles sizes of 1, 2.5 and 20 μm) and of the collection optics (forward or side detection - detection acceptance angles of 1.5° and 8.5°). In all cases, the light intensity distribution provided from the MC model is very close to the experimental results. The capability of the code to generate simulated images with spatial resolution equal to those of the experimental images has also been demonstrated.

- Analysis of different scattering orders in the intermediate scattering regime has been carried out using a crossed source-detector geometry. The influence of the detector acceptance angle, θ_a , and of the source-detector angle, β , is shown quantitatively. The best configuration for the detection of the relative singly scattered light is found to be at $\beta = 10^\circ$ and with a detection acceptance angle as close as possible to 0° . These investigations were performed considering a homogeneous collection of fuel droplets.
- The transition from the single scattering regime to the multiple scattering regime does not operate in the same manner for isotropic and anisotropic scattering. For isotropic scattering, the single scattering order is always the dominant one, until all orders become equal, when reaching high optical depths. On the contrary, when considering scattering phase functions with highly forward scattering lobes (with an anisotropy factor close to 1), the dominant scattering order changes from one to another as the optical depth increases. It has been observed in this case, that the dominant scattering order and the value of the optical depth are nearly the same.
- The presented MC code is not only applicable to spray diagnostics, and has also been employed for a variety of studies. In one case the code was used to study the scattering of light by single particles with detection in the far-field region. Another successful application is the investigation of image transfer through scattering volumes and the analysis of blurred images. Using the MC model, the reconstruction of an experimental object hidden behind a scattering medium has been performed. Such an approach is particularly promising for visibility issues such as imaging through the fog, mist or clouds. The third presented application, concerns the transmission of femtosecond laser pulses through diffusing media. It has been observed that the relative intensity of the ballistic light pulse depends, especially, on the forward scattering nature of scattering phase function considered. The more forward scattering the particles, the less visible the ballistic photon signal will be. Note that the detection acceptance angle and the optical depth, also play a significant role in the final temporal profile of the detected laser pulse. The last application of the MC model concerns the correction of the Beer-Lambert transmission from the multiple scattering contribution.

- To the author's knowledge, no previous attempts have been made to simulate photon transport within inhomogeneous polydisperse sprays with comparison against experimental results. This attempt has been successfully completed in this project showing that the laser sheet images of a typical hollow cone spray are affected by ~76% of multiply scattered laser light. As PDA measurements were still operable under such conditions, it has been deduced that most other sprays would encounter a superior amount of multiply scattered light. These results demonstrate how serious the effects of multiple scattering are in optical spray diagnostics. The use of computational models of the type developed here is, then, of fundamental importance for the development and testing of new optical instruments.

Recommendations for further work:

- Further improvements of the MC model could be performed. These improvements concern the tracking of both the phase and polarization of light. Inelastic scattering could also be considered and applied to the simulation of Laser Induce Fluorescence processes.
- A second important future work would be the modelling of the collection optics, in order to realistically simulate different configurations of the experimental detection. Output data of MC simulation could be used as an input source of a complementary ray-tracing code, which would simulate the propagation of photons through various successive optics.
- The transfer of image through turbid media via MC simulation has just been introduced in the last chapter. The technique has revealed important capabilities in the analysis of blurred images and requires further investigation.
- As shown within this dissertation, the combination of experimental measurements and MC calculations allows quantification, analysis and correction of the multiple scattering contribution for optical spray diagnostics. One promising future application concerns the calculation of photon time-of-flight for the optimization of modern time-gated detection based techniques. Another significant future work, would be the development of inverse MC models for the determination of droplet characteristics (size distribution and concentration with location) from the analysis of the scattered and multiply scattered radiation measured experimentally.

Bibliography

- Abubakirov, I. and Gusev, A. (1990). Estimation of the scattering properties of the lithosphere of kamchatka based on monte carlo simulation of rcord envrlope of a near earthquake. *Physics of the Earth and Planetary Interiors*, 64:52–67.
- Adrian, R. (1984). Scattering particles characteristics and their effect on pulsed laser measurements of fluid flow: speckle velocimetry vs. particle image velocimetry. *Applied Optics*, 23:1690–1691.
- Adrian, R. (2005). Twenty years of particle image velocimetry. *Experiments in Fluids*, 39:159–169.
- Aizu, Y., Durst, F., Grehan, G., Onofri, F., and Xu, T.-H. (1993). Pda-system without gaussian beam defects. *Proceeding of the 3rd International Congress on Optical Particle Sizing*.
- Albrecht, H., Borys, M., Damaschke, N., and Tropea, C. (1999). The imaging properties of scattering particles in laser beams. *Measurements Science and Technology*, 10:564–574.
- Arai, M., Shimizu, M., and Hiroyasu, H. (1985). Breakup length and spray angle of high speed jet. *Proceeding of the 3rd ICLASS (International Conference on Liquid Atomization and Spray System)*.
- Ariessohn, P., Sel, S., and R., E. (1980). Two-wavelength laser transmissometer for measurements of the mean size and concentration of coal ash droplets in combustion flows. *Applied Optics*, 19:3775–3781.
- Bachalo, W. (1980). Method for measuring the size and velocity of spheres by dual-beam light-scatter interferometry. *Applied Optics*, 19:363–370.
- Bachalo, W. (2000). Spray diagnostics for the twenty-first century. *Atomization and spray*, 10:439–474.

- Bachalo, W. and Houser, M. (1984). Phase/doppler spray analyzer for simultaneous measurements of drop size and velocity distributions. *Optical Engineering*, 23:583–590.
- Bachalo, W. and Houser, M. (1985). Spray size and velocity measurement measurements using the phase/doppler particle analyser. *Proceeding of the 3rd ICLASS (International Conference on Liquid Atomization and Spray System)*.
- Bartel, S. and Hielscher, A. (2000). Monte carlo simulations of the diffuse backscattering mueller matrix for highly scattering media. *Applied Optics*, 39:1580–1588.
- Berlman, I. (1971). *Handbook of Fluorescence spectra of aromatic molecules*. 2nd ed., Academic Press, New York and London.
- Berrocal, E., Jermy, M., Moukaideche, F., and Meglinski, I. (2005a). Dense spray analysis using optical measurements and monte carlo simulation. *Proceedings of the 18th ILASS-America (Institute for Liquid Atomization and Spray System)*.
- Berrocal, E., Meglinski, I., and Jermy, M. (2005b). New model for light propagation in highly inhomogeneous polydisperse turbid media with applications in spray diagnostics. *Optics Express*, 13:9181–9195.
- Berrocal, E., Romanov, V., Churmakov, D., and Meglinski, I. (2004). Low and high orders light scattering within the dispersible media. *SPIE Proceedings of the 6th conferrence in Optical Technologies in Biophysics and Medicine (invited paper)*, 5771:74–86.
- Bilenca, A., Desjardins, A., Bouma, B., and Tearney, G. (2005). Multicanonical monte carlo simulation of light propagation in biological media. *Optics Express*, 13:9822–9833.
- Bizheva, K., Siegel, A., and Boas, D. (1998). Path-length resolved dynamic light scattering in highly scattering random media: the transition to diffusing wave spectroscopy. *Physical Review*, 58:7664–7667.
- Boas, D., Culver, J., Stott, J., and Dunn, A. (2002). Three dimensional monte carlo code for photon migration through complex heterogeneous media including the adult human head. *Optics Express*, 10:159–170.
- Bohren, C. and Huffman, D. (1983). *Absorption and Scattering of Light by Small Particles*. Wiley-VCH.

- Born, M. and Wolf, E. (1986). *Principles of optics: Electromagnetic Theory of Propagation, Interference and Diffraction of Light*. London: Pergamon Press, 6th Edition.
- Bucher, E. (1973). Computer simulation of light pulse propagation for communication through thick clouds. *Applied Optics*, 12:2391–2400.
- Burby, M., Nars, G., and Cox, Y. (2006). Application of sprays in the painting and coating of materials with acoustic properties. *Proceeding of the 10th ICLASS (International Conference on Liquid Atomization and Spray System)*.
- Char, J., Kuo, K., and Hsieh, K. (1990). Observation of breakup processes of liquid jets using real-time x-ray radiography. *Journal of Propulsion and Power*, 6:544–551.
- Charalampous, G., Hardalupas, Y., and Taylor, P. (2004). Optimisation of the droplet sizing accuracy of the combined scattering (mie) / laser induced fluorescence (lif) technique. *Proceeding of the 12th International Symposium of Applications of Laser techniques to Fluid Mechanics*.
- Chigier, N. (1993). An assessment of spray technology-editorial. *Atomization and Sprays*, 3:365–371.
- Chigier, N. (2006). Challenge for future research in atomization and spray technology. *Proceeding of the 10th ICLASS (International Conference on Liquid Atomization and Spray System)*.
- Churmakov, D. (2005). *Multipurpose Computational Model for Modern Optical Diagnostics and its Biomedical Applications*. PhD thesis, Cranfield University.
- Cornillaut, J. (1972). Particle size analyzer. *Applied optics*, 11:265–268.
- Côté, D. and Vitkin, I. (2004). Robust concentration determination of optically active molecules in turbid media with validated three-dimensional polarization sensitive monte carlo calculations. *Optics Express*, 13:148–163.
- Dai, Z. and Faeth, G. (2001). Temporal properties of secondary drop breakup in the multimode breakup regime. *International Journal of Multiphase Flow*, 27:217–236.
- Damaschke, N., Gouesbet, G., Grehan, G., Mignon, H., and Tropea, C. (1998). Response of phase doppler anemometer systems to nonspherical droplets. *Applied Optics*, 37:1752–1761.
- Damaschke, N., Nobash, H., Nonn, T., Semidetnov, N., and Tropea, C. (2005). Multi-dimensional particle sizing techniques. *Experiments in Fluids*, 39:336–350.

- Doicu, A., Koser, J., Wriedt, T., and Bauckhage, K. (1998). Light scattering simulation and measurement of monodisperse spheroids using phase doppler anemometer. *Particle and Particle Systems Characterizations*, 15:257–262.
- Domann, R. (2002). *Characterization of Spray Unsteadiness*. PhD thesis, Imperial College of Science, Technology and Medicine, University of London.
- Domann, R. and Hardalupas, Y. (2003). Quantitative measurement of planar droplet sauter mean diameter in sprays using planar droplet sizing. *Particle and Particle Systems Characterizations*, 20:209–218.
- Driscoll, K., Sick, V., and Gray, C. (2003). Simultaneous air/fuel-phase piv measurements in a dense fuel spray. *Experiments in Fluids*, 35:112–115.
- Dullenkopf, K., Willmann, M., Wittig, S., Shone, F., Manfred, S., Tropea, C., and Mundo, C. (1998). Comparative mass flux measurements in sprays using a patternator and the phase-doppler technique. *Particle and Particle Systems Characterizations*, 15:81–89.
- Durst, F. (2000). Fluid mechanics developments and advancements in the 20th century. *Proceeding of the 10th International Symposium of Applications of Laser techniques to Fluid Mechanics*.
- Durst, F., Brenn, G., and Xu, T.-H. (1997). A review of the developpement and characteristics of planar phase doppler anemometry. *Measurements Science Technology*, 8:1203–1221.
- Durst, F., Tropea, C., and Xu, T.-H. (1994). The slit effect in phase doppler anemometry. *Proceeding of the 2nd Intenational Conference on Fluid Dynamics*.
- Durst, F. and Whitelaw, J. (1971). Optimization of optical anemometers. *Proceeding of the Royal Society of London, Serie A*, 324:157–181.
- Durst, F. and Zare, M. (1975). Laser doppler measurements in two-phase flows. *Proceeding of the Laser Doppler Anemometry Symposium*.
- Faeth, G. (1996). Spray combustion phenomena. *Twenty-Sixth Simposium (International) on Combustion*, 26:1596–1612.
- Faeth, G., Hsiang, L.-P., and Wu, P.-K. (1995). Sructure and breakup properties of sprays. *Int. J. Multiphase Flow*, 21:99–127.
- Farmer (1972a). Determination of a third orthogonal velocity component using two rotationally displaced laser doppler velocimeter systems. *Applied Optics*, 11:770–776.

- Farmer (1972b). Measurement of particle size, number density, and velocity using a laser interferometer. *Applied Optics*, 11:2603–2612.
- Galland, P., Liang, X., Wang, L., Breisacher, K., Liou, L., Ho, P., and Alphano, R. (1995). Time-resolved optical imaging of jet spray and droplets in highly scattering medium. *Proceedings of the American Society of Mechanical Engineers*.
- Gandjbakhche, A. and Weiss, G. (1995). Random walk and diffusion-like models of photon migration in turbid media. *Progress in Optics, Elsevier Science*, 34:333–402.
- Gangnus, S., Matcher, S., and Meglinski, I. (2004). Monte carlo modeling of polarized light propagation in biological tissues. *Laser Physics*, 14:886–891.
- Girasole, T., Ren, K., Lebrun, D., Gouesbet, G., and Grehan, G. (2000). Particle imaging sizing: Gtln simulations. *Journal of Visualization*, 3:195–202.
- Glantschnig, W. and W., C. (1981). Light scattering from water droplets in the geometrical optics approximation. *Applied Optics*, 20:2499–2509.
- Glover, A., Skippon, S., and Boyle, R. (1995). Interferometric laser imaging for droplet sizing: a method for droplet-size in sparse spray system. *Applied Optics*, 34:8409–8421.
- Gouesbet, G. and Grehan, G. (1982). A generalized lorenz-mie theory. *Journal of Optics (Paris)*, 13:97–103.
- Gougeon, P., Toulouzan, J., Gouesbet, G., and Thenard, C. (1987). Optical measurements of particles size and concentration in densely laden media using a visible/infrared double extinction technique. *Journal of Physics E: Scientific Instruments*, 20:1235–1242.
- Grehan, G., Gouesbet, G., Naqwi, A., and Durst, F. (1991). Evaluation of a phase doppler system using generalized lorenz-mie theory. *Proceeding of International Symposium on Multiphase Flow*.
- Grehan, G., Gouesbet, G., Naqwi, A., and Durst, F. (1992). Trajectory ambiguities in phase doppler systems: use of polarizers and additional detectors to suppress the effect. *Proceeding of the 6th International Symposium on Application of Laser Techniques to Fluid Mechanics*.
- Grousson, R. and Mallick, S. (1977). Study of flow pattern in a fluid by scattered laser light. *Applied Optics*, 16:2334–2336.
- Haenlein, A. (1932). Disintegration of a liquid jet. *NACA TM 659*.

- Hebden, J., Kruger, R., and Wong, K. (1991). Time resolved imaging through a highly scattering medium. *Applied Optics*, 30:788–794.
- Hesselbacher, K. Anders, K. and Frohn, A. (1991). Experimental investigation of gaussian beam effect on the accuracy of a droplet sizing method. *Applied Optics*, 30:4930–4935.
- Hirlemann, E. (1988). Modelling of multiple scattering effects in fraunhofer diffraction particle size analyser. *Particles and Particle Systems Characterizations*, 5:57–65.
- Hiroyasu, H., Arai, M., and Shimizu, M. (1991). Breakup length of a liquid jet and internal flow in a nozzle. *Proceeding of the 5th ICLASS (International Conference on Liquid Atomization and Spray System)*.
- Hogerheijde, M. and van der Tak, F. (2000). An accelerated monte carlo method to solve two-dimensional radiative transfer and molecular excitation. *Astronomy and Astrophysics*, 362:697–710.
- Hsiang, L.-P. and G., F. (1992). Near-limit drop deformation and secondary breakup. *International Journal of Multiphase Flow*, 18:635–652.
- Huzarewicz, S., Stewart, G., and Presser, C. (1991). Application of the singular value decomposition to the inverse fraunhofer diffraction problem. *Proceeding of the 5th ICLASS (International Conference on Liquid Atomization and Spray System)*.
- Ishimaru, A. (1978). *Wave Propagation and Scattering in Random Media*. New York: Academic Press.
- Jacques, S. and Wang, X. (1997). Path integral description of light transport versus monte carlo and diffusion theory. *Optical Tomography and Spectroscopy of Tissue: Theory, Instrumentation, Model, and Human StudiesII*, 2979:488–499.
- Jermy, M. and Greenhalgh, D. (2000). Planar dropsizing by elastic and fluorescence scattering in sprays too dense for phase doppler measurement. *Applied Physics B*, 71:703–710.
- Kandidov, V. (1996). Monte carlo method in nonlinear statistical optics. *Review of Topical Problems - Physics, Russian Academy of Sciences*, 39:1243–1272.
- Kawaguchi, T., Akasada, Y., and Maeda, M. (2002). Size measurements of droplets and bubbles by advanced interferometric laser imaging technique. *Measurement Science and Technology*, 13:308–316.

- Kaye, P. (1998). Spatial light-scattering analysis as a means of characterizing and classifying non-spherical particles. *Measurement Science and Technology*, 9:141–149.
- Keijzer, M. (1993). *Light Transport for Medical Laser Treatments*. PhD thesis, Delft University of Technology.
- Kokhanovsky, A. and Weichert, R. (2001). Multiple light scattering in laser particle sizing. *Applied Optics*, 40:1507–1513.
- König, G., Ander, K., and Frohn, A. (1986). A new light scattering technique to measure the diameter of periodically generated moving droplets. *Journal of Aerosol Science*, 17:157–167.
- Kurosawa, R., Hishida, K., and M., M. (2002). Combined measurement of lif and ilids for vapor concentration and droplet size and velocity in a spray. *Proceeding of the 11th International Symposium of Applications of Laser techniques to Fluid Mechanics*.
- Kuzmin, V. and Romanov, L. (1996). Coherent phenomena in light scattering from disordered systems. *Physics-Uspekhi*, 39:231–261.
- Kuzmin, V., Romanov, V., and Zubkov, L. (1994). Propagation and scattering of light in fluctuating media. *Physics Reports*, 248:71–368.
- Labs, J. and Parker, T. (2005). Multiple-scattering effects on infrared scattering measurements used to characterize droplet size and volume fraction distributions in diesel sprays. *Applied Optics*, 44:6049–6057.
- Labs, J. and Parker, T. (2006). Two-dimensional droplet size and volume fraction distributions from the near-injector region of high pressure diesel sprays. *Atomization and Sprays*, To appear.
- Lasheras, J. and Hopfinger, E. (2000). Liquid jet instability and atomization in a coaxial gas stream. *Annu. Rev. Fluid Mech.*, 32:275–308.
- Latimer, P., Brunsting, A., Pyle, B., and Moore, C. (1978). Effects of sphericity on single particle scattering. *Applied Optics*, 17:3152.
- Laven, P. (2006). Mieplot: A computer program for scattering of light from a sphere using mie theory and the debye series. <http://www.philiplaven.com/mieplot.htm>.
- Lavigne, C. (2001). *Etude Theorique et Experimentale de la Propagation du Rayonnement UV dans la Basse Atmosphere*. PhD thesis, Universite de Rouen.

- Le Gal, P. (1999). *Development of a laser sheet dropsizing technique for spray*. PhD thesis, Cranfield University.
- Le Gal, P., Farrugia, N., and Greenhalgh, D. (1999). Laser sheet dropsizing of dense sprays. *Optics and Laser Technology*, 31:75–83.
- L'Ecuyer, P. (1998). *Random Number Generation - Handbook of simulation*, chapter 4. Wiley - Interscience.
- Lee, K., Lee, C., and Joo, Y. (2003). Application of particle image velocimetry and entropy analysis to investigate spray structure for gasoline direct injection. *Measurement Science and Technology*, 14:953–964.
- Lee, S. and Reitz, R. (2001). Effect of liquid properties on the breakup mechanism of high-speed liquid drops. *Atomization and Sprays*, 11:1–19.
- Lefebvre, A. (1983). *Gas Turbine Combustion*. Hemisphere Publishing Corporation.
- Lefebvre, A. (1989). *Atomisation and Sprays*. Taylor & Francis.
- Lin, S. and Reitz, R. (1998). Drop and spray formation from a liquid jet. *Annual Review in Fluid Mechanics*, 30:85–105.
- Linne, M., Paciaroni, M., Sedarsky, D., Berrocal, E., and I., M. (2006). Ballistic imaging of the liquid core in the dense spray region. *PECS, paper in progress*.
- Linne, M., Paciaroni, M., Sedarsky, D., Gord, J., and Meyer, T. (2005). Ballistic imaging of the liquid core for a jet in cross flow. *Proceedings of the 18th ILASS-America (Institute for Liquid Atomization and Spray System)*.
- Lux, I. and Koblinger (1991). *Monte Carlo Particle Transport Methods: Neutron and Photon calculations*. CRC Press.
- Ma, X., Lu, J., Brock, S., Jacobs, K., Yang, P., and Xin, X.-H. (2003). Determination of complex refractive index polystyrene microspheres from 370 to 1610 nm. *Physics in Medicine and Biology*, 48:4165–4172.
- MacPhee, A., Tate, M., Powell, C., Yue, Y., Renzi, M., Ercan, A., Narayanan, S., Fontes, E., Walther, J., Schaller, J., and Gruner, S. Wang, J. (2002). X-ray imaging of shock waves generated by high-pressure fuel sprays. *Science*, 295:1261–1263.
- Maeda, M., Kawaguchi, T., and Hishida, K. (2000). Novel interferometric measurement of size and velocity distributions of spherical particles in fluid flows. *Measurement Science and Technology*, 11:L13–L18.

- Matheson, L. and Saunderson, J. (1952). *Optical and electric properties of polystyrene*, chapter Styrene: Its Polymers, Copolymers and Derivatives. New York: Reinhold.
- Matsuura, K., Zarogoulidis, K., Hardalupas, Y., Taylor, A., Kawagushi, T., Sugimoto, D., and Hishida, K. (2006). Simultaneous planar measurement of size and three-component velocity of droplets in an aero-engine airblast fuel spray by stereoscopic laser imaging technique. *Proceeding of the 10th ICLASS (International Conference on Liquid Atomization and Spray System)*.
- Meglinski, I. and Matcher (2001). Modelling the sampling volume for skin blood oxygenation measurements. *Medical and Biological Engineering and Computing*, 39:44–50.
- Meglinski, I., Romanov, V., Churmakov, D., Berrocal, E., Jermy, M., and Greenhalgh, D. (2004). Low and high order light scattering in particulate media. *Laser Physics Letters*, 1:387–390.
- Melling, A. (1997). Tracer particles and seedings for particle image velocimetry. *Measurement Science and Technology*, 8:1406–1416.
- Meynard, R. (1980). Equal velocity fringes in a rayleigh-benard flow by a speckle method. *Applied Optics*, 9:1385–1386.
- Meynard, R. (1983). Instantaneous velocity field measurements in unsteady gas flow by speckle velocimetry. *Applied Optics*, 22:535–540.
- Mie, G. (1908). Beitrage zur optik trubermedien, speziell kolloidaler metallosungen. *Annalen Physik*, 25:377–452.
- Mugele, R. and Evans, H. (1951). Droplet size distribution in sprays. *Industrial and Engineering Chemistry*, 43:1317–1324.
- Mulhem, B., Khoja, G., Fritsching, U., and Schulte, G. (2004). Photographic observation of breakup of hollow cone suspension sheet. *Proceedings of the 19th ILASS-Europe (Institute for Liquid Atomization and Spray System)*.
- Naqwi, A., Durst, F., and Kraft, G. (1991). Sizing of submicrometer particles using a phase-doppler system. *Applied Optics*, 30:4903–4913.
- Naqwi, A. and Zieme, M. (1992). Extended phase doppler anemometry for sizing particles less than 10 microns. *Journal of Aerosole Science*, 23:613–621.
- Nars, G., Yule, A., and Bending, L. (2002). *Industrial Sprays and Atomization: Design, Analysis and Applications*. Springer-Verlag London.

- Nikolov, I. and Ivanov, C. (2000). Optical plastic refractive index measurements in the visible and near-infrared regions. *Applied Optics*, 39:2067–2070.
- Oakley, D. (1995). The production of particles by spray drying. *Journal of Aerosol Science*, 26:1322–1323.
- Ohmi, K. and Li, H. (2000). Particle-tracking velocimetry with new algorithms. *Measurement Science and Technology*, 11:603–616.
- Onofri, F. (2005). Diffusion de la lumiere. *Seme Ecole d'Automne, Velocimetrie et Granulometrie Laser en Mecanique des Fluides*.
- Onofri, F., Grehan, G., Gouesbet, G., Xu, T. H., Brenn, G., and Tropea, C. (1994). Phase-doppler anemometry with dual burst technique for particle refractive index measurements. *Proceeding of the 7th International Symposium of Applications of Laser techniques to Fluid Mechanics*.
- Paciaroni, M. (2004). *Time-gated ballistic imaging through scattering media with application to liquid spray combustion*. PhD thesis, Colorado School of Mines.
- Paciaroni, M. and Linne, M. (2004). Single-shot, two-dimensional ballistic imaging through scattering media. *Applied Optics*, 43:5100–5109.
- Palero, R. and Ikeda, Y. (2002a). Droplet-size-classified stereoscopic piv for spray characterization. *Measurement Science and Technology*, 13:1050–1057.
- Palero, V. and Ikeda, Y. (2002b). 3d structures of evaporating fuel droplets by means stereoscopic piv. *Proceeding of the 11th International Symposium of Applications of Laser techniques to Fluid Mechanics*.
- Parker, T., Rainaldi, L., , and Rawlins, W. (1998). A comparative study of room-temperature and combusting fuel sprays near the injector tip using infrared laser diagnostics. *Atomization and Sprays*, 8:565–600.
- Pickering, C. and Halliwell, N. (1984). Laser speckle photography and particle image velocimetry: photographic film noise. *Applied Optics*, 23:2961–2969.
- Pilch, M. and Erdman, C. (1987). Use of breakup time data and velocity history data to predict the maximum size of stable fragments for acceleration-induced breakup of liquid drop. *International Journal of Multiphase Flow*, 13:741–757.
- Piskozub, J., Stramski, D., Terill, E., and Melville, W. (2004). Influence of forward and multiple light scatter on the measurement of beam attenuation in highly scattering marine environments. *Applied Optics*, 43:4723–4731.

- Pomraning, G. (1973). *The Equation of Radiation Hydrodynamics*. Oxford: Pergamon Press.
- Powell, C., Ciatti, S., Cheong, S.-K., Liu, J., and Wang, J. (2004). X-ray characterization of diesel sprays and effects of nozzle geometry. *Proceeding of the Diesel Engine Emission Reduction Conference*.
- Powell, C., Yue, Y., Poola, R., and Wang, J. (2000). Time-resolved measurements of supersonic fuel sprays using synchrotron x-rays. *Journal of Synchrotron Radiation*, 7:356–360.
- Prahl, S. (1988). *Light Transport in Tissue*. PhD thesis, University of Texas at Austin.
- Prasad, A. (2000). Particle image velocimetry. *Current Science*, 79:51–60,.
- Press, W., Teukolsky, S., Vetterling, W., and Flannery, B. (2002). *Numerical Recipes in C++*. Cambridge University Press.
- Ragucci, R., Cavaliere, A., and Massoli, P. (1990). Dropsizing by laser light scattering exploiting angular oscillation in the mie regime. *Particle and Particle Systems Characterizations*, 7:221–225.
- Ramella-Roman, J., Jacques, S., and Prahl, S. (2005a). Three monte carlo programs of polarized light transport into scattering media: part i. *Optics Express*, 13:10539–10551.
- Ramella-Roman, J., Jacques, S., and Prahl, S. (2005b). Three monte carlo programs of polarized light transport into scattering media: part ii. *Optics Express*, 13:10392–10405.
- Rayleigh, L. (1878). On the instability of jets. *Proc. London Math. Soc*, 10:4–13.
- Reitz, R. (1978). *Atomization and other breakup regimes of a liquid Jet*. PhD thesis, Princeton University.
- Réveillé, T. (2005). *A study of fuel injection and mixture formation for a gasoline direct injection engine*. PhD thesis, Cranfield University.
- Rizk, N. (1976). *Studies on liquid sheet disintegration in airblast atomizers*. PhD thesis, Cranfield University.
- Rizk, N. and Lefebvre, A. (1985). Drop-size distribution characteristics of spill-return atomisers. *AIAA J. Propul. Power*, 1:16–22.

- Roisman, I. and Tropea, C. (2000). Drops distribution and flux measurements in sprays using the phase doppler technique. *Proceeding of the 10th International Symposium of Applications of Laser techniques to Fluid Mechanics*.
- Rossmeißl, M. and Wirth, K.-E. (2004). Influence of the nozzle geometry on the atomization of superheated liquids. *Proceedings of the 19th ILASS-Europe (Institute for Liquid Atomization and Spray System)*.
- Royer, H. (1997). Holography and particle image velocimetry. *Measurement Science and Technology*, 8:1562–1572.
- Ruff, G., Sagar, A., and Faeth, G. (1989). Structure of the near-injector region of pressure atomized sprays. *J.Prop.Pow*, 7:221–230.
- Ruhnau, P., Guetter, C., Putze, T., and Schnrr, C. (2005). A variational approach for particle tracking velocimetry. *Measurement Science and Technology*, 16:1449–1458.
- Saffman, M. (1986). The use of polarized light for optical particle sizing. *Proceeding of the 3rd International Symposium on Application of laser for Flow Processes*.
- Schiller, L. (1922). Untersuchungen ueber laminare und turbulente stromung. *VDI Forschungsarbeit*, 248.
- Schweitzer, P. (1937). Mechanism of disintegration of liquid jets. *Journal of Applied Physics*, 8:513–521.
- Sedarsky, D., Paciaroni, M., Linne, M., Gord, J., and Meyer, T. (2005). Velocity imaging for the liquid-gas interface in the near field of an atomizing spray: proof of concept. *Optics Letters*, 31:906–908.
- Sedarsky, D., Paciaroni, M., Linne, M., Meyer, T., Kiel, B., and Gord, J. (2006). Ballistic imaging of the near field for jets in gaseous cross flow. *Proceeding of the 10th ICLASS (International Conference on Liquid Atomization and Spray System)*.
- Sedarsky, D. Paciaroni, M. Z. J. and Linne, M. (2007). Near field and dense wake structure analysis with ballistic imaging for jets in gaseous crossflow. *Proceedings of the 20th ILASS-America (Institute for Liquid Atomization and Spray System)*.
- Serpenguzel, A., Swindal, J., Chang, R., and Acker, W. (1992). Two-dimensional imaging of sprays with fluorescence, lasing and stimulated raman scattering. *Applied Optics*, 18:3543–3551.
- Serpenguzel, A. Küçükşenel, S. and Chang, R. (2002). Microdroplet identification and size measurement in sprays with lasing images. *Optics Express*, 10:1118–1132.

- Sick, V. and Stojkovic, B. (2001). Attenuation effects on imaging diagnostics of hollow-cone sprays. *Applied Optics*, 40:2435–2442.
- Sobol, I. (1974). *The Monte Carlo Method*. The University of Chicago Press.
- Suzzi, D., Berg, E., Pastor, J., Bianchi, G., and Tatschl, R. (2004). Simulation of primary breakup of diesel jets by a hybrid method combining vof-calculations and the classical ddm rate approach with 3d cfd code. *Proceedings of the 19th ILASS-Europe (Institute for Liquid Atomization and Spray System)*.
- Swithenbank, J., Beer, J., Taylor, D., Abbot, D., and McCreath, C. (1976). A laser diagnostic technique for the measurement of droplet and particle size distribution, experimental diagnostics in gas phase combustion systems. *Prog. In Astronaut and Aeronauts*, 53:421–447.
- Talley, D., Verdieck, J., Lee, S., McDonnell, V., and Samelsen, G. (1996). Accounting for laser sheet extinction in applying plif to sprays. *AIAA*, 96-0469.
- Tanner, F. (2004). Development and validation of a cascade atomization and drop breakup model for high-velocity dense sprays. *Atomization and sprays*, 14:20–32.
- Thurber, M. and R., H. (2001). Simultaneous imaging of temperature and mole fraction using acetone planar laser -induced fluorescence. *Experiments in Fluids*, 30:93–101.
- Tropea, C., Xu, T.-H., Onofri, F., Grehan, G., Haugen, P., and Stieglmeier, M. (1995). Dual mode phase doppler anemometer. *Proceeding of the 4th International Congress on Optical Particle Sizing*.
- Tseng, L.-K., Ruff, G., and Faeth, G. (1992). Effects of gas density on the structure of liquid jets in still gases. *AIAA*, 30:1537–1544.
- Tyler, F. (1933). Instability of liquid jets. *Phylosophical Magazine*, 16:504–518.
- Vahedi Tafreshi, H. and Pourdeyhimi, B. (2003). The effects of nozzle geometry on waterjet breakup at high reynolds number. *Experiments in Fluids*, 35:364–371.
- Van de Hulst, H. (1981). *Light Scattering by Small particles*. Dover.
- Van de Hulst, H. and Wang, R. (1991). Glare points. *Applied Optics*, 30:4755–4763.
- W., S. (1992). Interpreting mean drop diameters using distribution moments. *Atomization Sprays*, 2:1–15.

- Wang, J., Wang, Y., Im, K.-S., Fezzaa, K., and Lee, W. (2006). X-ray vision of air-assisted sprays: from radiography to quantitative phase-contrast imaging. *Proceeding of the 10th ICLASS (International Conference on Liquid Atomization and Spray System)*.
- Wang, X., Wang, L.-H., Sun, C.-W., and Yang (2003). Polarized light propagation through the scattering media: time-resolved monte carlo and experiments. *Journal of Biomedical Optics*, 8:608–617.
- Weiss, G. and Rubin, R. (1983). Random walks: Theory and selected applications. *Advances in Chemical Physics*, 52:363–505.
- Westerweel, J. (1997). Fundamentals of digital particle image velocimetry. *Measurement Science and Technology*, 8:1379–1392.
- Wigley, G. (1994). *Optical diagnostics for flow processes*. Plenum Press.
- Wigley, G., Goodwin, M., Pitcher, G., and Blondel, D. (2002). Imaging and pda analysis of a gdi spray in the near nozzle region. *Proceeding of the 11th International Symposium of Applications of Laser techniques to Fluid Mechanics*.
- Wigley, G., Hargrave, G., and Heath, J. (1999). A high power, high resolution lida/pda system applied to gasoline direct injection sprays. *Particle and Particle Systems Characterizations*, 16:11–19.
- Wilson, M. and R., W. (2001). A path-integral model of light scattered by turbid media. *Journal of Physics B*, 34:1453–1472.
- Xu, Q. and Nakajima, M. (2004). The generation of highly monodisperse droplets through the breakup of hydrodynamically focused microthread in a microfluidic device. *Applied Physics Letters*, 85:3726–3728.
- Xu, T.-H. and Tropea, C. (1994). Improving the performance of two-component phase dopper anemometers. *Measurements Science Technology*, 5:969–975.
- Yeh, C., Kosada, H., and Kamimoto, T. (1993). A fluorescence/scattering imaging technique for instantaneous 2-d measurement of particle size distribution in a transient spray. *Proceeding of the 3rd International Congress on Optical Particle Sizing*.
- Yeh, Y. and Cummins, H. (1964). Localized fluid flow measurement with he-ne laser spectrometer. *Applied Physics letters*, 4:176–178.

- Zama, Y., Kawahashi, M., , and Hirahara, H. (2005). Simultaneous measurement method of size and 3d velocity components of droplets in a spray field illuminated with a thin laser-light sheet. *Measurement Science and Technology*, 16:1977–1986.

Publications - Conferences - Recognitions

- **Recognitions:**

September 2006: Best paper presentation at the 10th International Conference on Liquid Atomization and Spray System (*Kyoto - Japan*).

March 2006: Selected for poster presentation by Britain's Top Younger Scientists, Engineers and Technologists at the House of Commons (*London - England*).

September 2005: Best presentation at the Young Researchers in Optics Meeting 2005 - Institute of Physics, Optical Group (*London - England*).

- **List of Journal Publications:**

Berrocal, E., Sedarsky, D., Paciaroni, M., Meglinski, I. and Linne, M. (2007) Laser light scattering in turbid media: Part I: Experimental and simulated results for the spatial intensity distribution. *Optics Express*, 15:10649-10665 .

Berrocal, E., Sedarsky, D., Paciaroni, M., Meglinski, I. and Linne, M. (2007) Laser light scattering in turbid media: Part II: Spatial and temporal analysis of individual scattering orders via Monte Carlo simulation. *Optics Express* (in progress).

Linne, M., Paciaroni, M., Sedarsky, D., **Berrocal, E.** and Meglinski I. (2007) Ballistic imaging of liquid breakup processes in dense sprays. *Proceedings of the Combustion Institute* (in progress).

Berrocal, E., Meglinski, I., Greenhalgh, D. and Linne, M. (2006) Image transfer through the complex turbid scattering media. *Laser Physics Letters*, 3:464-467.

Berrocal, E., Meglinski, I. and Jermy, M. (2005) New model for light propagation in highly inhomogeneous polydisperse turbid media with applications in spray diagnostics. *Optics Express*, 13:9181-9195.

Berrocal, E., Churmakov, D., Romanov, V., Jermy, M. and Meglinski, I. (2005) Crossed source/detector geometry for novel spray diagnostic: Monte Carlo and analytical results. *Applied Optics*, 44:2519-2529.

Meglinski, I., Romanov, V., Churmakov, D., **Berrocal, E.**, Jermy, M. and Greenhalgh, D. (2004) Low and high order light scattering in particulate media. *Laser Physics Letters*, 1:387-390.

Romanov V.P, Churmakov D.Y, **Berrocal, E.** and Meglinski I.V (2004) Low-order light scattering in multiple scattering disperse media. *Optics and Spectroscopy*, 97:796-802.

- **List of Proceeding Publications:**

Berrocal, E., Paciaroni, M., Sedarsky, D., Meglinski, I., Greenhagh, D. and Linne, M. (2006) Validation of a new computational model for multiple scattering of laser radiation in sprays. *Proceeding of the 10th ICLASS (International Conference on Liquid Atomization and Spray systems)*.

Berrocal, E., Romanov, V., Churmakov, D. and Meglinski, I. (2005) New Monte Carlo model of laser radiation propagation in sprays, aerosols and other complex polydisperse turbid media. *SPIE - Optical Technologies in Biophysics and Medicine VII* (Invited paper).

Berrocal, E., Jermy, M., Moukaideche, F. and Meglinski, I. (2005) Dense spray analysis using optical measurements and Monte Carlo simulation. *Proceeding of the 18th ICLASS – America (Intitute in Liquid Atomization and Spray systems)*.

Berrocal, E., Romanov, V., Churmakov, D. and Meglinski I. (2004) Low and high orders light scattering within dispersible media. *SPIE - Optical Technologies in Biophysics and Medicine VI* (Invited paper).

Jermy, M., **Berrocal, E.** and Moukaideche, F. (2004) Estimating the errors due to multiple scattering in spray imaging measurements: Experiments and simulation. *Proceeding of the 18th ICLASS – Europe (Intitute in Liquid Atomization and Spray systems)*.

Jermy, M., **Berrocal, E.** and Moukaideche, F. (2004) Errors in light sheet images of polydisperse sprays: Monte Carlo simulation of photon propagation, *Proceeding of the 12th International Symposium on Application of Laser Techniques to Fluid Mechanics*.

- **List of Oral Presentations:**

2006: Paper presentation at the 10th International Conference on Liquid Atomization and Spray Systems (*Kyoto - Japan*).

2006: Poster presentation at the Presentation by Britain's Top Younger Scientists, Engineers and Technologists at the House of Commons (*London - England*).

2005: Oral presentation at the Young Researchers in Optics Meeting - Institute of Physics (*Imperial College - London - England*).

2005: Paper presentation at the 18th ILASS-America conference (*Irvine - California - United States*).

2005: Poster presentation at Physics-2005, A century after Einstein - Institute of Physics (*University of Warwick - England*).

2004: Paper presentation at the 12th International Symposium on Application of Laser Techniques to Fluid Mechanics (*Lisbon - Portugal*).

2003: Oral presentation at the international conference in Laser Optics (*St Petersburg - Russia*).

Polystyrene Spheres Solutions - Complementary Data and Results

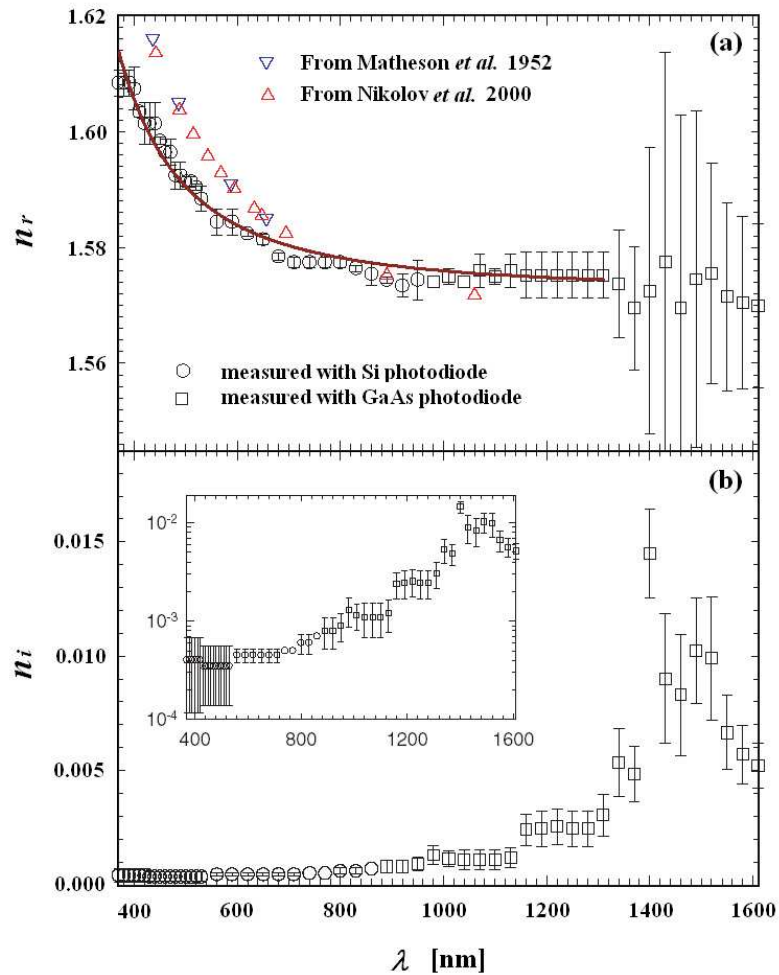


Figure B.1: Measured refractive indices of polystyrene microspheres as function of wavelength (Ma *et al.* 2003). (a) is the real part with the solid line as the fitting curve based on the Cauchy dispersion formula. (b) is the imaginary part with the inset illustrated on a log-scale.

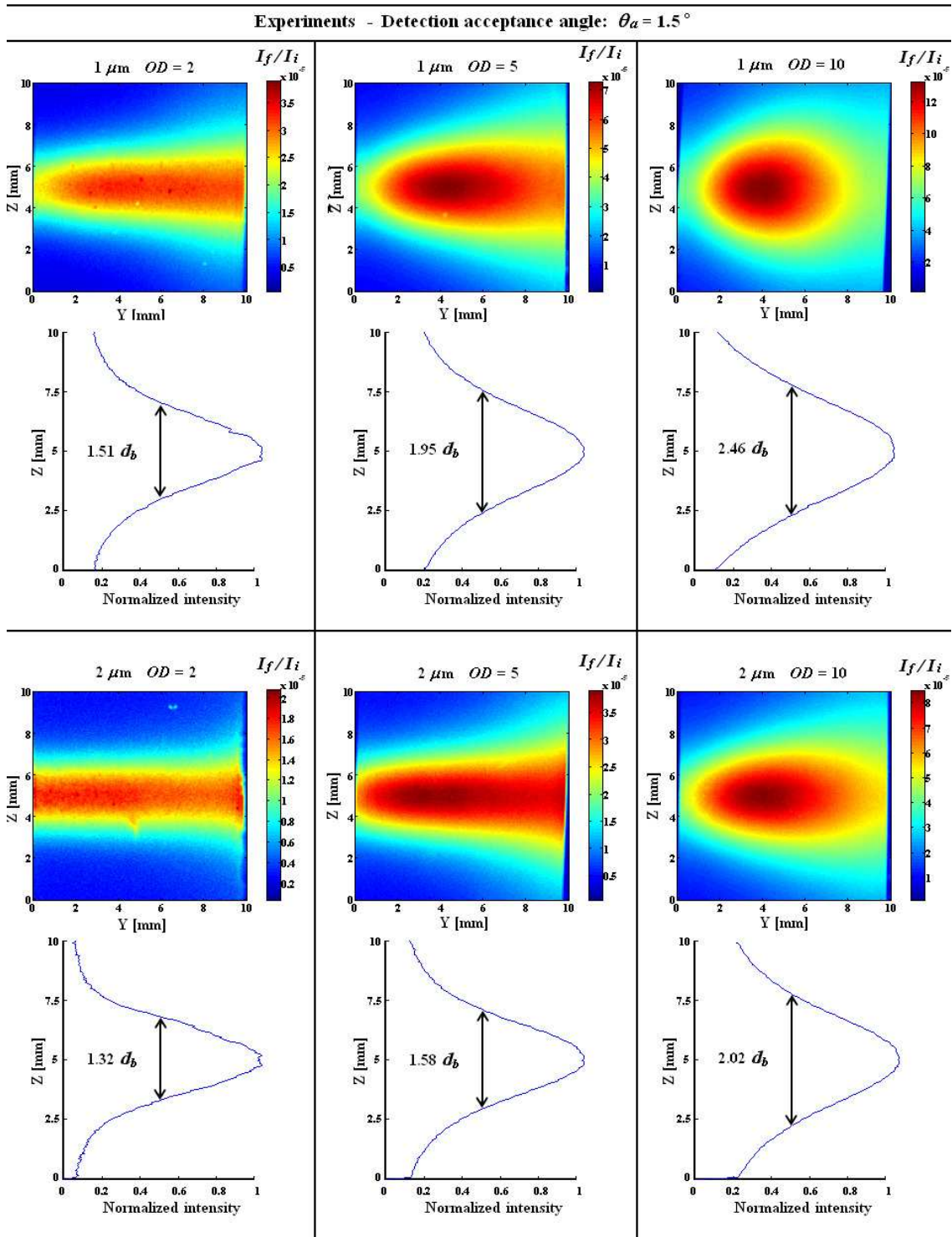


Figure B.2: Side face experimental images at detection acceptance angle $\theta_a = 1.5^\circ$. Two solutions of polystyrene spheres of $1 \mu\text{m}$ and $2 \mu\text{m}$ in diameter are considered at optical depths $OD = 2$, $OD = 5$ and $OD = 10$. The light intensity is normalized with the maximum intensity of the incident laser beam.

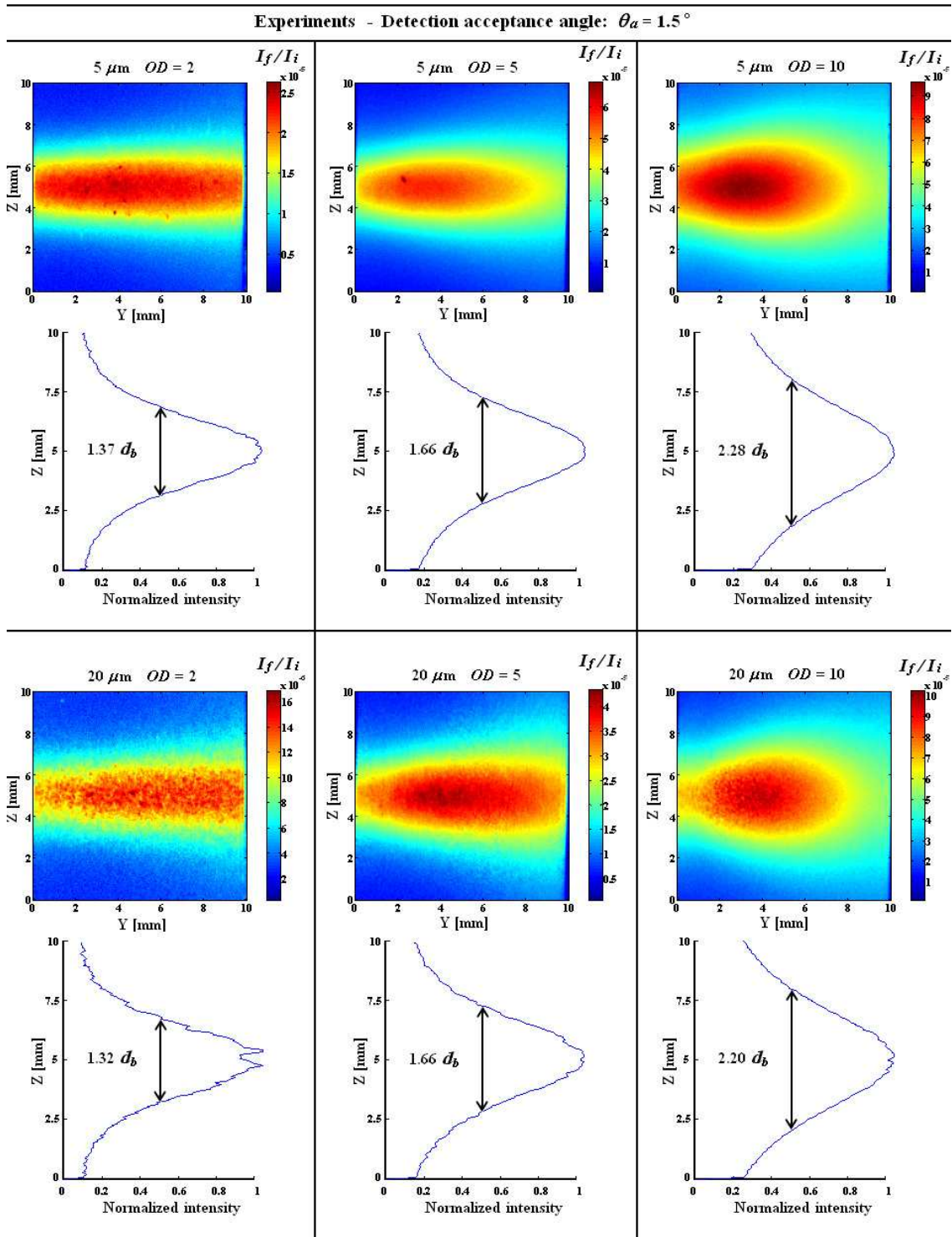


Figure B.3: Side face experimental images at detection acceptance angle $\theta_a = 1.5^\circ$. Two solutions of polystyrene spheres of 5 μm and 20 μm in diameter are considered at optical depths $OD = 2$, $OD = 5$ and $OD = 10$. The light intensity is normalized with the maximum intensity of the incident laser beam.

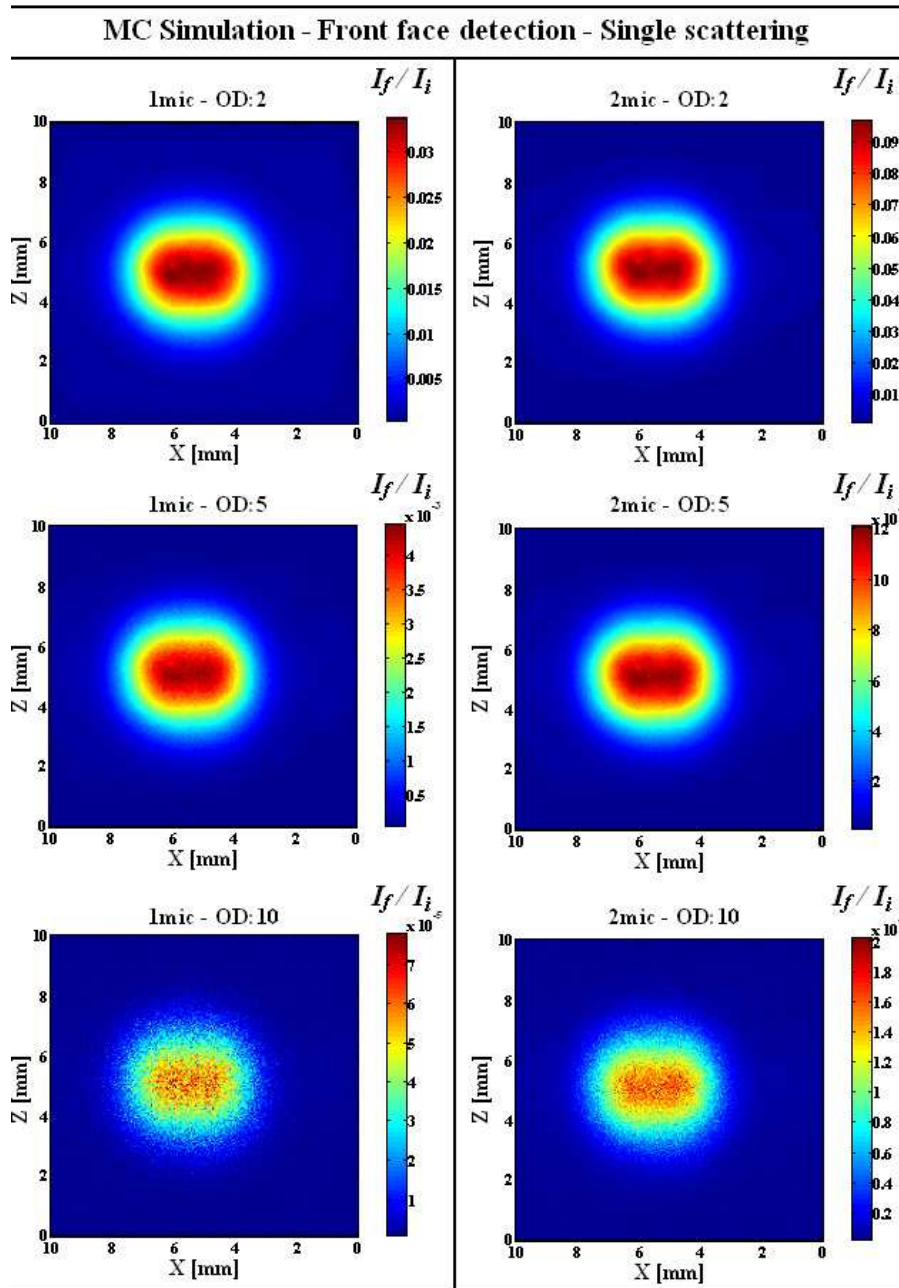


Figure B.4: Front face simulated images at detection acceptance angle $\theta_a = 8.5^\circ$ for the single scattering detection. Solutions of polystyrene spheres of $1 \mu\text{m}$ and $2 \mu\text{m}$ diameter are considered at various optical depths. 3 billions photons are sent. The intensity scale corresponds to the single light scattering intensity detected divided by the maximum value of the incident light intensity.

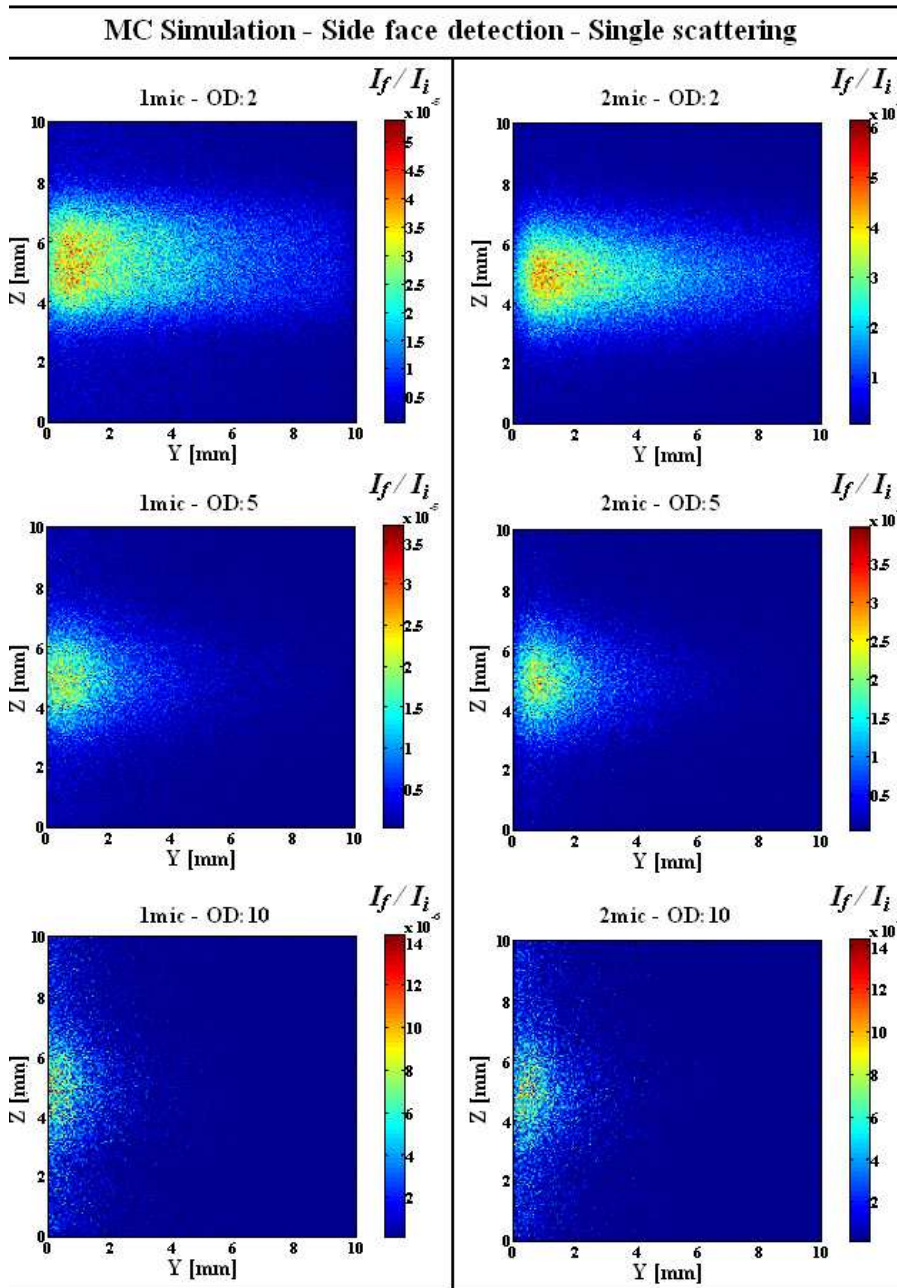


Figure B.5: Side face simulated images at detection acceptance angle $\theta_a = 8.6^\circ$ for the single scattering detection. Solutions of polystyrene spheres of $1 \mu\text{m}$ and $2 \mu\text{m}$ diameter are considered at various optical depths. 3 billions photons are sent. The intensity scale corresponds to the single light scattering intensity detected divided by the maximum value of the incident light intensity.

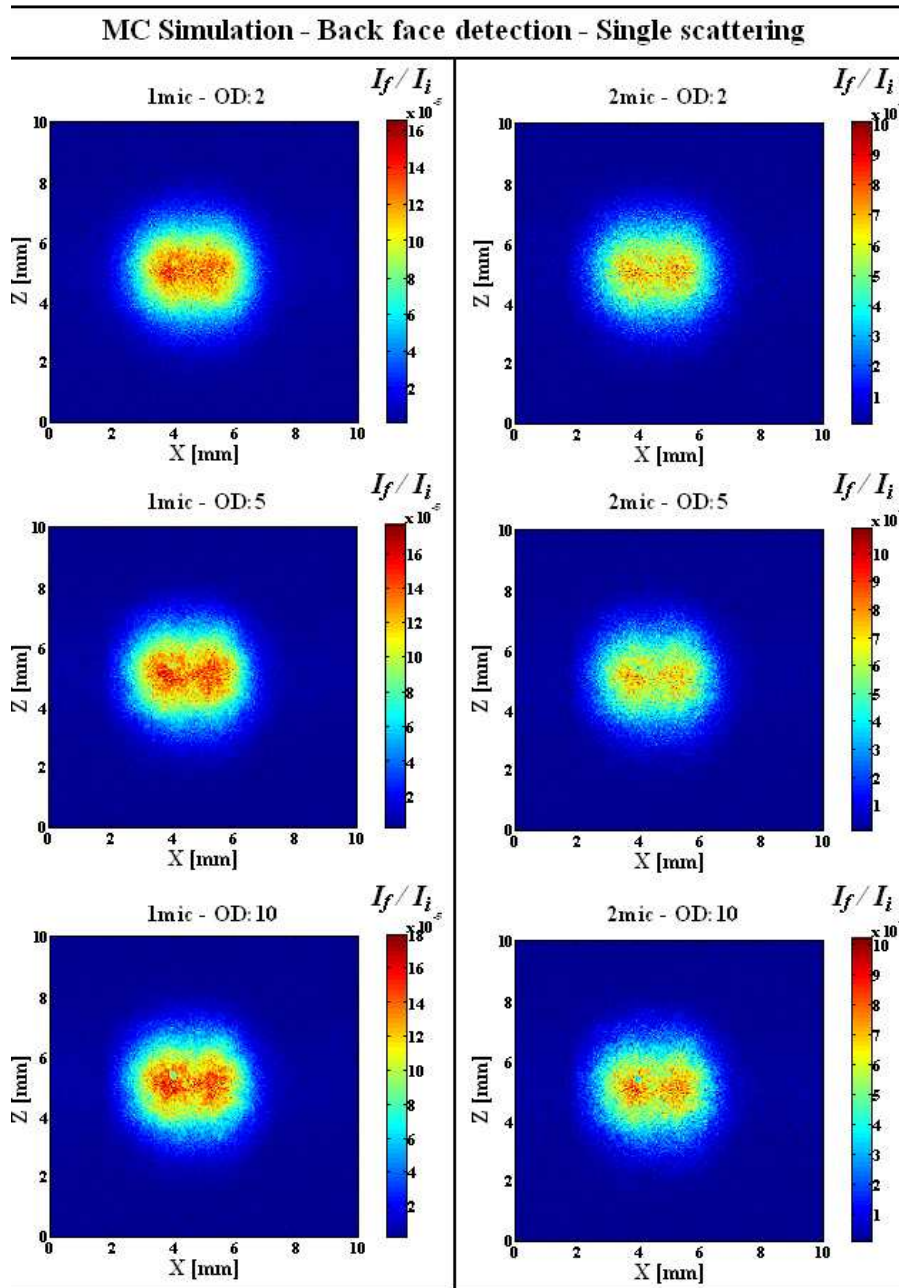


Figure B.6: Back face simulated images at detection acceptance angle $\theta_a = 8.6^\circ$ for the single scattering detection. Solutions of polystyrene spheres of 1 μm and 2 μm diameter are considered at various optical depths. 3 billions photons are sent. The intensity scale corresponds to the single light scattering intensity detected divided by the maximum value of the incident light intensity.

Hollow cone spray experiment - Complementary Data and Results

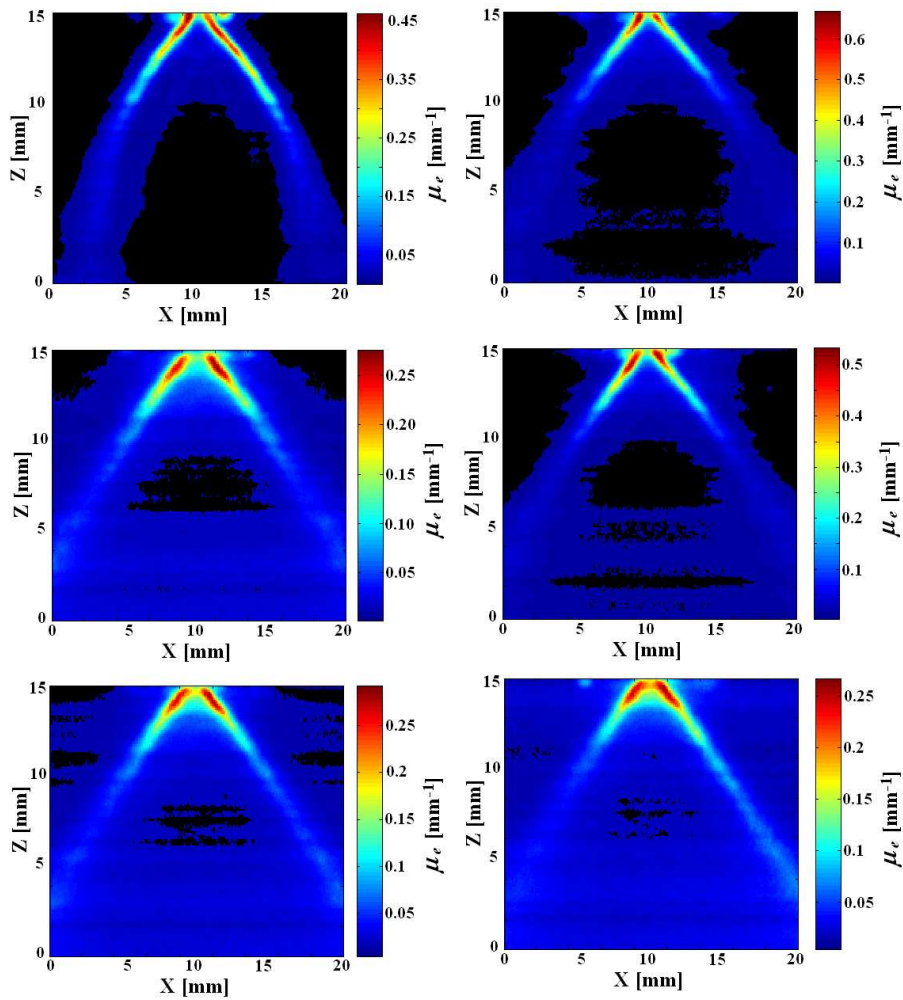


Figure C.1: 2D mapping of the extinction coefficient within the spray.

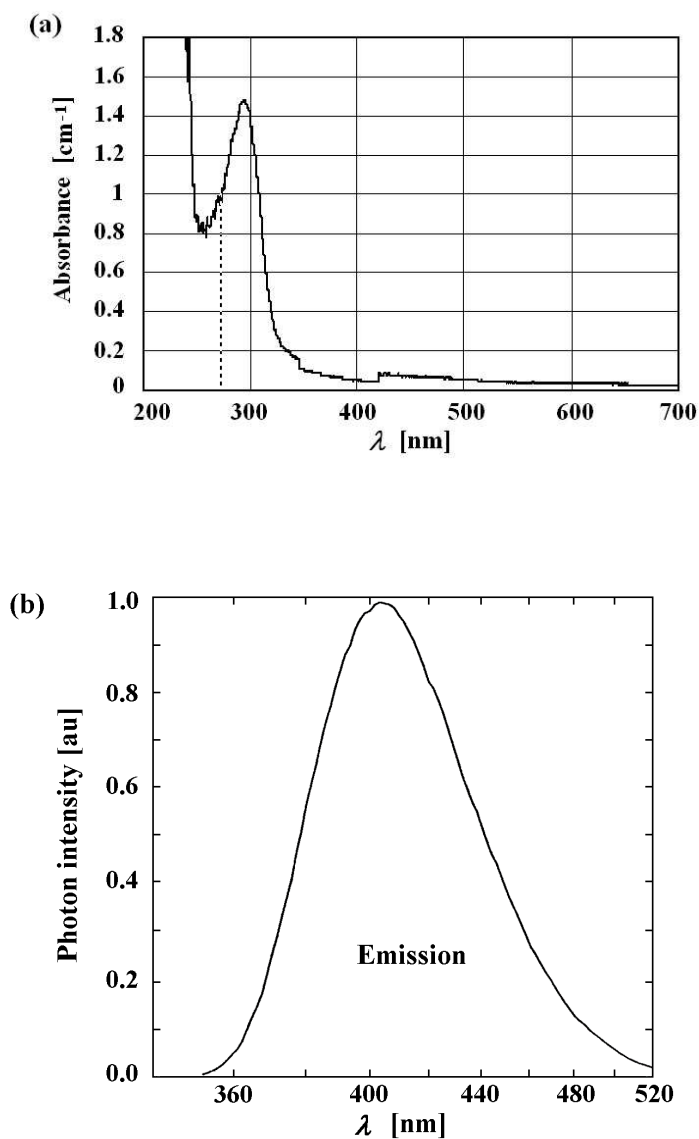


Figure C.2: (a) Absorbance spectrum of the solution of silicium salicylate at 0.058 g/l diluted in deionized water. (b) Example of emission spectrum for a solution of silicium salicylate solution at 0.29 g/l, when excited at 313 nm (Berlman 1971).

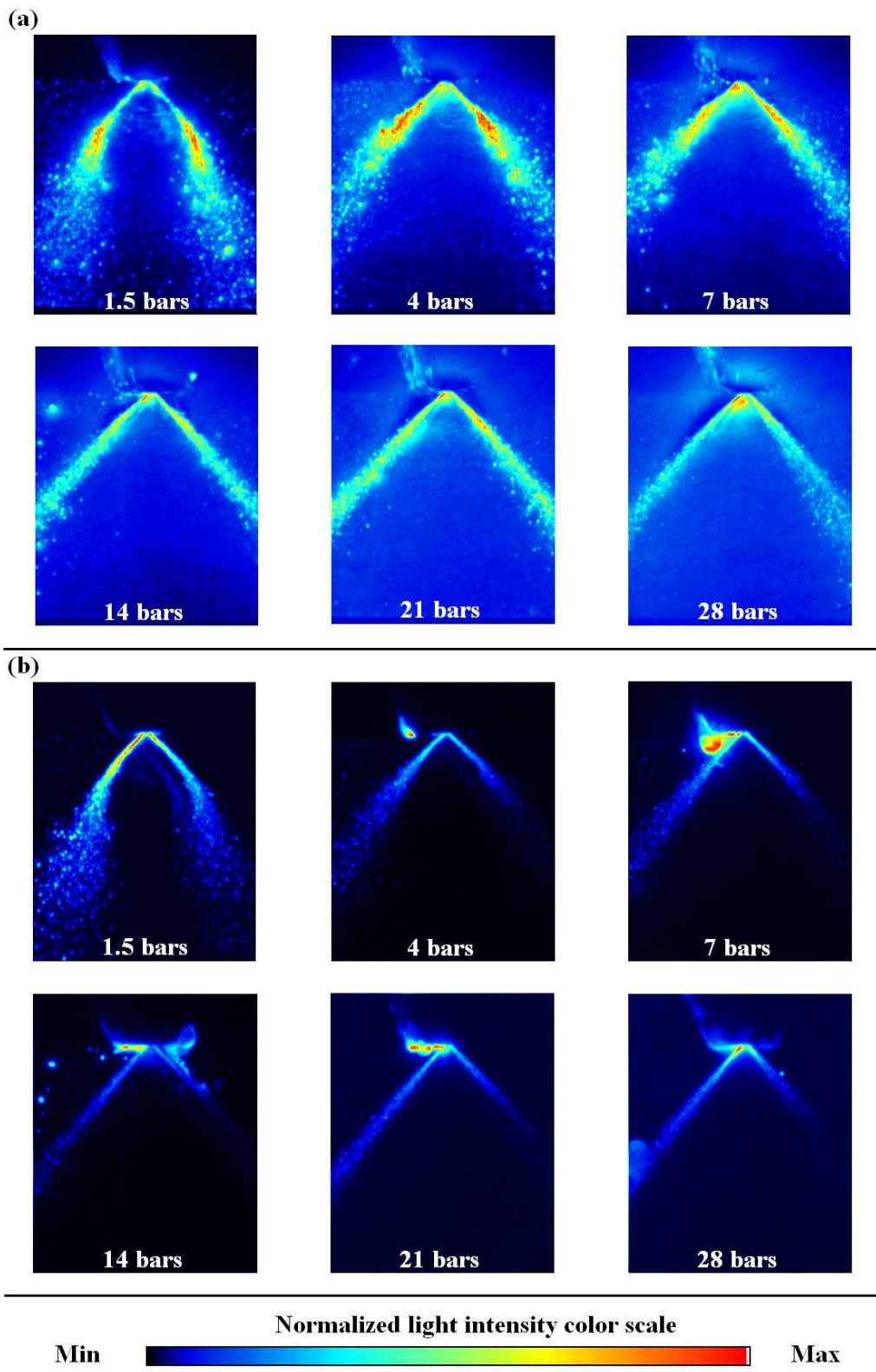


Figure C.3: Root Mean Square (RMS) for different conditions of pressure of injection. (a) is related to the 100 Mie images presented in Fig.7.4(b) and (b) corresponds to the 100 LIF images presented in Fig.7.5(b).

APPENDIX D

Monte Carlo code

```

/*****
*****/

Copyright: Edouard Berrocal, Cranfield University 2006
Cranfield School of Engineering,
Cranfield University MK43 0AL United Kingdom

Monte Carlo simulation of photon transport in
inhomogeneous polydisperse turbid media

Programming in ANSI standard C

*****/

Characteristics of the code:

Code calculation: 25 CPDF - Multi-cells

Input light: Laser beam in the middle of the Ymin face

Detection: General photon detection for all scattering orders
           Specific photon detection for a specific scattering order
           Mean path-length calculation
           Average scattering order calculation
           Scattering orders PDF within the complete scattering volume
           Scattering orders PDF of photons detected on a specific area

2D photon distribution profiles (2 dimensions arrays):
    6 arrays, 6 output files
    3 faces of the scattering volume: Ymin-Ymax-Xmax for MS and SS

Medium characteristics:
    Polydispersity - Homogeneous distribution
    Polydispersity - Heterogeneous distribution

*****/

#include <conio.h>
#include <io.h>
#include <stdlib.h>
#include <alloc.h>

#include <windows.h>
#include <stdio.h>
#include <math.h>
#define PI 3.14159265359
#define X_MaxNumber 147
#define Y_MaxNumber 101

```

```

long size[3]={0,0,0};
int far *si,*sj,*sk;
int far *source_strength;
float far *sourcetheta,*sourcephi;
float *CPDF;
float *CPDF1,*CPDF2,*CPDF3,*CPDF4,*CPDF5;
float *CPDF6,*CPDF7,*CPDF8,*CPDF9,*CPDF10;
float *CPDF11,*CPDF12,*CPDF13,*CPDF14,*CPDF15;
float *CPDF16,*CPDF17,*CPDF18,*CPDF19,*CPDF20;
float *CPDF21,*CPDF22,*CPDF23,*CPDF24,*CPDF25;
float *SCS_array;
float *number_density;
float *scat_cross_section;
float *diameter;

int Scat_CPDF_Size,Source_Size,Scat_Cross_Size;
int d1,d2,d3,d4,d5,d6,d7,d8,d9,d10;
int d11,d12,d13,d14,d15,d16,d17,d18;
int d19,d20,d21,d22,d23,d24,d25;
int sum_source_strength=0;
double phi_prim_reso=0.0;

long idum; //long idum=(-1);
char title[30];

void stop(char message[100]);
int photon_in_play(int i, int j, int k);
void input(void);
float ran2(long *idum);
void calculate(void);

/*****
// Structure of the code:

void main(int argc, char *argv[])
{
  if (argc > 2)
    stop("\nToo many command-line arguments");
  if (argc == 2) sscanf(argv[1],"%s",title);
  else sprintf(title,"default");
  input();
  calculate();
}

/*****

// Stop simulation:

void stop(char message[100])
{
  printf("%s",message);
  DestroyWindow(GetActiveWindow());
  exit(0);
}

/*****

// Verification of photons location:

int photon_in_play(int i, int j, int k)
{
  if ((i<=-1)|| (i>=size[0])) return (0);
  if ((j<=-1)|| (j>=size[1])) return (0);
  if ((k<=-1)|| (k>=size[2])) return (0);
  else return (1);
}

/*****

```

```

// Reading and recording input data:

void input(void)
{
    int count,source;
    float theta,phi;
    int i,j,k,m;
    float n,o,p,q;

    char infilename[34];
    char junk[1000];
    FILE *fin;

    sprintf(infilename,"%s.sin",title);
    printf("\nReading from input file %s\n",infilename);

    if ((fin = fopen(infilename,"r")) == 0)
        stop("\nError opening file\nExiting");

    fgets(junk,50,fin);
    printf("\n%s",junk);

    fgets(junk,50,fin);
    fscanf(fin,"%ld\t%ld\t%ld\n",&size[0],&size[1],&size[2]);

    fgets(junk,50,fin);
    fscanf(fin,"%d\n",&Scat_CPDF_Size);
    phi_prim_reso=(double)PI/(Scat_CPDF_Size-1);

    fgets(junk,1000,fin);
    fscanf(fin,"%d\t%d\t%d\t%d\t%d\t%d\t%d\t%d\t%d\t%d\t",&d1,&d2,&d3,&d4,&d5);
    fscanf(fin,"%d\t%d\t%d\t%d\t%d\t%d\t%d\t%d\t%d\t%d\t",&d6,&d7,&d8,&d9,&d10);
    fscanf(fin,"%d\t%d\t%d\t%d\t%d\t%d\t%d\t%d\t",&d11,&d12,&d13,&d14,&d15);
    fscanf(fin,"%d\t%d\t%d\t%d\t%d\t%d\t",&d16,&d17,&d18,&d19,&d20);
    fscanf(fin,"%d\t%d\t%d\t%d\t%d\t",&d21,&d22,&d23,&d24,&d25);

    if ((CPDF1 = (float *)farmalloc((int)Scat_CPDF_Size*sizeof(double)))==NULL)
        stop("Not enough memory to allocate CPDF1\n");
    if ((CPDF2 = (float *)farmalloc((int)Scat_CPDF_Size*sizeof(double)))==NULL)
        stop("Not enough memory to allocate CPDF2\n");
    if ((CPDF3 = (float *)farmalloc((int)Scat_CPDF_Size*sizeof(double)))==NULL)
        stop("Not enough memory to allocate CPDF3\n");
    if ((CPDF4 = (float *)farmalloc((int)Scat_CPDF_Size*sizeof(double)))==NULL)
        stop("Not enough memory to allocate CPDF4\n");
    if ((CPDF5 = (float *)farmalloc((int)Scat_CPDF_Size*sizeof(double)))==NULL)
        stop("Not enough memory to allocate CPDF5\n");
    if ((CPDF6 = (float *)farmalloc((int)Scat_CPDF_Size*sizeof(double)))==NULL)
        stop("Not enough memory to allocate CPDF6\n");
    if ((CPDF7 = (float *)farmalloc((int)Scat_CPDF_Size*sizeof(double)))==NULL)
        stop("Not enough memory to allocate CPDF7\n");
    if ((CPDF8 = (float *)farmalloc((int)Scat_CPDF_Size*sizeof(double)))==NULL)
        stop("Not enough memory to allocate CPDF8\n");
    if ((CPDF9 = (float *)farmalloc((int)Scat_CPDF_Size*sizeof(double)))==NULL)
        stop("Not enough memory to allocate CPDF9\n");
    if ((CPDF10 = (float *)farmalloc((int)Scat_CPDF_Size*sizeof(double)))==NULL)
        stop("Not enough memory to allocate CPDF10\n");
    if ((CPDF11 = (float *)farmalloc((int)Scat_CPDF_Size*sizeof(double)))==NULL)
        stop("Not enough memory to allocate CPDF11\n");
    if ((CPDF12 = (float *)farmalloc((int)Scat_CPDF_Size*sizeof(double)))==NULL)
        stop("Not enough memory to allocate CPDF12\n");
    if ((CPDF13 = (float *)farmalloc((int)Scat_CPDF_Size*sizeof(double)))==NULL)
        stop("Not enough memory to allocate CPDF13\n");
    if ((CPDF14 = (float *)farmalloc((int)Scat_CPDF_Size*sizeof(double)))==NULL)
        stop("Not enough memory to allocate CPDF14\n");
    if ((CPDF15 = (float *)farmalloc((int)Scat_CPDF_Size*sizeof(double)))==NULL)
        stop("Not enough memory to allocate CPDF15\n");
    if ((CPDF16 = (float *)farmalloc((int)Scat_CPDF_Size*sizeof(double)))==NULL)
        stop("Not enough memory to allocate CPDF16\n");
    if ((CPDF17 = (float *)farmalloc((int)Scat_CPDF_Size*sizeof(double)))==NULL)
        stop("Not enough memory to allocate CPDF17\n");
    if ((CPDF18 = (float *)farmalloc((int)Scat_CPDF_Size*sizeof(double)))==NULL)
        stop("Not enough memory to allocate CPDF18\n");

```

```

if ((CPDF19 = (float *)farmalloc((int)Scat_CPDF_Size*sizeof(double)))==NULL)
stop("Not enough memory to allocate CPDF19\n");
if ((CPDF20 = (float *)farmalloc((int)Scat_CPDF_Size*sizeof(double)))==NULL)
stop("Not enough memory to allocate CPDF20\n");
if ((CPDF21 = (float *)farmalloc((int)Scat_CPDF_Size*sizeof(double)))==NULL)
stop("Not enough memory to allocate CPDF21\n");
if ((CPDF22 = (float *)farmalloc((int)Scat_CPDF_Size*sizeof(double)))==NULL)
stop("Not enough memory to allocate CPDF22\n");
if ((CPDF23 = (float *)farmalloc((int)Scat_CPDF_Size*sizeof(double)))==NULL)
stop("Not enough memory to allocate CPDF23\n");
if ((CPDF24 = (float *)farmalloc((int)Scat_CPDF_Size*sizeof(double)))==NULL)
stop("Not enough memory to allocate CPDF24\n");
if ((CPDF25 = (float *)farmalloc((int)Scat_CPDF_Size*sizeof(double)))==NULL)
stop("Not enough memory to allocate CPDF25\n");

for (count=0;count<Scat_CPDF_Size;count++)
{
fscanf(fin,"%f\t",&n); *(CPDF1+count)=n;
fscanf(fin,"%f\t",&n); *(CPDF2+count)=n;
fscanf(fin,"%f\t",&n); *(CPDF3+count)=n;
fscanf(fin,"%f\t",&n); *(CPDF4+count)=n;
fscanf(fin,"%f\t",&n); *(CPDF5+count)=n;
fscanf(fin,"%f\t",&n); *(CPDF6+count)=n;
fscanf(fin,"%f\t",&n); *(CPDF7+count)=n;
fscanf(fin,"%f\t",&n); *(CPDF8+count)=n;
fscanf(fin,"%f\t",&n); *(CPDF9+count)=n;
fscanf(fin,"%f\t",&n); *(CPDF10+count)=n;
fscanf(fin,"%f\t",&n); *(CPDF11+count)=n;
fscanf(fin,"%f\t",&n); *(CPDF12+count)=n;
fscanf(fin,"%f\t",&n); *(CPDF13+count)=n;
fscanf(fin,"%f\t",&n); *(CPDF14+count)=n;
fscanf(fin,"%f\t",&n); *(CPDF15+count)=n;
fscanf(fin,"%f\t",&n); *(CPDF16+count)=n;
fscanf(fin,"%f\t",&n); *(CPDF17+count)=n;
fscanf(fin,"%f\t",&n); *(CPDF18+count)=n;
fscanf(fin,"%f\t",&n); *(CPDF19+count)=n;
fscanf(fin,"%f\t",&n); *(CPDF20+count)=n;
fscanf(fin,"%f\t",&n); *(CPDF21+count)=n;
fscanf(fin,"%f\t",&n); *(CPDF22+count)=n;
fscanf(fin,"%f\t",&n); *(CPDF23+count)=n;
fscanf(fin,"%f\t",&n); *(CPDF24+count)=n;
fscanf(fin,"%f\n",&n); *(CPDF25+count)=n;
}

fgets(junk,50,fin);
fscanf(fin,"%ld\n",&Source_Size);

if ((si=(int *) farmalloc((int)Source_Size*sizeof(int)))==NULL)
stop("Not enough memory to allocate source i array\n");
if ((sj=(int *) farmalloc((int)Source_Size*sizeof(int)))==NULL)
stop("Not enough memory to allocate source j array\n");
if ((sk=(int *) farmalloc((int)Source_Size*sizeof(int)))==NULL)
stop("Not enough memory to allocate source k array\n");
if ((source_strength=(int *) farmalloc((int)Source_Size*sizeof(int)))==NULL)
stop("Not enough memory to allocate source strength array\n");
if ((sourcetheta=(float *) farmalloc((int)Source_Size*sizeof(float)))==NULL)
stop("Not enough memory to allocate source theta array\n");
if ((sourcephi=(float *) farmalloc((int)Source_Size*sizeof(float)))==NULL)
stop("Not enough memory to allocate source phi array\n");

for (source=0;source<Source_Size;source++)
{
fscanf(fin,"%ld\t%ld\t%ld\t%ld\t%f\t%f\n",&i,&j,&k,&m,&theta,&phi);
*(si+source)=i;
*(sj+source)=j;
*(sk+source)=k;
*(source_strength+source)=m;
*(sourcetheta+source)=theta*PI/180;
*(sourcephi+source)=phi*PI/180;
sum_source_strength=sum_source_strength+m;
}

```

```

fgets(junk,500,fin);
if ((number_density=(float *) farmalloc((unsigned long)
size[0]*size[1]*size[2]*sizeof(float)))==NULL)
stop("Not enough memory to allocate number density array\n");
if ((scat_cross_section=(float *) farmalloc((unsigned long)
size[0]*size[1]*size[2]*sizeof(float)))==NULL)
stop("Not enough memory to allocate scat cross section array\n");
if ((diameter=(float *) farmalloc((unsigned long)
size[0]*size[1]*size[2]*sizeof(float)))==NULL)
stop("Not enough memory to allocate Diameter array\n");

for (count=0;count<(size[0]*(size[1]*(size[2]));count++)
{
fscanf(fin,"%d\t%d\t%d\t%f\t%f\t%f\n",&i,&j,&k,&n,&o,&p);

*(number_density+size[1]*size[2]*i+size[2]*j+k)=n;
*(scat_cross_section+size[1]*size[2]*i+size[2]*j+k)=o;
*(diameter+size[1]*size[2]*i+size[2]*j+k)=p;
}

printf("\nReading is finished\n");
}

/*****/

//Calculation of photon transport:

void calculate (void)
{
//Cells size in mm
float Coeff=1.0;

int source,count;
unsigned long photon;
unsigned long Total_photon_number;
unsigned long photon_factor=0;
unsigned long Photon_number=0;
unsigned long nb_photon=0;

float aperture;
float source_delta_x,source_delta_z;

//Cells and photons characteristics:
int i=0,j=0,k=0;
float di=0.0,dj=0.0,dk=0.0;
float xin=0.0,yin=0.0,zin=0.0;
float xout=0.0,yout=0.0,zout=0.0;
float deltaX=0.0,deltaY=0.0,deltaZ=0.0;

//Photon journey variables:
float l_before_scat=0.0;
float TPL=0.0,Path_Length=0.0;
float Total_path_lenght=0.0;
int Scatter_Counter=0;

//Source characterisation:
float x_source=0.0,y_source=0.0,z_source=0.0;
float Source_radius=0.0,Source_radius_X=0,Source_radius_Y=0;
float t_Rs2=0.0, t_Rss2=0.0;
float Source_pt_x=0.0,Source_pt_y=0.0;

//Scattering Angles variables:
float phi=0.0,theta=0.0;
float phi_prim=0.0,theta_prim=0.0;
float Rn_phi_prim=0.0,Rn_theta_prim=0.0;
float phi_prim_max=0.0,phi_prim_min=0.0;
float coeff1=0.0,coeff2=0.0;
float Delta_coeff=0.0,di_prim=0.0;
float du=0.0,dv=0.0,dw=0.0;
float delta_k=0.0,ijk_vector=0.0;

//Main input data:
float Number_density=0.0,Number_density_0=0.0;
float nd_coeff=0.0;
float Scat_cross_section=0.0;
float Mean_diam=0.0;

```

```

float drop_diam_min=2.0,drop_diam_max=200.0;
float drop_diameter=0.0;

float Percentage=0.0,Percc=0.0;

char photonfilename[34],outfilename[34];
FILE *fph,*fout;

char XmaxSSfilename[34],YmaxSSfilename[34],YminSSfilename[34];
FILE *XmaxSS,*YmaxSS,*YminSS;

char XmaxMSfilename[34],YmaxMSfilename[34],YminMSfilename[34];
FILE *XmaxMS,*YmaxMS,*YminMS;

//General detection for single and multiple scattering:

int Xout_max=0,Yout_max=0,Zout_max=0;
int Xout_min=0,Yout_min=0,Zout_min=0;
int Xout_max_1=0,Yout_max_1=0,Zout_max_1=0;
int Xout_min_1=0,Yout_min_1=0,Zout_min_1=0;
float P_Xmax=0.0,P_Ymax=0.0,P_Zmax=0.0;
float P_Xmin=0.0,P_Ymin=0.0,P_Zmin=0.0;
float Sum=0.0;

double Av_scat=0.0;
double Av_lenght=0.0;
unsigned long Nb_single=0;
double Av_lenght_single=0.0;

int Scat0=0,Scat1=0,Scat2=0,Scat3=0,Scat4=0,Scat5=0,Scat6=0;
int Scat7=0,Scat8=0,Scat9=0,Scat10=0,Scat11=0,Scat12=0,Scat13=0;
int Scat14=0,Scat15=0,Scat16=0,Scat17=0,Scat18=0,Scat_sup=0;

//Specific forward scattering detection:

float cos_ap=0.0,cos_theta=0.0;
float sin_phi=0.0,sin_theta=0.0;

float Detec_radius=0.0,radius=0.0;
float x_det_pt=0.0,y_det_pt=0.0;

float Delta_x=Coeff*size[0]/(X_MaxNumber-1);
float Delta_y=Coeff*size[1]/(X_MaxNumber-1);
double Av_scat_d=0.0;
double Av_lenght_fwd=0.0;
double Ratio_If_Ii=0.0;
unsigned long nb_photon_fwd=0;

int Scat0_d=0,Scat1_d=0,Scat2_d=0,Scat3_d=0,Scat4_d=0,Scat5_d=0,Scat6_d=0;
int Scat7_d=0,Scat8_d=0,Scat9_d=0,Scat10_d=0,Scat11_d=0,Scat12_d=0,Scat13_d=0;
int Scat14_d=0,Scat15_d=0,Scat16_d=0,Scat17_d=0,Scat18_d=0,Scat_sup_d=0;

float P0=0.0,P1=0.0,P2=0.0,P3=0.0,P4=0.0,P5=0.0,P6=0.0;
float P7=0.0,P8=0.0,P9=0.0,P10=0.0,P11=0.0,P12=0.0,P13=0.0;
float P14=0.0,P15=0.0,P16=0.0,P17=0.0,P18=0.0,Psup=0.0,Psum=0.0;

unsigned int Array_2D_SS_Xmax[X_MaxNumber][Y_MaxNumber];
unsigned int Array_2D_SS_Ymax[X_MaxNumber][Y_MaxNumber];
unsigned int Array_2D_SS_Ymin[X_MaxNumber][Y_MaxNumber];

unsigned int Array_2D_MS_Xmax[X_MaxNumber][Y_MaxNumber];
unsigned int Array_2D_MS_Ymax[X_MaxNumber][Y_MaxNumber];
unsigned int Array_2D_MS_Ymin[X_MaxNumber][Y_MaxNumber];

int ind=0;
int ind_x=0;
int ind_y=0;

```



```

for (ind_x=0;ind_x<X_MaxNumber;ind_x++)
{
for (ind_y=0;ind_y<Y_MaxNumber;ind_y++)
{
Array_2D_SS_Xmax[ind_x][ind_y]=0;
Array_2D_SS_Ymax[ind_x][ind_y]=0; Array_2D_SS_Ymin[ind_x][ind_y]=0;
Array_2D_MS_Xmax[ind_x][ind_y]=0;
Array_2D_MS_Ymax[ind_x][ind_y]=0; Array_2D_MS_Ymin[ind_x][ind_y]=0;
}
}

// Start with an initial Random Number

idum=-(long)time(NULL);

// Create Output files:

sprintf(photonfilename,"%s.sph",title);
if ((fph = fopen(photonfilename,"w")) == 0)
stop("\nError opening photon output file\nExiting");

sprintf(outfilename,"%s.sph",title);
if ((fout = fopen(photonfilename,"w")) == 0)
stop("\nError opening photon output file\nExiting");

sprintf(XmaxSSfilename,"%s.XmaxSS",title);
if ((XmaxSS = fopen(XmaxSSfilename,"w")) == 0) stop("\nError opening XmaxMS\nExiting");
sprintf(YmaxSSfilename,"%s.YmaxSS",title);
if ((YmaxSS = fopen(YmaxSSfilename,"w")) == 0) stop("\nError opening YmaxMS\nExiting");
sprintf(YminSSfilename,"%s.YminSS",title);
if ((YminSS = fopen(YminSSfilename,"w")) == 0) stop("\nError opening YminMS\nExiting");

sprintf(XmaxMSfilename,"%s.XmaxMS",title);
if ((XmaxMS = fopen(XmaxMSfilename,"w")) == 0) stop("\nError opening XmaxMS\nExiting");
sprintf(YmaxMSfilename,"%s.YmaxMS",title);
if ((YmaxMS = fopen(YmaxMSfilename,"w")) == 0) stop("\nError opening YmaxMS\nExiting");
sprintf(YminMSfilename,"%s.YminMS",title);
if ((YminMS = fopen(YminMSfilename,"w")) == 0) stop("\nError opening YminMS\nExiting");

// Initial data asked:

puts("\nTotal Number of photons:");
scanf("%ld",&Total_photon_number);
puts("\nDetection Aperture (in degrees):");
scanf("%f",&aperture);
puts("\nDelta X of the source (in mm):");
scanf("%f",&source_delta_x);
puts("\nDelta Z of the source (in mm):");
scanf("%f",&source_delta_z);

/*
Total_photon_number=100000000;
source_delta_x=0.0;
source_delta_z=0.0;
*/

aperture=aperture*PI/180;
cos_ap=cos(aperture);

source_delta_x=source_delta_x/Coeff; // program units
source_delta_z=source_delta_z/Coeff; // To move the source

//Diameter of the right detection area:

Detec_radius=10.0; // in mm
Detec_radius=Detec_radius/Coeff; // in program unit
Detec_radius=Detec_radius*Detec_radius; // radius in square

```

```

//Indication concerning the unfolding of the program:

photon_factor=Total_photon_number/(unsigned long)sum_source_strength;

printf("\nProgram unfolding:\n0%\t\t 100%\n ");

// Beginning of the "Source" loop:

for (source=0;source<Source_Size;source++)
{

    Photon_number=(source_strength+source)*photon_factor;

// Beginning of the "Photon" loop:

for (photon=0;photon<Photon_number;photon++)
{

    Percentage=floor((float) (photon*10)/Photon_number);
    Perc=(float) (photon*10)/Photon_number;
    if (fabs(Percentage-Perc)<1e-12) (printf("--"));

    Scatter_Counter=0;
    Total_path_lenght=0.0;
    Number_density_0=0.0;

// Source characteristics:

    Source_pt_x=(si+source); //Middle of the source
    Source_pt_y=(sk+source); // Program units

    x_det_pt=Source_pt_x; // Middle of the right
    y_det_pt=Source_pt_y; // detection area

    Source_pt_x=Source_pt_x+source_delta_x; //To move the source
    Source_pt_y=Source_pt_y+source_delta_z;

    Source_radius=1.0; // mm
    Source_radius=Source_radius/Coeff; // program units

    Source_radius_X=0.5; // mm
    Source_radius_X=Source_radius_X/Coeff; // program units

    Source_radius_Y=7.25; // mm
    Source_radius_Y=Source_radius_Y/Coeff; // program units

    t_Rss2=Source_radius*Source_radius;

/*
// To move the source:

do
{
    x_source=Source_pt_x + Source_radius*(2.0*ran2(&idum)-1.0);
    y_source=(sj+source)+1e-10;
    z_source=Source_pt_y + Source_radius*(2.0*ran2(&idum)-1.0);
    t_Rs2=(x_source-Source_pt_x)*(x_source-Source_pt_x)+(z_source-Source_pt_y)
    *(z_source-Source_pt_y);
}
while ((t_Rs2>t_Rss2)|| (x_source>size[1]) || (z_source>size[2])
|| (x_source<0.0) || (z_source<0.0));
*/

x_source=Source_pt_x + Source_radius_X*(2.0*ran2 (&idum)-1.0);
y_source=(sj+source)+1e-10;
z_source=Source_pt_y +Source_radius_Y*(2.0*ran2 (&idum)-1.0);

```

```

i=floor(x_source);
j=floor(y_source);
k=floor(z_source);

xout=x_source;
yout=y_source;
zout=z_source;

theta=(sourcetheta+source);
phi=(sourcephi+source);

if (fabs(phi-0.0)<1e-6)      (phi=1e-6);
if (fabs(phi-PI/2)<1e-6)    (phi=PI/2-1e-6);
if (fabs(phi-PI)<1e-6)     (phi=PI-1e-6);

if (fabs(theta-0.0)<1e-6)   (theta=1e-6);
if (fabs(theta-PI/2)<1e-6)  (theta=PI/2-1e-6);
if (fabs(theta-PI)<1e-6)   (theta=PI-1e-6);
if (fabs(theta-3*PI/2)<1e-6) (theta=3*PI/2-1e-6);
if (fabs(theta-2*PI)<1e-6)  (theta=2*PI-1e-6);

Number_density=(number_density+size[1]*size[2]*i+size[2]*j+k);
Scat_cross_section=(scat_cross_section+size[1]*size[2]*i+size[2]*j+k);

if ((fabs(Number_density-0.0)>1e-6) && (fabs(Scat_cross_section-0.0)>1e-6))
  l_before_scat=(-log(ran2(&idum))/(Number_density*Scat_cross_section))/Coeff;

photon_loop:

xin=xout;
yin=yout;
zin=zout;

//Determination of the initial path lenght and of the cell exit point:

if ( ((theta>0.0) &&(theta<PI/2)) &&( (phi>0.0) &&(phi<PI/2)) ) //1
{
  deltaX=(float) i+1.0-xin;
  deltaY=(float) j+1.0-yin;
  deltaZ=(float) k+1.0-zin;
}
if ( ((theta>PI/2) &&(theta<PI)) &&( (phi>0.0) &&(phi<PI/2)) ) //2
{
  deltaX=(float) i-xin;
  deltaY=(float) j+1.0-yin;
  deltaZ=(float) k+1.0-zin;
}
if ( ((theta>0.0) &&(theta<PI/2)) &&( (phi>PI/2) &&(phi<PI)) ) //3
{
  deltaX=(float) i+1.0-xin;
  deltaY=(float) j+1.0-yin;
  deltaZ=(float) k-zin;
}
if ( ((theta>PI/2) &&(theta<PI)) &&( (phi>PI/2) &&(phi<PI)) ) //4
{
  deltaX=(float) i-xin;
  deltaY=(float) j+1.0-yin;
  deltaZ=(float) k-zin;
}
if ( ((theta>3*PI/2) &&(theta<2*PI)) &&( (phi>0.0) &&(phi<PI/2)) ) //5
{
  deltaX=(float) i+1.0-xin;
  deltaY=(float) j-yin;
  deltaZ=(float) k+1.0-zin;
}
if ( ((theta>PI) &&(theta<3*PI/2)) &&( (phi>0.0) &&(phi<PI/2)) ) //6
{

```

```

deltaX=(float) i-xin;
deltaY=(float) j-yin;
deltaZ=(float) k+1.0-zin;
}
if ( ((theta>3*PI/2) &&(theta<2*PI)) &&((phi>PI/2) &&(phi<PI)) ) //7
{
deltaX=(float) i+1.0-xin;
deltaY=(float) j-yin;
deltaZ=(float) k-zin;
}
if ( ((theta>PI) &&(theta<3*PI/2)) &&((phi>PI/2) &&(phi<PI)) ) //8
{
deltaX=(float) i-xin;
deltaY=(float) j-yin;
deltaZ=(float) k-zin;
}

di=sin(phi)*cos(theta);
dj=sin(phi)*sin(theta);
dk=cos(phi);

Path_Length=2.0;
TPL=deltaX/di;
if ((TPL<Path_Length) && (TPL>0.0)) Path_Length=TPL;
TPL=deltaY/dj;
if ((TPL<Path_Length) && (TPL>0.0)) Path_Length=TPL;
TPL=deltaZ/dk;
if ((TPL<Path_Length) && (TPL>0.0)) Path_Length=TPL;

xout=xin+Path_Length*di;
yout=yin+Path_Length*dj;
zout=zin+Path_Length*dk;

Number_density=(number_density+size[1]*size[2]*i+size[2]*j+k);
Scat_cross_section=(scat_cross_section+size[1]*size[2]*i+size[2]*j+k);
Mean_diam=(diameter+size[1]*size[2]*i+size[2]*j+k);

// Calculation of the length before the scattering point:
if ((fabs(Number_density-0.0)>1e-6) && (fabs(Scat_cross_section-0.0)>1e-6))
{
if (fabs(Number_density_0-0.0)>1e-6)
{nd_coeff = Number_density_0/Number_density;
l_before_scatter = nd_coeff*l_before_scatter;}

Number_density_0=Number_density;

// Scattering point determination:
while (l_before_scatter<Path_Length)
{
Scatter_Counter=Scatter_Counter+1;
Total_path_length=Total_path_length+l_before_scatter;

xin=xin+l_before_scatter*di;
yin=yin+l_before_scatter*dj;
zin=zin+l_before_scatter*dk;

// Droplet diameter determination:
drop_diameter=Mean_diam;
if (fabs(drop_diameter<1e-6)) drop_diameter=30;
}

```

```

// Scattering CPDF Array deduced:

    if(drop_diameter<= d1) CPDF=(CPDF1);
    if ((drop_diameter> d1) &&(drop_diameter<= d2)) CPDF=(CPDF2);
    if ((drop_diameter> d2) &&(drop_diameter<= d3)) CPDF=(CPDF3);
    if ((drop_diameter> d3) &&(drop_diameter<= d4)) CPDF=(CPDF4);
    if ((drop_diameter> d4) &&(drop_diameter<= d5)) CPDF=(CPDF5);
    if ((drop_diameter> d5) &&(drop_diameter<= d6)) CPDF=(CPDF6);
    if ((drop_diameter> d6) &&(drop_diameter<= d7)) CPDF=(CPDF7);
    if ((drop_diameter> d7) &&(drop_diameter<= d8)) CPDF=(CPDF8);
    if ((drop_diameter> d8) &&(drop_diameter<= d9)) CPDF=(CPDF9);
    if ((drop_diameter> d9) &&(drop_diameter<= d10)) CPDF=(CPDF10);
    if ((drop_diameter> d10) &&(drop_diameter<= d11)) CPDF=(CPDF11);
    if ((drop_diameter> d11) &&(drop_diameter<= d12)) CPDF=(CPDF12);
    if ((drop_diameter> d12) &&(drop_diameter<= d13)) CPDF=(CPDF13);
    if ((drop_diameter> d13) &&(drop_diameter<= d14)) CPDF=(CPDF14);
    if ((drop_diameter> d14) &&(drop_diameter<= d15)) CPDF=(CPDF15);
    if ((drop_diameter> d15) &&(drop_diameter<= d16)) CPDF=(CPDF16);
    if ((drop_diameter> d16) &&(drop_diameter<= d17)) CPDF=(CPDF17);
    if ((drop_diameter> d17) &&(drop_diameter<= d18)) CPDF=(CPDF18);
    if ((drop_diameter> d18) &&(drop_diameter<= d19)) CPDF=(CPDF19);
    if ((drop_diameter> d19) &&(drop_diameter<= d20)) CPDF=(CPDF20);
    if ((drop_diameter> d20) &&(drop_diameter<= d21)) CPDF=(CPDF21);
    if ((drop_diameter> d21) &&(drop_diameter<= d22)) CPDF=(CPDF22);
    if ((drop_diameter> d22) &&(drop_diameter<= d23)) CPDF=(CPDF23);
    if ((drop_diameter> d23) &&(drop_diameter<= d24)) CPDF=(CPDF24);
    if ((drop_diameter> d24) &&(drop_diameter<= d25)) CPDF=(CPDF25);

// Scattering angle determination:

    Rn_theta_prim=ran2(&idum);
    theta_prim=Rn_theta_prim*(2.00*PI);

    Rn_phi_prim=ran2(&idum);
    for (count=0;count<Scat_CPDF_Size;count++)
    {
        if ((Rn_phi_prim>*(CPDF+count)) &&(Rn_phi_prim<=*(CPDF+count+1)))
        {
            coeff1=*(CPDF+count);
            coeff2=*(CPDF+count+1);

            Delta_coeff=coeff2-coeff1;
            phi_prim_max=(float)(count+1)*phi_prim_reso;
            phi_prim_min=(float)count*phi_prim_reso;
            break;
        }
    }
    phi_prim=phi_prim_min*(Rn_phi_prim-coeff1)/Delta_coeff+
        phi_prim_max*(coeff2-Rn_phi_prim)/Delta_coeff;

    if (fabs(phi_prim-0.0)<1e-6)          (phi_prim=1e-6);
    if (fabs(phi_prim-PI/2)<1e-6)        (phi_prim=PI/2-1e-6);
    if (fabs(phi_prim-PI)<1e-6)          (phi_prim=PI-1e-6);

    if (fabs(theta_prim-0.0)<1e-6)        (theta_prim=1e-6);
    if (fabs(theta_prim-PI/2)<1e-6)       (theta_prim=PI/2-1e-6);
    if (fabs(theta_prim-PI)<1e-6)         (theta_prim=PI-1e-6);
    if (fabs(theta_prim-3*PI/2)<1e-6)     (theta_prim=3*PI/2-1e-6);
    if (fabs(theta_prim-2*PI)<1e-6)       (theta_prim=2*PI-1e-6);

    du=sin(phi_prim)*cos(theta_prim);
    dv=sin(phi_prim)*sin(theta_prim);
    dw=cos(phi_prim);

    delta_k=1-dk*dk;

    if (delta_k>0.0)
    {

```

```

delta_k=sqrt(delta_k);
di_prim=(di*dk*du-dj*dv)/delta_k+di*dw;
dj=(dj*dk*du+di*dv)/delta_k+dj*dw;
dk=dk*dw-delta_k*du;
di=di_prim;
}
else
{
if (dk>0.0)
{di=du; dj=dv; dk=dw;}
else
{di=du; dj=dv; dk=-dw;}
}

ijk_vector=di*di+dj*dj+dk*dk;

if (fabs(ijk_vector-1.0)>=1e-10)
{
ijk_vector=sqrt(ijk_vector);
di=di/ijk_vector;
dj=dj/ijk_vector;
dk=dk/ijk_vector;
}

if (dk>=1.0) dk=1.0-(1e-10);
if (dk<=-1.0) dk=(1e-10)-1.0;

phi=acos(dk);
if (fabs(phi-0.0)<1e-6) (phi=1e-6);
if (fabs(phi-PI/2)<1e-6) (phi=PI/2-1e-6);
if (fabs(phi-PI)<1e-6) (phi=PI-1e-6);

if ((di>=0.0) && (dj>=0.0)) //1,3
{
dj=dj/sin(phi);
if (dj>=1.0) dj=1.0-1e-10;
if (dj<=-1.0) dj=1e-10-1.0;
theta=asin(dj);
}
if ((di<0.0) && (dj>=0.0)) //2,4
{
dj=dj/sin(phi);
if (dj>=1.0) dj=1.0-1e-10;
if (dj<=-1.0) dj=1e-10-1.0;
theta=PI-asin(dj);
}
if ((di>=0.0) && (dj<0.0)) //5,7
{
dj=dj/sin(phi);
if (dj>=1.0) dj=1.0-1e-10;
if (dj<=-1.0) dj=1e-10-1.0;
theta=2*PI+asin(dj);
}
if ((di<0.0) && (dj<0.0)) //6,8
{
dj=dj/sin(phi);
if (dj>=1.0) dj=1.0-1e-10;
if (dj<=-1.0) dj=1e-10-1.0;
theta=PI-asin(dj);
}

if (fabs(theta-0.0)<1e-6) (theta=1e-6);
if (fabs(theta-PI/2)<1e-6) (theta=PI/2-1e-6);
if (fabs(theta-PI)<1e-6) (theta=PI-1e-6);
if (fabs(theta-3*PI/2)<1e-6) (theta=3*PI/2-1e-6);
if (fabs(theta-2*PI)<1e-6) (theta=2*PI-1e-6);

//New cell exit point calculation:

di=sin(phi)*cos(theta);
dj=sin(phi)*sin(theta);
dk=cos(phi);

```

```

if ( ((theta>0.0) &&(theta<PI/2)) &&( (phi>0.0) &&(phi<PI/2)) ) // 1
{
  deltaX=(float) i+1.0-xin;
  deltaY=(float) j+1.0-yin;
  deltaZ=(float) k+1.0-zin;
}
if ( ((theta>PI/2) &&(theta<PI)) &&( (phi>0.0) &&(phi<PI/2)) ) // 2
{
  deltaX=(float) i-xin;
  deltaY=(float) j+1.0-yin;
  deltaZ=(float) k+1.0-zin;
}
if ( ((theta>0.0) &&(theta<PI/2)) &&( (phi>PI/2) &&(phi<PI)) ) // 3
{
  deltaX=(float) i+1.0-xin;
  deltaY=(float) j+1.0-yin;
  deltaZ=(float) k-zin;
}
if ( ((theta>PI/2) &&(theta<PI)) &&( (phi>PI/2) &&(phi<PI)) ) // 4
{
  deltaX=(float) i-xin;
  deltaY=(float) j+1.0-yin;
  deltaZ=(float) k-zin;
}
if ( ((theta>3*PI/2) &&(theta<2*PI)) &&( (phi>0.0) &&(phi<PI/2)) ) // 5
{
  deltaX=(float) i+1.0-xin;
  deltaY=(float) j-yin;
  deltaZ=(float) k+1.0-zin;
}
if ( ((theta>PI) &&(theta<3*PI/2)) &&( (phi>0.0) &&(phi<PI/2)) ) // 6
{
  deltaX=(float) i-xin;
  deltaY=(float) j-yin;
  deltaZ=(float) k+1.0-zin;
}
if ( ((theta>3*PI/2) &&(theta<2*PI)) &&( (phi>PI/2) &&(phi<PI)) ) // 7
{
  deltaX=(float) i+1.0-xin;
  deltaY=(float) j-yin;
  deltaZ=(float) k-zin;
}
if ( ((theta>PI) &&(theta<3*PI/2)) &&( (phi>PI/2) &&(phi<PI)) ) // 8
{
  deltaX=(float) i-xin;
  deltaY=(float) j-yin;
  deltaZ=(float) k-zin;
}

Path_Length=2.0;
TPL=deltaX/di;
if ((TPL<Path_Length) && (TPL>0.0)) Path_Length=TPL;
TPL=deltaY/dj;
if ((TPL<Path_Length) && (TPL>0.0)) Path_Length=TPL;
TPL=deltaZ/dk;
if ((TPL<Path_Length) && (TPL>0.0)) Path_Length=TPL;

xout=xin+Path_Length*di;
yout=yin+Path_Length*dj;
zout=zin+Path_Length*dk;

l_before_scat=(-log(ran2($idum))/(Number_density*Scat_cross_section))/Coeff;
}

l_before_scat=l_before_scat-Path_Length;

} //end of number density=10

Total_path_lenght=Total_path_lenght+Path_Length;

```

```

if (fabs(xout-i)<1e-6)
xout=i;
if (fabs(yout-j)<1e-6)
yout=j;
if (fabs(zout-k)<1e-6)
zout=k;
if (fabs(xout-(i+1))<1e-6)
xout=i+1;
if (fabs(yout-(j+1))<1e-6)
yout=j+1;
if (fabs(zout-(k+1))<1e-6)
zout=k+1;

if (xout>xin)
i=(int) floor(xout);
if ((xout<=xin) && (float)(xout-i)==0.0)
i=(int) floor(xout)-1;
if (yout>yin)
j=(int) floor(yout);
if ((yout<=yin) && (float)(yout-j)==0.0)
j=(int) floor(yout)-1;
if (zout>zin)
k=(int) floor(zout);
if ((zout<=zin) && (float)(zout-k)==0.0)
k=(int) floor(zout)-1;

if (photon_in_play(i,j,k)) goto photon_loop;

//Detection of the right photons:

if ( (fabs(xout-size[0])<1e-6) || (fabs(xout-0.0)<1e-6)
|| (fabs(yout-size[1])<1e-6) || (fabs(yout-0.0)<1e-6)
|| (fabs(zout-size[2])<1e-6) || (fabs(zout-0.0)<1e-6) )
{
//General multiple scattering detection:

Av_scat=(double) Av_scat+Scatter_Counter;
Av_lenght=Av_lenght+Total_path_lenght;

if (fabs(xout-size[0])<1e-6) {Xout_max=Xout_max+1; nb_photon=nb_photon+1;}
if (fabs(yout-size[1])<1e-6) {Yout_max=Yout_max+1; nb_photon=nb_photon+1;}
if (fabs(zout-size[2])<1e-6) {Zout_max=Zout_max+1; nb_photon=nb_photon+1;}

if (fabs(xout-0.0)<1e-6) {Xout_min=Xout_min+1; nb_photon=nb_photon+1;}
if (fabs(yout-0.0)<1e-6) {Yout_min=Yout_min+1; nb_photon=nb_photon+1;}
if (fabs(zout-0.0)<1e-6) {Zout_min=Zout_min+1; nb_photon=nb_photon+1;}

//General single scattering detection:

if (Scatter_Counter==1)
{Nb_single=Nb_single+1;
Av_lenght_single=Av_lenght_single+Total_path_lenght;}

if ((Scatter_Counter==1) && (fabs(xout-size[0])<1e-6)) Xout_max_1=Xout_max_1+1;
if ((Scatter_Counter==1) && (fabs(yout-size[1])<1e-6)) Yout_max_1=Yout_max_1+1;
if ((Scatter_Counter==1) && (fabs(zout-size[2])<1e-6)) Zout_max_1=Zout_max_1+1;

if ((Scatter_Counter==1) && (fabs(xout-0.0)<1e-6)) Xout_min_1=Xout_min_1+1;
if ((Scatter_Counter==1) && (fabs(yout-0.0)<1e-6)) Yout_min_1=Yout_min_1+1;
if ((Scatter_Counter==1) && (fabs(zout-0.0)<1e-6)) Zout_min_1=Zout_min_1+1;

//General scattering orders detection:

if(Scatter_Counter==0) Scat0=Scat0+1;
if(Scatter_Counter==1) Scat1=Scat1+1;
if(Scatter_Counter==2) Scat2=Scat2+1;
if(Scatter_Counter==3) Scat3=Scat3+1;
if(Scatter_Counter==4) Scat4=Scat4+1;
if(Scatter_Counter==5) Scat5=Scat5+1;

```



```

    if (Scatter_Counter==6) Scat6=Scat6+1;
    if (Scatter_Counter==7) Scat7=Scat7+1;
    if (Scatter_Counter==8) Scat8=Scat8+1;
    if (Scatter_Counter==9) Scat9=Scat9+1;
    if (Scatter_Counter==10) Scat10=Scat10+1;
    if (Scatter_Counter==11) Scat11=Scat11+1;
    if (Scatter_Counter==12) Scat12=Scat12+1;
    if (Scatter_Counter==13) Scat13=Scat13+1;
    if (Scatter_Counter==14) Scat14=Scat14+1;
    if (Scatter_Counter==15) Scat15=Scat15+1;
    if (Scatter_Counter==16) Scat16=Scat16+1;
    if (Scatter_Counter==17) Scat17=Scat17+1;
    if (Scatter_Counter==18) Scat18=Scat18+1;
    if (Scatter_Counter>18) Scat_sup=Scat_sup+1;

    cos_theta=cos(theta);
    sin_theta=sin(theta);
    sin_phi=sin(phi);

// 2D arrays detection of SS and MS:

//On the Ymax face

    if ((fabs(yout-size[1])<1e-6) &&(sin_theta>cos_ap) &&(sin_phi>cos_ap))
    {

        ind_x=(int)floor((Coeff*xout)/Delta_x+0.5);
        ind_y=(int)floor((Coeff*zout)/Delta_y+0.5);

        if (ind_x<0) (ind_x=0);
        if (ind_x>X_MaxNumber) (ind_x=X_MaxNumber);
        if (ind_y<0) (ind_y=0);
        if (ind_y>Y_MaxNumber) (ind_y=Y_MaxNumber);

        Array_2D_MS_Ymax[ind_x][ind_y]=Array_2D_MS_Ymax[ind_x][ind_y]+1;
        if (Scatter_Counter==1)
        (ind_x=(int)floor((Coeff*xout)/Delta_x+0.5);
        ind_y=(int)floor((Coeff*zout)/Delta_y+0.5);
        Array_2D_SS_Ymax[ind_x][ind_y]=Array_2D_SS_Ymax[ind_x][ind_y]+1;
        )

//On the Xmin face

    if ((fabs(xout-0.0)<1e-6) &&(-cos_theta>cos_ap) &&(sin_phi>cos_ap))
    {

        ind_x=(int)floor((Coeff*yout)/Delta_x+0.5);
        ind_y=(int)floor((Coeff*zout)/Delta_y+0.5);

        if (ind_x<0) (ind_x=0);
        if (ind_x>X_MaxNumber) (ind_x=X_MaxNumber);
        if (ind_y<0) (ind_y=0);
        if (ind_y>Y_MaxNumber) (ind_y=Y_MaxNumber);

        Array_2D_MS_Ymin[ind_x][ind_y]=Array_2D_MS_Ymin[ind_x][ind_y]+1;
        if (Scatter_Counter==1)
        (ind_x=(int)floor((Coeff*xout)/Delta_x+0.5);
        ind_y=(int)floor((Coeff*zout)/Delta_y+0.5);
        Array_2D_SS_Ymin[ind_x][ind_y]=Array_2D_SS_Ymin[ind_x][ind_y]+1;
        )

//On the Xmax face

    if ((fabs(xout-size[0])<1e-6) &&(cos_theta>cos_ap) &&(sin_phi>cos_ap))
    {
//Area detection: on Xmax

        nb_photon_fwd=nb_photon_fwd+1;
        Av_lenght_fwd=Av_lenght_fwd+Total_path_lenght;
        Av_scatt_d=Av_scatt_d+Scatter_Counter;
        if (Scatter_Counter==0) Scat0_d=Scat0_d+1;
        if (Scatter_Counter==1) Scat1_d=Scat1_d+1;
        if (Scatter_Counter==2) Scat2_d=Scat2_d+1;
        if (Scatter_Counter==3) Scat3_d=Scat3_d+1;

```

```

    if (Scatter_Counter==4) Scat4_d=Scat4_d+1;
    if (Scatter_Counter==5) Scat5_d=Scat5_d+1;
    if (Scatter_Counter==6) Scat6_d=Scat6_d+1;
    if (Scatter_Counter==7) Scat7_d=Scat7_d+1;
    if (Scatter_Counter==8) Scat8_d=Scat8_d+1;
    if (Scatter_Counter==9) Scat9_d=Scat9_d+1;
    if (Scatter_Counter==10) Scat10_d=Scat10_d+1;
    if (Scatter_Counter==11) Scat11_d=Scat11_d+1;
    if (Scatter_Counter==12) Scat12_d=Scat12_d+1;
    if (Scatter_Counter==13) Scat13_d=Scat13_d+1;
    if (Scatter_Counter==14) Scat14_d=Scat14_d+1;
    if (Scatter_Counter==15) Scat15_d=Scat15_d+1;
    if (Scatter_Counter==16) Scat16_d=Scat16_d+1;
    if (Scatter_Counter==17) Scat17_d=Scat17_d+1;
    if (Scatter_Counter==18) Scat18_d=Scat18_d+1;
    if (Scatter_Counter>18) Scat_sup_d=Scat_sup_d+1;

    ind_x=(int) floor((Coeff*yout)/Delta_x+0.5);
    ind_y=(int) floor((Coeff*zout)/Delta_y+0.5);

    if (ind_x<0) (ind_x=0;);
    if (ind_x>X_MaxNumber) (ind_x=X_MaxNumber;);
    if (ind_y<0) (ind_y=0;);
    if (ind_y>Y_MaxNumber) (ind_y=Y_MaxNumber;);

    Array_2D_MS_Xmax[ind_x][ind_y]=Array_2D_MS_Xmax[ind_x][ind_y]+1;
    if (Scatter_Counter==1)
    ( ind_x=(int) floor((Coeff*yout)/Delta_x+0.5);
      ind_y=(int) floor((Coeff*zout)/Delta_y+0.5);
      Array_2D_SS_Xmax[ind_x][ind_y]=Array_2D_SS_Xmax[ind_x][ind_y]+1;
    )

    } //end of right detection

} //end of Photon loop

} //end of Source loop

// Record data into files:

printf("\n\nXout_max=%d",Xout_max);
printf("\n\nYout_max=%d",Yout_max);
printf("\n\nZout_max=%d",Zout_max);
printf("\n\nXout_min=%d",Xout_min);
printf("\n\nYout_min=%d",Yout_min);
printf("\n\nZout_min=%d",Zout_min);

P_Xmax=(float) Xout_max/Total_photon_number*100;
P_Xmin=(float) Xout_min/Total_photon_number*100;
P_Ymax=(float) Yout_max/Total_photon_number*100;
P_Ymin=(float) Yout_min/Total_photon_number*100;
P_Zmax=(float) Zout_max/Total_photon_number*100;
P_Zmin=(float) Zout_min/Total_photon_number*100;
Sum=P_Xmax+P_Xmin+P_Ymax+P_Ymin+P_Zmax+P_Zmin;
Av_scat=(double) Av_scat/Total_photon_number;
Av_lenght=(double) Coeff*Av_lenght/Total_photon_number;
fprintf(fph, "\nGeneral Detection:\n\n");
fprintf(fph, "Number of photon sent: %ld\n", Total_photon_number);
fprintf(fph, "Number of photon detected: %ld", nb_photon);
fprintf(fph, "\n\nDetection on the faces:\n");
fprintf(fph, "Percentage xout max: %f %\n", P_Xmax);
fprintf(fph, "Percentage xout min: %f %\n", P_Xmin);
fprintf(fph, "Percentage yout max: %f %\n", P_Ymax);
fprintf(fph, "Percentage yout min: %f %\n", P_Ymin);
fprintf(fph, "Percentage zout max: %f %\n", P_Zmax);
fprintf(fph, "Percentage zout min: %f %\n", P_Zmin);
fprintf(fph, "Sum: %lf ", Sum);
fprintf(fph, "\n\nAverage scat order: %lf\n", Av_scat);
fprintf(fph, "Mean path length: %lf mm\n\n", Av_lenght);

```

```

if (Nb_single==0)Nb_single=1;
P_Xmax=(float) Xout_max_1/Nb_single*100;
P_Xmin=(float) Xout_min_1/Nb_single*100;
P_Ymax=(float) Yout_max_1/Nb_single*100;
P_Ymin=(float) Yout_min_1/Nb_single*100;
P_Zmax=(float) Zout_max_1/Nb_single*100;
P_Zmin=(float) Zout_min_1/Nb_single*100;
Sum=P_Xmax+P_Xmin+P_Ymax+P_Ymin+P_Zmax+P_Zmin;
Av_lenght_single=(double) Coeff*Av_lenght_single/Nb_single;
fprintf(fph,"*****");
fprintf(fph,"\n\nGeneral Single Scattering (SS) Detection:");
fprintf(fph,"\n\nTotal number SS: %ld",Nb_single);
fprintf(fph,"\n\nDetection on the faces:\n");
fprintf(fph,"Percentage xout max: %f %\n",P_Xmax);
fprintf(fph,"Percentage xout min: %f %\n",P_Xmin);
fprintf(fph,"Percentage yout max: %f %\n",P_Ymax);
fprintf(fph,"Percentage yout min: %f %\n",P_Ymin);
fprintf(fph,"Percentage zout max: %f %\n",P_Zmax);
fprintf(fph,"Percentage zout min: %f %\n",P_Zmin);
fprintf(fph,"Sum: %lf ",Sum);
fprintf(fph,"\n\nMean path length SS: %lf mm\n\n",Av_lenght_single);

P0=(float) Scat0/Total_photon_number*100;
P1=(float) Scat1/Total_photon_number*100; P2=(float) Scat2/Total_photon_number*100;
P3=(float) Scat3/Total_photon_number*100; P4=(float) Scat4/Total_photon_number*100;
P5=(float) Scat5/Total_photon_number*100; P6=(float) Scat6/Total_photon_number*100;
P7=(float) Scat7/Total_photon_number*100; P8=(float) Scat8/Total_photon_number*100;
P9=(float) Scat9/Total_photon_number*100; P10=(float) Scat10/Total_photon_number*100;
P11=(float) Scat11/Total_photon_number*100; P12=(float) Scat12/Total_photon_number*100;
P13=(float) Scat13/Total_photon_number*100; P14=(float) Scat14/Total_photon_number*100;
P15=(float) Scat15/Total_photon_number*100; P16=(float) Scat16/Total_photon_number*100;
P17=(float) Scat17/Total_photon_number*100; P18=(float) Scat18/Total_photon_number*100;
Psup=(float) Scat_sup/Total_photon_number*100;
Psum=P0+P1+P2+P3+P4+P5+P6+P7+P8+P9+P10+P11+P12+P13+P14+P15+P16+P17+P18+Psup;
fprintf(fph,"*****");
fprintf(fph,"\n\nGeneral Scattering Orders Detection:\n\n");
fprintf(fph,"General Detection:\n");
fprintf(fph,"Scat0:\t%f \n",P0);
fprintf(fph,"Scat1:\t%f \n",P1); fprintf(fph,"Scat2:\t%f \n",P2);
fprintf(fph,"Scat3:\t%f \n",P3); fprintf(fph,"Scat4:\t%f \n",P4);
fprintf(fph,"Scat5:\t%f \n",P5); fprintf(fph,"Scat6:\t%f \n",P6);
fprintf(fph,"Scat7:\t%f \n",P7); fprintf(fph,"Scat8:\t%f \n",P8);
fprintf(fph,"Scat9:\t%f \n",P9); fprintf(fph,"Scat10:\t%f \n",P10);
fprintf(fph,"Scat11:\t%f \n",P11); fprintf(fph,"Scat12:\t%f \n",P12);
fprintf(fph,"Scat13:\t%f \n",P13); fprintf(fph,"Scat14:\t%f \n",P14);
fprintf(fph,"Scat15:\t%f \n",P15); fprintf(fph,"Scat16:\t%f \n",P16);
fprintf(fph,"Scat17:\t%f \n",P17); fprintf(fph,"Scat18:\t%f \n",P18);
fprintf(fph,"Scat>18:%f \n",Psup);
fprintf(fph,"Total percentage: %f \n\n",Psum);

if(nb_photon_fwd==0) nb_photon_fwd=1;
P0=(float) Scat0_d/nb_photon_fwd*100;
P1=(float) Scat1_d/nb_photon_fwd*100; P2=(float) Scat2_d/nb_photon_fwd*100;
P3=(float) Scat3_d/nb_photon_fwd*100; P4=(float) Scat4_d/nb_photon_fwd*100;
P5=(float) Scat5_d/nb_photon_fwd*100; P6=(float) Scat6_d/nb_photon_fwd*100;
P7=(float) Scat7_d/nb_photon_fwd*100; P8=(float) Scat8_d/nb_photon_fwd*100;
P9=(float) Scat9_d/nb_photon_fwd*100; P10=(float) Scat10_d/nb_photon_fwd*100;
P11=(float) Scat11_d/nb_photon_fwd*100; P12=(float) Scat12_d/nb_photon_fwd*100;
P13=(float) Scat13_d/nb_photon_fwd*100; P14=(float) Scat14_d/nb_photon_fwd*100;
P15=(float) Scat15_d/nb_photon_fwd*100; P16=(float) Scat16_d/nb_photon_fwd*100;
P17=(float) Scat17_d/nb_photon_fwd*100; P18=(float) Scat18_d/nb_photon_fwd*100;
Psup=(float) Scat_sup_d/nb_photon_fwd*100;
Psum=P0+P1+P2+P3+P4+P5+P6+P7+P8+P9+P10+P11+P12+P13+P14+P15+P16+P17+P18+Psup;
Av_lenght_fwd=(double) Coeff*Av_lenght_fwd/nb_photon_fwd;
Av_scat_d=(double) Av_scat_d/nb_photon_fwd;
Ratio_If_Ii=(double) nb_photon_fwd/Total_photon_number;
fprintf(fph,"*****\n");
fprintf(fph,"\n\nScattering Orders on the Detection Area:\n\n");
fprintf(fph,"Scat0:\t%f \n",P0);
fprintf(fph,"Scat1:\t%f \n",P1); fprintf(fph,"Scat2:\t%f \n",P2);
fprintf(fph,"Scat3:\t%f \n",P3); fprintf(fph,"Scat4:\t%f \n",P4);
fprintf(fph,"Scat5:\t%f \n",P5); fprintf(fph,"Scat6:\t%f \n",P6);
fprintf(fph,"Scat7:\t%f \n",P7); fprintf(fph,"Scat8:\t%f \n",P8);
fprintf(fph,"Scat9:\t%f \n",P9); fprintf(fph,"Scat10:\t%f \n",P10);

```

```

fprintf(fph,"Scat11:\t%f \n",P11);   fprintf(fph,"Scat12:\t%f \n",P12);
fprintf(fph,"Scat13:\t%f \n",P13);   fprintf(fph,"Scat14:\t%f \n",P14);
fprintf(fph,"Scat15:\t%f \n",P15);   fprintf(fph,"Scat16:\t%f \n",P16);
fprintf(fph,"Scat17:\t%f \n",P17);   fprintf(fph,"Scat18:\t%f \n",P18);
fprintf(fph,"Scat>18:%f \n",Psup);
fprintf(fph,"Total percentage: %f \n",Psum);
fprintf(fph,"\nMean free path length detect: %lf mm\n",Av_lenght_fwd);
fprintf(fph,"Average scat order detected: %lf\n",Av_scat_d);
fprintf(fph,"Attenuation Ii/If: %lf\n",Ratio_If_Ii);

for (ind_x=0;ind_x<X_MaxNumber;ind_x++)
{
  fprintf(XmaxSS,"\n");
  fprintf(YmaxSS,"\n");
  fprintf(YminSS,"\n");
  fprintf(XmaxMS,"\n");
  fprintf(YmaxMS,"\n");
  fprintf(YminMS,"\n");

  for (ind_y=0;ind_y<Y_MaxNumber;ind_y++)
  {
    fprintf(XmaxSS,"%d\t",Array_2D_SS_Xmax[ind_x][ind_y]);
    fprintf(YmaxSS,"%d\t",Array_2D_SS_Ymax[ind_x][ind_y]);
    fprintf(YminSS,"%d\t",Array_2D_SS_Ymin[ind_x][ind_y]);

    fprintf(XmaxMS,"%d\t",Array_2D_MS_Xmax[ind_x][ind_y]);
    fprintf(YmaxMS,"%d\t",Array_2D_MS_Ymax[ind_x][ind_y]);
    fprintf(YminMS,"%d\t",Array_2D_MS_Ymin[ind_x][ind_y]);
  }
}

printf("\nTotal photon detected:%ld\n",nb_photon);
printf("\nBien joue Ed !!!\n\n");

// Close files:

fclose(fph);
fclose(fout);

return;
}

```

```

/*****
*****/

```